

# OPTICAL NEURAL INTERFACES FOR OPTOGENETIC INTERROGATION

by

Ronald W. Boutte

A dissertation submitted to the faculty of  
The University of Utah  
in partial fulfillment of the requirements for the degree of

Doctor of Philosophy

Department of Electrical and Computer Engineering

The University of Utah

May 2018

Copyright © Ronald W. Boutte 2018

All Rights Reserved

## STATEMENT OF DISSERTATION APPROVAL

by **Florian Solzbacher**, Chair/Dean of  
the Department/College/School of **Electrical and Computer Engineering**  
and by **David B. Kieda**, Dean of The Graduate School.

# ABSTRACT

Precise optical neural stimulation is an essential element in the use of optogenetics to elicit predictable neural action potentials within the brain, but accessing specific neocortical layers, light scattering, columniation, and ease of tissue damage pose unique challenges to the device engineer. This dissertation presents the design, simulation, microfabrication, and characterization of the Utah Optrode Array (UOA) for precise neural tissue targeting through three main objectives:

1. Maskless wafer-level microfabrication of optical penetrating neural arrays out of soda-lime glass: Utah Optrode Array.
2. Utah Optrode Array customization using stereotactic brain atlases and 3D CAD modeling for optogenetic neocortical interrogation in small rodents and nonhuman primates.
3. Single optrode characterization of the UOA for neocortical illumination.

Maskless microfabrication techniques were used to create 169 individual  $9 \times 9$  arrays  $3.85 \text{ mm} \times 3.85 \text{ mm}$  with 1.1 mm long optrodes from a single two inch glass wafer. The  $9 \times 9$  UOA was too large for precise targeting of the upper layers of the cortex in smaller animals such as mice, so an array customization method was developed using Solidworks and off-the-shelf brain atlases to create  $8 \times 6$  arrays  $3.45 \text{ mm} \times 2.45 \text{ mm}$  with  $400 \text{ }\mu\text{m}$  long optrodes. Stereotactic atlases were imported into Solidworks, splined, and lofted together to create a single 3D CAD model of a specific region of interest in the brain. Chronic and acute brain trauma showed excellent results for the  $8 \times 6$  arrays in C57BL/6 wild-type mice (*Mus musculus*) and macaque monkey (*Macaca fascicularis*).

Simulation, characterization, and radiometric testing of a single optrode of the  $9 \times 9$  array was necessary to prove the ability to transmit light directly to specific tissue. Zemax optical design software was used to predict the light transmission capabilities, and then these results were compared to actual bench-top results. Insertion loss was both predicted and measured to be 3.7 dB. Power budgeting showed 9% of the light was lost at the interfaces



of the UOA's backplane and tip in air, and 48% was lost through back-scattering, leaving 43% transmitting through the optrode with no measurable taper loss. Scanning electron microscopy showed small amounts of devitrification of the glass, and atomic force microscopy showed average surface roughness to be 13.5 nm and a root mean square roughness of 20.6 nm. The output beam was profiled in fluorescein dye with a total divergence angle of  $63^\circ$  with a cross over distance to adjacent beams at 255  $\mu\text{m}$ .

For Beth

It's been a helluva ride this go-round.  
Here's to the next chapter of our lives together.

*If you're good at a sport, they attach the medals to your shirt and then they shine  
in some museum. That which is earned by doing good deeds is  
attached to the soul and shines elsewhere.*

—**Gino Bartali**

*It's fine to celebrate success, but it is more important to heed the lessons of failure.*

—**Theodore Harold “Ted” Maiman**

# CONTENTS

<b>ABSTRACT</b> .....	<b>iii</b>
<b>LIST OF FIGURES</b> .....	<b>x</b>
<b>LIST OF TABLES</b> .....	<b>xix</b>
<b>ACKNOWLEDGEMENTS</b> .....	<b>xx</b>
<b>CHAPTERS</b>	
<b>1. INTRODUCTION</b> .....	<b>1</b>
1.1 Scientific relevance .....	2
1.2 Motivation .....	3
1.3 Background .....	3
1.3.1 Human brain organization .....	4
1.3.2 Optogenetics primer .....	6
1.4 Scope .....	6
1.5 Dissertation outline .....	8
1.5.1 Literature review: Current state of optogenetic devices .....	9
1.5.2 Biomedical microdevices: UOA wafer-level microfabrication .....	9
1.5.3 Neurophotonics: UOA customization and 3D brain CAD modeling ....	11
1.5.4 Biomedical microdevices: UOA optical characterization .....	12
1.5.5 Virtual computer aided machining: Disco DAD3220 dicing recipes ....	13
1.5.6 Virtual brain modeling in Solidworks .....	13
1.6 References .....	14
<b>2. REVIEW OF THE OPTICAL NEURAL INTERFACE LITERATURE</b> .....	<b>16</b>
2.1 Inserted and implanted single optical fibers .....	17
2.2 Inserted and implanted monolithic arrays .....	21
2.3 Implanted cannula .....	24
2.4 Implanted LED arrays .....	25
2.5 Conclusion .....	30
2.6 References .....	30
<b>3. MASKLESS WAFER-LEVEL MICROFABRICATION OF OPTICAL PENETRATING NEURAL ARRAYS OUT OF SODA-LIME GLASS: UTAH OPTRODE ARRAY</b> .....	<b>36</b>
3.1 Abstract .....	37
3.2 Introduction .....	37
3.3 Utah Optrode Array fabrication .....	38
3.3.1 Creating soda-lime glass wafers .....	39

3.3.2	Distinguishing between float and rolled SLG . . . . .	39
3.3.3	Virtual CAD/CAM . . . . .	39
3.3.4	Precision dicing . . . . .	40
3.3.5	Wet etching . . . . .	40
3.3.6	Array removal from carrier wafer . . . . .	41
3.3.7	Furnace firing schedule . . . . .	41
3.4	Results . . . . .	42
3.4.1	Dicing observations . . . . .	42
3.4.2	Wet etching observations . . . . .	42
3.4.3	Firing observations . . . . .	43
3.5	Conclusion . . . . .	43
3.6	References . . . . .	44
<b>4.</b>	<b>UTAH OPTRODE ARRAY CUSTOMIZATION USING STEREOTACTIC BRAIN ATLASES AND 3D CAD MODELING FOR OPTOGENETIC NEOCORTICAL INTERROGATION IN SMALL RODENTS AND NONHUMAN PRIMATES . . . . .</b>	<b>45</b>
4.1	Abstract . . . . .	47
4.2	Introduction . . . . .	47
4.3	Methods . . . . .	47
4.3.1	Marmoset ( <i>Callithrix jacchus</i> ) . . . . .	48
4.3.1.1	Prototype high density $13 \times 13$ UOA with through glass via . . . . .	48
4.3.1.2	Marmoset <i>in vivo</i> $13 \times 13$ UOA insertion . . . . .	49
4.3.1.3	Marmoset electrophysiology through the TGV . . . . .	49
4.3.2	Stereotaxic atlas plate utility in UOA design . . . . .	49
4.3.3	Solidworks 3D modeling of the brain's region of interest . . . . .	49
4.3.4	Customization of an $8 \times 6$ UOA . . . . .	50
4.3.5	Macaque ( <i>Macaca fascicularis</i> ) . . . . .	50
4.3.5.1	Macaque <i>in vivo</i> $8 \times 6$ UOA insertion . . . . .	51
4.3.5.2	Macaque postexplantation histology . . . . .	51
4.3.6	C57BL/6 wild-type ( <i>Mus musculus</i> ) . . . . .	51
4.3.6.1	Mouse <i>in vivo</i> insertion preparation . . . . .	51
4.3.6.2	Mouse <i>in vivo</i> insertion of a UOA with a Holobundle light delivery system . . . . .	51
4.4	Results . . . . .	51
4.4.1	Atlas 3D CAD brain modeling . . . . .	51
4.4.2	Customized $8 \times 6$ UOA fabrication . . . . .	51
4.4.3	Marmoset V1 tissue damage assessment . . . . .	52
4.4.4	Macaque V4D histology . . . . .	52
4.4.5	Displaced tissue reduction by controlling optrode shape . . . . .	52
4.4.6	Mouse <i>in vivo</i> insertion of a UOA-Holobundle . . . . .	52
4.5	Conclusion . . . . .	53
4.6	Disclosures . . . . .	54
4.7	Acknowledgments . . . . .	54
4.8	References . . . . .	54

<b>5. SINGLE OPTRODE CHARACTERIZATION OF THE UTAH OPTRODE ARRAY FOR NEOCORTICAL ILLUMINATION</b>	<b>56</b>
5.1 Introduction	56
5.1.1 Background	57
5.1.2 Light transmission	58
5.2 Methods	60
5.2.1 Input to optrode beam characterization	60
5.2.2 Zemax simulation setup	62
5.2.3 Optrode optical alignment	65
5.2.4 Visual characterization	65
5.2.4.1 Optical microscopy	66
5.2.4.2 Scanning electron microscopy	67
5.2.4.3 Atomic force microscopy	67
5.2.5 Average power and insertion loss	67
5.2.5.1 Input power ( $P_{in}$ ) measurement method	67
5.2.5.2 Output power ( $P_{out}$ ) measurement method	68
5.2.5.3 Insertion loss ( $IL$ ) calculation	68
5.2.6 Aqueous fluorescein dye beam profiling	68
5.3 Results	68
5.3.1 Optical performance predictions using Zemax	69
5.3.2 Visual characterization	69
5.3.2.1 Optical microscopy	69
5.3.2.2 SEM micrographs	71
5.3.2.3 Chemical composition of raised bumps	72
5.3.2.4 Atomic force microscopy	73
5.3.2.5 Insertion loss	75
5.3.2.6 Aqueous fluorescein beam profiling	75
5.4 Conclusion	76
5.5 References	77
<b>6. CONCLUSIONS AND FUTURE WORK</b>	<b>81</b>
6.1 Maskless wafer-level microfabrication	82
6.2 Utah Optrode Array customization	83
6.3 Single optrode characterization	85
6.4 Future work	86
6.4.1 Hybrid computer brain interface	86
6.4.2 UOA fabrication process improvements	87
6.4.3 $2 \times 2$ Ferrule Port for chronic <i>in vivo</i> quasi-binary patterning	90
6.4.4 <i>In vivo</i> quasi-binary patterning with four MEMS switches and a single source laser	90
6.5 Final words	92
6.6 References	94
<b>APPENDICES</b>	
<b>A. VIRTUAL CAM: DISCO DAD-3220 DICING RECIPES</b>	<b>95</b>
<b>B. VIRTUAL BRAIN MODELING IN SOLIDWORKS</b>	<b>109</b>

## LIST OF FIGURES

1.1	The main objective of this research was to create an optical brain implant suitable for acute and chronic optogenetic studies. A three-part process was used for this research: 1. wafer-level microfabrication, 2. customization/implantation, and 3. bench-top testing/simulation. . . . .	1
1.2	2D coronal section of human occipital lobe adapted from [8], [11] showing key areas of the brain. The cerebral cortex contains the six layers of the neocortex made up of minicolumns. A UOA is inserted into the cerebral cortex with its optrodes penetrating into the neocortical layers. Light will be transmitted into these layers and the cells that express the light sensitive protein will respond to the light accordingly. . . . .	5
1.3	Neocortical ascending (shown in red) and descending (shown in blue) process flows adapted from [12]. Each transmission layer either transmits to the columnar neurons adjacent to it, or it transmits to layers above or below it, or it transmits to other functional neurons deeper in the brain, and Layer IV is the reception center for feedback signals. . . . .	5
1.4	Solid models of both the $9 \times 9$ and the $8 \times 6$ Utah Optrode Arrays (shown upside down for clarity). The $9 \times 9$ array is a general purpose optical brain interface that is used to transmit light from its backplane, through the optrode tips, and into neocortical Layers V and VI. The $8 \times 6$ is a customized UOA for the specific targeting of mouse motor cortex and nonhuman primate visual cortex. Both devices are fabricated using a common process borrowed from the microelectronics and glass polishing industries. . . . .	7
2.1	Coronal representation on the left shows the neocortex (A) being illuminated by a single optical fiber (B) through a craniotomy (C). Electrical recordings are made with a single microelectrode (D). The scalp flap (E) is secured during the surgery for implantation. An implanted single fiber optrode dental cemented in place (F) is shown on the right. The scalp flap (E) has been allowed to heal over the surgical wound. . . . .	18
2.2	Coronal representation on the left shows the neocortex (A) being illuminated by a $10 \times 10$ optrode array (B) through a craniotomy (C). This array is shown backlit with a fiber bundle (D). The scalp flap (E) is secured during the surgery for implantation. An implanted optrode/fiber bundle dental cemented in place (F) is shown on the right. The scalp flap (E) has been allowed to heal over the surgical wound. This setup is stable for fMRI (functional magnet resonance imaging) experiments where metal would adversely affect the test subject. . .	21
2.3	Coronal representation showing neocortical (A) illumination using a single optical cannula (B) that has been secured using dental cement (C). A single	

	optical fiber (D) is connected to the light source and then inserted into a ceramic or stainless steel ferrule (E). The test subject is allowed to recover from the implantation surgery and need only be tethered to the source fiber when needed for experiments. Animal mobility is greatly improved with the use of an optical rotary joint. . . . .	25
2.4	Coronal representation of neocortical (A) illumination using a $1 \times 16$ LED array (B) that has been secured using dental cement (C). The test subject is allowed to recover from the implantation surgery and need only be tethered to the source electrical signal when needed for experiments. Animal mobility is greatly improved with the use of an optical rotary joint. . . . .	28
3.1	3D CAD rendering of 169 UOAs provides for the foundational design considerations used in Virtual CAD/CAM during wet grinding operations. A square soda-lime-silica wafer ( $2.4 \text{ mm} \times 50.8 \text{ mm} \times 50.8 \text{ mm}$ ) is affixed to a round ( $76.4 \text{ mm} \times 0.500 \text{ mm}$ ) silicon carrier wafer with Dynatex WaferGrip. . . . .	38
3.2	Utah Optrode Array Wafer-Level Microfabrication Process . . . . .	39
3.3	Grinding progression using Virtual CAD/CAM for cutting tips, optrodes, and die singulation. (Top Left) A beveled blade is used to trench cut pyramidal tips by aligning the center of the blade on the edge of the wafer and then offsetting the first cut by $125 \mu\text{m}$ . It is necessary to skip $500 \mu\text{m}$ between two adjacent arrays. (Top Right) A flat $250 \mu\text{m}$ resin blade cuts optrodes by aligning the center of the blade to the first row of pyramidal tips and offsetting the first cut by $-200 \mu\text{m}$ . Three cuts are required between adjacent arrays. (Bottom Left) Arrays are singulated into individual $9 \times 9$ die with the same $250 \mu\text{m}$ resin blade. Optrode pitch is $400 \mu\text{m}$ , lengths are $1.4 \text{ mm}$ , pre-etch width is $150 \mu\text{m}$ , with a $500 \mu\text{m}$ backplane. (Bottom Right) Completely diced Utah Optrode Array ready for wet etching. . . . .	40
3.4	(Left) Three 8" tape rings are stacked on top of each so that they match the thickness of the rubber mat in the middle of the rings. This mat is good for SLG wafers up to $3.2 \text{ mm}$ thick. (Middle) The rubber mat holds a silicon carrier wafer upside down suspending the SLG wafer inside the square hole cut from the middle. (Right) Double stacked rubber mats shown for SLG wafers up to $6.4 \text{ mm}$ thick. Care must be taken when taping thick material for the spring loaded tape station bed to not press so hard that the silicon carrier wafer is crushed during taping. . . . .	41
3.5	Shows the average etch rate of $2.5 \mu\text{m} \cdot \text{min}^{-1} \pm 0.9 \mu\text{m} \cdot \text{min}^{-1}$ (mean $\pm$ SD) for Armour Etch on soda-lime-silica glass where each data point is 10 samples. . . . .	41
3.6	(Left) Rough shaped optrodes after orthogonal dicing where the optrode dimensions are $150 \mu\text{m} \times 1,600 \mu\text{m}$ with a $45^\circ$ pyramidal tip. (Middle) Optrodes after 20 minutes of wet etching using a 5-minute pattern, repeated 4 times, of applying Armour Etch, rinsing with tap water, and drying with dry nitrogen/air. At this stage, the optrodes show substantial surface roughness from sodium and lime removal from the bulk of the soda lime glass by the fluoride ions of the Armour Etch paste. Optrodes have been reduced in size	



	to $90\text{ }\mu\text{m} \times 1,600\mu\text{m}$ . (Right) Polishing arrays greatly improves the surface roughness, while annealing helps mechanically strengthen optrodes. Final optrode dimensions are $100\text{ }\mu\text{m} \times 1,100\text{ }\mu\text{m}$ with a $37\text{ }\mu\text{m}$ radius of curvature lens tip and a $2^\circ$ taper. ....	42
3.7	An experimental $13\text{ mm} \times 13\text{ mm}$ SLG wafer of $9 \times 9$ arrays. Hydraulic fracturing on the far left of the wafer. Hydraulic fracturing occurs when there is not enough uncut sacrificial material left to buffer the internal stress as it builds within the wafer and is hit by a cross-axis specimen flow of water of $0.5\text{ L}\cdot\text{min}^{-1}$ . A sacrificial row of $>750\text{ }\mu\text{m}$ is sufficient to protect the final row of optrodes from being damaged. ....	42
3.8	A completed $9 \times 9$ (Left) Utah Optrode Array, mounted on Kapton tape, showing high surface roughness from insufficient firing. (Right) Properly fired array. AFM shows optrode average roughness and RMS roughness to be $R_a = 13.5\text{ nm}$ and $R_q = 20.6\text{ nm}$ respectively, and it shows $R_a = 12.3\text{ nm}$ and $R_q = 16.4\text{ nm}$ for the array's base. ....	43
3.9	A completed $9 \times 9$ Utah Optrode Array with $1100\text{ }\mu\text{m} \times 100\text{ }\mu\text{m}$ optrodes and a $500\text{ }\mu\text{m}$ planar back-plane. Several key design features can be seen: a $2^\circ$ optrode taper and round cross section, a convex lens tip which allows for large tissue volume illumination, a flat back-plane which allows for insertion using Blackrock's multielectrode array inserter, and curved grooves on the front-plane which allow tissue irrigation during testing. ....	43
4.1	Stereotactic method for customizing Utah Optrode Arrays. (a) 3D CAD brain modeling of macaque V4D using Calabrese atlas plates with highlighted Paxinos regions. A $10\text{ mm}$ section of V4D is selected for 3D CAD Modeling, and the section's 23 atlas plates have been spaced at $450\text{ }\mu\text{m}$ simulating their location within the macaque brain. (b) Two 3D CAD models of the Utah Optrode Array shown virtually implanted in V4D ( $13 \times 13$ array with through glass via and a smaller $8 \times 6$ ); both devices are shown implanted into the 3D CAD brain model. (c) A completed soda-lime glass $8 \times 6$ UOA, and (d) histological results showing successful macaque V4D implantation. ....	48
4.2	(a) A $13 \times 13$ Solidworks 3D model of the high density Utah Optrode Array with a $\varnothing 1.5\text{ mm}$ through glass via (TGV). (b) High density array shown just prior to insertion resting on a marmoset's primary visual cortex after craniotomy and durotomy have been performed. (c) Postfixation tissue damage assessment shows the array caused vascular damage as well as damage from the trauma of insertion, where high amounts of tissue have been compressed between the array's optrodes. Histological assessment of tissue damage was not performed due to the level of tissue damage seen following device explantation. The white arrows mark the insertion location of a single $150\mu\text{m}$ electrode which was successful in recording neural spiking during postinsertion optrode illumination. Active neural action potentials indicated the neural tissue close to the optrodes around the TGV were still firing. ....	48
4.3	(a) A portion of the Calabrese atlas plates as captured from The Scalable Brain Atlas viewer showing the Paxinos region V4D in Solidworks with each of the Paxnos regions outlined with a B-spline. (b) Conceptualized Solidworks	

	3D model with lofts between the Paxinos regions of each plate of V4D shown between the starting and ending plates. (c) Sagittal view of the 3D model of V4D with insertion marks where the $8 \times 6$ array has been virtually inserted. The white arrows mark the centroid of interest for illumination of layer IV. . .	49
4.4	(Top left) Design parameters for both $13 \times 13$ and the $8 \times 6$ arrays set to the same scale. (Top right) Side-by-side comparison of the $13 \times 13$ high density array and the much smaller $8 \times 6$ UOA. Key differences are wider optrode spacing and the removal of all sharp edges that may contact neural tissue on the UOA. Note: (Bottom left) Volumetric representation of neural tissue surrounding optrodes. Each optrode compresses the tissue into the space between optrodes as they penetrate: (a) the $1.50 \text{ mm} \times 0.250 \text{ mm} \times 0.250 \text{ mm}$ optrode has a tissue volume to optrode volume of $2.58 : 1$ , (b) the $0.500 \text{ mm} \times 0.250 \text{ mm} \times 0.250 \text{ mm}$ optrode has a tissue volume to optrode volume of $2.92 : 1$ , and the $0.500 \text{ mm} \times \varnothing 0.075 \text{ mm}$ optrode has a tissue volume to optrode volume of $40.1 : 1$ . (Bottom right) Paxinos region V4D with laminae conceptualized showing array tips at the boundary of layers III and IV. . . . .	50
4.5	(a) A customized $8 \times 6$ Utah Optrode Array to specifically target layer IV of Paxinos macaque area V4D. The UOA is fabricated out of soda-lime microscope slides using maskless wafer-level microfabrication processes. (b) Post perfusion histochemical staining with cytochrome oxidase of sagittal sections of area V4D showed the array was successfully inserted into V4D and reached the boundary between layers III and IV, which would allow for illumination of layer IV during optogenetic studies. The same device was successfully used for holographic projection into motor cortex of the common mouse. . . . .	52
4.6	(a) View of the cortical connector from below after alignment, projecting a pattern of 7 lit fibers. (b) The cortical connector with the UOA implanted in a mouse. . . . .	53
5.1	Three areas of study were used to fully characterize the Utah Optrode Array. Zemax simulation was used to understand how the device would function as an optogenetic implant. Visual characterization techniques of optical microscopy, scanning electron microscopy, electron dispersion spectroscopy, and atomic force microscopy were used to understand the physical characteristics of the device. Radiometric testing techniques were used to quantify insertion loss and the beam's profile. . . . .	57
5.2	Optical bench testing setup: 1. Laserglow 473 nm laser fixed in place, 2. Stray light shroud, 3. Vertically adjustable neutral density filter, 4. Vertically adjustable 20X objective lens, 5. Sample holder with $10\mu\text{M}$ fluorescein, 6. 3-axis positioner, and 7. 3-axis sample positioners with a 5MP 20-200X digital microscope. Optional (OPT) FC/PC Fiber Coupler. To the right of the test setup is Newport Dual Channel Power Meter model 2832-C and the Laserglow power supply. . . . .	61
5.3	Measured spot radii are plotted in black showing the propagation length along the $z$ direction. A curve fit shown in blue is the measured data with minimized error of $0.4 \mu\text{m}$ . It is seen that the beam waist is $6.4 \mu\text{m}$ and its divergence angle is $\theta = 487 \text{ mRAD}$ . . . . .	62

5.4	The input beam's spot size was characterized using a CMOS image sensor. It appears to be a top-hat shape due to the lack of resolution at this scale, but beam profilometry shows the beam to be closer to Gaussian. . . . .	63
5.5	ImageJ's Beam Profiling plugin [46], [47] measured the spot size of Figure 5.4 to be 14.6 $\mu\text{m}$ at the output of the 20X Mitutoyo objective lens with a 97.3% ellipticity. . . . .	64
5.6	Zemax simulation parameters. Single optrode cross section showing the beam waist ( $w_0 = 10 \mu\text{m}$ ) used to calculate the divergence angle ( $\theta_{div} = 2^\circ$ ). The blue dashed line shows the Gaussian beam profile, and the solid blue lines show the point source simulation path. . . . .	65
5.7	Process for optical alignment through a single optrode (tips encircled in white). A 20-200X digital microscope is used to magnify the base of the optrodes (top left). The optrode is micropositioned to align a single optrode by transmitting a 473 nm laser spot through the back-plane into the base of the optrode. Front-lighting ensures the beam is correctly placed (top middle). Removing all ambient lighting allows for the beam to be imaged (top right). The process is repeated with the tips in focus (bottom row), and the beam is minimized through the tip. . . . .	66
5.8	A 3D CAD file was simulated in Zemax with a 2 $\mu\text{W}$ point source is centered at the back-plane. 0.855 $\mu\text{W}$ are projected onto the color detector for a 43% throughput. Cross-section analysis showed 51% of the light was reflected out of the back-plane. Predicted insertion loss is 3.7 dB from this simulation. . . . .	70
5.9	Keyence VHX-5000 was used to characterize the $9 \times 9$ UOA. Optrode lengths measure 1.1 mm, tapers $2^\circ$ , are 112 $\mu\text{m}$ wide, and have a back-plane (not shown) measuring 500 $\mu\text{m}$ . The array has trough depths of 131 $\mu\text{m}$ , and the tips have 37 $\mu\text{m}$ radii of curvature. . . . .	71
5.10	Scanning electron micrographs of a single optrode showing high surface roughness caused by nucleation known as devitrification. Portions of the bulk of the glass showed devitrification as well. . . . .	72
5.11	Despite low x-ray counts, EDS showed no contamination on the glass nucleation sites. High silicon, sodium, and calcium were all expected because of the constituent chemicals of soda-lime glass; oxygen was negligible due to the low counts. Nickel and magnesium appear to be either spurious readings due to the EDS process or trace elements and are not exclusive to some contamination. . . . .	73
5.12	Two locations on the round optrode were randomly selected for 100 $\mu\text{m}^2$ atomic force microscopy to quantify the surface roughness. AFM confirmed the high surface roughness, which could interfere with light transmission. Optrode curvature was negligible in these short scan lengths. AFM confirmed the high surface roughness and showed no patterning of the nucleation. High topography was measured at a maximum of 120 nm on sample #1 (top) and 98 nm on sample #2 (bottom). . . . .	74
5.13	Fluorescein dye laser profilometry. (Left) Blue (473 nm) collimated light fluoresces in aqueous fluorescein through a single optrode. Divergence angle	

	is $62^\circ$ , and it is predicted that beam cross over would occur at a depth of $255\text{ }\mu\text{m}$ . No light leakage is seen along the tapered portion of the optrode. (Right) Blue light straight through the back-plane and not through an optrode. It was shown that 91% transmission could be obtained through the back-plane for graduated illumination of tissue. . . . .	75
6.1	A completed $9 \times 9$ Utah Optrode Array with $1100\text{ }\mu\text{m} \times 100\text{ }\mu\text{m}$ optrodes and a $500\text{ }\mu\text{m}$ planar back-plane. Several key design features can be seen: a $2^\circ$ optrode taper and round cross section, a convex lens tip which allows for large tissue volume illumination, a flat back-plane which allows for insertion using Blackrock's multielectrode array inserter, and curved grooves on the front-plane which allow tissue irrigation during testing. Used by permission from Biomedical Microdevices [1]. . . . .	83
6.2	Fully rendered conceptual 3D model of a $3 \times 3$ hybrid computer brain interface (hCBI). The hCBI is capable of simultaneous illumination and electrical recording. Each optrode is individually addressed with a $\mu\text{LED}$ for independent illumination. . . . .	87
6.3	Process steps for the $3 \times 3$ hCBI: A. Soda-Lime Wafer Blank, B. Diced Tips, C. Shanks diced and wet etched, D. Metalization, E. Singulate metalization, F. Wet etch tips if needed, G. Flexible circuit board added, H. Conductive epoxy connects flex-print's traces to hybrid electrodes, I. $\mu\text{LED}$ Board added, J. Flexible/Wire-bond circuit board added, K. Paralene passivation of entire device, L. Etch passivation layer at tips. . . . .	88
6.4	Three error types had a negative impact on the overall UOA yield. A. Post-firing optrode fracture, B. Prefiring optrode hydraulic fracturing, and C. Over-temperature optrode sagging. . . . .	89
6.5	Cross section of the $2 \times 2$ Ferrule Port used to secure a single fiber optic patch cable with two pairs of $125\text{ }\mu\text{m}$ diameter fibers. A. Biocompatible threaded plastic port B. Threaded cap secures the compression ring (E.) in place around the outer diameter of the patch cable C. Optical fiber portion of the cannulae D. Shows the ceramic ferrule of the cannulae where bare fiber couples to the cannulae fibers. . . . .	91
6.6	Binary illumination with a single source and MEMS fiber optic switches: A. Single light source, B. $1 \times 4$ MEMS switch operated at its fastest rate creating a mock "always-on" signal, C. fiber optic MEMS on/off switches (qty. 4), and D. is a $2 \times 2$ Ferrule Port with $2 \times 2$ UOA. . . . .	92
6.7	Quasi-binary illumination patterning: A. is a mock "always-on" pattern generated by switching the $1 \times 4$ MEMS switch at its fastest rate, whereas B. is the quasi-binary pattern produced by a single on/off switch. By combining the four on/off switches it is possible to produce quasi-binary patterns such as 1000, 1100, 1110, 0111, etc. . . . .	93
A.1	The wafer stack $[W_S]$ and the glass wafer's $[W_T]$ thicknesses are measured and subtracted from each other yielding the "Tape thickness" $[T_t]$ for input into the Device Data screen of the DAD3220. It is more correct to call $T_t$ the "Effective Tape Thickness." . . . . .	96

A.2	Blade cross-section schematic showing key parameters for calculating “Blade Height” $[BH]$ . (Left) $B_w$ is the blade’s overall width supplied by the manufacturer; $B_f$ is the flat portion of the blade, and $\theta$ is the bevel’s angle also supplied by the blade’s manufacturer. (Right) $O_p$ is the optrodes’ pitch as supplied by the neuroscientist; $a$ is the half-width of the freshly cut optrodes; and $b$ is the pyramidal height of the optrodes’ tips. . . . .	97
A.3	Key parameters for calculating “Blade Height” $[BH]$ . (Left) The rough optrode length $[R_t]$ will lose 20% of its length, so the optrodes desired final length $[OPT_L]$ must be known from layers of interest within the animal under study. Backplane $[B_p]$ thickness is determined for structural stability during fabrication and insertion. (Right) The blade’s flat height $[Bf_h]$ is the distance from the front plane to the flat portion of the blade. $[b]$ is the aforementioned distance the blade must be lowered to get the desired optrode pitch. . . . .	98
A.4	$8 \times 6$ Tip Dicing with the Disco DAD 3220 “Device Data” screen. . . . .	100
A.5	$8 \times 6$ Virtual CAM worksheet for $60^\circ$ tips. . . . .	101
A.6	$8 \times 6$ “Device Data” entry items for $60^\circ$ tips. . . . .	102
A.7	$8 \times 6$ Shank Dicing with the Disco DAD 3220 “Device Data” screen. . . . .	103
A.8	$8 \times 6$ Virtual CAM worksheet for shanks. . . . .	104
A.9	$8 \times 6$ “Device Data” entry items for shanks. . . . .	105
A.10	$8 \times 6$ Array singulation with the Disco DAD 3220 “Device Data” screen. . . . .	106
A.11	$8 \times 6$ Virtual CAM worksheet for array singulation. . . . .	107
A.12	$8 \times 6$ “Device Data” entry items for array singulation. . . . .	108
B.1	The Scalable Brain Atlas [2] showing the Calabrese et al. [1] atlas plate with Paxinos V4D: Visual Area 4, Dorsal overlaid. This plate is 26.4 mm posterior of the anterior commissure. The Calabrese atlas has $75 \mu\text{m}$ MRI slices spaced at $450 \mu\text{m}$ ; these measurements will be transferred to Solidworks. . . . .	110
B.2	Planes are created, in Solidworks, for the screen captured atlas plates. Each plane is placed at $525 \mu\text{m}$ which is the MRI slices’ thicknesses of $75 \mu\text{m}$ and slice spacing at $450 \mu\text{m}$ . It is helpful to only create the visible portion of the plane roughly the same size as the atlas plate; this will reduce confusion later as more plates are added. . . . .	111
B.3	An atlas plate is place on Plane2 where the Paxinos [3] region for V4D is highlighted. The perimeter of this region is to be traced using the “Spline” sketch tool in Solidworks for each atlas plate in the region. Plane2’s perimeter is shown for alignment purposes of the plate. This will be turned off after the plate is positioned. . . . .	112
B.4	All atlas plates for V4D have been placed on planes. Each plane perimeter has been hidden from view, which makes the plates easier to see. In this manner, the plates can now individually be hidden from view as well, and this will make is easier to see the V4D’s perimeter on each plate to be splined. . . . .	113
B.5	A small portion of the V4D slice is shown with the regions’ perimeter splined	

	together. No two brains have the exact same shapes or sizes, so it is not necessary to be exact with the splining operation. Splines can be adjusted for better fit by moving the handles shown on the blue line. . . . .	114
B.6	Two plate splines are shown where one of the plates has been hidden for clarity. The larger spline is the next plate in the series as they were captured from The Scalable Atlas [2] viewer for the Calabrese et al. [1] macaque brain atlas.	115
B.7	Simultaneously viewing all splines can be confusing, but Solidworks allows for the area to be rotated for easier viewing. Each of these splined perimeters will be linked via the “Loft” command, which is the 3D version of the Spline command. . . . .	116
B.8	Lofting must not create overlapping shapes or else Solidworks will display an error. Overlapping loft errors can occur in brain modeling because the slice regions may change size rapidly. It is shown here that each spline has been connected properly with no errors. . . . .	117
B.9	Loft contour is seen in this image by dark shading on the virtual surface that has been created. Once each spline is lofted together, and the surface contours are shown, a solid model is automatically created at the same time. . . . .	118
B.10	Front view of the modeled V4D as spline/lofted together in Solidworks. Some error is seen in the image, but overall this model is sufficient for designing a computer brain interface. . . . .	119
B.11	Right view of V4D, where the concave nature of the region is clearly shown. There is a thin walled region in the center where it is critical to make sure the optrodes of the UOA do not penetrate. . . . .	120
B.12	Rear view of modeled V4D. . . . .	121
B.13	Left view of modeled V4D. . . . .	122
B.14	Front view of modeled V4D rendered in contrasting color. The contrast will highlight the implanted array’s optrodes when it is virtually inserted. . . . .	123
B.15	Front view of modeled V4D rendered in contrasting color with 13×13 UOA with through glass via. The TGV allows for a microelectrode to be passed, so electrical neurophysiological signals can be recorded. . . . .	124
B.16	Close up view of the 13×13 inserted on the surface. It is clear from the image that the 3D model cannot compress, so the implant rests tangentially against the tight radius of curvature of the tissue and the front-plane of the array. Microscopic scale peaks and valleys can be seen where the loft model was created. Contours are not actual sulci of the brain due to the scale of this model. . . . .	125
B.17	An important feature of the 3D model is that its transparency can be changed to allow the device engineer to “see inside” the virtual tissue to make sure the implant is fully contained in the region of interest. It can be seen here the UOA is fully enclosed in tissue, proving this device capable of inserting fully into the region. Tissue compression is not represented with this technique. . . .	126
B.18	The narrow cavity on the back side of V4D is shown with a UOA that does not	

fall completely within the boundary of the atlas plates; therefore, a redesign  
of the array is necessary to reduce the length of the optrodes to better target  
the neocortical layers of interest. . . . . 127

## LIST OF TABLES

2.1	Single Optical Fiber Optrodes . . . . .	19
2.2	Optrode Arrays . . . . .	22
2.3	Cannulae Optrodes . . . . .	26
2.4	Penetrating LEDs . . . . .	29
3.1	Furnace Firing Schedule. . . . .	41
4.1	Ratio of Volumetric Tissue Affected by a Single Optrode . . . . .	53
5.1	Neocortical Layers by Species Near 1 mm Deep (adapted from: [17]) . . . . .	71
A.1	Disco Diamond Blade Parameters . . . . .	99



## ACKNOWLEDGEMENTS

*Do you not know? Have you not heard? The Everlasting God, the Lord, the Creator of the ends of the earth does not become weary or tired. His understanding is inscrutable. He gives strength to the weary, and to him who lacks might He increases power. Though youths grow weary and tired, and vigorous young men stumble badly, yet those who wait for the Lord will gain new strength; they will mount up with wings like eagles, they will run and not get tired, they will walk and not become weary.*

### Isaiah 40:28-31

Pursuing the PhD has been one of the most difficult things I have done either academically or professionally. I have completed this while working full-time at Northrop Grumman Corporation. To all of you at Northrop Grumman, thank you so much for your support, and patience: Kelly Perkins, you have been one of my biggest proponents; without your mentorship and patience I would not have been able to complete this work. Shane Sammon, Mike Weems, and Dr. Charlie Volk, I have appreciated your support and the use of some of the tools available at work. Brandon Griffiths, you have helped me in so many ways that I cannot possibly repay your generosity.

I'd like to express gratitude for each of my academic colleagues from the University of Utah and Technion-Israel Institute of Technology. It was pleasure working with Dr. Tanya Abaya. I have spent 5 years working on the Utah Optrode Array, and there is not a day that goes by that I am more impressed with the novelty of the work you did and handed off to me. Rohit Sharma, Trent Parry, and Chase Vanderpool your direct support to the Utah Optrode Array project has helped me tremendously. Dr. Alessandra Angelucci and Dr. Sam Merlin, of the Moran Eye Center, without both of you the Utah Optrode Array would just be cut glass. I hope that my work has complemented your efforts in understanding how vision is processed in the brain. Dr. Ian Harvey, thank you for the help with the USTAR project funding and help in the Nanofab. Dr. Guy Yona, Dr. Shy Shoham, and Dr. Itamar Kahn I would like to thank you for your work and the opportunity to customize an array for

your Hollowbundle work. Collaborating with you all was a great experience. Finally, I have had the benefit of excellent university mentors: Dr. Gregory Clark, Dr. Cindy Furse, Dr. Florian Solzbacher, Dr. Prashant Tathireddy, and my committee chairman Dr. Steve Blair. Each of you are giants in your respective fields of study, and it has truly been a pleasure standing on your shoulders. I am especially grateful for the independence to pursue the items I valued as important to the Utah Optrode Array, but I have also valued the guidance that helped me see where I was going astray.

As a child, I watched as my grandfather struggled to get places in his wheelchair. He suffered a spinal cord injury while working, and he was paralyzed from the waist down. I used to help him in and out of the car, up the stairs to his barber, or even help empty his urinary leg bag. His struggle and resilience has always inspired me. As a father, I have watched my son struggle with epilepsy and Type 1 diabetes. One day I watched him as the paramedics struggled to wake him from a seizure. At first we all thought the seizure was caused by a low blood-glucose level, but when we checked his glucose, as he seized, we noticed he actually had a high blood-glucose level. Never have I felt so helpless. Epilepsy has kept my son from doing many of the things that most others take for granted like driving or riding a bike. Both my grandfather and my son's struggles with neurological tissue damage and disease motivated me to get involved in this project. I hope that my work on this project will live on and help others not need to witness their loved ones go through what mine went through.

I felt strongly enough about this research that in the absence of external financial support of the first 3.5 to 4 years I was able to leverage Northrop Grumman's tuition assistance program and my own personal funds to keep the project moving forward. I am extremely thankful for the USTAR funds for assisting in the fabrication of the  $8 \times 6$  optrode array by matching my company and personal funds for that work. I am also grateful for the NSF support I have received in the final year of my program under grant 1310564. This work would not have succeeded without these funds.

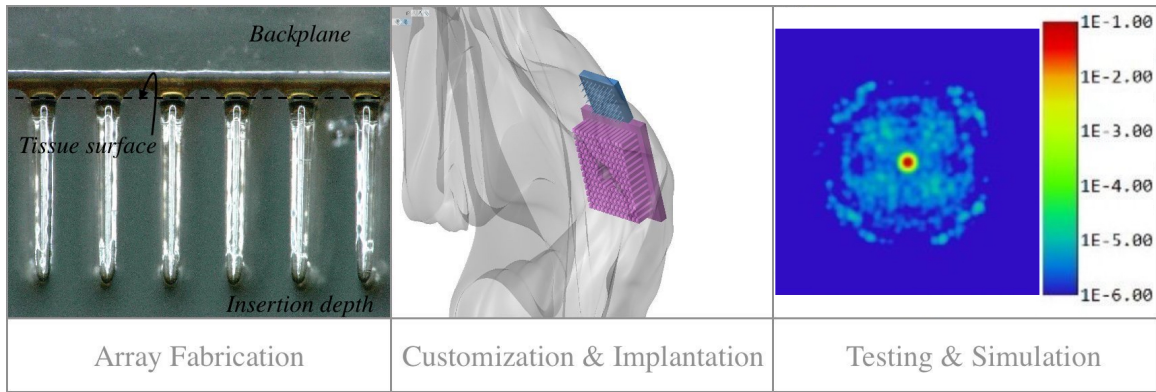
I would be remiss not to mention all the hassle Beth, Karen, Gavan, and Reagan have been through while I missed or limited my time at all those fun family things. I did my best as a husband, lover, and father to balance it all; hopefully we can all settle down now. I love you!

# CHAPTER 1

## INTRODUCTION

The subject of this dissertation is an optical neural interface, called the Utah Optrode Array (UOA), for spatiotemporal optogenetic illumination of the neocortical layers 0.300 mm–1.8 mm deep. Figure 1.1 shows the three aims and the flow of this research: 1. Improve the initial wafer-level microfabrication processes for  $9 \times 9$  UOAs, 2. Customize an  $8 \times 6$  UOA for *in vivo* insertion into mice motor and nonhuman primate visual cortices using 3D computer aided design (CAD) to model the brain regions of interest (ROI) and the array, and 3. Quantify the UOA’s insertion loss, sources of loss, and output illumination patterning, through bench-top testing and simulation of a single optrode. This UOA is suitable for acute studies for understanding brain function/processing as well as chronic behavioral studies.

Optogenetics is the control of neuronal ensembles by the introduction of light of various colors onto brain or central nervous tissue that has been genetically modified to respond



**Figure 1.1.** The main objective of this research was to create an optical brain implant suitable for acute and chronic optogenetic studies. A three-part process was used for this research: 1. wafer-level microfabrication, 2. customization/implantation, and 3. bench-top testing/simulation.

to the light, and it has quickly become the go-to method for understanding the brain and its functions since being named “Method of the Year” in 2010 [1]. In some instances the light is used to elicit neural activity by stimulating the neurons to fire, and in others the light is used to inhibit neuronal activity. By modulating the neural pathways of interest, the neuroscientist can map the pathway and eventually understand its morphology and functionality. It is hoped that by understanding the brain’s morphology and function that exciting new methods of healing traumatic injuries and curing disease can be developed.

## 1.1 Scientific relevance

The UOA will serve as the main support structure for a device that integrates light transmission, postsynaptic potential recording, and wireless signal transmission. It is the first device of its type to be mass-producible using standard processes borrowed from the microelectronic industry. This is an important step to bringing a stand-alone device to the optogenetics community at large. Most of today’s optogenetic studies utilize low count optical fibers/cannulae which are quite difficult to place at precise locations within the tissue; the UOA greatly simplifies this process by placing a high number of optrode tips at the same depth in tissue. Each optrode of the array is to be metalized for electrical action potential recording at the same location of stimulation. This will help the neuroscientist understand exactly how the animal’s physiology is responding to external stimuli. The location also reduces the error of recording with a separate electrode by reducing the distance from optrode to electrode. Each optrode will be independently backlit with an array of mounted light emitting diodes (LED). Individually addressable LEDs allows for spatial and temporal modulation of the neurons under study. A small flexible circuit will transmit action potentials off the array to a port or a future wireless antenna for signal processing.

A large portion of this research has been to understand many tissue damage causes and optimizing the design to reduce the damage. Optrode pitch and lateral spacing has been optimized to target cortical columns and reduce the damage from displaced tissue at the same time. A slight tapered optrode is designed to reduce the pressure placed on vasculature after insertion; it is thought that this will help in chronic applications with improved blood flow. Sharp edges have all been removed through the firing process, and strength has been added through the annealing process.

## 1.2 Motivation

According to a 2013 Christopher & Dana Reeve Foundation study approximately 5.4 million people are living with paralysis in the United States [2]. The report identifies several causes of spinal cord injuries leading to paralysis: motor vehicle accidents, physical labor, falls, sporting accidents, shooting and assault victims, and unknown causes. A similar study by the Centers for Disease Control shows 1.7 million traumatic brain injuries in the United States, where 52,000 died from their injuries, but the vast majority of patients received some form of unsuccessful medical care [3]. In addition to traumatic brain injuries (TBI) and central nervous system injuries (CNSI), the prevalence of neurological disorders (ND) is also very high. Diseases like Alzheimer's, Amyotrophic Lateral Sclerosis (ALS), brain tumors, Parkinson's, stroke, epilepsy, and others make up almost 1.5 million annual cases [4], [5]. It is foreseen that inroads into understanding the major mechanisms of CNSIs, TBIs, and many NDs can be made through the use of optogenetics as long as the optogenetic viral vectors and light can be precisely directed within the brain. The main motivation for this work is to assist neuroscientists in their quest to understand how the brain operates, and in turn help heal patients who suffer from CNSIs, TBIs, or NDs.

A recent Scientific American article forecasts the use of optogenetics in human clinical trials for chronic pain management, neurological disorders, and the study of neurodegenerative diseases such as Alzheimer's and Parkinson's [6], [7]. A common theme in this rapidly changing research environment is the need for a chronically implantable brain interface that can be easily customized.

## 1.3 Background

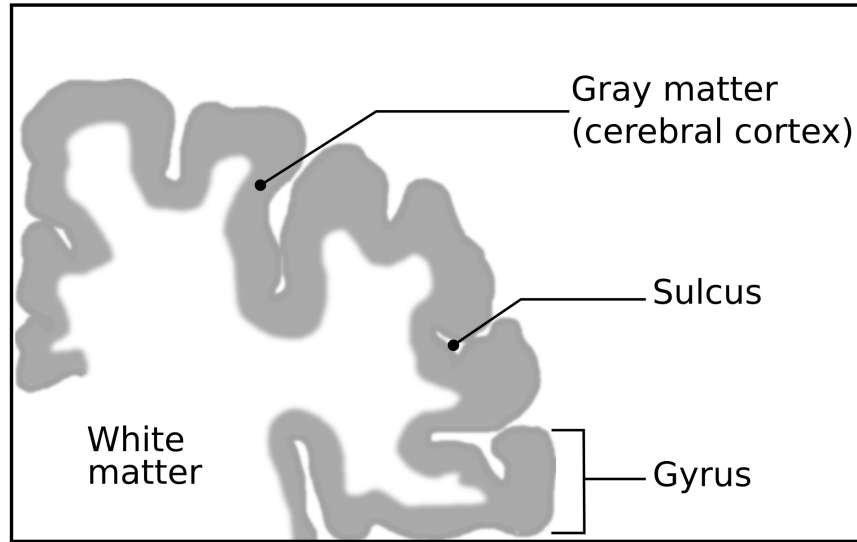
This section introduces a few items that will help create the knowledge for the later chapters of this dissertation such as an overview of the human brain organization and a primer on optogenetics. A brief word on the use of animal models in this research: Current comparative neuroanatomical understanding is that there are many similarities between all vertebrates, and that there is much to be learned from the brains of mice and nonhuman primates that directly applies to the brains of humans. Each vertebrate brain may have anatomical structures such as olfactory bulbs, somatosensory and motor cortices, and even though the sizes and numbers of dedicated neurons will vary from species to

species, the general functionality is believed to be the same because the neurons themselves are the same. For example, human neocortex is the same basic construct as the marmoset neocortex; therefore, there is a high-level of utility in the study of marmoset visual cortex to understand the human visual cortex.

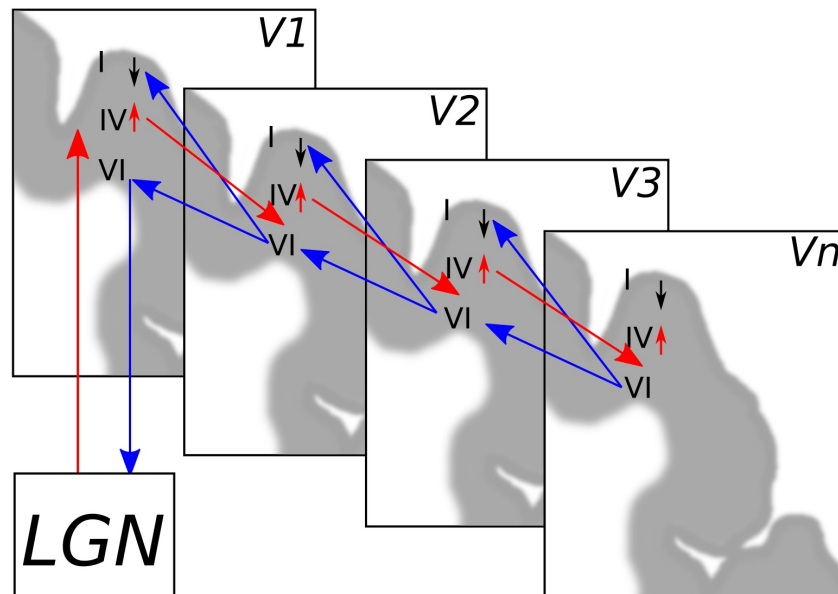
### 1.3.1 Human brain organization

The human brain is an extremely complex organ organized into three main parts: 1. the brainstem, 2. the cerebellum, and 3. the cerebrum [8]. The cerebrum is further divided into four lobes: 1. the occipital, 2. the temporal, 3. the parietal, and 4. the frontal. The frontal lobe is responsible for judgement, personality, speech recognition, movement, etc.; the parietal lobe processes senses like touch, vision, hearing, memory, etc. The interpretation of color vision, light, and movement is handled by the occipital lobe, and finally memory, hearing, organization, and understanding language is the responsibility of the temporal lobe. The brain’s surface—the cerebral cortex—is folded into gyri where the crevices are called sulci. The cerebral cortex is made up of six layers called the neocortex [9]. Mountcastle pointed out that the neocortex is a 3–4 mm thick tissue with surface area  $\sim 2600 \text{ cm}^2$  containing  $28 \times 10^9$  neurons. He further showed that the basic unit of the neocortex is the minicolumn, where in primates the neocortex contains  $\sim 80$ – $100$  neurons excluding the striate cortex where the number of neurons rises to  $\sim 200$ – $250$  per column [10]. Each minicolumn extends across Layers II through VI and connects to a major functional area within the brain. Figure 1.2 shows a 2D human coronal slice to illustrate the major structures of the brain, and Figure 1.3 shows the ascending and descending process flows of the neocortex.

There are two main cell types that make up the brain: glia and neurons, and there are four types of glia cells: astroglia, oligoglia, ependymal, and microglia [8]. Glia support the functioning of the neurons by providing support, blood-brain barrier regulation, digestion of dead portions of neurons, etc. There are many neuronal cell types, and they relay signals through bioelectrochemical “action potentials.” Neuroscientists measure the presence of action potentials to understand what causes them to fire; conversely neuroscientists measure the inhibition or cessation of action potentials to understand what causes that behavior. Neuroscientists believe that by controlling the on/off nature of the neuron they



**Figure 1.2.** 2D coronal section of human occipital lobe adapted from [8], [11] showing key areas of the brain. The cerebral cortex contains the six layers of the neocortex made up of minicolumns. A UOA is inserted into the cerebral cortex with its optrodes penetrating into the neocortical layers. Light will be transmitted into these layers and the cells that express the light sensitive protein will respond to the light accordingly.



**Figure 1.3.** Neocortical ascending (shown in red) and descending (shown in blue) process flows adapted from [12]. Each transmission layer either transmits to the columnar neurons adjacent to it, or it transmits to layers above or below it, or it transmits to other functional neurons deeper in the brain, and Layer IV is the reception center for feedback signals.

can understand how functional ROIs within the brain operate.

### 1.3.2 Optogenetics primer

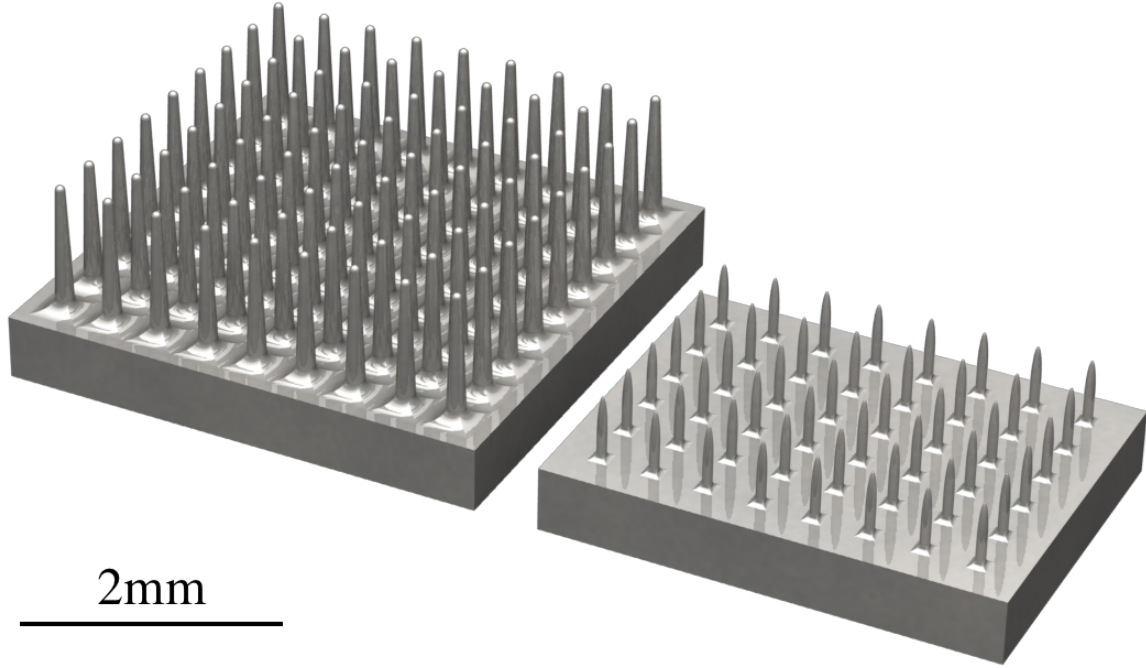
Optogenetics has been developed to interrogate the neurons within the column by genetically modifying the cells to respond to light. Optogenetic studies are a six-step process 1. Combine the light gated protein ion channel (opsin) of choice to a promoter. 2. Place the promoter/protein combination into a virus (typically a modified rabies virus). 3. Inject the virus in the brain and allow the virus to express the the opsin throughout the targeted tissue during the surgical recovery process. 4. Place optical illumination device; this can be an optical fiber, cannulae, or optrode array. 5. Transmit light into the tissue at the desired wavelengths using laser or LED. Multiple wavelengths can be combined for simultaneous excitation and inhibition. 6. Record the electrophysiological results with electrodes or behavioral results using a pressure sensitive voltage transducer under the animal or a video camera above the animal [13].

## 1.4 Scope

This dissertation research is to produce two UOAs which can be implanted into an ROI and illuminate specific layers within the cortices of small rodents and nonhuman primates. An  $8 \times 6$  and a  $9 \times 9$  (Figure 1.4) will be fabricated proving their mass-production capability, customizability, limited tissue insertion damage, long-term viability, and key optical properties. The  $9 \times 9$  serves as a general purpose implant that can be deployed for many different studies, but the  $8 \times 6$  device is a custom device for targeting mouse motor cortex and V4 of the nonhuman primate visual cortex.

Previous Utah Optrode Arrays have been made using expensive materials, difficult processes to replicate, required photolithography for patterning and alignment, and certified cleanrooms to control particulate contamination to the devices, so the first portion of this research was to improve the initial process by creating and documenting a wafer-level process for better repeatability and eliminate the need for the cleanroom altogether [14]–[18]. A process for CAD modeling the array and then transferring the dimensions to machine language (CAM) of the dicing saw were created called Virtual CAD/CAM (VCC). Both the  $9 \times 9$  and the  $8 \times 6$  UOAs utilize the common VCC process with only small changes needed





**Figure 1.4.** Solid models of both the  $9 \times 9$  and the  $8 \times 6$  Utah Optrode Arrays (shown upside down for clarity). The  $9 \times 9$  array is a general purpose optical brain interface that is used to transmit light from its backplane, through the optrode tips, and into neocortical Layers V and VI. The  $8 \times 6$  is a customized UOA for the specific targeting of mouse motor cortex and nonhuman primate visual cortex. Both devices are fabricated using a common process borrowed from the microelectronics and glass polishing industries.

to the dicing recipes (see Appendix A for all the  $8 \times 6$  dicing recipes). Demonstration of the wafer-level process was done with a 54 mm square wafer to create  $9 \times 9$  general purpose UOAs.

A method was developed to create a 3D CAD model of ROI V4 from brain slice images (plates) taken from readily available brain atlases such as the Calabrese et al. [19] atlas on the Scalable Brain internet application [20]. Each plate was exported from The Scalable Brain and imported into Solidworks where the Paxinos [21] V4 region was highlighted. Solidworks was used to “Basis-spline” these Paxinos [21] regions together on each plate and then the plates were linked together using the “Loft” feature. To complete the V4 3D CAD model, the plates were hidden from view leaving only the lofted regions. Next a slice was created in the model and neocortical layers were simulated in the virtual tissue, where the cell layer boundaries became the depth of interest within the ROI. This depth was transferred to the optrode length of an  $8 \times 6$  UOA. The  $8 \times 6$  device was modeled

in Solidworks, and virtually implanted using the “Combine–Subtract” function to create punctures in the ROI 3D model. The ROI/UOA 3D model was then rotated and studied to ensure the UOA did not protrude out of the ROI. All design parameters were then fabricated into a soda-lime  $8 \times 6$  UOA using the VCC wafer-level process. Two custom UOAs were inserted into C57BL/6 wild-type mouse (*Mus musculus*) ROI motor cortex and into macaque (*Macaca fascicularis*) ROI V4.

It was necessary to ensure the device would work as designed and transmit light from the backplane out of the tip of the optrodes. This was done through characterization of the device using optical, scanning electron, and atomic force microscopy to fully understand the shape of the device and the surface imperfections that could negatively affect the optrodes’ ability to deliver light. Insertion loss was quantified using a blue laser ( $\lambda=473$  nm), where the optical characterization was used to understand the causes of the majority of the insertion loss such as surface roughness, coupling inefficiency, etc. Zemax simulation was used to predict the optical characteristics and to compare simulated loss to actual insertion loss.

## 1.5 Dissertation outline

This dissertation is organized into 6 chapters and 2 appendices. Chapter 1 introduces the UOA and its fit within the optogenetics community. Chapter 2 is a literature review to capture the current state of devices used to illuminate transfected tissue. Chapter 3 is a journal paper, which was published in Biomedical Microdevices titled “Maskless wafer-level microfabrication of optical penetrating neural arrays out of soda-lime glass: Utah Optrode Array” [22]. Chapter 4 was published in a special Brain 2017 edition of Neurophotonics, “Utah Optrode Array customization using stereotactic brain atlases and 3D CAD Modeling for optogenetic neocortical interrogation in small rodents and nonhuman primates” [22]. Chapter 5 is a journal paper projected for publication in Biomedical Microdevices titled “Single optrode characterization of the Utah Optrode Array for neocortical illumination.” Chapter 6 concludes the dissertation with research results, draws key conclusions, and offers suggestions for future work. Finally, the appendices archive the key processing steps for the UOAs, so future work can be built on tools used in this work.

### 1.5.1 Literature review: Current state of optogenetic devices

The literature is full of devices required to shed light on neurons that have been altered to react. Four main types of devices are seen in the literature: 1. Direct optical fiber insertion, 2. Monolithic arrays, 3. Cannula(e), and 4. LED arrays. Each device's general design anatomy is presented in this chapter as a quick reference to those needing it. There are 10 general design types of direct fiber optic insertion into tissue, 5 types of monolithic arrays, 7 types of cannula(e) devices, and 4 types of insertable LED devices. Each has its own merits in optogenetic studies.

The general trends in device designs are that they can be inserted into the tissue for a temporary period of time, or they can be affixed in place for chronic studies. Electrophysiological measurement capabilities are widespread in the literature as well. Many have simply coupled microelectrodes directly to the optical devices while others have inserted a separate microelectrode proximal to the optrode. Several designers have begun to integrate electrical recording capabilities directly on the optrode through metalization techniques. Light source integration is the next wave of innovation in implantable devices with some groups directly inserting LEDs into tissue, while others are coupling laser diode arrays, spatial light modulators, and LED arrays onto implantable devices.

### 1.5.2 Biomedical microdevices: UOA wafer-level microfabrication

This paper is concerned with the improvement of fabrication processes of the original UOA in several areas:

1. Create a process which was easily transferable to a trained operator.
2. Create dicing recipes that were easily modified for neuroscientist specified design constraints such as animal species, craniotomy size, and targeted layer.
3. Replace hydrofluoric acid etchant with ammonium bifluoride for a more controlled etch rate on soda-lime-silica glass (SLG).
4. Replace 50.8 mm diameter fused silica wafers with 50.8 mm square soda-lime-silica glass.
5. Reduce the firing temperature from 1100°C to 700°C for better control over station's temperature range.

6. Eliminate the need for all cleanroom processes of mask creation, patterning and masking photoresist.
7. Optimize dicing process for individual die yield percentage.

Prior to commencing with this work, the Disco dicing saw DAD641, a key piece of fabrication equipment for first generation UOAs, was lost because of a bent spindle, so this precipitated the need for converting all recipes over to a new DAD3220 also by Disco. Unfortunately, none of these recipes was portable due the one-off nature of the fabrication methods chosen for those arrays. Three recipes were created for the DAD3220 and are included in Appendix A: 1. 60° and 45° Tips, 2. Shank (optrode) cutting, 3. Die singulation. Each of these recipes requires some modification each time they are used due to the thickness variations of materials, so a spreadsheet was created to calculate the dynamic parameters which change each time a new wafer is cut. The spreadsheet and tip dicing recipe requires the specific targeted neocortical layer to be entered as well. This is important information that needs to come from the neuroscientist. Standard optrode lengths can also be created with these dicing recipes based on published layer dimensions.

Prior generation UOAs were cut from expensive 50.8 mm diameter round fused silica wafers. Fused silica (FS) has an etch rate of  $2 \mu\text{m}\cdot\text{min}^{-1}$  in hydrofluoric acid (HF). HF is widely known to be an extremely hazardous acid requiring a full chemical suit, gloves, over shoes, as well as a safety goggles and face shield. Hands should have a two layers, one a protective nitrile/latex glove in direct contact to skin and a rubber over-glove that extends to the elbow over the sleeved arms of the chemical protective suit. Unfortunately, this level of personal protective equipment (PPE) is cumbersome when working with the small wafers of UOAs. Replacement of fused silica with SLG allowed for a safer chemical etchant paste to be used to etch the wafers: ammonium bifluoride. Ammonium bifluoride has an etch rate of  $2 \mu\text{m}\cdot\text{min}^{-1}$  on soda-lime-silica, so dynamic etch method was created to keep the paste moist and in contact with the SLG during 40-minute etch times. The PPE needed for etching with ammonium bifluoride was greatly reduced to just safety glass and nitrile/latex rubber gloves. SLG also had a lower glass transition temperature and annealing point than did FS which allowed for lower reflow/annealing temperatures and shorter times. This was important because the annealing furnace's maximum temperature of 1200°C was only 100°C above the annealing point of FS. By not having enough headroom in temperature

the anneals on FS were unpredictable and surface roughness varied greatly. Exchanging round wafer for square wafers allowed for a completely maskless/cleanroomless process.

Many items were changed between DAD641 and DAD3220 dicing saws to improve wafer yield of the cutting processes, since most UOA die were lost or damaged during dicing. First water flow was optimized to reduce hydraulic fracture and SLG stress during dicing to  $0.5 \text{ L}\cdot\text{min}^{-1}$ , and feed speed was controlled to  $1 \text{ mm}\cdot\text{sec}^{-1}$ . Depth steps were set to  $250 \text{ }\mu\text{m}$  for all flat blade dicing recipes to reduce the amount of stress build up in the glass and blade during cutting; without this the blades would prematurely break as well as the glass optrodes would be destroyed. Blade grit was set to 600, and this parameter was not changed from the initial setting in the blades; it will be left to future work to optimize the blade grit.

This paper documented the process which was able to be used for repeatably fabricating UOAs; it also showed that arrays could be fabricated to custom geometries using calculations made with a process call Virtual CAD/CAM (VCC). VCC was the process of using Excel to make the necessary calculations for input into the DAD3220 recipes. UOA design elements are taken from a 3D CAD model that is created and approved by the neuroscientist prior to device fabrication and input into the VCC spreadsheet to then calculate the Blade Height for the tip recipe. Appendix A documents the dicing process.

### 1.5.3 Neurophotonics: UOA customization and 3D brain CAD modeling

Array customization came about from a failed implantation of a first-generation UOA into a marmoset (*Callithrix jacchus*). The UOA that was implanted had high optrode count ( $13 \times 13$ ), and narrow optrode spacing ( $140 \text{ }\mu\text{m}$ ) combined with wide optrode shanks ( $250 \text{ }\mu\text{m}$ ). This combination caused extensive damage upon implantation with broken blood supply vessels and high compression of tissue. A meeting after the surgery was conducted to discuss the device's failure, and it was during that meeting that it became obvious that the design and fabrication of future UOAs needed to have more biological impact studies done beforehand. Brain atlases proved to be the best method of reducing the insertion impact to the animals under study. Atlases for many species of animals are widespread, so they became the go-to items for array customization for not only surgical placement, but also for the targeting of specific functional areas.

Several items of interest are covered in the customization paper:

1. Creation of a 3D CAD model for the neuroscientist's brain's region of interest.
2. 3D CAD design of a UOA that will fit in all 3 dimensions within the region of interest.
3. Fabrication of an SLG UOA using the same maskless wafer-level microfabrication techniques as the standard 2<sup>nd</sup>-generation UOAs.
4. Evaluation of the *in vivo* insertion damage.

Each brain atlas contains images called “plates” of a slice of brain, and each plate is separated by some distance. These plates have been used for many years to orient neuroscientists within the brain for particular regions of interest. By importing all the plates that make up a specific region of interest it was possible to create a 3D CAD model of that area in Solidworks. The model could then be rotated and manipulated, with the neuroscientist's help, to create a suitable implantation analog, which in turn could be virtually implanted with a UOA. A fully custom  $8 \times 6$  array was designed as a solid model in Solidworks. The array was  $3.45 \text{ mm} \times 2.65 \text{ mm}$  with  $400 \mu\text{m}$  optrodes and was suitable for implantation into C57BL/6 wild-type mice (*Mus musculus*) and small nonhuman primates like the marmoset (*Callithrix jacchus*) and the macaque (*Macaca fascicularis*). At the time of this writing, a single mouse has had the  $8 \times 6$  UOA implanted in its motor cortex for over 8 months, proving that not only was the animal capable of recovering from the implantation surgery but also showing the device is suitable for chronic behavioral studies in small animals.

#### 1.5.4 Biomedical microdevices: UOA optical characterization

After proving the UOA could be repeatably made, and then customized to target specific tissue, it became necessary to characterize the array for its geometric tolerances, and its light transmission characteristics. Light coupling and transmission characterization was greatly important for the future of the UOA. Future iterations of the UOA are to individually address each optrode with a single LED mounted to the backplane, so all of the characterization was done on a single optrode rather than the full array while illuminating the entire backplane.

An .stl file of a single optrode was created in Solidworks and imported into Zemax OpticStudio. Nonsequential analysis mode was then used to simulate 10,000 rays through

the single optrode and to visualize a predicted spot size and shape on a color detector in the software. A point source was virtually placed on the backplane and axially aligned through the center of the optrode. The point source and the material were selected to closely match those of the input laser and the soda-lime glass.

An optical bench-top setup was created to test the light transmission through a single optrode, and then these results were compared to the simulation results. The bench-top tests included optical alignment, insertion loss measurements using average power, aqueous fluorescein dye beam profilometry, and index of refraction measurement. Each measurement required careful optical alignment of the laser to each of the components, and to the single optrode of the UOA. Each experiment required the verification of optical alignment with a 20—200X digital microscope.

### **1.5.5 Virtual computer aided machining: Disco DAD3220 dicing recipes**

To reduce the amount of time needed to transition from conceptualized design to finished design, Virtual CAD/CAM was created. The spreadsheets and Disco dicing recipes are recorded for the  $8 \times 6$  array, but they are easily extended to any array geometries barring they have some key design features such as a thick enough backplane to mitigate stress propagation during dicing (500  $\mu\text{m}$  was selected for this work), and wide enough spacing between optrodes to also reduce stress during cutting (400  $\mu\text{m}$  was selected for this work).

### **1.5.6 Virtual brain modeling in Solidworks**

This work came about after a failed insertion attempt of an improperly fabricated first generation UOA. Rather than experiment with animals, a method had to be developed that would allow for designers to virtually experiment with brain ROIs without the need to harm living animals for trial and error experiments. Appendix B includes all the atlas plates used to create a 3D CAD model of ROI V4D. Each plate was imported into Solidworks on its own plane that was properly spaced as noted in the atlas. These models are not true to the exact shape of the brain ROI, but they allow for the customization of UOAs, and other brain implants, with enough specificity to target ROIs and layers of interest. It is left to future work to investigate the efficacy of widespread use of this technique and its associated errors.

## 1.6 References

- [1] “Method of the year 2010,” *Nature Methods*, vol. 8, pp. 1–1, Dec 2010.
- [2] A. Cahill and R. Patterson, “Policy data brief: Paralysis in the U.S.: Christopher & Dana Reeve Foundation Paralysis Resource Center,” 2012.
- [3] CDC, “Get the stats on traumatic brain injury in the United States,” *Center for Disease Control: USA*, pp. 0–1, 2006.
- [4] C. V. Borlongan, J. Burns, N. Tajiri, C. E. Stahl, N. L. Weinbren, H. Shojo, P. R. Sanberg, D. F. Emerich, Y. Kaneko, and H. R. van Loveren, “Epidemiological survey-based formulae to approximate incidence and prevalence of neurological disorders in the United States: A meta-analysis,” *PLoS ONE*, vol. 8, p. e78490, Oct 2013.
- [5] K. K. Watson and M. L. Platt, “Of mice and monkeys: Using non-human primate models to bridge mouse- and human-based investigations of autism spectrum disorders,” *Journal of Neurodevelopmental Disorders*, vol. 4, Jul 2012.
- [6] S. Sutherland, “Revolutionary neuroscience technique slated for human clinical trials,” *Scientific American*. Internet: <https://www.scientificamerican.com/article/revolutionary-neuroscience-technique-slated-for-human-clinical-trials/>. Apr. 2016 [Feb. 21, 2018].
- [7] E. Sokullu, “Optogenetic strategies for the treatment of neurodegenerative diseases,” *Anatomy*, vol. 9, pp. 177–181, Dec 2015.
- [8] T. Hines, “Mayfield certified health information: Brain anatomy, anatomy of the human brain.” Internet: <https://www.mayfieldclinic.com/PE-AnatBrain.htm>. Apr. 2016 [Feb. 21, 2018].
- [9] V. B. Mountcastle, “The columnar organization of the neocortex,” *Brain*, vol. 120, pp. 701–722, Apr 1997.
- [10] V. B. Mountcastle, “An organizing principle for cerebral function: The unit model and the distributed system,” in *The Mindful Brain* (G. M. Edelman and V. V. Mountcastle, eds.), pp. 7–50, Cambridge, MA: MIT Press, 1978.
- [11] E. Oto, “Brain Coronal Section Stock Illustration: Getty Images.” Internet: <http://www.gettyimages.com/detail/illustration/brain-coronal-section-stock-graphic/543369403>. Mar. 2017 [Sep. 9, 2017].
- [12] B. Dubuc, “The brain from top to bottom.” Internet: [http://thebrain.mcgill.ca/flash/a/a\\_07/a\\_07\\_p/a\\_07\\_p\\_tra/a\\_07\\_p\\_tra.html](http://thebrain.mcgill.ca/flash/a/a_07/a_07_p/a_07_p_tra/a_07_p_tra.html). 2016 [Sep. 10, 2017].
- [13] L. Buchen, “Neuroscience: Illuminating the brain,” *Nature*, vol. 465, pp. 26–28, May 2010.
- [14] T. V. F. Abaya, M. Diwekar, S. Blair, P. Tathireddy, L. Rieth, G. A. Clark, and F. Solzbacher, “Glass optrode arrays for optogenetic stimulation,” in *Optogenetics: Optical Methods for Cellular Control* (S. K. Mohanty and N. V. Thakor, eds.), SPIE, Mar 2013.



- [15] T. Abaya, S. Blair, P. Tathireddy, L. Rieth, and F. Solzbacher, “A 3d glass optrode array for optical neural stimulation,” *Biomedical Optics Express*, vol. 3, p. 3087, Nov 2012.
- [16] J. Lee, I. Ozden, Y.-K. Song, and A. Nurmikko, “Multifunctional transparent opto-electrode array for in-vivo optogenetic studies,” in *CLEO: 2015*, OSA, 2015.
- [17] J. Zhang, F. Laiwalla, J. A. Kim, H. Urabe, R. V. Wagenen, Y.-K. Song, B. W. Connors, F. Zhang, K. Deisseroth, and A. V. Nurmikko, “Integrated device for optical stimulation and spatiotemporal electrical recording of neural activity in light-sensitized brain tissue,” *Journal of Neural Engineering*, vol. 6, p. 055007, Sep 2009.
- [18] F. Wu, E. Stark, M. Im, I.-J. Cho, E.-S. Yoon, G. Buzsáki, K. D. Wise, and E. Yoon, “An implantable neural probe with monolithically integrated dielectric waveguide and recording electrodes for optogenetics applications,” *Journal of Neural Engineering*, vol. 10, p. 056012, Aug 2013.
- [19] E. Calabrese, A. Badea, C. L. Coe, G. R. Lubach, Y. Shi, M. A. Styner, and G. A. Johnson, “A diffusion tensor MRI atlas of the postmortem rhesus macaque brain,” *NeuroImage*, vol. 117, pp. 408–416, Aug 2015.
- [20] R. Bakker, P. Tiesinga, and R. Kötter, “The scalable brain atlas: Instant web-based access to public brain atlases and related content,” *Neuroinformatics*, vol. 13, pp. 353–366, Feb 2015.
- [21] G. Paxinos, X. Huang, and A. Toga, *The Rhesus Monkey Brain in Stereotaxic Coordinates*. San Diego, CA. Academic Press, 2000.
- [22] R. W. Boutte and S. Blair, “Maskless wafer-level microfabrication of optical penetrating neural arrays out of soda-lime glass: Utah optrode array,” *Biomedical Microdevices*, vol. 18, Dec 2016.

## CHAPTER 2

# REVIEW OF THE OPTICAL NEURAL INTERFACE LITERATURE

This literature review covers four categories of penetrating optogenetic devices 1. Optical fibers, 2. Monolithic optical arrays, 3. Cannula, and 4. Penetrating LEDs. These devices are typically reserved for *in vivo* applications; although, they can be used in vitro with little to no modifications. While optogenetics is the most recent use for the introduction of light into living tissue, it is not, however, the first-time light has been used to evoke biological responses within animals. Several have introduced light into tissue such as intact heart [1]–[4], central nervous system [5]–[7], and in the brains of freely moving animals [8], [9].

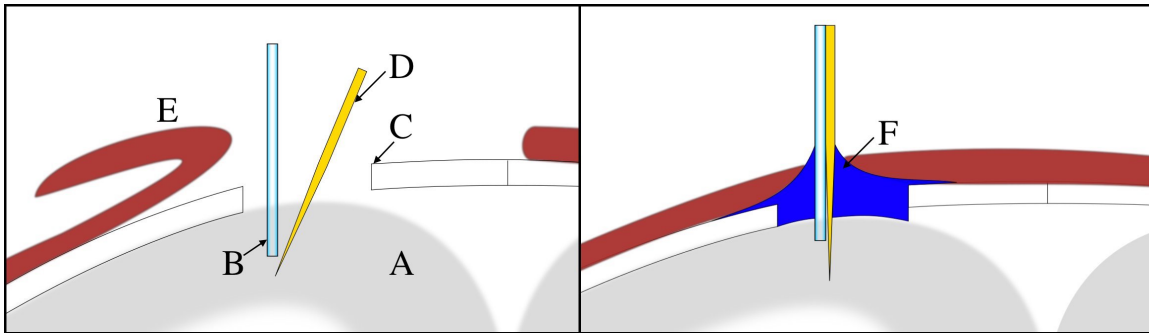
The current optrode landscape is dominated by single optical fiber/cannula insertions and implantations. Single optical fibers are usually connected directly to a laser, or LED light source, and to the tissue to be illuminated. Behavioral studies require the animal be freely moving, but optical fibers can be very stiff. High stiffness from the tethered fiber can cause an adverse reaction in the animal under study, so an optical rotary joint or slip-ring is used to allow the animal to move somewhat freely [10]–[12]. Stiffness makes high fiber counts into tissue impractical, so monolithic arrays have been developed. A key benefit to optrode arrays is that multiple light sources can be fabricated on-board the device itself. The light sources for monolithic arrays are usually LED arrays [13]–[15]. Cannulae are small devices where a short piece of optical fiber is inserted into the tissue of interest, but is decoupled from the light source with the use of a hollow ceramic or stainless steel ferrule. Decoupling allows the animal to recover from the implantation surgery without being permanently attached to the tethered source fiber. The ferrule supports a small piece of implanted fiber, and when it is time for the animal to be tethered, the source fiber is connected to the ferrule [16]. Finally, penetrating LEDs are a method of directly illuminating the tissue of interest without the need of a separate light source.

One of the earliest uses of the term “optrode” was by Neunlist [4] to describe an optical probe that could deliver light to the frog’s heart in Ringer’s solution while simultaneously imaging fluorescence from the stained ventricle. Zhang [17] adapted the term optrode for optogenetics to describe a sharpened/metallized optical fiber because of the fiber’s ability to illuminate tissue and simultaneously record neurophysiological electroactivity. In 2012 Abaya [18] used optrode to include just the optical transmission portion of the optogenetic neural interface and further cemented this definition in [19]–[21]. It is this expanded definition that will be used throughout this review.

Many current opsins used for optogenetics require light from the visible spectrum between 400–700 nm [22]. For short distances into the brain of  $\sim 100\ \mu\text{m}$  surface illumination is sufficient. For deeper brain stimulation  $\geq 150\ \mu\text{m}$  an optical device of some sort must be used to transmit light to overcome scattering and absorption of the brain tissue and its cerebrospinal fluid [23]. Each of these optical devices penetrates the brain to deliver light directly into the tissue of interest, and while these methods are invasive, many great results have been seen in both short and long-term *in vivo* experiments. Noninvasive methods using sound waves, red-shifted light, near-infrared light, and x-rays have been devised, but these are not discussed in this review [24]–[28].

## 2.1 Inserted and implanted single optical fibers

Early optogenetic devices were simply optical fibers connected to a light source on one end and directly inserted into the tissue on the other end. Many experiments were *in vitro*, so there was no need for an animal to move about freely. The bare end of the optical fiber was inserted with micrometer stages that could be precisely maneuvered into position. Electrodes were separately placed to record the evoked responses. There are two types of *in vivo* studies shown in Figure 2.1: head restrained (HRA) and freely moving animals (FMA). For HRAs, long optical fibers are directly inserted with little to no modification of the stereotactic. For FMAs, the optical fibers are secured with dental cement so they aren’t accidentally pulled out of place during the experiment. HRAs have the fibers “inserted,” and FMAs have the fiber “implanted.” Optical fibers are easily modified through etching and metallization, so newer devices have dual illumination and electrical recording capabilities. All of these devices can be either inserted and removed following the surgical procedure, or



**Figure 2.1.** Coronal representation on the left shows the neocortex (A) being illuminated by a single optical fiber (B) through a craniotomy (C). Electrical recordings are made with a single microelectrode (D). The scalp flap (E) is secured during the surgery for implantation. An implanted single fiber optrode dental cemented in place (F) is shown on the right. The scalp flap (E) has been allowed to heal over the surgical wound.

they can be left in place and implanted using dental cement or equivalent biocompatible adhesive.

Table 2.1 shows many of the devices categorized as “single optical fiber optrodes.” For purposes of this literature review, the optical fibers are directly connected between tissue and a laser/LED light source. Early optogenetic research used multimodal fibers due to the large diameters ( $\leq 600 \mu\text{m}$ ) and high numerical apertures of  $\leq 0.5\text{NA}$  [29]–[31]. Multimode fibers are typically reserved for telecommunication systems, but their use in optogenetics takes advantage of the high beam-spread out of the fiber to illuminate large areas of tissue. Fibers can be tapered and sharpened by wet etching, and this allows them to be inserted into tissue more easily. Tapered fibers can be distinguished by their flattened tip, while sharpened fibers come to a very sharp point [17], [32], [33].

Quite often the neuroscientist requires electrophysiology measurements of neural action potentials. There are two main methods seen in literature for recording action potentials: 1. separate microelectrodes which are co-inserted/implanted with the optical fiber, or 2. applying metal directly onto the fiber itself. Simultaneous illumination and electrical recording has been a rich source of optogenetic research with some attaching a separate microelectrode directly to the optical fiber [7], [33]–[36] and others placing electrodes around the optical fiber [37]. Some have taken a novel approach to side illumination by angle cleaving the end of the metallized fiber [38].

There are some novel devices that do not fit well into any category, so they are included

**Table 2.1.** Single Optical Fiber Optrodes






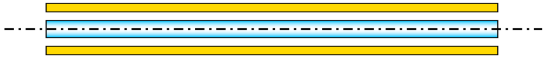

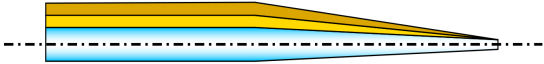

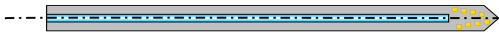
Profile	Adapted from:	Explanation
	[29]–[31]	Single multimode optical fiber projects light onto opsin-expressing neurons causing them to depolarize or hyperpolarize. Optical rotary joints are needed for <i>in vivo</i> behavioral studies.
	[32]	Tapered multimode single optical fiber that is directly inserted into the tissue of interest and is tethered to the light source. Sharpening the fiber improves the insertion, and it reduces the illumination cone for higher specificity in neuronal targeting.
	[43]	Coaxial metallized fiber for simultaneous illumination and electrical recording. It is stereotactically inserted for high precision physiological measurements. <i>In vivo</i> experiments are usually performed on immobilized animals.
	[7], [34]–[36]	Single optical fiber with micro-electrode attached for simultaneous illumination and electrical recording. Electrode tip is usually placed within a few microns from the illumination aperture.
	[17]	Sharpened/metalized optical fiber for simultaneous illumination and electrical recording. The electrode was used as part of a Utah Electrode Array for highly precise spatiotemporal action potential recording.

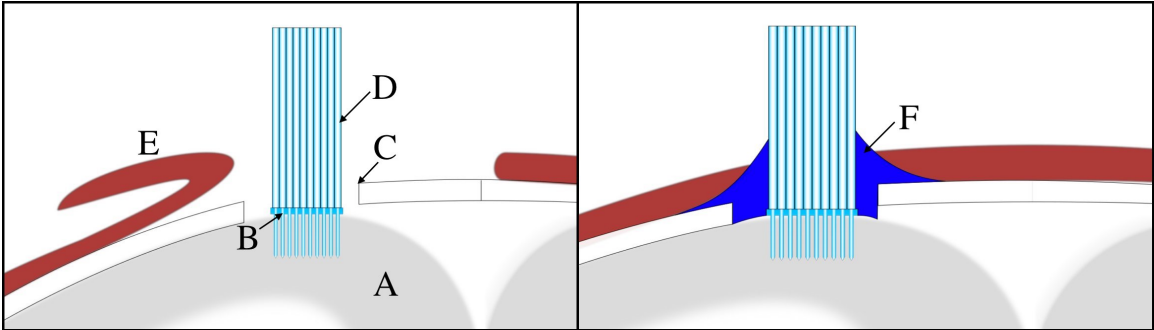
Table 2.1. Continued

Profile	Adapted from:	Explanation
	[37]	Single fiber surrounded by electrodes capable of recording from many neurons. Electrodes have high spatial density and can record action potentials as they spread from the point of illumination.
	[39], [40]	Sharpened and metallized fiber with small windows opened in the metallization layer. Each window can be individually illuminated by varying the angle of the incident laser beam. Appropriate for immobilized animals.
	[33]	Tapered optical fiber with double-barreled electrode design for simultaneous illumination, action potential recording, and ion concentration measurements.
	[38]	Angle cleaved fiber creates a side emitting profile for lateral illumination; this fiber is metallized for recording as well.
	[41], [42]	Rectangular waveguide running the length of a silicon substrate that has 8 microelectrode pads at the exit aperture of the waveguide.

in the single optical fiber category. Salter [39] and Pisanello [40] have etched windows into a sharpened and metallized fiber, where each window can be illuminated by varying the input angle of incident beam on the bare end of the fiber. Rectangular waveguides have been deposited onto silicon substrates that transmit light and into tissue [41], [42]. These devices typically have microelectrode pads at the tip near the exit aperture of the waveguide to measure neural action potentials.

## 2.2 Inserted and implanted monolithic arrays

Figure 2.2 shows an array inserted and backlit with an optical fiber bundle for *in vivo* HRA, and it shows an FMA animal with an implanted array also backlit with the tethered fiber bundle. Optical arrays have recently been added to the repertoire of optogenetic devices (see Table 2.2). Abaya was one of the first to explore the use of a  $10 \times 10$  optrode array in optogenetic use for neuronal ensemble illumination. Her hypothesis was that many implanted optrodes would be able to illuminate larger tissue volumes by overcoming the light loss in brain tissue. This was accomplished by converting the Utah Electrode Array's geometry to fused silica, and even though her devices had no electrical recording capabilities, they were successful in proving a high amount of light ( $> 90\%$ ) could be transmitted into tissue [18]–[21].



**Figure 2.2.** Coronal representation on the left shows the neocortex (A) being illuminated by a  $10 \times 10$  optrode array (B) through a craniotomy (C). This array is shown backlit with a fiber bundle (D). The scalp flap (E) is secured during the surgery for implantation. An implanted optrode/fiber bundle dental cemented in place (F) is shown on the right. The scalp flap (E) has been allowed to heal over the surgical wound. This setup is stable for fMRI (functional magnet resonance imaging) experiments where metal would adversely affect the test subject.

Table 2.2. Optrode Arrays

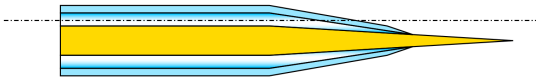
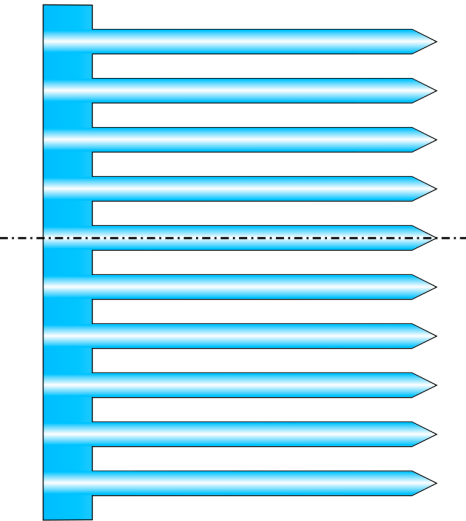
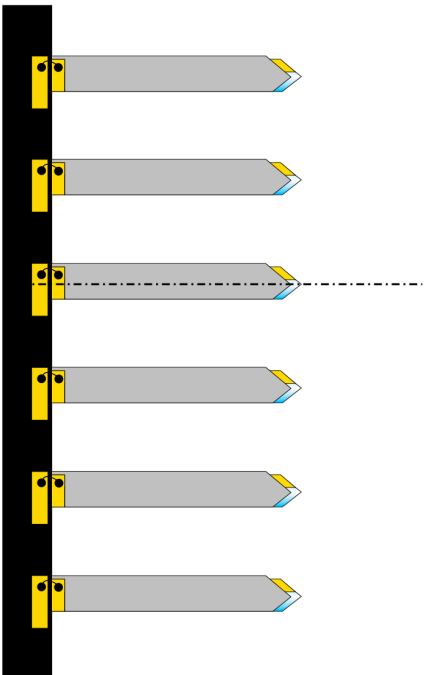
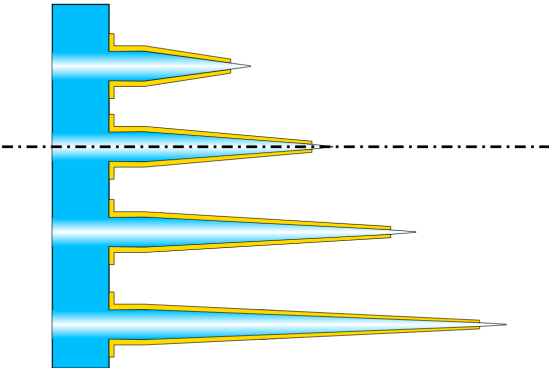
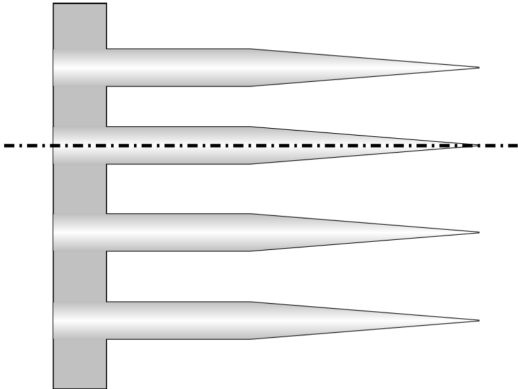
Profile	Adapted from:	Explanation
	[44]	$2 \times 2$ : Four sharpened optical fibers surrounding a single microelectrode. Individual optrodes are illuminated by a single optical fiber split by optical couplers.
	[18]–[21]	$10 \times 10$ : Glass array capable of illuminating large volumes of tissue. Tip angles can be adjusted for overlapping beams or narrowed for high targeting specificity. The high aspect ratio allows for deep penetration into neocortical layers. Optrode pitch can be varied from $\geq 250 \mu\text{m}$ .
	[45]	$1 \times 6$ : (Top View) Array of canulae with simultaneous illumination and electrical recording. This device has a coaxial design with an insulated metalization layer that is wirebonded to bond pads located across an MT (multifiber) connector. Care is taken to restrict the animals' motion from fiber optic stiffness.



Table 2.2. Continued

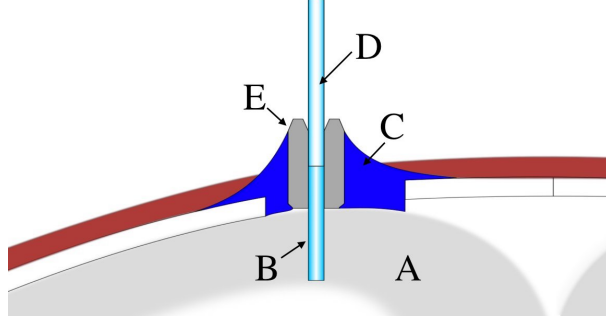
Profile	Adapted from:	Explanation
	[13]–[15]	$4 \times 4$ : LED backlit polymer array with simultaneous illumination and electrical recording. Polymer optrodes are tapered and staggered into a “slanted array pattern” to illuminate different neocortical layer depths.
	[46]	$4 \times 4$ : Array exploits the electrooptical properties of Zinc Oxide. ZnO is transparent in the visible spectrum, and it is intrinsically electrically active so the device can illuminate and record action potentials simultaneously.

Several additional arrays have been developed. Tamura [44] showed a  $2 \times 2$  array of specially sharpened fibers that surround a microelectrode, where each fiber can be individually illuminated for simultaneous illumination and electrical recording. Optical fiber and polymers also make up the optrode array landscape [13]–[15], [45]. The  $1 \times 6$  optical fiber array by [45] utilizes a multifiber (MT) connector to couple to the fibers, and the electrical interconnects are wire-bonded to the metallized surface of the optrodes. LED backlit polymer  $4 \times 4$  arrays been tuned into a slanted array shape to address several neocortical layers simultaneous with both light and electrical recording capabilities. Researchers from Brown University demonstrated a  $4 \times 4$  array that exploits the electrooptical properties of Zinc Oxide [46]. ZnO is transparent, so LED light is transmitted down the optrode and into tissue. The very same optrode records right at the tip of illumination.

### 2.3 Implanted cannula

The workhorse of the optogenetics community is the cannula shown in Figure 2.3. Optical cannulae are usually created by inserting a short length ( $\sim 20$  mm) of optical fiber into a ceramic or stainless steel ferrule a short distance and then bonding it in place [16], [47], [48]. The other side of the ferrule is hollow, and this allows for a source connected fiber to be butt-coupled inside the ferrule. The advantage of this method is that the cannula can remain in the animal, but the animal can be untethered when not under study. Cannulae are cleaved to length, implanted through a craniotomy, and dental cemented in place, leaving the animal to completely recover. Table 2.3 shows the types of optical cannulae found throughout literature.

A single cannula was used by [49] to “casually manipulate selective cell types” by inhibiting (hyperpolarizing) and exciting (depolarizing) neurons at-will. The flat cleaved end of the cannula is capable of illuminating large volumes of neurons close to the tip, while a single microelectrode measures the electrophysiology. Taylor [50] used the cannula for studying the “local and long-range neural network dynamics.” This study concluded that their cannula illumination technique coupled with reverse microdialysis, and a silicon probe measuring electrophysiology, could elucidate “the short and long-term effects of specific neurotransmitter- and voltage-gated channels on laser-modulated firing.” Single sharpened fiber cannulae have been used by [51]–[55] in optogenetics experiments as well.



**Figure 2.3.** Coronal representation showing neocortical (A) illumination using a single optical cannula (B) that has been secured using dental cement (C). A single optical fiber (D) is connected to the light source and then inserted into a ceramic or stainless steel ferrule (E). The test subject is allowed to recover from the implantation surgery and need only be tethered to the source fiber when needed for experiments. Animal mobility is greatly improved with the use of an optical rotary joint.

The sharpened fiber cannula is easier to insert, but the trade-off is a narrowed illumination pattern. These fibers' narrow output allow for a smaller amount of neurons to be illuminated in the neocortical column.

Metallization of cannulae, like optical fibers, have assisted in the recording of action potentials [56], [57] generated from the illumination through the cannula. A major differentiator seen in the literature for the optical cannula is the addition of microelectrodes [58]–[60]. Electrode placement is determined by the location of desired recording in relation to the output aperture of the fiber. Laxpati [61] placed a single optrode in between 4 slanted microelectrodes for proximal and distal recording.

Cannulae have also been bonded together into a  $1 \times 2$  optrode array [62], [63]. For *in vivo* behavioral studies, these arrays are usually illuminated with a single light source and rotary stage for better mobility in the animal under study. A counter balance is also typically used to reduce the weight of the over amount of fiber, so the animal can act more normally during testing.

## 2.4 Implanted LED arrays

Rounding out the major contributions to optogenetic devices are implantable  $\mu$ LEDs like those shown in Figure 2.4. As opposed to LEDs that sit on the cortical surface, implantable  $\mu$ LEDs are typically fabricated on a silicon or sapphire substrate and emit

Table 2.3. Cannulae Optrodes

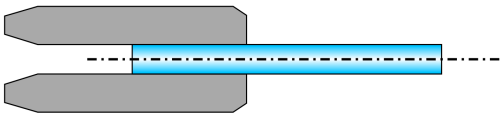
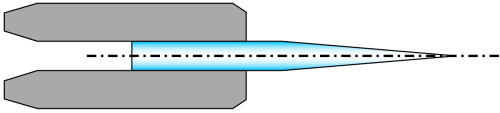
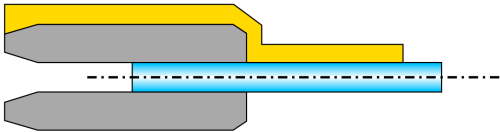
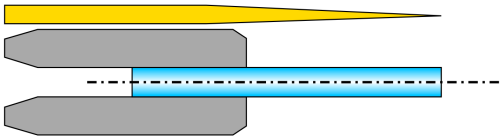
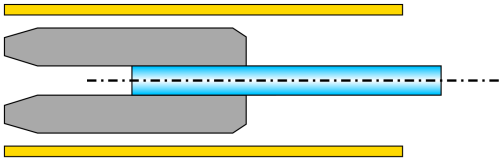
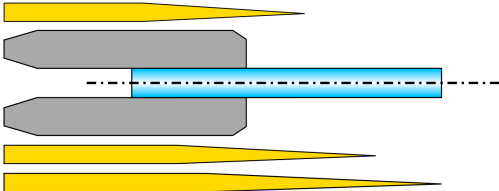
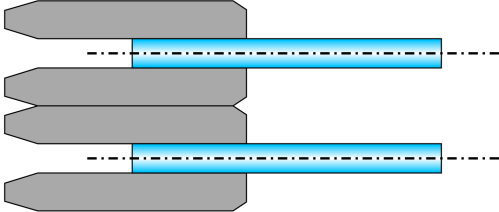
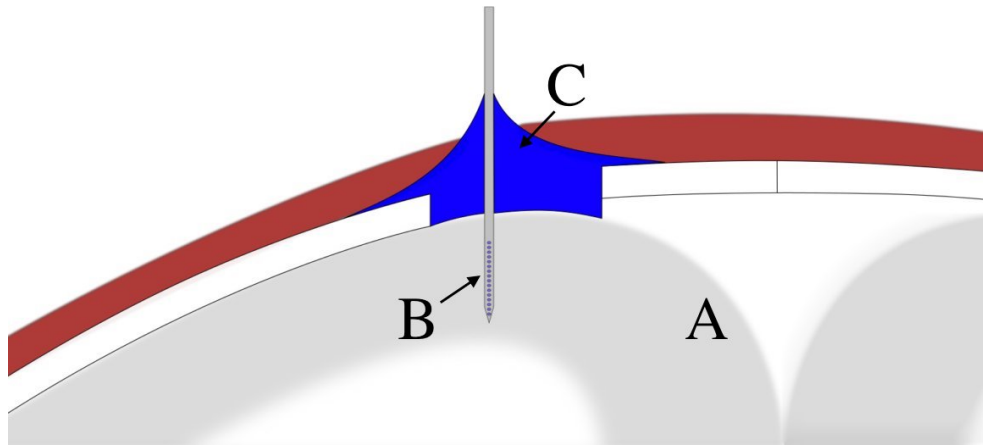
Profile	Adapted from:	Explanation
	[16], [47]–[50]	Single optical cannula is a short piece of optical fiber (typically 20 mm) that is bonded a short distance up a ceramic or stainless-steel fiber optic ferrule.
	[51]–[55]	Sharpened single optical cannula produces a narrow illumination cone.
	[56], [57]	Metalized cannula allows for simultaneous illumination and electrical recording. Metalization layer stops short of the end of the fiber.
	[58]	Independent cannula/electrode insertion. Action potentials from various neocortical layers can be interrogated.

Table 2.3. Continued

Profile	Adapted from:	Explanation
	[59], [60]	Cannula surrounded by electrodes. Used for spatiotemporal neuronal firing studies. Typically, the electrodes are cobonded with the cannula for simultaneous insertion and interrogation.
	[61]	Slanted electrode array with cobonded cannula. The slanted electrodes can record from multiple layers of the neocortex.
	[62], [63]	Dual cannulae array capable of illuminating large volume of tissue. Alignment is achieved from bonding the two ferrules together.



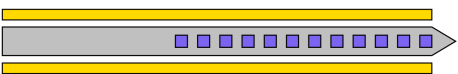
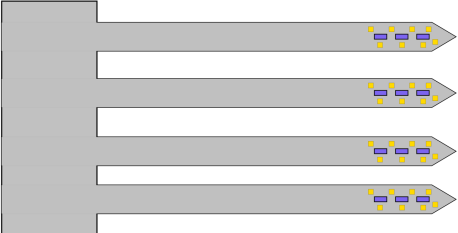


**Figure 2.4.** Coronal representation of neocortical (A) illumination using a  $1 \times 16$  LED array (B) that has been secured using dental cement (C). The test subject is allowed to recover from the implantation surgery and need only be tethered to the source electrical signal when needed for experiments. Animal mobility is greatly improved with the use of an optical rotary joint.

omnidirectionally. The substrate is used as the main support structure for penetrating the cortex. The advantage of these devices is that they typically have electrical recording sites very near to the  $\mu$ LED. One additional feature is that they are considered “side emitting” because they cannot illuminate through the substrate. This can be advantageous to precise targeting of neurons within the neocortical column.

Several penetrating  $\mu$ LEDs have been developed as shown in Table 2.4, but they all share a common architecture of linearly aligned LEDs and electrical recording capabilities in some devices. Scharf [64] and Guo [65] fabricated  $\mu$ LEDs along a single row; this allows for precise implantation, and the LEDs can be tuned to the exact neocortical layers under study. Schwaerzle [66] fabricated alternating  $\mu$ LEDs and microelectrodes for a devices capable of recording up through the layers of the neocortex. Similarly, Ayub [67] fabricated a row of LEDs, but placed 2 microelectrodes along side the  $1 \times 12$  array. Depth recording was handled by moving the microelectrodes along the shaft of the array. A  $1 \times 3 \times 4$  array was created with 8 precisely placed microelectrode pads interlaced through the LEDs to record in the direct proximity of the illumination from the LED [68].

Table 2.4. Penetrating LEDs

Profile	Adapted from:	Explanation
	[64], [65]	$1 \times 16$ : Array of LEDs capable of individually addressing lamina of the neocortex.
	[66]	$1 \times 7$ : Alternating electrode and LED array for simultaneous illumination and electrical recording.
	[67]	$1 \times 12$ : LED array with dual adjacent microelectrodes for simultaneous illumination and action potential recording.
	[68]	$1 \times 3 \times 4$ : An array of LED arrays with 8 electrodes per insertion shank. Electrode spacing is optimized for recording from the layers of the neocortex.

## 2.5 Conclusion

The literature describes 4 types of optogenetic devices currently in use: 1. Single optical fibers directly inserted into tissue and connected to a light source, 2. Optical neural arrays that allow for large volume illumination and spatiotemporal light patterning into tissue, 3. Optical cannulae that are implanted into the cortex of an animal and allow for the animal to freely move after a recovery period of time, and 4. Penetrating  $\mu$ LED arrays that can precisely target multiple layers of the neocortex simultaneously. Single optical fibers and cannulae require some tethering mechanism like an optical rotary joint to allow the animal under *in vivo* behavioral studies to move about freely. Arrays offer rich ground for development of standalone and wireless devices that can allow for the animal to be untethered. Penetrating  $\mu$ LED arrays have the advantage of being fabricated along side microelectrodes for simultaneous illumination and electrophysiological recording electrodes. This literature review gives the reader a sense of the common shapes of the devices currently in use for optogenetic light transmission into tissue.

## 2.6 References

- [1] T. A. Bowmaster, C. C. Davis, and V. Krauthamer, "Excitation and detection of action potential-induced fluorescence changes through a single monomode optical fiber," *Biochimica et Biophysica Acta (BBA) - Molecular Cell Research*, vol. 1091, pp. 9–14, Jan 1991.
- [2] P. M. Bradley, D. Murphy, S. Kasparov, J. Croker, and J. F. Paton, "A micro-optrode for simultaneous extracellular electrical and intracellular optical recording from neurons in an intact oscillatory neuronal network," *Journal of Neuroscience Methods*, vol. 168, pp. 383–395, Mar 2008.
- [3] G. Lee, R. M. Ikeda, D. Stobbe, C. Ogata, A. Embi, M. C. Chan, R. L. Reis, and D. T. Mason, "Intraoperative use of dual fiberoptic catheter for simultaneous *in vivo* visualization and laser vaporization of peripheral atherosclerotic obstructive disease," *Catheterization and Cardiovascular Diagnosis*, vol. 10, no. 1, pp. 11–16, 1984.
- [4] M. Neunlist, S. Zou, and L. Tung, "Design and use of an 'optrode' for optical recordings of cardiac action potentials," pp. 611–617, 1992.
- [5] Y. Kudo, T. Nakamura, and K. Akita, "Measurement of the intracellular  $\text{Ca}^{2+}$  concentration in a localized region by a single photofiber fluorometric device," *Neuroscience Research Supplements*, vol. 14, pp. S19–S19, 1991.
- [6] Y. Kudo, K. Akita, T. Nakamura, A. Ogura, T. Makino, A. Tamagawa, K. Ozaki, and A. Miyakawa, "A single optical fiber fluorometric device for measurement of



intracellular  $\text{Ca}^{2+}$  concentration: Its application to hippocampal neurons in vitro and in vivo,” *Neuroscience*, vol. 50, no. 3, pp. 619–625, 1992.

- [7] S. Nakamura, M. V. Baratta, and D. C. Cooper, “A method for high fidelity optogenetic control of individual pyramidal neurons *In vivo*,” *Journal of Visualized Experiments*, Sep 2013.
- [8] M. Duff Davis and J. J. Schmidt, “*In vivo* spectrometric calcium flux recordings of intrinsic caudate-putamen cells and transplanted imr-32 neuroblastoma cells using miniature fiber optrodes in anesthetized and awake rats and monkeys,” *Journal of Neuroscience Methods*, vol. 99, no. 1, pp. 9–23, 2000.
- [9] S. Mottin, P. Laporte, and R. Cespuglio, “Inhibition of NADH oxidation by chloramphenicol in the freely moving rat measured by picosecond time-resolved emission spectroscopy,” *Journal of Neurochemistry*, vol. 84, pp. 633–642, Jan 2003.
- [10] Z. Ji, D. Jia, Q. Xu, H. Zhang, H. Zhang, D. Zhang, and Y. Zhang, “Design and implementation of a plastic fiber optical rotary joint using upside down taper lens,” *Optics Communications*, vol. 292, pp. 57–61, Apr 2013.
- [11] D. C. Klorig and D. W. Godwin, “A magnetic rotary optical fiber connector for optogenetic experiments in freely moving animals,” *Journal of Neuroscience Methods*, vol. 227, pp. 132–139, Apr 2014.
- [12] Y. Shi, L. Klafter, and E. Harstead, “A dual-fiber optical rotary joint,” *Journal of Lightwave Technology*, vol. 3, pp. 999–1004, Oct 1985.
- [13] K. Y. Kwon, H.-M. Lee, M. Ghovanloo, A. Weber, and W. Li, “Design, fabrication, and packaging of an integrated, wirelessly-powered optrode array for optogenetics application,” *Frontiers in Systems Neuroscience*, vol. 9, May 2015.
- [14] K. Y. Kwon, A. Khomenko, M. Haq, and W. Li, “Integrated slanted microneedle-LED array for optogenetics,” in *2013 35th Annual International Conference of the IEEE Engineering in Medicine and Biology Society (EMBC)*, IEEE, Jul 2013.
- [15] H.-M. Lee, K.-Y. Kwon, W. Li, and M. Ghovanloo, “A wireless implantable switched-capacitor based optogenetic stimulating system,” in *2014 36th Annual International Conference of the IEEE Engineering in Medicine and Biology Society*, IEEE, Aug 2014.
- [16] “Thorlabs implantable fiber optic cannulae.” Internet: [https://www.thorlabs.com/navigation.cfm?guide\\_id=2256](https://www.thorlabs.com/navigation.cfm?guide_id=2256). Updated: 2018 [Feb. 21, 2018].
- [17] J. Zhang, F. Laiwalla, J. Kim, H. Urabe, R. V. Wagenen, Y.-K. Song, B. Connors, and A. Nurmikko, “A microelectrode array incorporating an optical waveguide device for stimulation and spatiotemporal electrical recording of neural activity,” in *2009 Annual International Conference of the IEEE Engineering in Medicine and Biology Society*, IEEE, Sep 2009.
- [18] T. Abaya, S. Blair, P. Tathireddy, L. Rieth, and F. Solzbacher, “A 3d glass optrode array for optical neural stimulation,” *Biomedical Optics Express*, vol. 3, no. 12, p. 3087, 2012.

- [19] T. Abaya, M. Diwekar, S. Blair, P. Tathireddy, L. Rieth, G. Clark, and F. Solzbacher, "Characterization of a 3d optrode array for infrared neural stimulation," *Biomedical Optics Express*, vol. 3, p. 2200, Aug 2012.
- [20] T. V. F. Abaya, *Implantable light delivery interfaces for optical neural stimulation*. PhD dissertation, University of Utah, 2013.
- [21] T. V. Abaya, M. Diwekar, S. Blair, P. Tathireddy, L. Rieth, and F. Solzbacher, "Deep-tissue light delivery via optrode arrays," *Journal of Biomedical Optics*, vol. 19, p. 015006, Jan 2014.
- [22] L. Fenno, O. Yizhar, and K. Deisseroth, "The development and application of optogenetics," *Annual Review of Neuroscience*, vol. 34, pp. 389–412, Jul 2011.
- [23] S. I. Al-Juboori, A. Dondzillo, E. A. Stubblefield, G. Felsen, T. C. Lei, and A. Klug, "Light scattering properties vary across different regions of the adult mouse brain," *PLoS ONE*, vol. 8, p. e67626, Jul 2013.
- [24] S. Ibsen, A. Tong, C. Schutt, S. Esener, and S. H. Chalasani, "Sonogenetics is a non-invasive approach to activating neurons in *Caenorhabditis elegans*," *Nature Communications*, vol. 6, p. 8264, Sep 2015.
- [25] F. Schneider, M. Prigge, S. Tsunoda, and P. Hegemann, "Color shifted channelrhodopsins- towards red light optogenetics," *Biophysical Journal*, vol. 98, p. 538a, Jan 2010.
- [26] T. Sasaki, "Probing neuronal activity using genetically encoded red fluorescent calcium indicators," in *Optogenetics*, pp. 149–158, Springer Japan, 2015.
- [27] S. Hososhima, H. Yuasa, T. Ishizuka, M. R. Hoque, T. Yamashita, A. Yamanaka, E. Sugano, H. Tomita, and H. Yawo, "Near-infrared (NIR) up-conversion optogenetics," *Scientific Reports*, vol. 5, Nov 2015.
- [28] R. Berry, M. Getzin, L. Gjestebj, and G. Wang, "X-optogenetics and u-optogenetics: Feasibility and possibilities," *Photonics*, vol. 2, pp. 23–39, Jan 2015.
- [29] M. Y. Cheng, E. H. Wang, W. J. Woodson, S. Wang, G. Sun, A. G. Lee, A. Arac, L. E. Fenno, K. Deisseroth, and G. K. Steinberg, "Optogenetic neuronal stimulation promotes functional recovery after stroke," *Proceedings of the National Academy of Sciences*, vol. 111, pp. 12913–12918, Aug 2014.
- [30] S. Guo, S. Chen, Q. Zhang, Y. Wang, K. Xu, and X. Zheng, "Optogenetic activation of the excitatory neurons expressing CaMKII $\alpha$  in the ventral tegmental area upregulates the locomotor activity of free behaving rats," *BioMed Research International*, vol. 2014, pp. 1–11, 2014.
- [31] W. R. Stauffer, A. Lak, A. Yang, M. Borel, O. Paulsen, E. S. Boyden, and W. Schultz, "Dopamine neuron-specific optogenetic stimulation in rhesus macaques," *Cell*, vol. 166, pp. 1564–1571.e6, Sep 2016.
- [32] L. Acker, E. N. Pino, E. S. Boyden, and R. Desimone, "FEF inactivation with improved optogenetic methods," *Proceedings of the National Academy of Sciences*, vol. 113, pp. E7297–E7306, Nov 2016.

- [33] S. Dufour, P. Dufour, O. Chever, R. Vallée, and F. Amzica, “*In vivo* simultaneous intra- and extracellular potassium recordings using a micro-optrode,” *Journal of Neuroscience Methods*, vol. 194, pp. 206–217, Jan 2011.
- [34] J. T. Paz and J. R. Huguenard, “Optogenetics and epilepsy: Past, present and future,” *Epilepsy Currents*, vol. 15, pp. 34–38, Jan 2015.
- [35] D. C. Millard, C. J. Whitmire, C. A. Gollnick, C. J. Rozell, and G. B. Stanley, “Electrical and optical activation of mesoscale neural circuits with implications for coding,” *The Journal of Neuroscience*, vol. 35, pp. 15702–15715, Nov 2015.
- [36] B. Sadrian and D. A. Wilson, “Optogenetic stimulation of lateral amygdala input to posterior piriform cortex modulates single-unit and ensemble odor processing,” *Frontiers in Neural Circuits*, vol. 9, Dec 2015.
- [37] G. Gagnon-Turcotte, A. Kisomi, R. Ameli, C.-O. Camaro, Y. LeChasseur, J.-L. Néron, P. Bareil, P. Fortier, C. Bories, Y. de Koninck, and B. Gosselin, “A wireless optogenetic headstage with multichannel electrophysiological recording capability,” *Sensors*, vol. 15, pp. 22776–22797, Sep 2015.
- [38] A. Castonguay, S. Thomas, F. Lesage, and C. Casanova, “Repetitive and retinotopically restricted activation of the dorsal lateral geniculate nucleus with optogenetics,” *PLoS ONE*, vol. 9, p. e94633, Apr 2014.
- [39] M. Salter, M. Demarco, A. Law, B. Jaar, R. Parekh, and D. Segev, “Age disparities in discussions about kidney transplantation among dialysis patients,” *American Journal Of Transplantation*, vol. 13, pp. 109–109, Apr 2013.
- [40] M. Pisanello, A. Della Patria, L. Sileo, B. Sabatini, M. De Vittorio, and F. Pisanello, “Modal demultiplexing properties of tapered and nanostructured optical fibers for in vivo optogenetic control of neural activity,” *Biomedical Optics Express*, vol. 6, pp. 4014–4026, Oct 2015.
- [41] F. Wu, E. Stark, M. Im, I.-J. Cho, E.-S. Yoon, G. Buzsáki, K. D. Wise, and E. Yoon, “An implantable neural probe with monolithically integrated dielectric waveguide and recording electrodes for optogenetics applications,” *Journal of Neural Engineering*, vol. 10, p. 056012, Aug 2013.
- [42] K. Kampasi, E. Stark, J. Seymour, K. Na, H. G. Winful, G. Buzsáki, K. D. Wise, and E. Yoon, “Fiberless multicolor neural optoelectrode for in vivo circuit analysis,” *Scientific Reports*, vol. 6, Aug 2016.
- [43] I. Ozden, J. Wang, Y. Lu, T. May, J. Lee, W. Goo, D. J. O’Shea, P. Kalanithi, I. Diester, M. Diagne, K. Deisseroth, K. V. Shenoy, and A. V. Nurmikko, “A coaxial optrode as multifunction write-read probe for optogenetic studies in non-human primates,” *Journal of Neuroscience Methods*, vol. 219, pp. 142–154, Sep 2013.
- [44] K. Tamura, Y. Ohashi, T. Tsubota, D. Takeuchi, T. Hirabayashi, M. Yaguchi, M. Matsuyama, T. Sekine, and Y. Miyashita, “A glass-coated tungsten microelectrode enclosing optical fibers for optogenetic exploration in primate deep brain structures,” *Journal of Neuroscience Methods*, vol. 211, pp. 49–57, Oct 2012.

- [45] S. Chen, W. Pei, Q. Gui, Y. Chen, S. Zhao, H. Wang, and H. Chen, "A fiber-based implantable multi-optrode array with contiguous optical and electrical sites," *Journal of Neural Engineering*, vol. 10, p. 046020, Jul 2013.
- [46] J. Lee, I. Ozden, Y.-K. Song, and A. V. Nurmikko, "Transparent intracortical microprobe array for simultaneous spatiotemporal optical stimulation and multichannel electrical recording," *Nature Methods*, vol. 12, pp. 1157–1162, Oct 2015.
- [47] D. R. Sparta, A. M. Stamatakis, J. L. Phillips, N. Hovelsø, R. van Zessen, and G. D. Stuber, "Construction of implantable optical fibers for long-term optogenetic manipulation of neural circuits," *Nature Protocols*, vol. 7, pp. 12–23, Dec 2011.
- [48] K. Ung and B. R. Arenkiel, "Fiber-optic implantation for chronic optogenetic stimulation of brain tissue," *Journal of Visualized Experiments*, Oct 2012.
- [49] J. A. Cardin, M. Carlén, K. Meletis, U. Knoblich, F. Zhang, K. Deisseroth, L.-H. Tsai, and C. I. Moore, "Targeted optogenetic stimulation and recording of neurons in vivo using cell-type-specific expression of channelrhodopsin-2," *Nature Protocols*, vol. 5, pp. 247–254, Jan 2010.
- [50] H. Taylor, J. T. Schmiedt, N. Çarçak, F. Onat, G. D. Giovanni, R. Lambert, N. Leresche, V. Crunelli, and F. David, "Investigating local and long-range neuronal network dynamics by simultaneous optogenetics, reverse microdialysis and silicon probe recordings *in vivo*," *Journal of Neuroscience Methods*, vol. 235, pp. 83–91, Sep 2014.
- [51] J. Wang, F. Wagner, D. A. Borton, J. Zhang, I. Ozden, R. D. Burwell, A. V. Nurmikko, R. van Wagenen, I. Diester, and K. Deisseroth, "Integrated device for combined optical neuromodulation and electrical recording for chronic in vivo applications," *Journal of Neural Engineering*, vol. 9, p. 016001, Dec 2011.
- [52] M. Sakaguchi, K. Kim, L. Yu, Y. Hashikawa, Y. Sekine, Y. Okumura, M. Kawano, M. Hayashi, D. Kumar, E. Boyden, T. Mchugh, and Y. Hayashi, "Inhibiting the activity of CA1 hippocampal neurons prevents the recall of contextual fear memory in inducible archt transgenic mice," *PLoS ONE*, vol. 10, Jun 2015.
- [53] N. Takata, K. Yoshida, Y. Komaki, M. Xu, Y. Sakai, K. Hikishima, M. Mimura, H. Okano, and K. F. Tanaka, "Optogenetic activation of CA1 pyramidal neurons at the dorsal and ventral hippocampus evokes distinct brain-wide responses revealed by mouse fMRI," *PLoS ONE*, vol. 10, p. e0121417, Mar 2015.
- [54] D. V. Gutierrez, M. D. Mark, O. Masseck, T. Maejima, D. Kuckelsberg, R. A. Hyde, M. Krause, W. Kruse, and S. Herlitze, "Optogenetic control of motor coordination by Gi/oProtein-coupled vertebrate rhodopsin in cerebellar purkinje cells," *Journal of Biological Chemistry*, vol. 286, pp. 25848–25858, May 2011.
- [55] X. Liu, S. Ramirez, P. T. Pang, C. B. Puryear, A. Govindarajan, K. Deisseroth, and S. Tonegawa, "Optogenetic stimulation of a hippocampal engram activates fear memory recall," *Nature*, Mar 2012.
- [56] B. A. Duffy, M. Choy, M. R. Chuapoco, M. Madsen, and J. H. Lee, "MRI compatible optrodes for simultaneous LFP and optogenetic fMRI investigation of seizure-like afterdischarges," *NeuroImage*, vol. 123, pp. 173–184, Dec 2015.

- [57] K. R. Dhakal, L. Gu, S. Shivalingaiah, T. S. Dennis, S. A. Morris-Bobzean, T. Li, L. I. Perrotti, and S. K. Mohanty, “Non-scanning fiber-optic near-infrared beam led to two-photon optogenetic stimulation in-vivo,” *PLoS ONE*, vol. 9, p. e111488, Nov 2014.
- [58] J. Dai, I. Ozden, D. I. Brooks, F. Wagner, T. May, N. S. Agha, B. Brush, D. Borton, A. V. Nurmikko, and D. L. Sheinberg, “Modified toolbox for optogenetics in the nonhuman primate,” *Neurophotonics*, vol. 2, p. 031202, May 2015.
- [59] P. Anikeeva, A. S. Andalman, I. Witten, M. Warden, I. Goshen, L. Grosenick, L. A. Gunaydin, L. M. Frank, and K. Deisseroth, “Optetrode: A multichannel readout for optogenetic control in freely moving mice,” *Nature Neuroscience*, vol. 15, pp. 163–170, Dec 2011.
- [60] S. Hardung, M. Alyahyay, D. Eriksson, and I. Diester, “A toolbox for optophysiological experiments in freely moving rats,” *Frontiers in Systems Neuroscience*, vol. 11, May 2017.
- [61] N. G. Laxpati, B. Mahmoudi, C.-A. Gutekunst, J. P. Newman, R. Zeller-Townson, and R. E. Gross, “Real-time in vivo optogenetic neuromodulation and multielectrode electrophysiologic recording with NeuroRighter,” *Frontiers in Neuroengineering*, vol. 7, Oct 2014.
- [62] K. Xie, G. E. Fox, J. Liu, and J. Z. Tsien, “512-channel and 13-region simultaneous recordings coupled with optogenetic manipulation in freely behaving mice,” *Frontiers in Systems Neuroscience*, vol. 10, Jun 2016.
- [63] M. R. Warden, J. A. Cardin, and K. Deisseroth, “Optical neural interfaces,” *Annual Review of Biomedical Engineering*, vol. 16, pp. 103–129, Jul 2014.
- [64] R. Scharf, T. Tsunematsu, N. McAlinden, M. D. Dawson, S. Sakata, and K. Mathieson, “Depth-specific optogenetic control in vivo with a scalable, high-density  $\mu$ LED neural probe,” *Scientific Reports*, vol. 6, Jun 2016.
- [65] W. Guo, A. E. Hight, J. X. Chen, N. C. Klapoetke, K. E. Hancock, B. G. Shinn-Cunningham, E. S. Boyden, D. J. Lee, and D. B. Polley, “Hearing the light: Neural and perceptual encoding of optogenetic stimulation in the central auditory pathway,” *Scientific Reports*, vol. 5, May 2015.
- [66] M. Schwaerzle, F. Pothof, O. Paul, and P. Ruther, “High-resolution optrode with integrated light source for deeper brain regions,” *Procedia Engineering*, vol. 120, pp. 924–927, 2015.
- [67] S. Ayub, F. Barz, O. Paul, and P. Ruther, “Heterogeneous 3d optrode with variable spatial resolution for optogenetic stimulation and electrophysiological recording,” in *2016 38th Annual International Conference of the IEEE Engineering in Medicine and Biology Society (EMBC)*, IEEE, Aug 2016.
- [68] F. Wu, E. Stark, P.-C. Ku, K. D. Wise, G. Buzsáki, and E. Yoon, “Monolithically integrated  $\mu$ LEDs on silicon neural probes for high-resolution optogenetic studies in behaving animals,” *Neuron*, vol. 88, pp. 1136–1148, Dec 2015.

## **CHAPTER 3**

# **MASKLESS WAFER-LEVEL MICROFABRICATION OF OPTICAL PENETRATING NEURAL ARRAYS OUT OF SODA-LIME GLASS: UTAH OPTRODE ARRAY**

Publication is reprinted with permission from Biomedical Microdevices-Springer Nature

Volume 18: 115 (6), pp.1-9, 2016



# Maskless wafer-level microfabrication of optical penetrating neural arrays out of soda-lime glass: Utah Optrode Array

Ronald W. Boutte<sup>1</sup> · Steve Blair<sup>1</sup>

Published online: 9 December 2016  
 © Springer Science+Business Media New York 2016

**Abstract** Borrowing from the wafer-level fabrication techniques of the Utah Electrode Array, an optical array capable of delivering light for neural optogenetic studies is presented in this paper: the Utah Optrode Array. Utah Optrode Arrays are micromachined out of sheet soda-lime-silica glass using standard backend processes of the semiconductor and microelectronics packaging industries such as precision diamond grinding and wet etching.  $9 \times 9$  arrays with  $1100\mu\text{m} \times 100\mu\text{m}$  optrodes and a  $500\mu\text{m}$  back-plane are repeatably reproduced on 2in wafers 169 arrays at a time. This paper describes the steps and some of the common errors of optrode fabrication.

**Keywords** Microfabrication · Maskless · Utah optrode Array (UOA) · Optogenetics · Neurophotonics · MEMS

## 1 Introduction

Optogenetics is the use of light to trigger neural excitation or inhibition, and after being named Nature Methods' "Method of the Year 2010," has seen unprecedented growth in the study of the central and peripheral nervous systems (Method of the year 2010). Neural tissue is transfected or transgenetically modified with a light sensitive protein and is illuminated with the specific wavelength of light needed to interrogate neuronal activity. A principal consideration in

optogenetics is how to get light onto the modified neurons and several methods have been introduced: 1) Direct tissue illumination, 2) Optical fiber insertion, 3) Optetrodes, 4) Michigan-style probes with small LEDs along the shanks, 5) Single glass optrodes, 6) Glass optrode arrays, 7) Red shifted optogenetics (Jaws) using the scattering properties of the brain's tissue and the long wavelength of red light, and 8) ZnO array with electrical recording capabilities (Abaya et al. 2012a, b; Zhang et al. 2009; Wu et al. 2013; Hira et al. 2009; Sparta et al. 2011; Anikeeva et al. 2011; Ludwig et al. 2006; Chuong et al. 2014; Ozden et al. 2008). Optical cannulae, such as those from Thorlabs (2016), have become the de facto standard for in vivo illumination of tissue. These cannulae are capable of insertions up to 20mm deep, where the optical fiber portion of the cannula is forced into the tissue to a desired depth. The ferrule portion is dental cemented into the craniotomy, such that a single optical fiber can be inserted, and the animal is allowed to recover for in vivo behavioral studies. Noninvasive techniques for neural activation have emerged as well: 1) Sonogenetics uses ultrasound, 2) X-Optogenetics uses x-rays, and 3) U-Optogenetics uses infrared to interrogate neurons (Pooh et al. 2011; Berry et al. 2015).

Each of these methods have advantages and disadvantages, but direct tissue illumination is currently the most widespread method of interrogating neurons. Many have used direct tissue illumination to discern neural functionality like cascading epileptic waveform recording, behavioral studies etc... (Zhang et al. 2009; Wu et al. 2013; Ayaz et al. 2011). It has been shown that a sharpened and metalized optical fiber could be placed into center position of a Multielectrode Array (MEA) and used to stimulate, and simultaneously record, epileptic activity in vitro transgenic mouse brain slices. The sharpened optical fiber could also be directly inserted deep into neural tissue. Optical

Ronald W. Boutte  
 r.boutte@utah.edu

<sup>1</sup> Department of Electrical and Computer Engineering,  
 University of Utah, 50 South Central Campus Dr., Room MEB  
 2110, Salt Lake City, UT 84112, USA

cannulae have been affixed within a small array of recording electrodes to stimulate and simultaneously record in vivo epileptic action potentials within the hippocampus (Laxpati et al. 2014). Several cannulae can be pressed towards each other to target large volumes of neural tissue. This is problematic for specificity because many times multiple cannulae fibers will overlap within the tissue or be insufficiently inserted to depth. First generation optical arrays (1st-gen UOA) with a high number of penetrating optrodes ( $10 \times 10$  and  $13 \times 13$ ) have been micromachined from 50.8mm round fused silica and fused quartz wafers (Abaya et al. 2012a). The 1st-gen UOAs were fabricated from fused silica/quartz wafers and were very difficult to micromachine because they required patterned photoresist, 49 % hydrofluoric acid (HF) for dynamic and static etching, and  $> 1150^\circ\text{C}$  annealing. Selection of round wafers required masking and patterning of photoresist, which was very difficult to see with the dicing saw's microscope. Round wafers also had a large amount of wasted space. Wet etching with large volumes ( $\sim 650\text{ml}$ ) highly concentrated HF posed a significant safety risk, so it required specialized personal protective equipment which was cumbersome and not conducive to process repeatability. Arrays made from the fused silica and fused quartz wafers required very high temperature annealing, which only cured surface imperfections and did little to change the shape of the optrode itself leaving them with pyramidal tips, square cross-sections, and long straight edges capable of slicing blood vesicles. Uneven heating was also observed on peripheral optrodes causing them to slump due to overheating, while optrodes closer to the center of the array showed signs of insufficient surface healing. The  $13 \times 13$  high density arrays were made with narrow optrode spacing ( $140\mu\text{m}$ ) which caused traumatic brain injury rendering the tissue unusable for in vivo studies (Boutte et al. 2013). This fabrication method

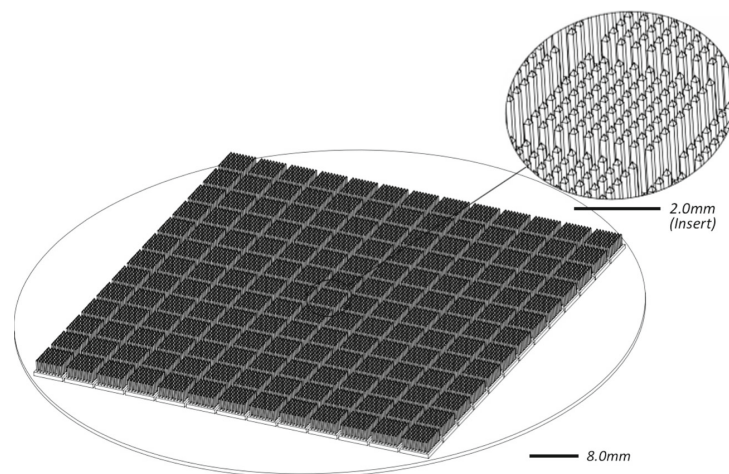
was sufficient for small quantity fabrication lots but not for the high volumes needed to support the growing optogenetic community needs.

This work presents the wafer-level microfabrication process to mass produce  $9 \times 9$  Generation-2 Utah Optrode Arrays (UOA) from square soda-lime wafers ( $2.4\text{mm} \times 50.8\text{mm} \times 50.8\text{mm}$ ) supported during cutting on a  $76.4\text{mm} \times 500\mu\text{m}$  silicon carrier wafer shown in Fig. 1. Each array optrode has  $400\mu\text{m}$  pitch with a minimum of  $250\mu\text{m}$  spacing and  $2^\circ$  of taper to allow for displaced tissue to rest. Each optrode has a round cross-sectional shape and convex shaped tip. Wafer-level fabrication has several advantages over the first generation fabrication process: 1) readily available and inexpensive soda-lime-silica glass replaces fused silica/quartz for easier grinding, wet etching, and lower temperature firing, 2) square wafers eliminate the need for wafer-level masking and photoresist patterning, 3) ammonium bifluoride paste replaces the need for 49 % HF, and 4) geometrical control of bulk micro-machined shapes are more easily maintained with lower annealing and polishing temperatures. This work also introduces a method for integrating 3D computer-aided design (CAD) and computer-aided machining (CAM), called Virtual CAD/CAM, to precisely control the optrode arrays' critical geometries during the wet grinding operations.

## 2 Utah Optrode Array fabrication

Plate glass wafers made of soda-lime-silica glass (SLG) are micromachined using standard back-end processes borrowed from the silicon wafer processing industry. Wet diamond saw blades are rastered across an SLG wafer's plate surface to create tips, diced into optrodes, and then singulated into arrays. Once the SLG has been properly

**Fig. 1** 3D CAD rendering of  $169 \times 9 \times 9$  UOAs provides for the foundational design considerations used in Virtual CAD/CAM during wet grinding operations. A square soda-lime-silica wafer ( $2.4\text{mm} \times 50.8\text{mm} \times 50.8\text{mm}$ ) is affixed to a round ( $76.4\text{mm} \times 0.500\text{mm}$ ) silicon carrier wafer with Dynatex WaferGrip<sup>®</sup>





diced into arrays, they are wet etched using Armor Etch<sup>®</sup> ammonium bifluoride paste, fire polished, and annealed. Gen-2 UOAs do not require any masking or cleanroom processes. Figure 2 shows an overview of the UOA wafer-level microfabrication process flow.

### 2.1 Creating soda-lime glass wafers

SLG was selected due to the availability of inexpensive raw materials in large thickness ranges (1.0mm – 22.0mm), low glass slumping temperature ( $T_s \sim 720^\circ\text{C}$ ), ease of wet etching, and its excellent biocompatibility (Davis et al. 1972). Since suitable biocompatible material is so readily available, it is not necessary to purchase from a custom manufacturer. The transmission spectra for SLG is 80 % – 90 % for wavelengths from  $\sim 300\text{nm}$  –  $2000\text{nm}$  making it suitable for most wavelength ranges currently used in optogenetic research (V.P. Glass 2016). Gardner Glass Products (2.4mm  $\times$  304.8mm  $\times$  254.0mm) clear replacement glass sheet (Lowes Item# 20751) is reduced to (2.4mm  $\times$  101.6mm  $\times$  101.6mm) using a commercial-off-the-shelf glass cutter and framing square (Lowes 2016). Rough cutting this way is quick, but causes chipping and jagged edges unsuitable for the fine dicing needed to grind arrays; however, the edge is good enough to align against for further wafer reduction. A DAD3220 Precision Dicing Saw is used to reduce the wafer to its final size of (2.4mm  $\times$  50.8mm  $\times$  50.8mm) and to produce an edge suitable for maskless alignment. A 600 grit Disco resin blade (Model# R07-SD600-BB200-50 58 $\times$ 0.25A2 $\times$ 40) is used for dicing the thick SLG. Standard (1.2mm  $\times$  76.4mm  $\times$  25.4mm) microscope slides can be made into UOAs when the desired neural tissue depth of penetration is  $\leq 700\mu\text{m}$ , and since slides are readily available in the laboratory environment they make good candidates for UOAs.

### 2.2 Distinguishing between float and rolled SLG

Two types of SLG were encountered during this work: float glass and rolled glass. Float glass is SLG that is made by floating molten soda-lime-silica on top of molten tin, and rolled glass is made by rolling super-heated SLG between two stainless steel rollers. Both types of SLG are acceptable

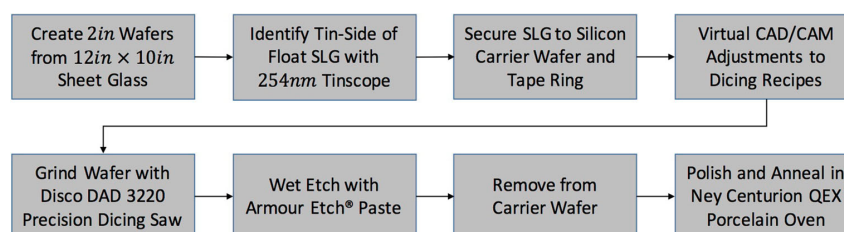
for the Gen-2 UOA with the caveat that float glass has a layer of tin, and if that is not machined away it can cause an organometallic toxicity when chronically implanted. It has been shown that the diffusion of tin onto the surface of float glass samples was 8 –  $9\mu\text{m}$ ; furthermore, it's been shown that tin is neurotoxic, and with the UOA's direct neural tissue contact it is necessary to remove the tin during micromachining operations (Yang et al. 1994; Chang 1990). Surface diffused tin is clear and colorless under normal lighting conditions, but under 254nm wavelength light the tin side will produce a cloudy appearance. A UVP Model# UCG-4 (Blak-Ray<sup>®</sup>) tinscope was held at  $45^\circ$  to each side of the glass. The tin side of the float SLG is marked with an asymmetrical identification label, so that it is easily distinguishable during subsequent micromachining steps. The non-tin side of the float SLG is called the air side and will not show any UV reflectance. Rolled glass, such as those in standard SLG microscope slides, will appear to have air sides on all the surfaces of the SLG. Regardless of the source of the SLG, it is necessary to determine if there is a presence of tin to prevent inadvertent neurological exposure.

### 2.3 Virtual CAD/CAM

This group discussed a principal strength of UOAs as being easily tuned to specific applications in neuroscience by customizing length, width, tip angle, and optrode spacing (Abaya et al. 2012b). Virtual CAD/CAM (shown in Fig. 3) eases the design and fabrication process of the UOA by virtually connecting any 3D CAD package with a 3 step CAM (DAD3220) grinding processes: Step 1) pyramidal tip creation, Step 2) optrode creation, and Step 3) singulation into individual UOAs. Several DAD3220 recipe parameters are calculated from actual wafer measurements, so a spreadsheet is used to bridge the 3D CAD model and the CAM needed for dicing saw control.

For the  $9 \times 9$  UOA, a 3D model of a single die cube (2.4mm  $\times$  3.85mm  $\times$  3.85mm) solid is drafted. Next a beveled blade profile is drawn to match Disco's beveled blade (Model# B1N862 SD600L75MT38 54 $\times$ 0.55  $\times$  40  $\times$   $45^\circ \times 0.15$ ). Alignment is done along the outer perimeter of the cube and an offset of  $125\mu\text{m}$  is applied mimicking how the dicing saw actually cuts. This profile is then

Fig. 2 Utah optrode array wafer-level microfabrication process



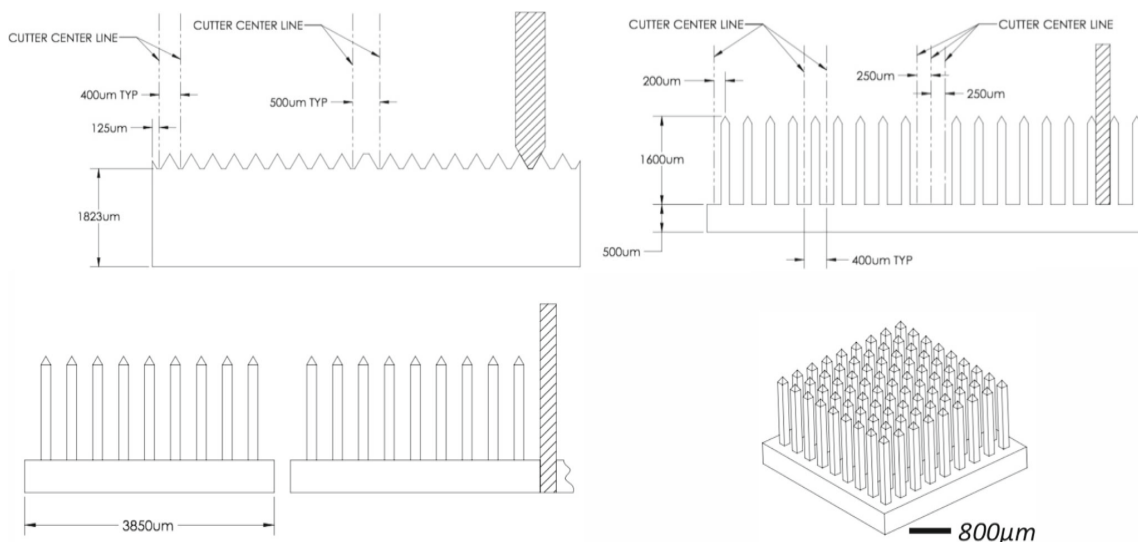


Fig. 3 Grinding progression using Virtual CAD/CAM for cutting tips, optrodes, and die singulation. (Top Left) A beveled blade is used to trench cut pyramidal tips by aligning the center of the blade on the edge of the wafer and then offsetting the first cut by 125µm. It is necessary to skip 500µm between two adjacent arrays. (Top Right) A flat 250µm resin blade cuts optrodes by aligning the center of the blade to

the first row of pyramidal tips and offsetting the first cut by ~200µm. Three cuts are required between adjacent arrays. (Bottom Left) Arrays are singulated into individual  $9 \times 9$  die with the same 250µm resin blade. Optrode pitch is 400µm, lengths are 1.4mm, pre-etch width is 150µm, with a 500µm backplane. (Bottom Right) Completely diced Utah Optrode Array ready for wet etching

virtually “lowered” onto the top surface of the 3D cube 10 times to cut beveled channels every 400µm, and then the cube is rotated 90° in the  $-xy$  plane. Once again the pattern is repeated creating pyramidal tips in the model. Optrodes and the die’s outer flanges are virtually diced using Disco’s resin blade (Model# R07-SD600-BB200-50 58×0.25A2×40) profile, drawn in the model, by lowering it onto the solid cube to depth resulting a 500µm thick backplane. This pattern is repeated until the final  $9 \times 9$  is modeled as with the beveled blade. In order to simulate the cutting of the SLG wafer, the 3D solid modeled parts were placed into an assembly of arrays. This was necessary to account for the spacing created by Disco’s resin blade (Model# R07-SD600-BB200-50 58×0.25A2×40) is then used to simulate singulation into individual die by copying and pasting the single array die into an array of arrays with 250µm spacing. The 3D models’ cutting simulations are used to create a recipe for the DAD3220 in a spreadsheet and then programmed into the DAD3220’s “Device Data” screen.

#### 2.4 Precision dicing

First-generation UOA cutting processes for the  $10 \times 10$  fused silica arrays were adapted for use on the DAD3220

for cutting SLG into the  $9 \times 9$  arrays. The SLG wafers are mounted onto a 76.4mm × 0.500mm round silicon carrier wafer using Dynatex WaferGrip<sup>TM</sup>, and then the carrier wafer is mounted to an 8 inch tape ring using a 3.0mm thick piece of rubber to offset the SLG from the bed of the tape station (see Fig. 4). The tape ring secures the carrier/SLG wafer to the dicing saw’s air chuck during grinding. Linear feed rate (1.0mm/sec), spindle speed (5000RPM), cut depth steps (250µm), and coolant flow (0.5L/min) are added to the Device Data recipe. Additional cut lengths are programmed into the saw to allow for the blades to be raised and lowered without inadvertently contacting the glass wafer, so each cut length is 60mm long, rather than 50.8mm. A notable exception to the 250µm depths steps is on the metal beveled blade because it has a propensity to wear quicker than the flat resin blades. Pyramidal tips are cut with a single plunge cut of 280µm.

#### 2.5 Wet etching

Rough cut optrodes are 150µm, so thinning is required to reach the desired 90µm optrode widths. Thinning of optrodes is achieved by wet etching the SLG wafers using Armour Etch<sup>®</sup> (ammonium bifluoride) paste while still attached to the carrier wafer. The paste preferentially etches

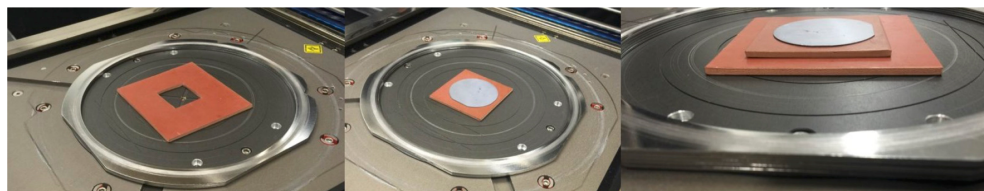
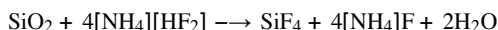


Fig. 4 (Left) Three 8" tape rings are stacked on top of each so that they match the thickness of the rubber mat in the middle of the rings. This mat is good for SLG wafers up to 3.2mm thick. (Middle) The rubber mat holds a silicon carrier wafer upside down suspending the SLG wafer inside the square hole cut from the middle. (Right) Double

stacked rubber mats shown for SLG wafers up to 6.4mm thick. Care must be taken when taping thick material for the spring loaded tape station bed to not press so hard that the silicon carrier wafer is crushed during taping

the glass and not the silicon wafer according the chemical reaction:



Armour Etch<sup>®</sup> paste tends to dry quickly, so a method of multiple applications is used to thin the optrodes. The paste is well shaken, so that it is mixed well and then applied with a wooden stick to sufficiently coat the entire SLG wafer with a thick layer of material such that no glass can be seen. During etching, the paste is continually worked across the entire wafer, with a nylon bristle paint brush, so as to continually provide a fresh active ingredient to the surface of the glass. After 5 minutes the SLG and Si carrier wafer are then thoroughly rinsed with tap water to remove the spent Armour Etch<sup>®</sup>. This process was repeated 3 additional times, such that the wafer was etched for a total of 20 minutes. Figure 5 shows the observed etch rate of Armour Etch<sup>®</sup> paste on SLG wafers as measured on a Pratt &

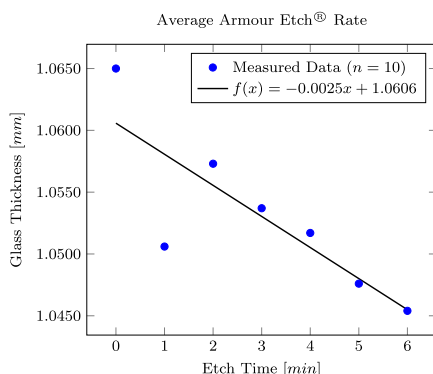


Fig. 5 Shows the average etch rate of  $2.5\mu\text{m}/\text{min} \pm 0.9\mu\text{m}/\text{min}$  (mean  $\pm$  SD) for Armour Etch<sup>®</sup> on soda-lime-silica glass where each data point is 10 samples

Whitney Supermicrometer with four decimals of precision. Ten samples were coated with paste and allowed to sit 1, 2, 3, 4, 5, and 6 minutes each, rinsed with deionized (DI) water, and then measured. Etch rate was measured to be  $2.5\mu\text{m}/\text{min} \pm 0.9\mu\text{m}/\text{min}$  (mean  $\pm$  SD).

## 2.6 Array removal from carrier wafer

Individual arrays are released from the carrier wafer by soaking for 10 minutes in xylene at  $135^\circ\text{C}$ ; a second soak in xylene removes any residual WaferGrip<sup>™</sup> that remains on the UOAs. The arrays are rinsed with n-butyl acetate to remove the xylene residue, and a final rinse in DI water ensures the die are completely clean. Finally, the arrays are dried in a  $60^\circ\text{C}$  oven after removing the bulk of the remaining water by carefully placing the extremely fragile arrays face down on a dry cleanroom towel.

## 2.7 Furnace firing schedule

Arrays are picked and placed onto a sheet of Fuseworks<sup>®</sup> Kiln Paper, containing vitreous aluminosilicate, to prevent them from sticking to anything within the furnace during firing. Dicing and etching causes the glass to have an extremely rough surface and builds stress within the array. Table 1 shows the firing schedule used for the reflow and anneal of the UOA. Surface roughness is smoothed out by getting the arrays close to their slumping temperature of

Table 1 Furnace firing schedule

Segment [units]	1	2	3	4	5
Rate [ $^\circ\text{C}/\text{min}$ ]	150	220	220	220	9999*
Temperature [ $^\circ\text{C}$ ]	650	720	485	350	RT
Hold Time [min]	24	6	54	0	indef.

720° C for 6 minutes. During this high temperature dwell the arrays take on their final shape of a smooth surface, round cross-sections, and rounded tips. Stress is relieved from within the arrays with a 24 minute soak just above SLG's annealing temp (650° C).

### 3 Results

Many of the wafer-scale fabrication benefits of the Utah Electrode Array were also realized for the UOA fabrication, in particular batch fabrication, reproducible geometric shapes, and precise customization of stimulating sites (Bhandari et al. 2010). While the principal benefits of wafer-level fabrication of UOAs are large array batch processing and high shape reproducibility, 100 % yield was not achieved for the UOAs. Key design elements of the UOAs are round cross-sectional optrodes, convex tips, flat back-plane, curved troughs between optrodes on the front-plane, and a wide area between optrodes. Each of the four main processing steps—dicing, wet etching, carrier wafer releasing, and fire polishing—introduced error which reduced the overall process yield. Figure 6 shows two optrodes of a completed  $9 \times 9$  array after each major step of the fabrication process.

#### 3.1 Dicing observations

Two main considerations needed to be very well controlled so as to reduce dicing errors: 1) Controlling heat build up during cutting, and 2) Leaving enough sacrificial



Fig. 6 (Left) Rough shaped optrodes after orthogonal dicing where the optrode dimensions are  $150\mu\text{m} \times 1,600\mu\text{m}$  with a  $45^\circ$  pyramidal tip. (Middle) Optrodes after 20 minutes of wet etching using a 5-minute pattern, repeated 4 times, of applying Armour Etch<sup>®</sup>, rinsing with tap water, and drying with dry nitrogen/air. At this stage, the optrodes show substantial surface roughness from sodium and lime removal from the bulk of the soda lime glass by the fluoride ions of the Armour Etch<sup>®</sup> paste. Optrodes have been reduced in size to  $90\mu\text{m} \times 1,600\mu\text{m}$ . (Right) Polishing arrays greatly improves the surface roughness, while annealing helps mechanically strengthen optrodes. Final optrode dimensions are  $100\mu\text{m} \times 1,100\mu\text{m}$  with a  $37\mu\text{m}$  radius of curvature lens tip and a  $2^\circ$  taper

material during cutting so as to prevent hydraulic fracturing of arrays' final rows. Heat builds as the coolant flow rate is dropped to 0.5L/ min and the linear feed speed is at 1.0mm/ sec, and this heat had a tendency to intermittently weaken the WaferGrip's<sup>™</sup> adhesion to the SLG. To prevent this from happening, the SLG, WaferGrip<sup>™</sup>, and silicon carrier wafer, prior to dicing, are placed in a vacuum-oven at 125° C while pulling a  $2 \times 10^{-3}$  Torr vacuum for 15 minutes or until a no voids were visible through the glass. Weight was added to fully seat the SLG into the WaferGrip<sup>™</sup>.

As the saw blades grind through the SLG, stress is built up in the residual glass, and it is easily seen as diffraction rings on the cut surface. When there is sufficient material, this stress is simply left until the glass is annealed, which relieves the internal stresses. When insufficient material is left behind the stress causes rows of optrodes to be broken as the cross axial coolant flow hits the kerf as the blade removes material; this is known as hydraulic fracturing. Figure 7 shows an experimental SLG wafer with a row of mostly missing optrodes because the  $500\mu\text{m}$  of remaining material was insufficient to buffer the stress built up as the blade cut;  $> 750\mu\text{m}$  was sufficient remaining material to prevent the optrode breakage.

#### 3.2 Wet etching observations

Buffered etchant was key to even removal of material, so it was necessary to continually agitate and turn over the etchant. Etchant turnover was done using a small nylon brush to constantly work the paste into the optrodes. There

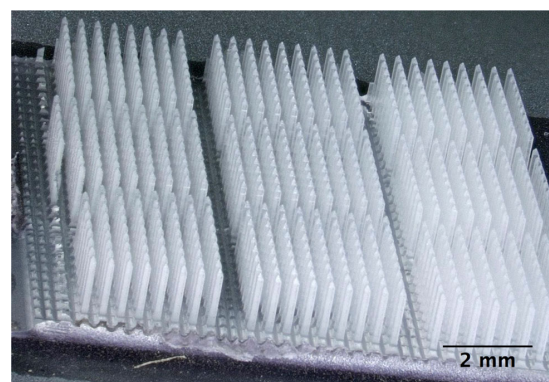
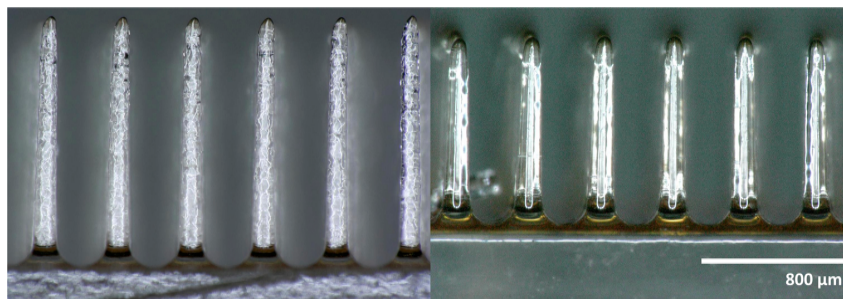


Fig. 7 An experimental  $13\text{mm} \times 13\text{mm}$  SLG wafer of  $9 \times 9$  arrays. Hydraulic fracturing on the far left of the wafer. Hydraulic fracturing occurs when there is not enough uncut sacrificial material left to buffer the internal stress as it builds within the wafer and is hit by a cross-axis specimen flow of water of 0.5L/ min. A sacrificial row of  $> 750\mu\text{m}$  is sufficient to protect the final row of optrodes from being damaged



Fig. 8 A completed  $9 \times 9$  (Left) Utah Optrode Array showing high surface roughness from insufficient firing. (Right) Properly fired array. AFM shows optrode average roughness and RMS roughness to be  $R_a = 13.5\text{nm}$  and  $R_q = 20.6\text{nm}$  respectively, and it shows  $R_a = 12.3\text{nm}$  and  $R_q = 16.4\text{nm}$  for the array's base



were two, easily handled with material turn over, errors seen during wet etching: 1) scaling due to insoluble oxides remaining on the surface of the glass, and 2) ammonium bifluoride crystals, with high etch rates, cutting into the glass causing uneven etching. A third observation was made due to Armour Etch<sup>®</sup> paste drying out during long exposure times, so it was necessary to reduce the etch time to 5 minute intervals with a tap water rinse in between.

### 3.3 Firing observations

Over-firing caused some optrodes to slump over making them unsuitable for implantation, and under-fired optrodes show an orange peel effect. Figure 8 shows a completed UOA that has been under fired with an orange-peel appearance, and the figure shows a completely fired array with smooth appearance. Atomic Force Microscopy (AFM) shows the average surface roughness of the final optrodes to be  $R_a = 13.5\text{nm}$  and RMS roughness to be  $R_q = 20.6\text{nm}$ , while AFM of the base shows the UOA's base to be  $R_a = 12.3\text{nm}$  and the RMS roughness to be  $R_q = 16.4\text{nm}$ .

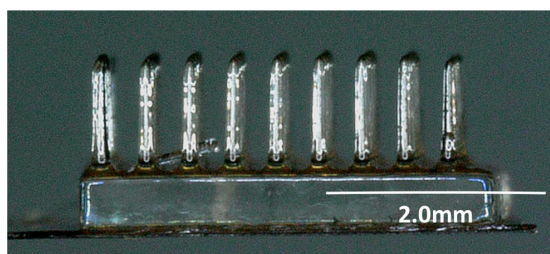


Fig. 9 A completed  $9 \times 9$  Utah Optrode Array with  $1100\mu\text{m} \times 100\mu\text{m}$  optrodes and a  $500\mu\text{m}$  planar back-plane. Several key design features can be seen: a  $2^\circ$  optrode taper and round cross section, a convex lens tip which allows for large tissue volume illumination, a flat back-plane which allows for insertion using Blackrock's multielectrode array inserter, and curved grooves on the front-plane which allow tissue irrigation during testing

## 4 Conclusion

Figure 9 shows a completed UOA suitable for both acute and chronic optogenetic studies. It has  $1100\mu\text{m} \times 100\mu\text{m}$  optrodes and a  $500\mu\text{m}$  planar back-plane. The  $9 \times 9$  array was developed for a general purpose array that is capable of being implanted into several types of tissue. Insertion depth can be controlled by adjusting the insertion pressure of Blackrock's multielectrode array inserter. At its maximum insertion, Layers IV–VI of the nonhuman primate brain can be optogenetically interrogated. Round vs. square cross-sectional geometry reduces insertion damage by  $\sim 25\%$ . Round corners reduce the damage to the blunt force seen during insertion by eliminating the four sharp corners which may lacerate blood vessels.

Soda-lime silica glass has been notoriously difficult to micromachine, but the process of fabricating a  $9 \times 9$  Utah Optrode Array uses standard microelectronic back-end processes of dicing, wet etching, and fire polishing without need of a cleanroom or masking. UOAs made for this work are set for use in optogenetic studies of non-human primate visual cortex to interrogate neurons. Neurons will be polarized, depolarized, or hyperpolarized using specific opsins that have been genetically modified to respond to light within the visual spectrum of  $\sim 390\text{nm} - 700\text{nm}$  by launching light onto the back-plane of the UOA and transmitting it to a depth of  $1.5\text{mm}$  deep below the surface of the brain. It has been shown that the UOA can be repeatedly fabricated in large batch quantities sufficient to support the growing optogenetics community with arrays capable of large tissue volume illumination, capable of both acute and chronic implantation, and  $25\%$  reduced tissue damage from previous fused silica/quartz optrode arrays.

**Acknowledgments** The majority of this work was self-funded by Mr. Ronnie Boutte, but he would like thank the Utah Science Technology and Research (USTAR) for providing seed funding under the Student-Oriented Project initiative for the Virtual CAD/CAM work for 404 a Tunable UOA. Dr. Steve Blair would like to thank the NSF for ancillary support provided under grant 1310654.

## References

- T. Abaya, S. Blair, P. Tathireddy, L. Rieth, F. Solzbacher, A 3d glass optrode array for optical neural stimulation. *Biomed. Opt. Express* 3(12), 3087 (2012a). doi:[10.1364/boe.3.003087](https://doi.org/10.1364/boe.3.003087)
- T. Abaya, M. Diwekar, S. Blair, P. Tathireddy, L. Rieth, G. Clark, F. Solzbacher, Characterization of a 3d optrode array for infrared neural stimulation. *Biomed. Opt. Express* 3(9), 2200 (2012b). doi:[10.1364/boe.3.002200](https://doi.org/10.1364/boe.3.002200)
- P. Anikeeva, A.S. Andalman, I. Witten, M. Warden, I. Goshen, L. Grosenick, L.A. Gunaydin, L.M. Frank, K. Deisseroth, Optetrode: A multichannel readout for optogenetic control in freely moving mice. *Nat. Neurosci.* 15(1), 163–170 (2011). doi:[10.1038/nn.2992](https://doi.org/10.1038/nn.2992)
- H. Ayaz, P.A. Shewokis, S. Bunce, B. Onaral, An optical brain computer interface for environmental control. in 2011 Annual International Conference of the IEEE Engineering in Medicine and Biology Society, Institute of Electrical & Electronics Engineers (IEEE), (2011). doi:[10.1109/iembs.2011.6091561](https://doi.org/10.1109/iembs.2011.6091561)
- R. Berry, M. Getzin, L. Gjesteb, G. Wang, X-Optogenetics and U-Optogenetics: Feasibility and Possibilities. in *Photonics, Multidisciplinary Digital Publishing Institute*, Vol. 2, (2015), pp. 23–39
- R. Bhandari, S. Negi, F. Solzbacher, Wafer-scale fabrication of penetrating neural microelectrode arrays. *Biomed. Microdevices* 12(5), 797–807 (2010). doi:[10.1007/s10544-010-9434-1](https://doi.org/10.1007/s10544-010-9434-1)
- R.W. Boutte, M. Bijanzadeh, A. Cutrone, F. Federer, S. Johnson, S. Merlin, L. Nurminen, S. Blair, A. Angelucci, Nonhuman primate visual cortex damage assessment of in vivo laser illumination and implanted 13X13 Utah Optrode array. in *Neural Engineering Research Group Presentation (University of Utah)*, (2013)
- L.W. Chang, The neurotoxicology and pathology of organomercury, organolead, and organotin. *J. Toxicol. Sci.* 15(SupplementIV), 125–151 (1990). doi:[10.2131/jts.15.supplementiv.125](https://doi.org/10.2131/jts.15.supplementiv.125)
- A.S. Chuong, M.L. Miri, V. Busskamp, G.A. Matthews, L.C. Acker, A.T. Sørensen et al., Noninvasive optical inhibition with a red-shifted microbial rhodopsin. *Nat. Neurosci.* 17(8), 1123–1129 (2014)
- S.D. Davis, D.F. Gibbons, R.L. Martin, S.R. Levitt, J. Smith, R.V. Harrington, Biocompatibility of ceramic implants in soft tissue. *J. Biomed. Mater. Res.* 6(5), 425–449 (1972). doi:[10.1002/jbm.820060509](https://doi.org/10.1002/jbm.820060509)
- R. Hira, N. Honkura, J. Noguchi, Y. Maruyama, G.J. Augustine, H. Kasai, M. Matsuzaki, Transcranial optogenetic stimulation for functional mapping of the motor cortex. *J. Neurosci. Methods* 179(2), 258–263 (2009). doi:[10.1016/j.jneumeth.2009.02.001](https://doi.org/10.1016/j.jneumeth.2009.02.001)
- N.G. Laxpati, B. Mahmoudi, C.A. Gutekunst, J.P. Newman, R. Zeller-Townson, R.E. Gross, Real-time in vivo optogenetic neuromodulation and multielectrode electrophysiologic recording with neuro-igher. *Front. Neuroeng.* 7 (2014). doi:[10.3389/fneng.2014.00040](https://doi.org/10.3389/fneng.2014.00040)
- Lowes, Gardner glass products 3/32-in x 12-in x 10-in clear replacement glass for windows, cabinets, and picture frames. <http://www.lowes.com/pd/Gardner-Glass-Products-3-32-in-x-12-in-x-10-in-Clear-Replacement-Glass-for-Windows-Cabinets-and-Picture-Frames/3121139>, accessed: 2016-10-09 (2016)
- K.A. Ludwig, J.D. Uram, J. Yang, D.C. Martin, D.R. Kipke, Chronic neural recordings using silicon microelectrode arrays electrochemically deposited with a poly(3,4-ethylenedioxythiophene) (PEDOT) film. *J. Neural. Eng.* 3(1), 59–70 (2006). doi:[10.1088/1741-2560/3/1/007](https://doi.org/10.1088/1741-2560/3/1/007)
- Method of the year. *Nat. Methods* 8(1), 1–1 (2010). doi:[10.1038/nmeth.f.321](https://doi.org/10.1038/nmeth.f.321)
- I. Ozden, H.M. Lee, M.R. Sullivan, S.S.H. Wang, Identification and clustering of event patterns from in vivo multiphoton optical recordings of neuronal ensembles. *J. Neurophysiol.* 100(1), 495–503 (2008). doi:[10.1152/jn.01310.2007](https://doi.org/10.1152/jn.01310.2007)
- R.K. Pooh, K.W. Choy, L.T. Yeung, T.K. Lau, Sonogenetics: A breakthrough in prenatal diagnosis. *Donald School Journal of Ultrasound in Obstetrics and Gynecology* 5(1), 73–77 (2011)
- D.R. Sparta, A.M. Stamatakis, J.L. Phillips, N. Hovelsø, R. van Zessen, G.D. Stuber, Construction of implantable optical fibers for long-term optogenetic manipulation of neural circuits. *Nat. Protoc.* 7(1), 12–23 (2011). doi:[10.1038/nprot.2011.413](https://doi.org/10.1038/nprot.2011.413)
- Thorlabs, Implantable fiber optic cannulae (2016)
- V.P. Glass, Soda lime glass: Internal transmittance [2mm] accessed: 2016-10-09 (2016)
- F. Wu, E. Stark, M. Im, I.J. Cho, E.S. Yoon, G. Buzsáki, K.D. Wise, E. Yoon, An implantable neural probe with monolithically integrated dielectric waveguide and recording electrodes for optogenetics applications. *J. Neural. Eng.* 10(5), 056.012 (2013). doi:[10.1088/1741-2560/10/5/056012](https://doi.org/10.1088/1741-2560/10/5/056012)
- B. Yang, P.D. Townsend, S.A. Holgate, Cathodoluminescence and depth profiles of tin in float glass. *J. Phys. D: Appl. Phys.* 27(8), 1757–1762 (1994). doi:[10.1088/0022-3727/27/8/026](https://doi.org/10.1088/0022-3727/27/8/026)
- J. Zhang, F. Laiwalla, J.A. Kim, H. Urabe, R.V. Wagenen, Y.K. Song, B.W. Connors, F. Zhang, K. Deisseroth, A.V. Nurmikko, Integrated device for optical stimulation and spatiotemporal electrical recording of neural activity in light-sensitized brain tissue. *J. Neural. Eng.* 6(5), 055.007 (2009). doi:[10.1088/1741-2560/6/5/055007](https://doi.org/10.1088/1741-2560/6/5/055007)

## **CHAPTER 4**

# **UTAH OPTRODE ARRAY CUSTOMIZATION USING STEREOTACTIC BRAIN ATLASES AND 3D CAD MODELING FOR OPTOGENETIC NEOCORTICAL INTERROGATION IN SMALL RODENTS AND NONHUMAN PRIMATES**

Publication is reprinted with permission from Neurophotonics-SPIE

Volume 4(4), pp.1-14, 2017

# Neurophotonics

neurophotonics.SPIEDigitalLibrary.org

## **Utah optrode array customization using stereotactic brain atlases and 3-D CAD modeling for optogenetic neocortical interrogation in small rodents and nonhuman primates**

Ronald W. Boutte  
Sam Merlin  
Guy Yona  
Brandon Griffiths  
Alessandra Angelucci  
Itamar Kahn  
Shy Shoham  
Steve Blair



Ronald W. Boutte, Sam Merlin, Guy Yona, Brandon Griffiths, Alessandra Angelucci, Itamar Kahn, Shy Shoham, Steve Blair, "Utah optrode array customization using stereotactic brain atlases and 3-D CAD modeling for optogenetic neocortical interrogation in small rodents and nonhuman primates," *Neurophoton.* **4**(4), 041502 (2017), doi: 10.1117/1.NPh.4.4.041502.



# Utah optrode array customization using stereotactic brain atlases and 3-D CAD modeling for optogenetic neocortical interrogation in small rodents and nonhuman primates

Ronald W. Boutte,<sup>a,b,\*</sup> Sam Merlin,<sup>c</sup> Guy Yona,<sup>d</sup> Brandon Griffiths,<sup>b</sup> Alessandra Angelucci,<sup>c</sup> Itamar Kahn,<sup>d</sup> Shy Shoham,<sup>d</sup> and Steve Blair<sup>a,\*</sup>

<sup>a</sup>University of Utah, Department of Electrical and Computer Engineering, Salt Lake City, Utah, United States

<sup>b</sup>Northrop Grumman Corporation, Salt Lake City, Utah, United States

<sup>c</sup>University of Utah, Moran Eye Institute, Department of Ophthalmology, Salt Lake City, Utah, United States

<sup>d</sup>Technion–Israel Institute of Technology, Haifa, Israel

**Abstract.** As the optogenetic field expands, the need for precise targeting of neocortical circuits only grows more crucial. This work demonstrates a technique for using Solidworks® computer-aided design (CAD) and readily available stereotactic brain atlases to create a three-dimensional (3-D) model of the dorsal region of area visual cortex 4 (V4D) of the macaque monkey (*Macaca fascicularis*) visual cortex. The 3-D CAD model of the brain was used to customize an 8 × 6 Utah optrode array (UOA) after it was determined that a high-density (13 × 13) UOA caused extensive damage to marmoset (*Callithrix jacchus*) primary visual cortex as assessed by electrophysiological recording of spiking activity through a 1.5-mm-diameter through glass via. The 8 × 6 UOA was customized for optrode length (400 μm), optrode width (≤100 μm), optrode pitch (400 μm), backplane thickness (500 μm), and overall form factor (3.45 mm × 2.65 mm). Two 8 × 6 UOAs were inserted into layer VI of macaque V4D cortices with minimal damage as assessed in fixed tissue cytochrome oxidase staining in nonrecoverable surgeries. Additionally, two 8 × 6 arrays were implanted in mice (*Mus musculus*) motor cortices, providing early evidence for long-term tolerability (over 6 months), and for the ability to integrate the UOA with a Holobundle light delivery system toward patterned optogenetic stimulation of cortical networks. © 2017 Society of Photo-Optical Instrumentation Engineers (SPIE) [DOI: 10.1117/1.NPh.4.4.041502]

Keywords: optogenetics; macaque monkey; neocortical stimulation; optical interrogation; computer–brain interface; 3-D CAD model. Paper 17039SSPR received Mar. 31, 2017; accepted for publication Jun. 8, 2017; published online Jul. 12, 2017.

## 1 Introduction

The burgeoning field of optogenetics is increasingly branching into new areas of the brain and is expanding into new species of study, which in-turn requires device engineers to be able to respond rapidly with customized optrodes to meet these changing needs.<sup>1–4</sup> In the absence of a large catalog of previously built intracortical probes for light delivery as reference, it was necessary to develop a method to target specific areas of the brain and laminae of the cerebral cortex, which was also applicable to a wide variety of animals, by taking advantage of commercially available brain atlases to reduce the need for live animals. The current *de facto* standard for intracortical light delivery is a fiber optic-coupled cannula from makers such as Thorlabs.<sup>5</sup> Several different methods have been created to deliver light to larger volumes of tissue and to target specific neocortical regions.<sup>6–9</sup> Arrays of cannulae get too cumbersome and are difficult to fabricate and insert, so research groups have devised arrays to illuminate tissue.<sup>10</sup>

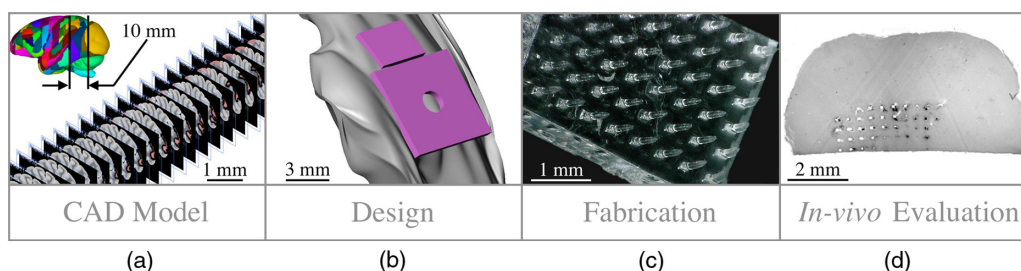
The goal of this study was to develop a method of customizing Utah optrode array (UOA)'s using Solidworks® to model a brain's region of interest in three-dimensions (3-D). A major benefit of this work was to reduce the number of animals needed

for experimentation by virtually implanting a 3-D model of a UOA into the brain's region of interest 3-D model. The method demonstrated in this study is easily transferred to any animal species or anatomical region in which an atlas has been created; the atlas only needs to have individualized anatomical plates from optical images, computer tomographic scan, magnetic resonance images, etc, which can be converted into .jpg images and imported into Solidworks®. Stereotaxic measurements were used in this study's 3-D models, but any reference dimensions could have been used to create the brain's region of interest 3-D model. Figure 1 provides a schematic overview of the stereotaxic method for customizing UOAs.

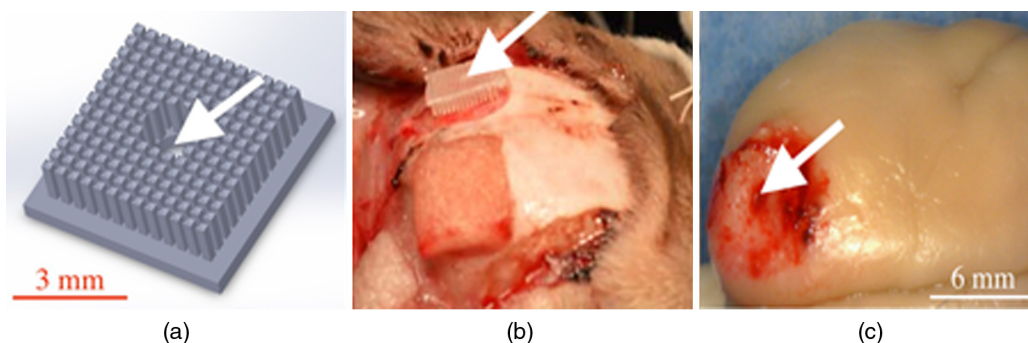
## 2 Methods

The foundation for this work was laid using a 13 × 13 high-density 6 mm × 6 mm UOA with 1.5-mm-long/square optrodes as shown in Fig. 2, which was largely based upon prior work by this group to create an optical array based on the widely used Utah electrode array.<sup>11–15</sup> This prototype 13 × 13 device caused significant tissue damage in marmoset (*Callithrix jacchus*) visual cortex, so it was determined that it was necessary to design a more suitable array for small nonhuman primates and small rodents using a Solidworks® 3-D computer-aided design

\*Address all correspondence to: Ronald W. Boutte, E-mail: [r.boutte@utah.edu](mailto:r.boutte@utah.edu); Steve Blair, E-mail: [blair@ece.utah.edu](mailto:blair@ece.utah.edu)



**Fig. 1** Stereotactic method for customizing UOAs. (a) 3-D CAD brain modeling of macaque V4D using Calabrese<sup>17</sup> atlas plates with highlighted Paxinos<sup>16</sup> regions. A 10-mm section of V4D is selected for 3-D CAD modeling, and the section's 23 atlas plates have been spaced at 450  $\mu\text{m}$  simulating their location within the macaque brain. (b) Two 3-D CAD models of the UOA shown virtually implanted in V4D (13  $\times$  13 array with TGV and a smaller 8  $\times$  6); both devices are shown implanted into the 3-D CAD brain model. (c) A completed soda-lime glass 8  $\times$  6 UOA, and (d) histological results showing successful macaque V4D implantation.



**Fig. 2** (a) A 13  $\times$  13 Solidworks<sup>®</sup> 3-D model of the high-density UOA with a  $\varnothing$ 1.5-mm TGV. (b) High density array shown just prior to insertion resting on a marmoset's primary visual cortex after craniotomy and durotomy have been performed. (c) Postfixation tissue damage assessment shows the array caused vascular damage as well as damage from the trauma of insertion, where high amounts of tissue have been compressed between the array's optrodes. Histological assessment of tissue damage was not performed due to the level of tissue damage seen following device explantation. The white arrows mark the insertion location of a single 150- $\mu\text{m}$  electrode which was successful in recording neural spiking during postinsertion optrode illumination. Active neural action potentials indicated the neural tissue close to the optrodes around the TGV were still firing.

(CAD). From the 3-D brain model, an 8  $\times$  6 UOA was designed and modeled to target individual laminae within the neocortices of small animals, and the UOA model was fabricated using wafer-scale microfabrication techniques.<sup>12</sup> The customized 8  $\times$  6 device was then inserted into two macaque monkeys (*Macaca fascicularis*) during nonrecoverable surgeries to assess the acute tissue damage caused during the implantation process. Two 8  $\times$  6 devices were later inserted into two C57BL/6 wild-type mice (*Mus musculus*) during recoverable surgeries with excellent long-term tolerability.

## 2.1 Marmoset (*Callithrix jacchus*)

To assess cortical damage caused by the array, a single marmoset that was undergoing an acute electrophysiological recording procedure for unrelated experiments was implanted with a 13  $\times$  13 UOA at the end of the recording session. This reduced the number of animals needed for the two separate studies. The unrelated electrophysiological experiments took place in the

right hemisphere, and the UOA was inserted into the left hemisphere.

### 2.1.1 Prototype high density 13 $\times$ 13 UOA with through glass via

This device was fabricated from fused silica using orthogonal dicing techniques<sup>13</sup> and a  $\varnothing$ 1.5 mm through glass via (TGV) to allow for insertion of a recording electrode through the UOA. Optrodes were obelisk-shaped with 45-deg pyramidal tips, 1.5-mm long, 250- $\mu\text{m}$  wide, set at 400- $\mu\text{m}$  pitch, leaving a gap between them of 150  $\mu\text{m}$ . The backplane was 500  $\mu\text{m}$  thick and had an outer perimeter of 6 mm  $\times$  6 mm. The TGV was created by grit ablation through a partially completed 13  $\times$  13 array just prior to wet etching and annealing. The array's backplane was masked using Kapton<sup>®</sup> tape with a 500- $\mu\text{m}$  window exposed to allow the grit to access the glass for etching. The array was then placed into a cardboard carrier that supported the array during the aggressive grit blasting. 25- $\mu\text{m}$  alumina ( $\text{Al}_2\text{O}_3$ )

grit was sprayed through a  $\varnothing 2.0$ -mm tip at  $\sim 100$  PSI for  $\sim 5$  min until a  $\varnothing 1.5$ -mm hole was drilled on the front side of the array. The TGV removed nine inner optrodes, so it was necessary to ensure no sharp edges remained of partially etched optrodes.

### 2.1.2 Marmoset in vivo $13 \times 13$ UOA insertion

Marmoset was anesthetized as described in detail for macaques in Sec. 2.5.1. A prototype  $13 \times 13$  UOA was sterilized and placed on the primary visual cortex of a sufentanil-anesthetized [6 to 12 ( $\mu\text{g/kg}$ )/h] marmoset monkey, as shown in Fig. 2(b), after craniotomy and durotomy, and it was inserted using a perpendicularly positioned, actuated pneumatic hammer (Blackrock, Salt Lake City, Utah; 16 PSI, 600- $\mu\text{m}$  depth range). Significant tissue damage can be seen in Fig. 2, following post-fixation removal of the device.

### 2.1.3 Marmoset electrophysiology through the TGV

Following insertion of the  $13 \times 13$  high density array, a high impedance epoxylite-coated tungsten microelectrode (1 to 2 M $\Omega$ , FHC Inc., Bowdoin, Maine) was advanced through the TGV using a hydraulic micropositioner (Kopf Instruments, Tujunga, California). Spikes were amplified and bandpass filtered between 400 Hz and 5 kHz, and sampled at 22 kHz by a dual-processor G5 Power Mac, running custom scripts on EXPO software (courtesy of Dr. Peter Lennie, University of Rochester, Rochester, New York). Visually evoked spiking activity was recorded in response to high contrast (100%) drifting (2 to 5 Hz) sinusoidal gratings (spatial frequency 0.5 to 4 cycles/deg) of varying orientation. Spikes were displayed on a Sony GDM-C520K monitor with a mean luminance of 45  $\text{cdm}^{-2}$  and at a viewing distance of 57 cm. However, visually driven spiking activity was sluggish and spikes were rapidly decaying, most likely due to the damage from insertion of the high-density array.

## 2.2 Stereotaxic Atlas Plate Utility in UOA Design

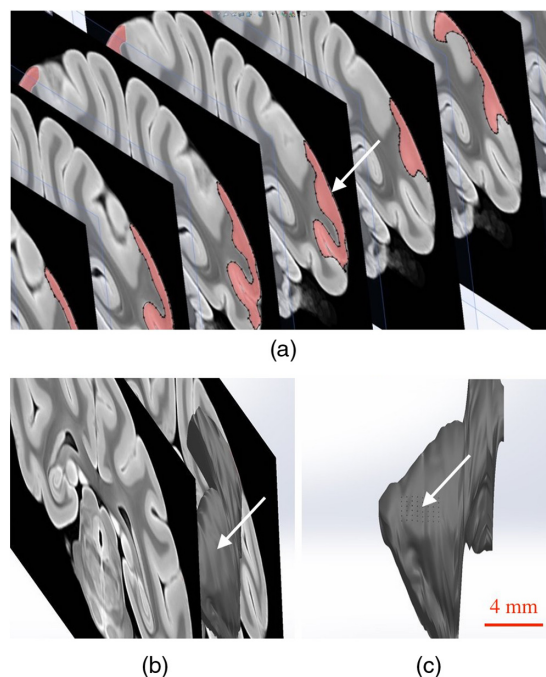
The tissue damage caused by the prototype array prompted a complete redesign of the device with anatomical considerations, such as Paxinos<sup>16</sup> region of interest, cortical layer(s) of interest, and minimal invasiveness as a goal, using stereotaxic coordinate atlases. A key feature of the stereotaxic coordinate system is that it is based on standard right-handed 3-D Cartesian coordinate system, where the  $x$ ,  $y$ , and  $z$  axes have been mapped to anatomical structures of the skull. The  $x$  or mediolateral (ML) axis is the distance away from the sagittal suture or midline; the  $y$  or anteroposterior (AP) axis is mapped to the interaural line; and the  $z$  or dorsoventral (DV) axis is mapped to the distance from the top of the skull at the 0 point. For this paper, the stereotaxic coordinates are referenced to bregma and will look like their Cartesian analog (ML, AP, and DV). These coordinates have enormous utility for the neuroscientist in that they can be used for targeting specific areas without the need to harm animals in trial and error experiments. Stereotaxic coordinate systems afford device engineers opportunities to exploit the targeting of areas with customizing neural prostheses to the area within the atlas plates of interest. By placing the atlas plates covering the region of interest into a 3-D CAD program such as Solidworks®, the designer can create a 3-D model of the space in between plates that can then be used to create a custom

computer-brain interface and place it into the correct location that is planned during the surgery.

### 2.3 Solidworks® 3-D Modeling of the Brain's Region of Interest

Solidworks® 3-D CAD was used to create a 3-D CAD model of the region of interest in the brain by importing brain atlas plates with stereotaxic coordinates, stitching the regions of interest together, and rendering as a 3-D CAD solid. The 3-D CAD model was then used to design a custom  $8 \times 6$  UOA that was capable of laying entirely within the region of interest in all 3-D and virtually placed. Once placed, the array's precise placement was converted to stereotaxic coordinates for actual placement. Maskless wafer-level microfabrication techniques for UOA microfabrication<sup>12</sup> were used to create the  $8 \times 6$  UOA to target layer VI of the dorsal region of visual area V4 (V4D) of the macaque monkey (*M. fascicularis*) visual cortex. The  $8 \times 6$  device was inserted with minimal acute tissue damage when compared to the previous marmoset work and was suitable for implantation into small rodents such as the common mouse (*M. musculus*).

Calabrese<sup>17</sup> atlas plates, with Paxinos<sup>16</sup> V4D, were captured from the Scalable Brain Atlas<sup>18</sup> and then placed onto individual planes within the Solidworks® CAD environment spaced at the precise spacing they would be within the atlas (410  $\mu\text{m}$ ). Each Paxinos<sup>16</sup> region was outlined on each of the 23 plates of V4D



**Fig. 3** (a) A portion of the Calabrese<sup>17</sup> atlas plates as captured from the Scalable Brain Atlas<sup>18</sup> viewer showing the Paxinos<sup>16</sup> region V4D in Solidworks® with each of the Paxinos<sup>16</sup> regions outlined with a B-spline. (b) Conceptualized Solidworks® 3-D model with lofts between the Paxinos<sup>16</sup> regions of each plate of V4D shown between the starting and ending plates. (c) Sagittal view of the 3-D model of V4D with insertion marks where the  $8 \times 6$  array has been virtually inserted. The white arrows mark the centroid of interest for illumination of layer IV.

with a B-spline (see Fig. 3), and the splines were lofted together to create a single 3-D CAD model of the V4D region. A centroid of interest was identified within the 3-D CAD model for ideal UOA placement. The customized UOA was placed at the centroid of interest and virtually inserted at (ML = 25.7 mm, AP = -29.3 mm, DV = 27.1 mm). Figure 3 shows the spline and lofting process along with the 3-D CAD model of V4D.

In principal, essentially any 3-D CAD package capable of drawing basis-splines and 3-D lofts could be used for creating the 3-D models of the brain, and during this research AutoCAD®, ImageJ®, Solidworks®, and the Scalable Brain Atlas were explored. Solidworks® proved to be better suited for importing .jpg images directly into the model space. It was possible to draw directly onto the .jpg in Solidworks® without affecting the 3-D model that was created because the modeling environment interpreted the .jpg as infinitely thin; thus, the .jpg had no volume to skew the 3-D solid model.

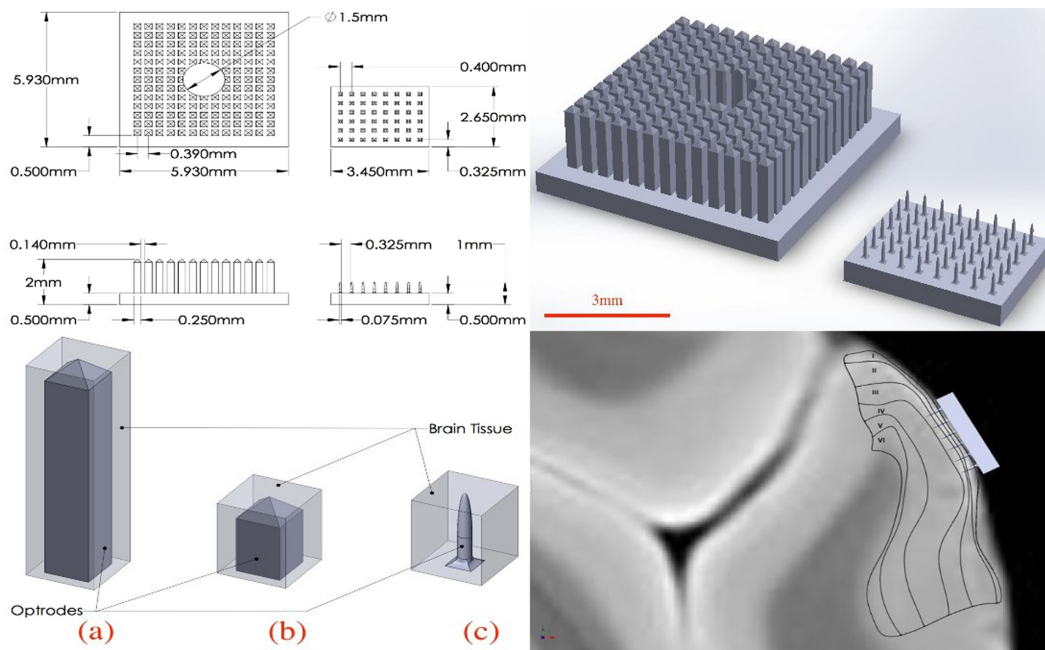
## 2.4 Customization of an 8×6 UOA

Array design improvement started with a careful study of the fine structures of the brain, using Paxinos<sup>16</sup> regions, with the goal of targeting a smaller area of the brain to minimize the contact surface area of the array and its optrodes. Stereotaxic coordinate system atlases are widespread, and typically show coronal cross-sections of species specific brains, e.g., Fig. 3.<sup>16,19,20</sup> The Scalable Brain Atlas<sup>18</sup> is an internet-based atlas viewer

where researchers can display many different species: macaque, mouse, rat, human, marmoset, and opossum. It is necessary to select an atlas to view in the Scalable Brain's<sup>18</sup> user interface, where the interface is broken into three main compartments: (1) sagittal hemispherical cartoon view of atlas plates, (2) coronal view of region of interest slice with Paxinos<sup>16</sup> outlines, and (3) regional hierarchy showing a list of regions present in the selected atlas slice. The Calabrese<sup>17</sup> et al. atlas is an MRI + DTI atlas and did not use stereotaxic coordinates, so it was necessary to convert the distances to stereotaxic coordinates using the Scalable Brain's<sup>18</sup> measurement system. Screen selections were captured from the Scalable Brain's<sup>18</sup> Atlas plate viewer of gradient echo (GRE)-stained Calabrese<sup>17</sup> plates, with Paxinos<sup>16</sup> region highlighted and imported into Solidworks®. UOA fabrication has been well characterized in the previous work<sup>13-15</sup> where the general purpose<sup>12</sup> UOA's key features of 400- $\mu$ m optrode pitch, 250- $\mu$ m outer flange, and 500- $\mu$ m-thick backplane have been incorporated into a custom array. Figure 4 shows conversion from the 13×13 high density array to the 8×6 custom array.

## 2.5 Macaque (*Macaca fascicularis*)

Two anesthetized macaques were implanted with the customized 8×6 UOA during a scheduled nonrecoverable surgery. As with the marmoset, these animals were part of an unrelated electrophysiological experiment, and the implantation of the



**Fig. 4** (Top left) Design parameters for both 13×13 and the 8×6 arrays set to the same scale. (Top right) Side-by-side comparison of the 13×13 high density array and the much smaller 8×6 UOA. Key differences are wider optrode spacing and the removal of all sharp edges that may contact neural tissue on the UOA. Note: (Bottom left) Volumetric representation of neural tissue surrounding optrodes. Each optrode compresses the tissue into the space between optrodes as they penetrate: (a) the 1.50 mm × 0.250 mm × 0.250 mm optrode has a tissue volume to optrode volume of 2.58:1, (b) the 0.500 mm × 0.250 mm × 0.250 mm optrode has a tissue volume to optrode volume of 2.92:1, and (c) the 0.500 mm × 0.075 mm optrode has a tissue volume to optrode volume of 40.1:1. (Bottom right) Paxinos<sup>16</sup> region V4D with laminae conceptualized showing array tips at the boundary of layers III and IV.



UOA was accomplished after those experiments were completed.

### 2.5.1 Macaque in vivo $8 \times 6$ UOA insertion

*In vivo* insertion of the  $8 \times 6$  UOA was done on two macaque monkeys (*M. fascicularis*) to assess the damage caused during insertion, for comparison to the original marmoset (*C. jacchus*) and to determine if V4D layer IV was properly targeted by the device as designed. Monkeys were initially anesthetized with ketamine (30 mg/kg i.m.), isoflurane (2% in oxygen), followed by continuous sufentanil citrate [7–10 ( $\mu\text{g/kg}$ )/h i.v.], fluid infusion [5 (ml/kg)/h i.v.], and artificially ventilated. Anesthetic depth was assessed continuously via end-tidal  $\text{CO}_2$ , oximetry, heart rate, and blood pressure monitoring. Craniotomy and durotomy were performed to expose cortical surface. Following insertion of the UOA, the durotomy was closed with a layer of sterile Gelfoam®, and the craniotomy was sealed with dental cement. The experiment was terminated with a lethal dose of pentobarbital (60 mg/kg i.v.), and the animal perfused with 4% paraformaldehyde and the brain removed for histology.

Prior to insertion, the optrodes were sterilized in chlorhexidine solution. One optrode was placed on the cortical surface in an area devoid of large surface vasculature and inserted using a perpendicularly positioned, actuated pneumatic hammer (Blackrock, Salt Lake City, Utah; 10 PSI, 0.6-mm depth range) at stereotaxic coordinates (ML = 25.7 mm, AP = -29.3 mm, and DV = 27.1 mm).

### 2.5.2 Macaque postexplantation histology

The optrode was removed from the brain following fixation, brains were postfixed in 4% paraformaldehyde for 6 h and cryoprotected in 30% sucrose. Brains were frozen-sectioned sagittally at 40  $\mu\text{m}$  and reacted for cytochrome oxidase. Sections were mounted, dehydrated, defatted, and coverslipped. Sections were photographed at low power (1.25 $\times$  objective) on a Zeiss Axioskop 2 (Zeiss, Oberkochen, Germany) using Neurolucida software (MicroBrightField Bioscience, Williston, Vermont).

## 2.6 C57BL/6 Wild-Type (*Mus musculus*)

One UOA was implanted into a single mouse as part of a scheduled recoverable surgery. The array was to gauge the animal's recovery and long-term tolerability of the device. A second mouse was implanted as part of a Holobundle light delivery system.<sup>21</sup>

### 2.6.1 Mouse in vivo insertion preparation

Mice were anesthetized with isoflurane (2%), mounted on a surgical frame and had their body temperature maintained. Analgesia was administered locally (kamacaine, 8 mg/kg s.c.), topically (lidocaine HCl 2%), and systemically (buprenorphine 0.1 mg/kg s.c.), dexamethasone (0.2 mg/kg s.c.) were administered to reduce brain edema, meloxicam (0.1 mg/kg s.c.) was administered to prevent inflammation and occlusion of the glass implant, and eye ointment (Duratears, Alcon-Couvreur) was applied to prevent dryness. The right parietal bone was removed from the midline to 4 mm lateral to the midline. Post-op treatment included injections of broad-spectrum antibiotics (penicillin-streptomycin) and analgesia (buprenorphine).

### 2.6.2 Mouse in vivo insertion of a UOA with a Holobundle light delivery system

The UOA was used in conjunction with a specialized optogenetic light delivery system for transmitting defined light patterns through the highly scattering mouse cortex.<sup>22</sup> The modified Holobundle system, based on the early apparatus described by Farah et al.,<sup>21</sup> uses computer-generated holography to project light patterns into a custom fiber bundle matching the UOA's  $8 \times 6$  arrangement, which is designed to transmit the light pattern into the bore of an MRI machine. The bundle's termination was encased in a guide coupled to a cortical connector for aligning the bundle and the UOA during repeated insertions, and a beam for fixing the animal head to the MRI cradle. The assembly was 3-D printed, MRI compatible, and bonded together with cyanoacrylate prior to surgery. In addition, connected UOAs were inserted into the cortex of two mice: wild-type C57BL/6 mouse (*M. musculus*) and a transgenic mouse expressing channelrhodopsin-2-eYFP under a Thy1.2 promoter (strain: B6.Cg-Tg(Thy1-COP4/EYFP)9Gfng/J, Jackson Laboratories, Bar Harbor, Maine). The dimensions of the  $8 \times 6$  UOA match the distance between the bregma and lambda points of the mouse skull and supports removal of the parietal bone along the suture lines to avoid excessive bleeding or damage to brain tissue.

## 3 Results

The  $8 \times 6$  UOA was successfully designed and fabricated using the same wafer-level techniques as previously described.<sup>12</sup> Implantation of the customized UOA showed far less blunt force trauma and vasculature laceration than was seen with the high density  $13 \times 13$  optrode array. The  $8 \times 6$  custom array was also successful in targeting the boundary between layer III and layer IV, which would allow illumination of layer IV as designed. In addition, it is shown that the UOA could be customized to target specific neurons within the motor cortex of C57BL/6 wild-type mouse (*M. musculus*).

### 3.1 Atlas 3-D CAD Brain Modeling

The Calabrese<sup>17</sup> plates were not readily available in an image format suitable for Solidworks® 3-D CAD modeling, so it was necessary to retrieve .jpg images, with the Paxinos<sup>16</sup> regions of V4D, from the Scalable Brain Atlas<sup>18</sup> as 23 individual screen shots. Lofting between the Solidworks® splined regions was far from ideal because of the complex shapes of some of the plates' splines. The loft generator had a tendency to miscalculate the loft when the spline perimeter tended to compress, so some of the lofts appeared to have singularities where an MRI 3-D scan would not have these singularities. Overall, the 3-D generated model was successful in allowing the virtual placement of the custom  $8 \times 6$  UOA within the atlas plates. Paxinos's<sup>16</sup> atlas plates were used to measure the predicted layer thicknesses for the 3-D model of the  $8 \times 6$  optrode lengths, because the Calabrese<sup>17</sup> atlas plates did not sufficiently highlight the layers of V4D.

### 3.2 Customized $8 \times 6$ UOA Fabrication

Array fabrication was successfully accomplished (see Fig. 5) using the maskless microfabrication techniques previously reported by this group.<sup>12</sup> Soda-lime microscope slides were used to create the custom  $8 \times 6$  UOA used in this work.

Dicing and wet etching were as predicted, but firing the arrays to remove the surface roughness of the dicing and etching processes proved difficult. Over-temperature or over-timed firing caused the optrodes to slump, making them not suitable for implantation, so it was necessary to adjust the firing schedule to better fire the shorter optrodes of the custom UOA. Firing also caused the optrodes to shrink by up to 25% during firing and widen from 75 to 100  $\mu\text{m}$ . Each of these effects was successfully accounted for in the final devices that were implanted in this study.

### 3.3 Marmoset V1 Tissue Damage Assessment

The high-density UOA caused significant damage and some blood loss in marmoset (*C. jacchus*) primary visual cortex,<sup>23</sup> as seen in Fig. 2. Postmortem inspection showed the high-density device displaced  $>400\ \mu\text{m}$  of gray matter and compressed it in between 150  $\mu\text{m}$  of optrode spacing. Lacerations were observed due to high amount of blunt force trauma of the square optrodes. This damage made it necessary to improve the array's design and microfabrication techniques, and at the same time eliminate the need for *in vivo* trial insertion iterations for array improvement using stereotaxic coordinate atlases. Stereotaxic coordinate system atlases are commonplace, so they were used to identify the location of the array's placement, the array's perimeter, and the overall size of the craniotomy that was needed to insert the device with minimal invasiveness. This method was adapted to the microfabrication technique of the UOA.<sup>12</sup>

The prototype  $13 \times 13$  device's failure as an implant was somewhat offset by the success of a  $\varnothing 1.5\text{-mm}$  TGV that was grit ablated through the backplane of the array. Electrical recordings were made through the TGV with a stereotactic-mounted 150- $\mu\text{m}$  monopolar microelectrode. This indicated that while the prototype device caused damage, there were still viable neurons within the neocortical columns capable of firing. This was an important discovery with the prototype device because it was initially unknown whether or not tissue compression would damage the neurons directly below the TGV.

### 3.4 Macaque V4D Histology

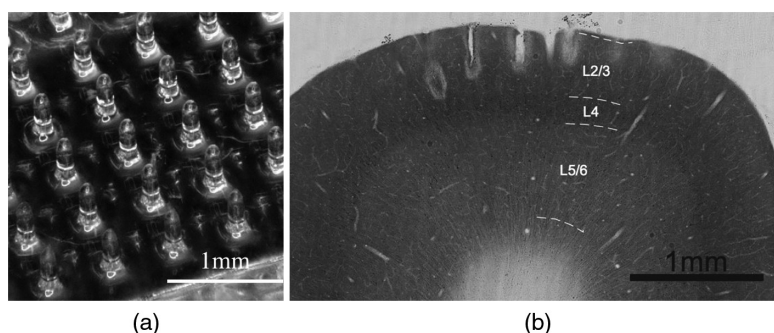
Upon array explantation, histology of sagittal sections of area V4D showed the device's tips reached the boundaries of layer III and layer IV of V4D as designed. Cytochrome oxidase staining highlights revealed force trauma to cortical layers as the light gray "halo" seen throughout the insertion wound of Fig. 5. Histology was not performed on the marmoset when the high density  $13 \times 13$  device was explanted because of the damage suggesting the macaque implant represented an improvement in design.

### 3.5 Displaced Tissue Reduction by Controlling Optrode Shape

Figure 4 shows three CAD models of optrodes surrounded by a rectangular volume of tissue, and Table 1 shows the ratio of tissue volume to optrode volume for the three optrode models. Ratio of tissue-affected volume was quantified using a ratio of total tissue volume to optrode-displaced tissue volume. A single bullet-shaped optrode from the  $8 \times 6$  UOA has a tissue-affected volume ratio of 40:1 that means there is 40 times more surrounding tissue for the optrode's displaced tissue to push into. On the contrary, there is only a 2.56:1 ratio for the 1.5-mm-square optrode of the  $13 \times 13$  UOA.

### 3.6 Mouse In Vivo Insertion of a UOA-Holobundle

Connectors with the UOA were successfully implanted in two mice. The first mouse implanted with the UOA exhibits normal behavior and has not developed any adverse symptoms, infections, or occlusion of the implant for more than 6 months. The modified Holobundle system shown in Fig. 6 can control all the individual fibers and project various patterns at the glass endplate of the bundle (except for a single misassembled fiber in the corner of the array), with negligible insertion loss of the fiber bundle to the cortical connector and minimal output power instability during repeated attachments. A second transgenic mouse expressing channelrhodopsin-2 was implanted with the aligned connector (see Fig. 6) without serious post-op complications, and will be used to validate the device

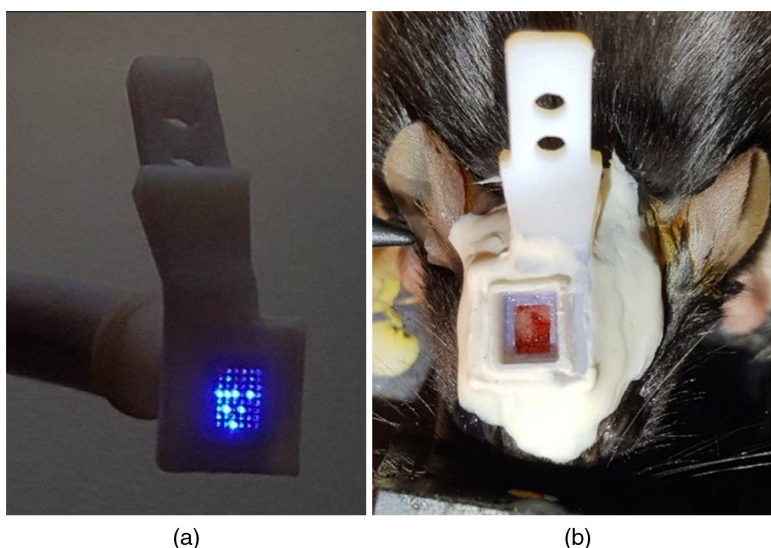


**Fig. 5** (a) A customized  $8 \times 6$  UOA to specifically target layer IV of Paxinos<sup>16</sup> macaque area V4D. The UOA is fabricated out of soda-lime microscope slides using maskless wafer-level microfabrication processes.<sup>12</sup> (b) Postperfusion histochemical staining with cytochrome oxidase of sagittal sections of area V4D showed the array was successfully inserted into V4D and reached the boundary between layers III and IV, which would allow for illumination of layer IV during optogenetic studies. The same device was successfully used for holographic projection into motor cortex of the common mouse.

**Table 1** Ratio of volumetric tissue affected by a single optrode.

Figure 4 optrode	Optrode dimensions (mm)	Tissue dimensions (mm)	Optrode type	Tissue volume (mm <sup>3</sup> )	Optrode volume (mm <sup>3</sup> )	Tissue to optrode ratio
(a)	1.50 × 0.250 × 0.250	1.50 × 0.390 × 0.390	Square with pyramidal tip	0.228	0.0890	2.56:1
(b) <sup>a</sup>	0.500 × 0.250 × 0.250	0.500 × 0.390 × 0.390	Square with pyramidal tip	0.076	0.0260	2.92:1
(c)	0.500 × Ø0.075	0.500 × 0.400 × 0.400	Bullet	0.078	0.0019	40.1:1

<sup>a</sup>Conceptualized optrode created for ratio comparison.



**Fig. 6** (a) View of the cortical connector from below after alignment, projecting a pattern of seven lit fibers. (b) The cortical connector with the UOA implanted in a mouse.

effectiveness for optogenetic stimulation, and will be reported at a later publication.

#### 4 Conclusion

This study shows that UOA's can be customized using Solidworks® 3-D CAD model of the visual cortical area V4D of the macaque and of the motor cortex of C57BL/6 wild-type mouse. The 8 × 6 UOA has been inserted in wild-type mouse for over 6 months with no adverse reactions, showing excellent biocompatibility. Based on a histological assessment, the device causes a small amount of sharp force trauma at the base of the optrode tips, but this damage is easily repaired during postimplantation recovery. A customized 8 × 6 array was successfully fabricated reducing blunt force trauma and laceration of tissue, and the device successfully inserted at the boundary between layers III and IV for optogenetic illumination of layer IV. Insertion damage was far less than that caused by using a 13 × 13 high density UOA. Final dimensions of the customized 8 × 6 were optrode length (400 μm), optrode width (75 μm), optrode pitch (400 μm), backplane thickness (500 μm), and overall form factor (3.45 mm × 2.65 mm). It was reported that a TGV was fabricated using 25-μm grit ablation to drill through the backplane of the 8 × 6 UOA. This design allows

for simultaneous electrical recording in the middle of the UOA and backplane illumination.

Solidworks® 3-D CAD was successfully used to create a 3-D model of Paxinos<sup>16</sup> region visual macaque visual cortical area V4D. Calabrese<sup>17</sup> atlas plates were imported into Solidworks® from the Scalable Brain,<sup>18</sup> the region of interest was B-splined, and each B-splined region was lofted together. The UOA was designed, modeled in Solidworks®, and virtually inserted into the 3-D CAD model of the brain region of interest. This allowed for the array design to be iterated without the need of multiple insertions into a live animal reducing the cost of animals for future study. The major differences between the prototype and the stereotactically designed UOAs are rounded optrodes, tuned optrode length for specific layer targeting, smaller footprint, reduced numbers of optrodes per array, and lower light intensity requirements. In each of the parameters, we see a marked improvement over the 13 × 13 array.

This study proves that previous anatomical atlases can be exploited to create virtual 3-D anatomical models to customize implantable multioptrode and multielectrode arrays without the use of animals in trial and error experiments. Prior to *in vivo* experimentation, researchers can use 3-D CAD software to create a 3-D anatomical model of the region of interest and use that

virtual model to design a device suitable for implantation to minimize invasiveness and injury to the animal. By eliminating the need for live animals to design a device, this method dramatically accelerates device development by optimizing the device for size and placement within the anatomical region of interest. An additional benefit of this research is that it shows that atlas coordinate systems can be used in conjunction with 3-D CAD to assist in the placement of the actual device. This is achieved using the 3-D CAD anatomical model, virtually placing the device, and using the CAD's internal measurement system to determine the placement during the actual surgery. In this work, stereotaxic coordinates were used in both the 3-D anatomical model as well as the virtual placement of the device; the virtual placement measurements were then transferred to the stereotactic-mounted pneumatic hammer used for UOA placement. Overall, this work shows great utility to the functional anatomist as well as the neuroscientist.

### Disclosures

All nonhuman primate surgical and experimental procedures conformed to guidelines of the National Institutes of Health (NIH) and were approved by the University of Utah Animal Care and Use Committee (15-12008). All rodent experiments were conducted in accordance with the Institutional Animal Care and Use Committee (IACUC) at the Technion-Israel Institute of Technology. The authors declare no financial conflicts of interest.

### Acknowledgments

Mr. Ronnie Boutte and Dr. Steve Blair would like to acknowledge the generous support of the Utah Science and Research Initiative (USTAR) for their support of the Tunable Optrode Array student funded research and the National Science Foundation (NSF) under grant 1310654 for its support of the atlas-based 3-D CAD design work. Mr. Ronnie Boutte and Mr. Brandon Griffiths would like to thank their employer, Northrop Grumman Corporation, for the use of Solidworks® and the computer hardware needed to create the 3-D CAD Models of V4D, and all of the UOAs, used in this work. Dr. Alessandra Angelucci acknowledges the support by the National Institutes of Health (National Eye Institute grants R01 EY019743 and R01 EY026812), the National Science Foundation (grants IOS 1355075 and EAGER 1649923), the University of Utah Research Foundation (seed grant 10040877), and a grant from Research to Prevent Blindness to the Department of Ophthalmology, University of Utah. Drs. Alessandra Angelucci and Steve Blair acknowledge the National Institute of Neurological Disorders and Stroke BRAIN grant U01 NS099702. This project has received funding from the European Union's Horizon 2020 research and innovation program under the ERC grant agreement #648927. Mr. Guy Yona and Drs. Shy Shoham and Itamar Kahn would like to acknowledge support by the Israeli Ministry of Science, Technology and Space. They would also like to thank Alexandra Levinsky, Inbar Brosh, and the Technion Preclinical Research Authority and Nadav Cohen for their assistance with rodent care.

### References

1. P. Anikeeva et al., "Optrode: a multichannel readout for optogenetic control in freely moving mice," *Nat. Neurosci.* **15**, 163–170 (2011).
2. H. Ayaz et al., "An optical brain computer interface for environmental control," in *Annual Int. Conf. of the IEEE Engineering in Medicine and*

- Biology Society*, Institute of Electrical and Electronics Engineers (IEEE) (2011).
3. R. Hira et al., "Transcranial optogenetic stimulation for functional mapping of the motor cortex," *J. Neurosci. Methods* **179**, 258–263 (2009).
4. I. Ozden et al., "Identification and clustering of event patterns from in vivo multiphoton optical recordings of neuronal ensembles," *J. Neurophysiol.* **100**, 495–503 (2008).
5. Thorlabs, Inc., "Implantable fiber optic cannulae," [https://www.thorlabs.com/navigation.cfm?guide\\_id=2256](https://www.thorlabs.com/navigation.cfm?guide_id=2256) (accessed 28 March 2017).
6. F. Wu et al., "An implantable neural probe with monolithically integrated dielectric waveguide and recording electrodes for optogenetics applications," *J. Neural Eng.* **10**, 056012 (2013).
7. J. Zhang et al., "Integrated device for optical stimulation and spatiotemporal electrical recording of neural activity in light-sensitized brain tissue," *J. Neural Eng.* **6**, 055007 (2009).
8. T. Abaya et al., "Characterization of a 3D optrode array for infrared neural stimulation," *Biomed. Opt. Express* **3**, 2200–2219 (2012).
9. R. Berry et al., "X-optogenetics and u-optogenetics: feasibility and possibilities," *Photonics* **2**, 23–39 (2015).
10. N. G. Laxpati et al., "Real-time in vivo optogenetic neuromodulation and multielectrode electrophysiologic recording with NeuroRighter," *Front. Neuroeng.* **7**, 40 (2014).
11. R. Bhandari, S. Negi, and F. Solzbacher, "Wafer-scale fabrication of penetrating neural microelectrode arrays," *Biomed. Microdevices* **12**, 797–807 (2010).
12. R. W. Boutte and S. Blair, "Maskless wafer-level microfabrication of optical penetrating neural arrays out of soda-lime glass: Utah optrode array," *Biomed. Microdevices* **18**, 115 (2016).
13. T. Abaya et al., "A 3D glass optrode array for optical neural stimulation," *Biomed. Opt. Express* **3**, 3087 (2012).
14. T. V. F. Abaya et al., "Glass optrode arrays for optogenetic stimulation," *Proc. SPIE* **8586**, 85860V (2013).
15. T. V. Abaya et al., "Deep-tissue light delivery via optrode arrays," *J. Biomed. Opt.* **19**, 015006 (2014).
16. G. Paxinos, X.-F. Huang, and A. W. Toga, *The Rhesus Monkey Brain in Stereotaxic Coordinates*, Academic Press, San Diego, California (2000).
17. E. Calabrese et al., "A diffusion tensor MRI atlas of the postmortem rhesus macaque brain," *NeuroImage* **117**, 408–416 (2015).
18. R. Bakker, P. Tiesinga, and R. Kitter, "The scalable brain atlas: instant web-based access to public brain atlases and related content," *Neuroinformatics* **13**, 353–366 (2015).
19. X. Palazzi and N. Bordier, *The Marmoset Brain in Stereotaxic Coordinates*, Springer, New York (2008).
20. K. S. Saleem and N. K. Logothetis, *A Combined MRI and Histology Atlas of the Rhesus Monkey Brain in Stereotaxic Coordinates*, Academic Press, London, Waltham, Massachusetts (2012).
21. N. Farah et al., "Holographic fiber bundle system for patterned optogenetic activation of large-scale neuronal networks," *Neurophotonics* **2**, 045002 (2015).
22. G. Yona et al., "Realistic numerical and analytical modeling of light scattering in brain tissue for optogenetic applications," *eNeuro* **3**, 1–9 (2016).
23. R. W. Boutte et al., "Nonhuman primate visual cortex damage assessment of in vivo laser illumination and implanted 13 × 13 Utah optrode array," University of Utah, Neural Engineering Research Group Presentation (2013).

**Ronald W. Boutte** is a PhD candidate (expected December 2017) at the University of Utah while working full-time at Northrop Grumman Corporation. He received a BSEE and an MSME. Currently, he is employed as an advanced optoelectronic system test engineer at Northrop Grumman. His research interests are optical neural prosthetics and advanced optical communication systems. He has a special interest in MEMS, MOEMS, and NEMS device research and development.

**Sam Merlin** is currently a neuroscientist employed at Western Sydney University, whose research is focused on understanding the neurocircuitry that underlies early visual processing. He utilizes functional imaging techniques in conjunction with anatomical tracers and electrophysiological recordings, and then functionally manipulates



these circuits using optogenetic approaches. His initial optogenetic approaches highlighted the need for customizable implantable devices to target deeper brain structures, without adversely impacting neural circuits.

**Guy Yona** is a PhD candidate in the Autonomous Systems Program at the Technion–Israel Institute of Technology. He received his BS degree in electrical engineering and his BA degree in physics from the Technion–Israel Institute of Technology, Haifa, in 2009 and his MS degree in electrical engineering from Tel-Aviv University, Israel, in 2013. His research interests are closed-loop systems in the brain, optical neural interfaces, and functional imaging.

**Brandon J. Griffiths** is the lead engineer in the Automation Group at Northrop Grumman Corporation. He holds a BS degree in mechanical engineering technology from Southern Utah University and an MS in engineering management from California State University Northridge. His work at Northrop Grumman includes tool design and manufacturing engineering. He is a certified Solidworks® professional and received Technical Innovation awards for design work that resulted in Trade Secret IP awards.

**Alessandra Angelucci** is a professor of ophthalmology/visual science at University of Utah's Moran Eye Institute. She holds an MD degree from the University of Rome, a PhD in neuroscience from MIT, and was a postdoctoral fellow at University College London. Her research focuses on understanding the computations of neural circuits in the visual cortex of nonhuman primates, employing

neuroanatomical, imaging, electrophysiological, and optogenetic techniques. She is on the editorial boards of *Visual Neuroscience* and *Frontiers in Neuroscience*.

**Itamar Kahn** is an assistant professor of neuroscience at the Rappaport Faculty of Medicine at Technion–Israel Institute of Technology. His research focuses on understanding the basic principles of communication between brain systems. He has worked on methods for awake mouse imaging, including combining optogenetic control with fMRI in mice and fMRI of awake passive and behaving mice in intact animals and genetic models of developmental disorders.

**Shy Shoham** is a professor of biomedical engineering at the Technion. He holds a BSc in physics from Tel Aviv University, a PhD in bioengineering from the University of Utah, and was a Lewis-Thomas postdoctoral fellow at Princeton University. His lab develops photonic, acoustic and computational tools for spatiotemporal interfacing with neural circuits. He is a member of the editorial boards of the *Journal of Neural Engineering* and of *Translational Vision Science & Technology*.

**Steve Blair** received his BS and MS degrees from Rose-Hulman Institute of Technology in 1991 and 1993, respectively, and his PhD from the University of Colorado at Boulder in 1998. Since 1998, he has been with the electrical and computer engineering department at the University of Utah in Salt Lake City. His research interests include neural interfaces, plasmonics, slow-light nonlinear optics, photonic microsystems, and microarray technology.

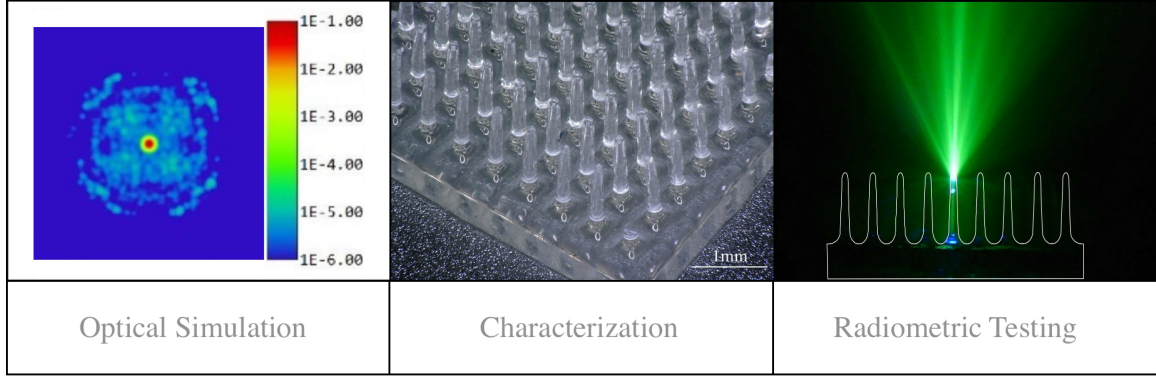
# CHAPTER 5

## SINGLE OPTRODE CHARACTERIZATION OF THE UTAH OPTRODE ARRAY FOR NEOCORTICAL ILLUMINATION

Optogenetics continues to grow at a rapid rate and development of devices to get light deep into neural tissue continues to be a rich field of research. This research presents the optical simulation, characterization, and testing of a  $9 \times 9$  Utah Optrode Array (UOA). The array has 1.1 mm long optrodes, a 500  $\mu\text{m}$  flat back-plane, 112  $\mu\text{m}$  diameter cross sections,  $2^\circ$  of taper, and 74  $\mu\text{m}$  hemispherical tip. Surface roughness was shown to have an average roughness of  $R_a = 13.5$  nm with a root mean squared of  $R_q = 20.6$  nm. A focused 14.6  $\mu\text{m}$  beam was projected into a single optrode where it exits the hemispherical tip and expands at  $62^\circ$ . The transmitted beam will cross over its neighboring optrodes' outputs at 255  $\mu\text{m}$ . The single optrode insertion loss measures 3.6 dB which is confirmed with Zemax simulation results of 3.7 dB.

### 5.1 Introduction

This research describes the simulation, characterization, and radiometric testing of the UOA (Figure 5.1). A  $9 \times 9$  optrode array is shown in Figure 5.1 (middle), which has been fabricated to penetrate 1.1 mm into the neocortex for optogenetic studies [1]–[4]. Optrode pitch is 400  $\mu\text{m}$  with a minimum of 250  $\mu\text{m}$  of spacing between optrodes to reduce the acute tissue damage from insertion as well as reduce vasculature constriction from compressed tissue. This  $9 \times 9$  UOA has a 500  $\mu\text{m}$  back-plane and a 3.85 mm $\times$ 3.85 mm form-factor. The planar back-plane allows for the Utah Electrode Array pneumatic inserter to be used for implantation [5]. The back-plane can also accept several different types of illumination methods such as butt-coupled optical fibers, microLED arrays, direct illumination of individual optrodes, or full array illumination using a single source.



**Figure 5.1.** Three areas of study were used to fully characterize the Utah Optrode Array. Zemax simulation was used to understand how the device would function as an optogenetic implant. Visual characterization techniques of optical microscopy, scanning electron microscopy, electron dispersion spectroscopy, and atomic force microscopy were used to understand the physical characteristics of the device. Radiometric testing techniques were used to quantify insertion loss and the beam’s profile.

Zemax was used to simulate a single point source placed on the back-plane of the array to illuminate a single optrode; these results were compared to the measured radiometric results. Four categories of device characterization were performed: optical microscopy, scanning electron microscopy, electron dispersion spectroscopy, and atomic force microscopy. Radiometric testing was used to quantify the amount of light entering and exiting the optrode, to determine the insertion loss of the optrode, and to profile the beam shape of both the input and output beams.

### 5.1.1 Background

Optogenetics is the science of using light to interrogate neural tissue by stimulating or inhibiting neural signals in the brain [6]. Light is used to activate optogenetic actuators—light-sensitive proteins called “opsins”—such as channelrhodopsin (VChR1 and ChR2), halorhodopsin (NpHR), and archaerhodopsin (Arch-3), which causes the labeled neurons to depolarize (activate) or hyperpolarize (inhibit) based on the optogenetic actuator used. Many other optogenetic actuators have been synthesized for optogenetic studies, and each responds to its corresponding wavelength of light [7]: 1. ChR2 (470 nm), 2. PAC $\alpha$  (~470 nm), 3. Opto- $\alpha$ /Opto- $\beta$ 1AR (500 nm), 4. Arch-3 (566 nm), 5. VChR1 (570 nm), 6. NpHR (589 nm) 7. Phytochrome (650 nm). Simultaneous depolarization and hyperpolarization can be obtained by combining optogenetic actuators [8].

Viral infection and transgenesis are two of the most popular methods for the expression of opsins through the walls of the neurons' cell bodies [9]–[12]. Once expressed, the opsin is dormant until the correct wavelength of light is shown onto the cell in sufficient irradiance levels, usually  $1\text{--}10\text{ mW}\cdot\text{mm}^{-2}$ , to activate the opsin [13]. The activated neurons' change in membrane potential induces action potentials[14].

Neurons are arranged into six layers within mammalian brain; these layers are called “neocortices” [15]. The six laminae of the neocortex are labeled by cell type from the top surface of the brain down (I–VI) to the white matter (WM). Some species such as humans have subdivided layers, and are labeled alphanumerically as  $\text{IV}\alpha$ ,  $\text{IV}\beta$ , etc. [16], [17]. Targeting specific layers within the neocortex is a key concern when discerning brain function, so careful geometrical control of penetrating devices is a key concern and has been previously reported by this group [4]. This group has also reported a high-volume/mass production process that was used to produce the devices under test in this characterization research [3].

### 5.1.2 Light transmission

Noninvasive and invasive neurostimulation techniques have been developed to transmit light onto opsin expressing neurons. Some completely noninvasive methods include sonogenetics, x- and u-optogenetics [18], [19]. Sonogenetics uses sound; x-optogenetics uses X-rays; and u-optogenetics uses infrared light to penetrate the brain and affect the neurons. Each of these methods can be considered indiscriminate because their smallest tissue affected volumes are limited to the sizes of their respective penetration depths. Fine neuron ensemble control, or even individual neuronal control, is currently limited to invasive optogenetic techniques.

Direct illumination of the surface of the cortex with LED arrays, direct laser projection, and two-photon microscopy are some of the leading methods for minimally invasive optogenetic neurostimulation [20]–[22]. These methods effectively stimulate the neocortical layers I to III, but heat on the surface must be controlled so as not to damage tissue or cause adverse experimental results. Much of the current optogenetic research is focused on the deeper layers of the neocortex and its connectivity to other functional areas of the brain such as the occipital lobe, dentate gyrus, lateral geniculate nucleus, motor cortex, etc. [23]–[27]

In order to reach many of these areas of the brain, light needs to be transmitted along a penetrating waveguide or penetrating LEDs because light attenuation, absorption, and scattering within the brain's neocortices reduce the depths in which noninvasive methods can illuminate [28].

Spatiotemporal control of large portions of cortex is possible with optical penetrating arrays by individually addressing optrodes. Several different patterning techniques have been developed such as multiple MEMS optical fiber switches, holographic/optical fiber light pipes (Holobundle), spatial light modulators, liquid crystal displays, LED arrays [29]–[32]. Devices of these types are usually tethered to a power source, and often times they are tethered to their optical sources as well. Tethering limits the amount of addressable optrodes that are available because optical fibers and electrical cables can be heavy for the animal to support. More importantly, however, stiffness becomes a major mobility problem as the number of fibers increases, making behavior studies difficult when large fiber counts are required [33]. Several methods have been devised to overcome some of the problems associated with tethered experiments, but the current trend is towards a standalone device that has an onboard light source(s), electrical recording capabilities, and wireless transmission [34]. One commonality between these illumination methods is the need for a suitable brain interface that can be inserted into the tissue and transmit the light from its backside into the tissue. Optrode arrays have been developed for such applications [35]–[37].

The most common illumination method in current use is directly inserting a fiber optic cannula into tissue [38]. Once inserted, the cannula is dental cemented onto the skull through a small craniotomy. After a recovery period an optical fiber is inserted into the cannula and the animal is allowed to interact within a behavioral arena. These devices require separate electrical recording electrodes which are implanted at the same time as the optical cannula [39]–[41]. Cannulae can be combined to create a small array—usually  $2 \times 2$  [42]. Recent advances in arrays have seen the marriage of electrical and optical brain interfaces with zinc oxide optrodes [43]. ZnO arrays rely upon the transparency of the penetrating optrode to deliver light and the electrical properties for recording. Each of these devices are of a one-off nature and not currently suitable for widespread use. Glass optrode arrays have been fabricated using standard microelectronic wafer-level fabrication

techniques, and can be easily and widely deployed [1]–[4].

## 5.2 Methods

A key need in this research was to ascertain how the UOA would function as a conduit for guiding light into tissue using simulation and testing. Figure 5.2 shows the optical bench testing setup; it was necessary to fully understand the laser’s beam as it projected from #1 thru #4. Zemax was used to predict the light transmission characteristics for a comparison to actual data. A  $9 \times 9$  UOA was then placed in a square cuvette optrode holder (#5) with aqueous fluorescein, optically aligned such that only the beam projected through a single optrode, and photographed.

UOA morphology was confirmed using optical microscopy, which indicated roughness that led to scanning electron (SEM) and atomic force microscopy (AFM) analyses. Finally, insertion loss (IL) was measured and compared to the Zemax simulation results.

### 5.2.1 Input to optrode beam characterization

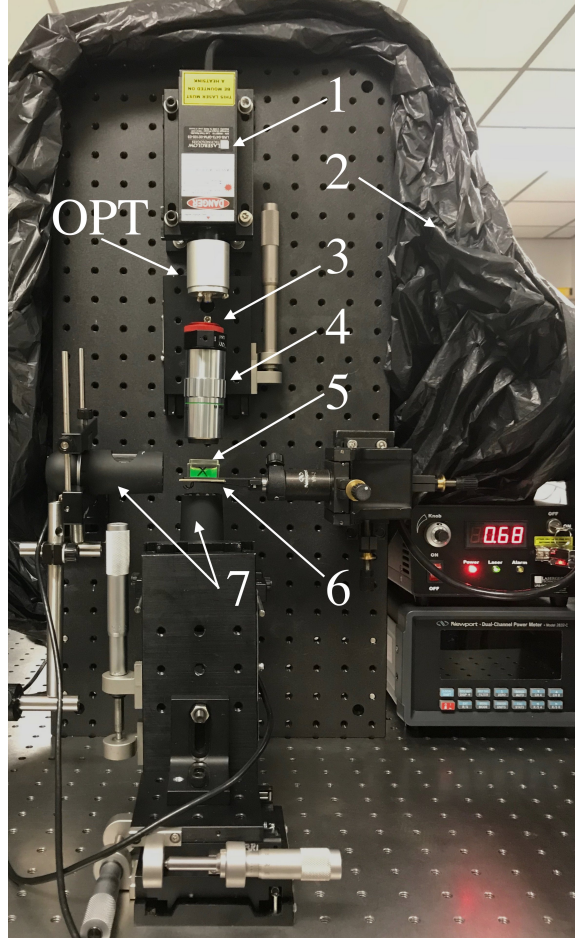
Figure 5.2 shows the optical test setup that was used to project the laser’s beam through the optrode, but prior to optrode testing the beam needed to be profiled. Laserglow’s 473 nm laser was projected through a Mitutoyo M Plan APO 20X objective lens and onto a bare 5MP CMOS image sensor. The sensor was mounted to #6 shown in Figure 5.2 and used to measure along the laser beam.

Several radius measurements were made through the beam’s cross section near its waist, and these measurements were then fit to Equation 5.1.

$$w_z = w_0 \sqrt{1 + \frac{\lambda^2 z}{\pi^2 w_0^4}} \quad (5.1)$$

Figure 5.3 shows the radii measurements as well as the curve fit of the beam’s profile when  $\lambda = 473 \text{ nm}$ ,  $w_0 = 2.95 \text{ }\mu\text{m}$  and  $z$  was set every  $50 \text{ }\mu\text{m}$  between  $-4.60 \text{ mm}$  and  $2.40 \text{ mm}$ . The beam waist ( $w'_0$ ) and divergence angle ( $\theta'$ ) are then reported from the curve fit data of as  $w'_0 = 6.4 \text{ }\mu\text{m}$  and  $\theta = 487 \text{ mRad}$ .

The minimum measured size of the beam’s spot diameter was  $D'_0 = 2w'_0 = 12.8 \text{ }\mu\text{m}$ . This spot size corresponds to the theoretical spot size according to Equation 5.2 and Equation 5.3, when  $w'_0 = 6.4 \text{ }\mu\text{m}$ ,  $\theta = 487 \text{ mRad}$ ,  $\lambda = 473 \text{ nm}$ , input beam spot diameter  $D'_0$  is  $1 \text{ mm}$ ,



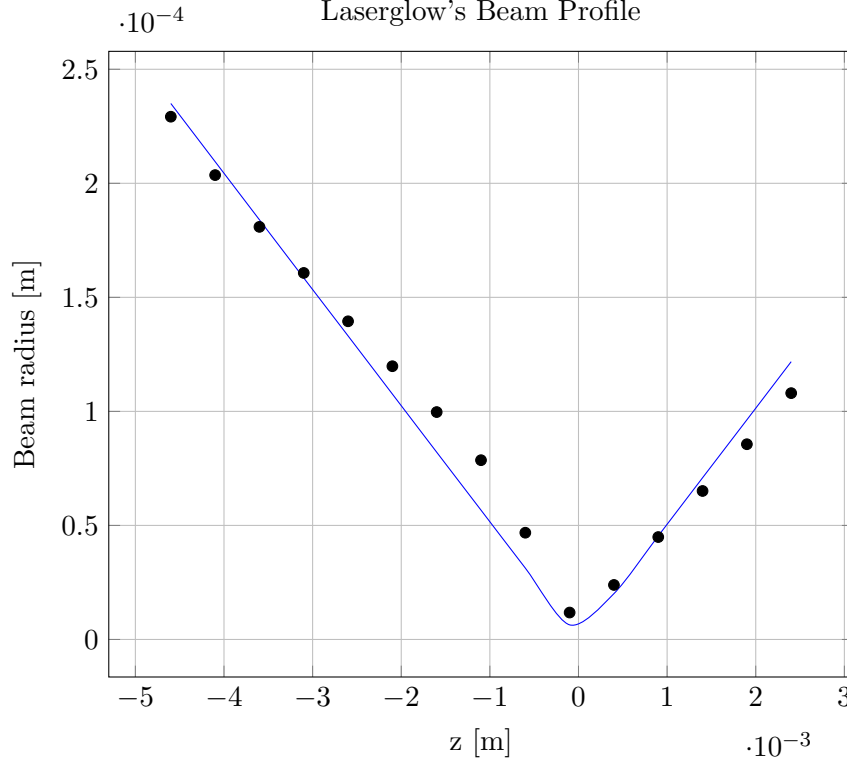
**Figure 5.2.** Optical bench testing setup: 1. Laserglow 473 nm laser fixed in place, 2. Stray light shroud, 3. Vertically adjustable neutral density filter, 4. Vertically adjustable 20X objective lens, 5. Sample holder with 10µM fluorescein, 6. 3-axis positioner, and 7. 3-axis sample positioners with a 5MP 20-200X digital microscope. Optional (OPT) FC/PC Fiber Coupler. To the right of the test setup is Newport Dual Channel Power Meter model 2832-C and the Laserglow power supply.

and the objective's focal length is  $f = 10$  mm.  $M^2$  is known as the “beam's focusability factor.” There is a 2.3% error between the calculated minimum spot size and the measured.

$$M^2 = \frac{\theta \pi w'_0}{\lambda} = 2.069 \quad (5.2)$$

$$d_1 = (M^2) \frac{4\lambda f}{\pi D'_0} = 12.5 \text{ } \mu\text{m} \quad (5.3)$$

Figure 5.4 and Figure 5.5 show the measured input beam's minimum diameter of 14.6 µm with a high quality beam of ellipticity 97.3% according to Equation 5.4. Figure 5.4



**Figure 5.3.** Measured spot radii are plotted in black showing the propagation length along the  $z$  direction. A curve fit shown in blue is the measured data with minimized error of  $0.4 \mu\text{m}$ . It is seen that the beam waist is  $6.4 \mu\text{m}$  and its divergence angle is  $\theta = 487 \text{ mRAD}$ .

shows the qualitative results, and Figure 5.5 shows the quantitative results of the input beam's profile. There is an error of 12.3% between the calculated  $D'_0$  and the measured; this is mostly due to the lack of pixel resolution on this image sensor.

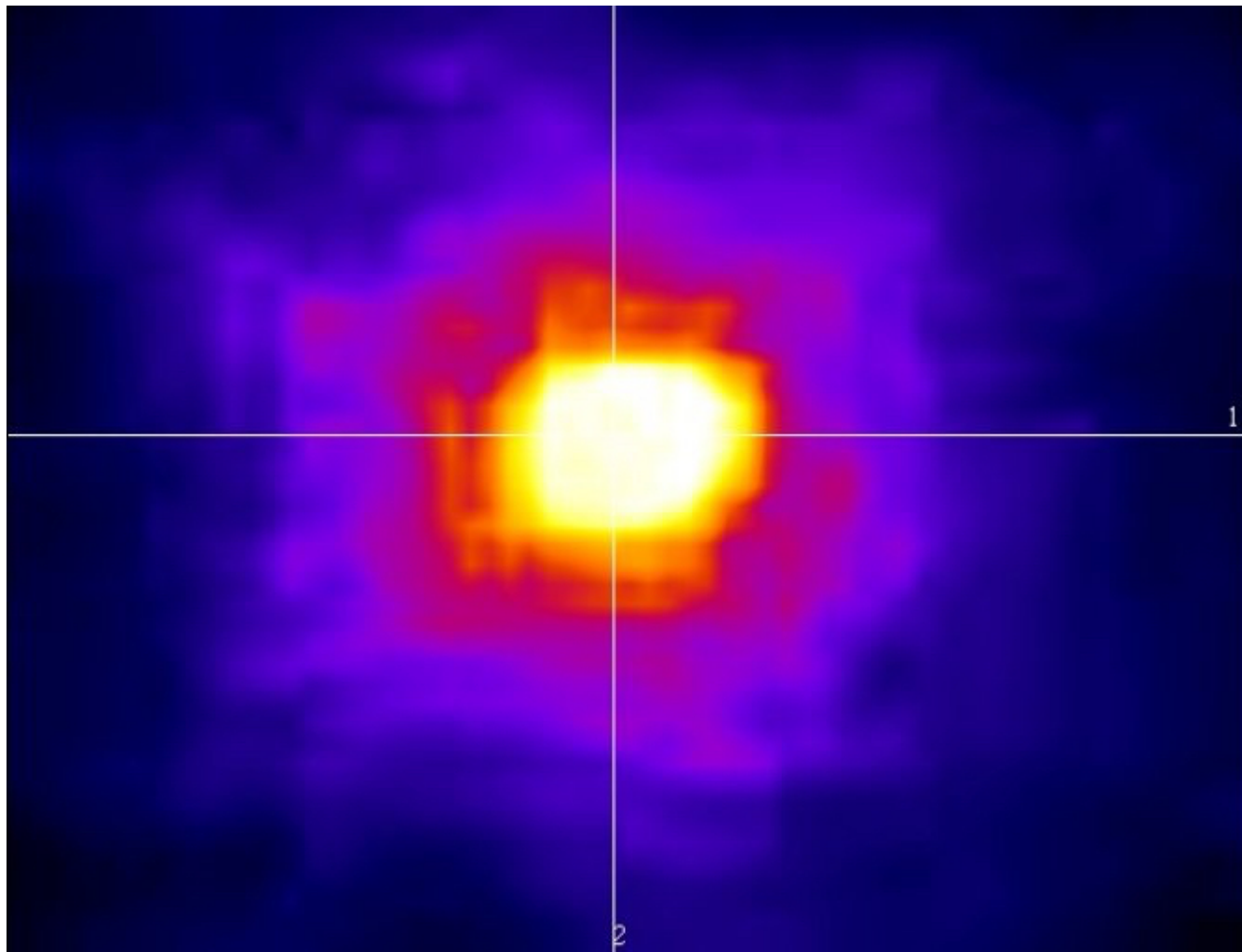
$$E_{spot} = 1 - \left[ \frac{Maj - Min}{Maj} \right] \cdot 100\% \quad (5.4)$$

where  $Maj = 15.0 \mu\text{m}$  and  $Min = 14.6 \mu\text{m}$  are the major and minor diameters of the beam's spot.

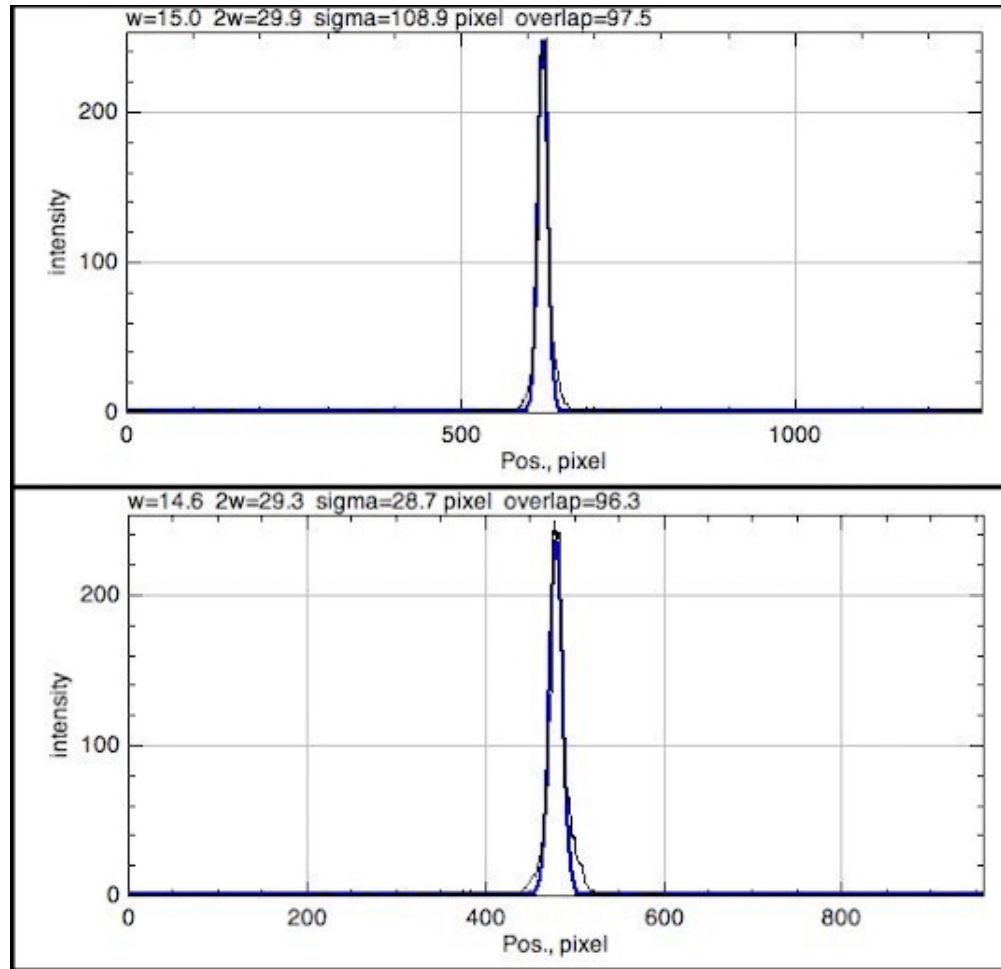
### 5.2.2 Zemax simulation setup

The back-plane of the UOA is reserved for individually addressed light sources coupled to each optrode. Zemax Nonsequential modal analysis was used to understand the transmission characteristics of a single optrode. These soda-lime float glass UOAs are constructed from craft store-bought plate glass, so its index of refraction and Abby number ( $n = 1.530$  and Abby number  $V_d = 63.97$ ) were input as the “material” into the simulation [44], [45].





**Figure 5.4.** The input beam's spot size was characterized using a CMOS image sensor. It appears to be a top-hat shape due to the lack of resolution at this scale, but beam profilometry shows the beam to be closer to Gaussian.



**Figure 5.5.** ImageJ's Beam Profiling plugin [46], [47] measured the spot size of Figure 5.4 to be 14.6  $\mu\text{m}$  at the output of the 20X Mitutoyo objective lens with a 97.3% ellipticity.

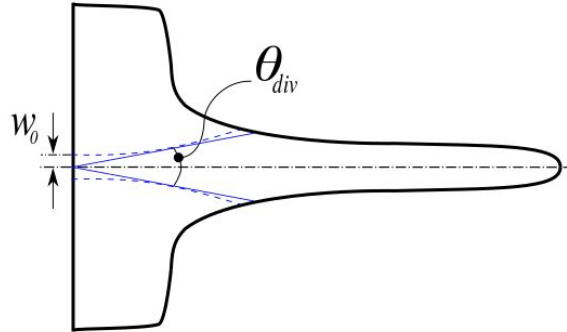
Figure 5.6 shows a point source placed at the center of the optrode's back-plane, and its beam spread angle was set to  $\theta_{div} = 360^\circ \lambda / \pi^2 w_0 = 2^\circ$  where  $w_0$  is an ideal Gaussian source's beam waist for 10  $\mu\text{m}$ . A color detector was placed at the tip of the optrode, and its distance was optimized through iterative runs of the simulation to the optrode's near field exit length of 50  $\mu\text{m}$ .

### 5.2.3 Optrode optical alignment

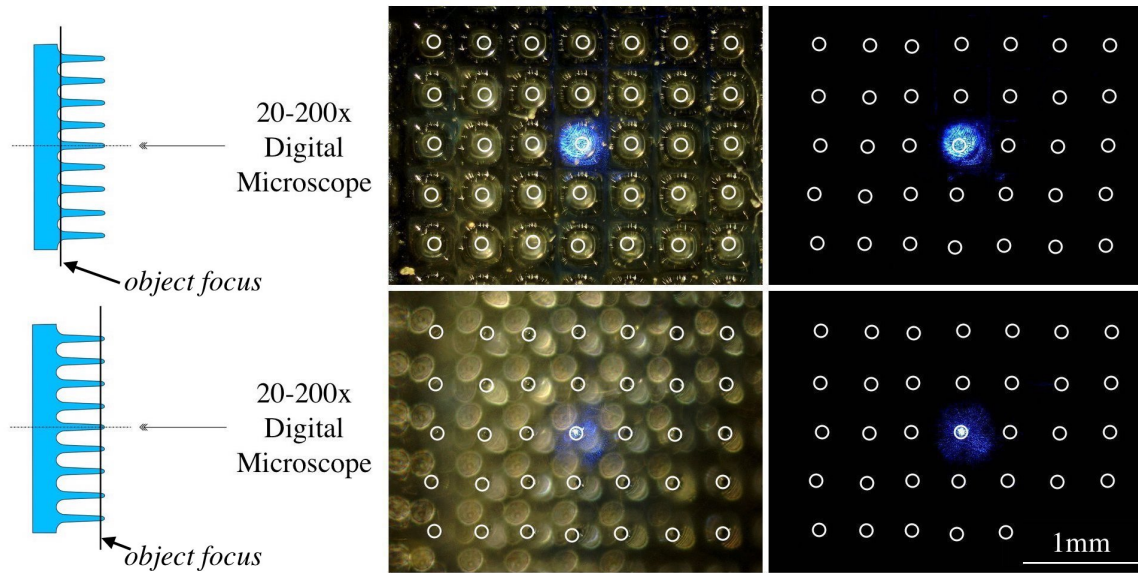
Optical alignment is achieved with the vertical axis digital microscope after all the optical elements have been properly leveled. This is done by first centering the camera on the beam, then adjusting the array holder's x- and y- positioners until an optrode is centered on the beam. Next, the z- positioners of the array holder and the objective/filter stages are adjusted so that the laser's beam is focused on the optrode of the array. Beam focus was confirmed by spot size minimization with the digital microscope. Figure 5.7 shows the array with the 473 nm spot minimized on the back-plane and exiting the tip with a focused beam.

### 5.2.4 Visual characterization

Optical microscopy, SEM, and AFM measurements were done on the UOA to fully characterize the device prior to optogenetic implantation. Two- and three-dimensional optical microscopy was performed using Keyence VHX-5000 3D microscope. SEM and



**Figure 5.6.** Zemax simulation parameters. Single optrode cross section showing the beam waist ( $w_0 = 10 \mu\text{m}$ ) used to calculate the divergence angle ( $\theta_{div} = 2^\circ$ ). The blue dashed line shows the Gaussian beam profile, and the solid blue lines show the point source simulation path.



**Figure 5.7.** Process for optical alignment through a single optrode (tips encircled in white). A 20-200X digital microscope is used to magnify the base of the optrodes (top left). The optrode is micropositioned to align a single optrode by transmitting a 473 nm laser spot through the back-plane into the base of the optrode. Front-lighting ensures the beam is correctly placed (top middle). Removing all ambient lighting allows for the beam to be imaged (top right). The process is repeated with the tips in focus (bottom row), and the beam is minimized through the tip.

Energy Dispersive Spectroscopy (EDS) were performed on a Hitachi S-3000N scanning electron microscope. A Bruker Dimension Icon was used to perform AFM.

#### 5.2.4.1 Optical microscopy

Keyence's VHX-5000 3D microscope is a high resolution optical microscope capable of up to 2 kX magnification, and it is also capable of stitching together multiple images while rastering both horizontally and vertically to create a high resolution 3D image of the UOA. Figure 5.1 (middle) shows the 3D isometric image taken with the VHX-5000. Its on-board measurement capabilities were used to measure several key parameters of the UOA:

1. Back-plane thickness
2. Optrode pitch
3. Optrode spacing
4. Optrode width
5. Optrode length from base to tip

6. Optrode taper from base to tip
7. Tip radius of curvature
8. Outer flange width

#### 5.2.4.2 Scanning electron microscopy

Hitachi's S-3000N SEM was used to image the surface of an optrode at 7 kX with an accelerating voltage of 15 kV. A key concern for the SEM analysis was to better understand some of the surface defects seen during optical microscopy. The surface roughness was verified as raised bumps on the surface of the freshly fired optrode. The Hitachi's EDAX was then used to perform EDS on the raised bumps for chemical composition.

#### 5.2.4.3 Atomic force microscopy

Based upon the SEM/EDS results, the Bruker Dimension Icon AFM was used to quantify the average and root mean square surface roughness. The sample was orthogonally mounted to a silicon carrier-wafer that was then placed in the vacuum chuck of the Bruker. The optrodes' round cross-sections required small scan ranges of 5-10  $\mu\text{m}$  in order to avoid large cantilever deflections and subsequent measurement contamination.

### 5.2.5 Average power and insertion loss

Newport Dual Channel Power Meter model 2832-C and 818-SL silicon photodetector (PD) were used to measure both the input and output power of the laser beam.

#### 5.2.5.1 Input power ( $P_{in}$ ) measurement method

The laser's beam was roughly centered on the face of the 818-SL PD in the -x and -y direction with the 3-axis positioner, and the spot size was visually reduced with the z-positioner. Next, ambient lights were turned off and the stray light shroud was lowered to reduce spurious light from entering the PD. While observing the average power in  $[\mu\text{W}]$  on of the Newport 2832-C the power was maximized signifying the PD was optically aligned on the focal point of the beam out of the 20X Mitutoyo objective lens.

### 5.2.5.2 Output power ( $P_{out}$ ) measurement method

A UOA was placed directly on the 818-SL filter, and the laser's beam was optically aligned to one of the optrodes, as described earlier, but without the use of the digital microscopes. Measurements were made through an optrode and through the front-plane to capture the maximum power that could be transmitted.

### 5.2.5.3 Insertion loss ( $IL$ ) calculation

Single optrode insertion loss was calculated by measuring the power into the PD ( $P_{in}$ ) and measuring the power through the array ( $P_{out}$ ) according to  $IL = 10 \log_{10} P_{in}/P_{out}$  [dB].

## 5.2.6 Aqueous fluorescein dye beam profiling

The output beam was imaged using 10  $\mu$ M aqueous fluorescein dye and the 20-200X digital microscope. Fluorescein dye has been used extensively in ophthalmology [48]. Fluorescein absorbs blue light between the wavelengths of approximately 425 nm and 500 nm and fluoresces green between roughly 550 nm and 675 nm [49]. This input spectrum matched the Laserglow's center frequency of 473 nm. The 10  $\mu$ M dye was placed in a 2 cm $\times$ 2 cm  $\times$ 1 cm cuvette. A 9  $\times$  9 UOA was floated on top of the dye; the small array naturally centered in the dye due to gravity and the meniscus. The menisci on each side of the cuvette caused an inverted hemispherical dome for the array to settle into. A 3-axis positioner aligned the array into the beam as previously described in Figure 5.7. This setup allowed the beam to enter the back-plane of the array and to be imaged from the side. The beam profile, divergence angles, and cross over depth were extracted using ImageJ [46].

## 5.3 Results

Three categories of errors were seen during the fabrication that needed to be thoroughly understood: Bulk defects, surface defects, and slumping [1]–[4]. Bulk defects included pre-firing microcracking and postfiring inclusions. Surface defects were visible surface roughness and deep grooves on the back-plane. Heat caused slumping defects caused all optrodes to decrease in length, all corners to be rounded off, and the tips to become circular. In some cases slumping was so severe so as to cause some optrodes to bend making them unsuitable for implantation.

Many of the defects were corrected through careful control of stress during dicing and

heat during reflowing, but surface roughness was a nagging problem that required a careful characterization process. First it was determined that the surface roughness was due to a process known as devitrification and not due to contamination. Devitrification is driven by overheating. It can be controlled with a furnace capable of controlled up and down temperature ramping. It was determined through light radiometry that the devitrification did not have any deleterious effects on light transmission, and thus some devitrification was acceptable in the final UOA.

### 5.3.1 Optical performance predictions using Zemax

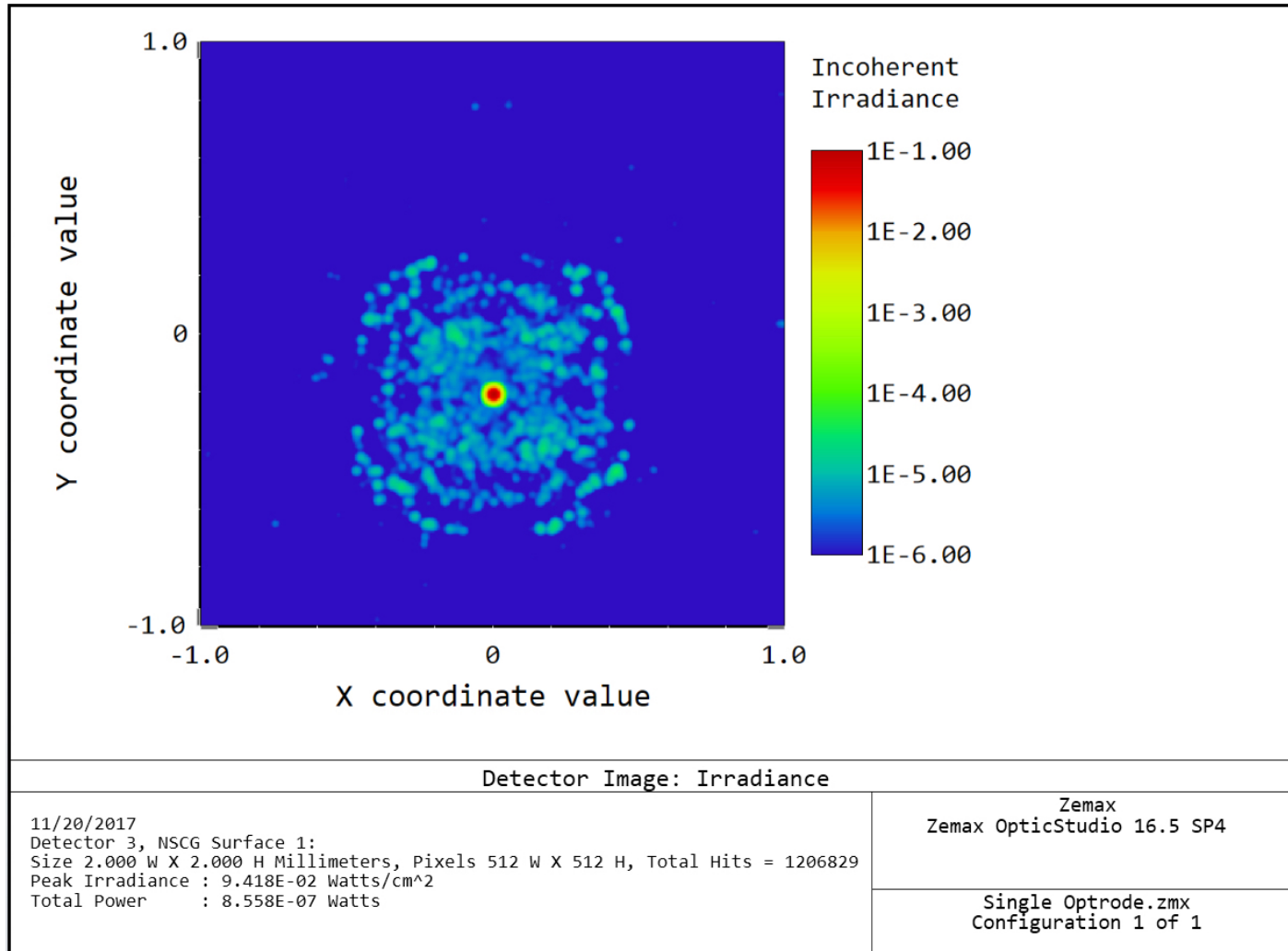
Zemax OpticStudio v16.5 was used for ray tracing simulation to predict insertion loss. Figure 5.8 shows the output simulation results on a color detector in Zemax. According to the simulation 43% of the light is transmitted to the detector, 51% of the light that is launched by the point source is reflected back out of the optrode's back-plane, and there is a 6% power loss due to coupling inefficiency. Insertion loss is calculated at 3.7 dB with a 2  $\mu$ W input power and a 0.855  $\mu$ W output power.

### 5.3.2 Visual characterization

The first sets of characterization are the optical tests to show the device was fabricated correctly, to identify any anomalies that needed to be understood and either eliminated or controlled during fabrication. Optical microscopy was performed with both a Keyence VHX-5000 where the images indicated surface roughness of an unknown origin, so SEM/EDS were used to ascertain the nature of the roughness. In glass several types of surface roughness can be present such as hardened bubbles, surface/bulk contamination, devitrification, etc. AFM was used to determine any periodicity of the roughness.

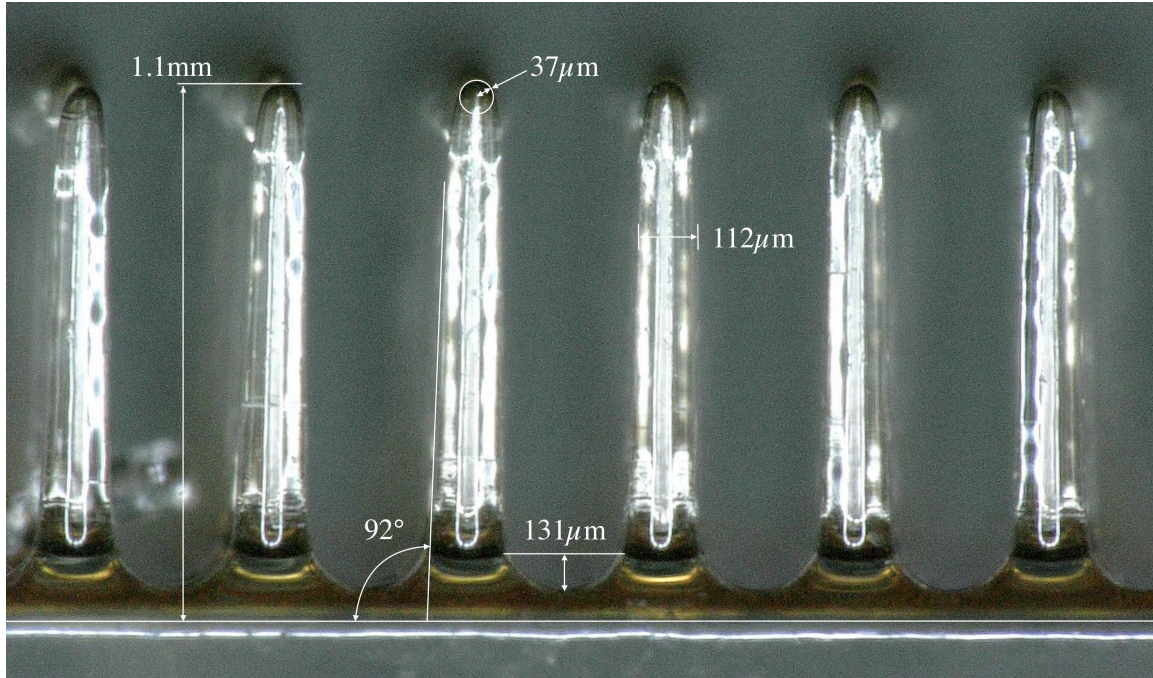
#### 5.3.2.1 Optical microscopy

Figure 5.9 shows optrodes along the first row of the array which are 1.1mm long, 112  $\mu$ m wide, and have a 2° tapered shank. Tip radii of curvature are 37  $\mu$ m, and the optrode base creates a trough that is 131  $\mu$ m deep. Not shown in the micrograph is the back-plane of the device which measured 500  $\mu$ m and was optically clear. The overall perimeter of the device was as designed at 3.85 mm  $\times$  3.85 mm; therefore, the UOA was fabricated as designed. Not apparent in the micrograph is the surface roughness which required special angles to



**Figure 5.8.** A 3D CAD file was simulated in Zemax with a 2  $\mu\text{W}$  point source is centered at the back-plane. 0.855  $\mu\text{W}$  are projected onto the color detector for a 43% throughput. Cross-section analysis showed 51% of the light was reflected out of the back-plane. Predicted insertion loss is 3.7 dB from this simulation.





**Figure 5.9.** Keyence VHX-5000 was used to characterize the  $9 \times 9$  UOA. Optrode lengths measure 1.1 mm, tapers  $2^\circ$ , are  $112 \mu\text{m}$  wide, and have a back-plane (not shown) measuring  $500 \mu\text{m}$ . The array has trough depths of  $131 \mu\text{m}$ , and the tips have  $37 \mu\text{m}$  radii of curvature.

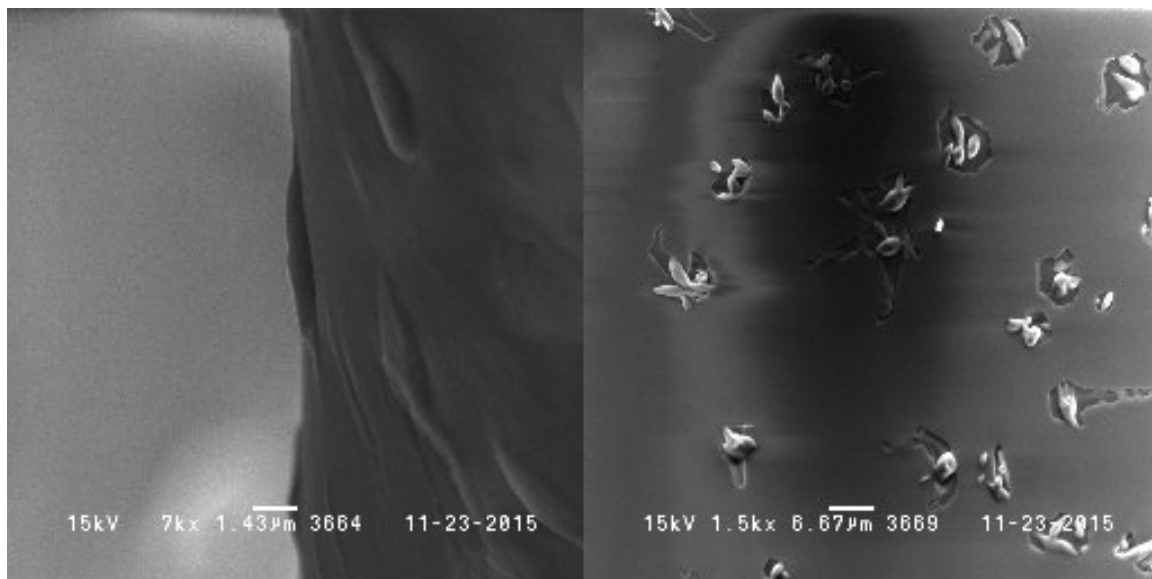
see but were too difficult to optically image. Table 5.1 shows the neocortical layers that 1.1 mm long optrodes can illuminate by species.

### 5.3.2.2 SEM micrographs

Scanning electron micrographs in Figure 5.10 show surface imperfections on the surface of an optrode from the  $9 \times 9$  UOA. The raised bumps were bombarded with electrons from the SEM, and it was determined that the SEM could not penetrate the bumps which indicated these were indeed bumps and not air-filled bubbles. Nucleation can be seen in the micrographs, further confirming the raised bumps not to be air-filled bubbles.

**Table 5.1.** Neocortical Layers by Species Near 1 mm Deep (adapted from: [17])

Cortical Region of Interest	Human	Dog	Cat	Goat	Rabbit	Rat	Mouse
Frontal	III	WM	VI	III	V	V	WM
Parietal	III	IV	V	V	IV	V	WM
Occipital	IV	VI	WM	IV	IV	V	WM

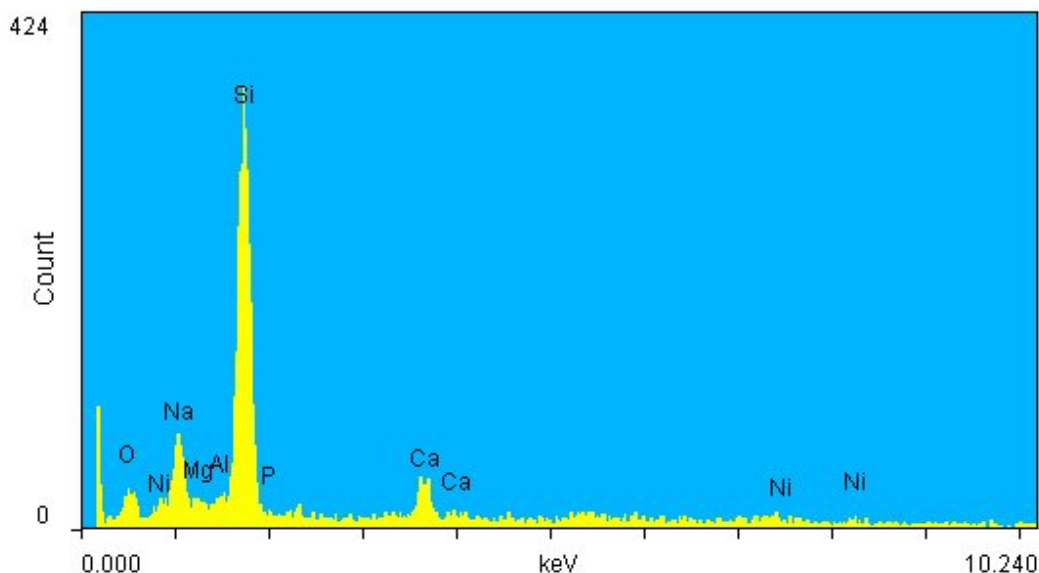


**Figure 5.10.** Scanning electron micrographs of a single optrode showing high surface roughness caused by nucleation known as devitrification. Portions of the bulk of the glass showed devitrification as well.

### 5.3.2.3 Chemical composition of raised bumps

Qualitative analysis of the raised bumps was performed using EDS to determine the presence of contamination that could have been present during fabrication, or find an explanation for the formation of the bumps. Figure 5.11 shows the majority of atoms present in the bumps on the sample were silicon, sodium, and calcium and matched those from the bulk glass material. Elemental nickel, aluminum, and magnesium can be seen on the EDS scan as well, and these were either actual trace elements from the glass—which are unknown—or they were spurious data points. Either way, the trace elements did not explain the raised bumps seen in the SEM images, since the trace elements were also seen in controlled area micrographs where the bumps were not present. Oxygen was negligible in the samples due to the low resolution of the older SEM used for this analysis.

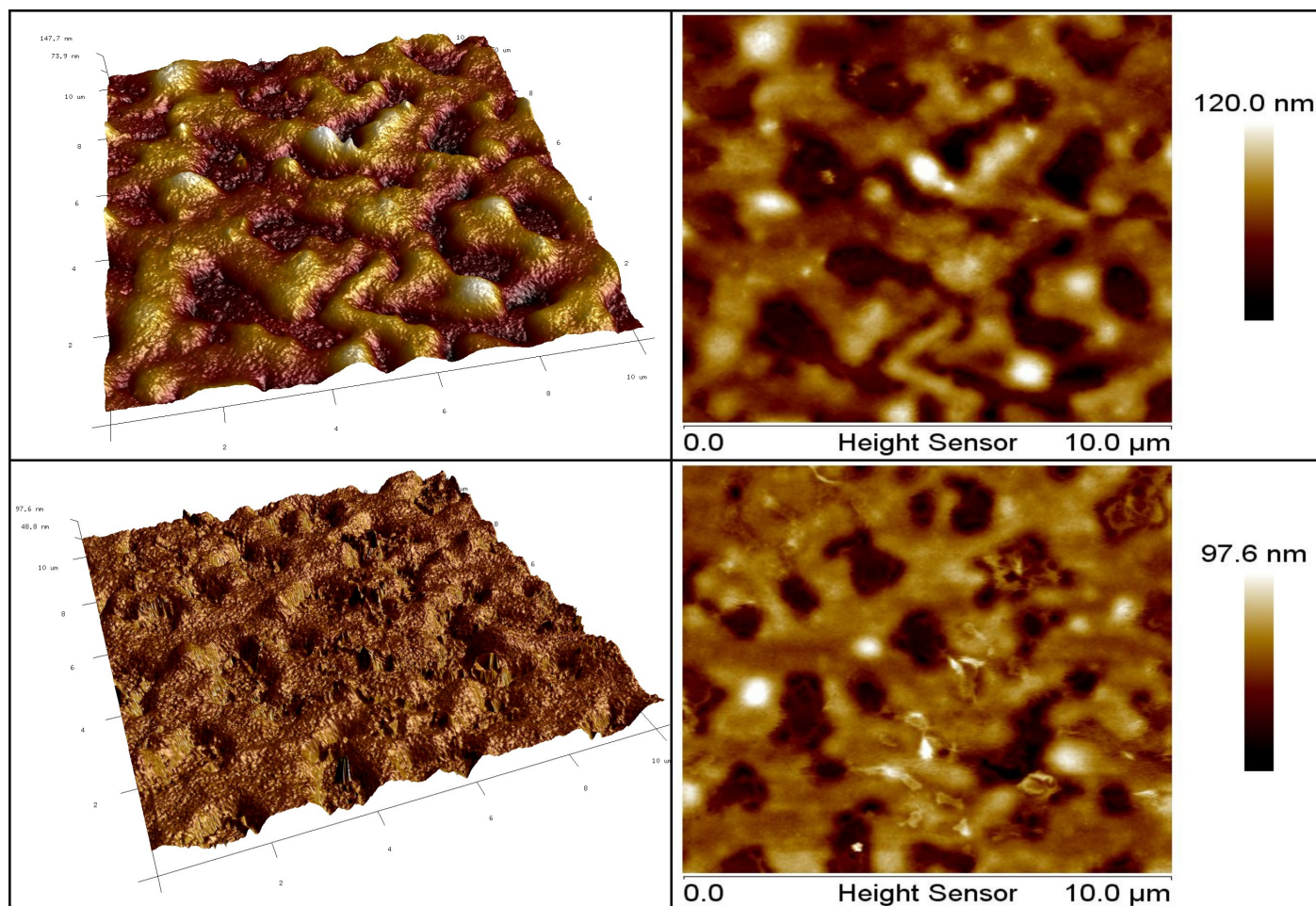
Nucleation and bulk inclusions seen at the tips under high SEM magnification are indicative of devitrification—the crystallization of glass—which can be prevented by reducing the time the glass dwells at elevated temperatures [50]. EDS supports the finding of devitrification.



**Figure 5.11.** Despite low x-ray counts, EDS showed no contamination on the glass nucleation sites. High silicon, sodium, and calcium were all expected because of the constituent chemicals of soda-lime glass; oxygen was negligible due to the low counts. Nickel and magnesium appear to be either spurious readings due to the EDS process or trace elements and are not exclusive to some contamination.

#### 5.3.2.4 Atomic force microscopy

AFM was used to determine the magnitude of the devitrification and if the roughness caused by it could cause light to be lost. The  $10\text{ }\mu\text{m} \times 10\text{ }\mu\text{m}$  square scan areas were set up to reduce the effects of the optrodes' round cross section. Topographical structures measured as much as 120 nm across the scan range. Average surface roughness ( $R_a$ ) was measured to be 13.5 nm, and the root mean squared ( $R_q$ ) was measured to be 20.6 nm. Figure 5.12 shows representative samples of the AFM micrographs taken at two different areas on the optrode. The larger surface topography was taken very near the tip of the optrode, and it shows higher amplitude than does the second scan that was taken midway down the optrode. This indicates the optrodes' tips experienced more heat exposure during firing, and thus the devitrification was more pronounced in this area. Periodicity proved negligible in most areas because nucleation is a random process, so this result further supports the devitrification diagnosis for the high surface roughness.



**Figure 5.12.** Two locations on the round optrode were randomly selected for  $100\ \mu\text{m}^2$  atomic force microscopy to quantify the surface roughness. AFM confirmed the high surface roughness, which could interfere with light transmission. Optrode curvature was negligible in these short scan lengths. AFM confirmed the high surface roughness and showed no patterning of the nucleation. High topography was measured at a maximum of 120 nm on sample #1 (top) and 98 nm on sample #2 (bottom).

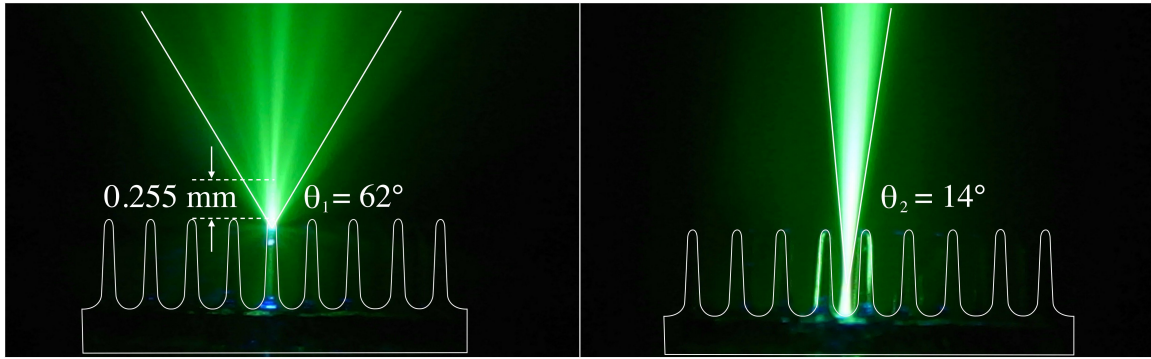


### 5.3.2.5 Insertion loss

High surface roughness could negatively impact the transmission of light through the optrodes, so it became necessary to compare insertion loss between Zemax and measured data.  $P_{in}$  was measured at 551.65  $\mu\text{W}$  and  $P_{out}$  measured 238.72  $\mu\text{W}$ . Insertion loss for the single optrode calculates to 3.63 dB, which is ostensibly the same as the Zemax simulation of 3.69 dB. Power budgeting shows the actual optrode has a  $\sim 4.5\%$  Fresnel loss at the back-plane,  $\sim 4.5\%$  Fresnel loss at the tip, 48% backscattering out of the optrode, and 43% transmission.

### 5.3.2.6 Aqueous fluorescein beam profiling

Output beam profiling was performed using 10  $\mu\text{M}$  aqueous fluorescein dye. The aligned beam was transmitted through a single optrode with a well defined diverging beam. After purposeful misalignment, the beam was reimaged (see Figure 5.13) directly through the back- and front-planes where the power meter measured 91% transmission—as before total Fresnel loss was 9%. The beam fluoresces in the dye as a single diverging beam. No light leakage was seen along the taper of the optrode despite surface roughness. Based on the beam's  $62^\circ$  spread out of the tip of the optrode, it is predicted that the adjacent beams would cross over at a distance of 255  $\mu\text{m}$ .



**Figure 5.13.** Fluorescein dye laser profilometry. (Left) Blue (473 nm) collimated light fluoresces in aqueous fluorescein through a single optrode. Divergence angle is  $62^\circ$ , and it is predicted that beam cross over would occur at a depth of 255  $\mu\text{m}$ . No light leakage is seen along the tapered portion of the optrode. (Right) Blue light straight through the back-plane and not through an optrode. It was shown that 91% transmission could be obtained through the back-plane for graduated illumination of tissue.

## 5.4 Conclusion

Despite some observed surface roughness, the UOA is more than capable of interfacing with the brain during optogenetic studies, and due to its excellent biocompatibility it is capable of being used in either acute or chronic studies [51]. The UOA can be backlit with individually addressable light sources to optrodes such as individual LEDs, butt-coupled optical fibers, spatial light modulators, small full color displays, etc. One of the strengths of the UOA is the versatility to be used for large tissue volume illumination or for fine single neuron illumination by spatiotemporal light patterning.

Insertion loss was measured at 3.6 dB with 43% light transmission, 48% light backscattering out of the optrode, and a total of 9% Fresnel loss from the interfaces of the back-plane and the optrode tip. These results were comparable to the Zemax ray trace simulation which predicted a 3.7 dB insertion loss.

Visual inspection showed the UOA had 1.1 mm long optrodes suitable for accessing several different neocortical layers of many different species of animals including humans. Each round optrode is 112  $\mu\text{m}$  with a round 37  $\mu\text{m}$  tip radius of curvature. A 500  $\mu\text{m}$  back-plane is thick enough to support all the optrodes during the insertion process. Two degrees of optrode taper assists in the insertion process by pushing displaced tissue away from the thicker optrode areas near the front-plane, where there is a trough to relieve pressure at the front-plane. All of these geometric features serve to reduce the trauma to tissue during implantation by reducing the amount of tissue squeezed between the optrodes and sliced by sharp edges. Surface roughness was observed during SEM and AFM, but SEM/EDS analyses showed the roughness to be devitrification. Devitrification is the unwanted crystallization process in glass due to excessive heat; it is characteristically seen on the surface of glass as nucleation sites as those seen on some of the UOA's optrodes during SEM analysis. Average and root mean square roughness were measured as  $R_a = 13.5$  nm and  $R_q = 20.6$  nm, respectively, with maximum amplitude of roughness reaching 120 nm in some scans. Despite the high surface roughness the UOA was able to produce a  $62^\circ$  diverging beam that would cross over its neighboring beam at a tissue depth of 255  $\mu\text{m}$ .

## 5.5 References

- [1] T. Abaya, S. Blair, P. Tathireddy, L. Rieth, and F. Solzbacher, "A 3d glass optrode array for optical neural stimulation," *Biomedical Optics Express*, vol. 3, p. 3087, Nov 2012.
- [2] T. Abaya, M. Diwekar, S. Blair, P. Tathireddy, L. Rieth, G. Clark, and F. Solzbacher, "Characterization of a 3d optrode array for infrared neural stimulation," *Biomedical Optics Express*, vol. 3, p. 2200, Aug 2012.
- [3] R. W. Boutte and S. Blair, "Maskless wafer-level microfabrication of optical penetrating neural arrays out of soda-lime glass: Utah optrode array," *Biomedical Microdevices*, vol. 18, Dec 2016.
- [4] R. W. Boutte, S. Merlin, G. Yona, B. Griffiths, A. Angelucci, I. Kahn, S. Shoham, and S. Blair, "Utah optrode array customization using stereotactic brain atlases and 3-d CAD modeling for optogenetic neocortical interrogation in small rodents and nonhuman primates," *Neurophotonics*, vol. 4, p. 041502, Jul 2017.
- [5] P. J. Rousche and R. A. Normann, "A method for pneumatically inserting an array of penetrating electrodes into cortical tissue," *Annals of Biomedical Engineering*, vol. 20, pp. 413–422, Jul 1992.
- [6] K. Deisseroth, "Optogenetics: Development and application," *Neuroscience Research*, vol. 65, p. S26, Jan 2009.
- [7] S. C. Alford, J. Wu, Y. Zhao, R. E. Campbell, and T. Knpfel, "Optogenetic reporters," *Biology of the Cell*, vol. 105, pp. 14–29, Dec 2012.
- [8] A. Guru, R. J. Post, Y.-Y. Ho, and M. R. Warden, "Making sense of optogenetics," *International Journal of Neuropsychopharmacology*, vol. 18, p. pyv079, Jul 2015.
- [9] J. A. Cardin, M. Carlén, K. Meletis, U. Knoblich, F. Zhang, K. Deisseroth, L.-H. Tsai, and C. I. Moore, "Targeted optogenetic stimulation and recording of neurons in vivo using cell-type-specific expression of channelrhodopsin-2," *Nature Protocols*, vol. 5, no. 2, p. 247, 2010.
- [10] O. Yizhar, L. E. Fenno, T. J. Davidson, M. Mogri, and K. Deisseroth, "Optogenetics in neural systems," *Neuron*, vol. 71, pp. 9–34, Jul 2011.
- [11] L. Madisen, T. Mao, H. Koch, J.-m. Zhuo, A. Berenyi, S. Fujisawa, Y.-W. A. Hsu, A. J. Garcia III, X. Gu, S. Zanella, *et al.*, "A toolbox of cre-dependent optogenetic transgenic mice for light-induced activation and silencing," *Nature Neuroscience*, vol. 15, p. 793, Apr 2012.
- [12] K. M. Tye and K. Deisseroth, "Optogenetic investigation of neural circuits underlying brain disease in animal models," *Nature Reviews Neuroscience*, vol. 13, p. 251, Apr 2012.
- [13] X. Han, B. Y. Chow, H. Zhou, N. C. Klapoetke, A. Chuong, R. Rajimehr, A. Yang, M. V. Baratta, J. Winkle, R. Desimone, *et al.*, "A high-light sensitivity optical neural silencer: development and application to optogenetic control of non-human primate cortex," *Frontiers in Systems Neuroscience*, vol. 5, p. 18, 2011.

- [14] K. Deisseroth, “Optogenetics,” *Nature Methods*, vol. 8, p. 26, Dec 2011.
- [15] V. B. Mountcastle, “The columnar organization of the neocortex,” *Brain: A Journal of Neurology*, vol. 120, no. 4, pp. 701–722, 1997.
- [16] P. Balaram and J. H. Kaas, “Towards a unified scheme of cortical lamination for primary visual cortex across primates: insights from NeuN and VGLUT2 immunoreactivity,” *Frontiers in Neuroanatomy*, vol. 8, p. 81, Aug 2014.
- [17] J. DeFelipe, “The evolution of the brain, the human nature of cortical circuits, and intellectual creativity,” *Frontiers in Neuroanatomy*, vol. 5, p. 29, 2011.
- [18] A. S. Chuong, M. L. Miri, V. Busskamp, G. A. C. Matthews, L. C. Acker, A. T. Sørensen, A. Young, N. C. Klapoetke, M. A. Henninger, S. B. Kodandaramaiah, M. Ogawa, S. B. Ramanlal, R. C. Bandler, B. D. Allen, C. R. Forest, B. Y. Chow, X. Han, Y. Lin, K. M. Tye, B. Roska, J. A. Cardin, and E. S. Boyden, “Noninvasive optical inhibition with a red-shifted microbial rhodopsin,” *Nature Neuroscience*, vol. 17, pp. 1123–1129, Jul 2014.
- [19] R. Berry, M. Getzin, L. Gjestebj, and G. Wang, “X-optogenetics and u-optogenetics: Feasibility and possibilities,” *Photonics*, vol. 2, pp. 23–39, Jan 2015.
- [20] K. L. Montgomery, A. J. Yeh, J. S. Ho, V. Tsao, S. M. Iyer, L. Grosenick, E. A. Ferenczi, Y. Tanabe, K. Deisseroth, S. L. Delp, *et al.*, “Wirelessly powered, fully internal optogenetics for brain, spinal and peripheral circuits in mice,” *Nature Methods*, vol. 12, pp. 969–974, Aug 2015.
- [21] K. Dhakal, S. Batabyal, W. Wright, Y.-t. Kim, and S. Mohanty, “Optical delivery of multiple opsin-encoding genes leads to targeted expression and white-light activation,” *Light: Science & Applications*, vol. 4, p. e352, Nov 2015.
- [22] J. P. Rickgauer and D. W. Tank, “Two-photon excitation of channelrhodopsin-2 at saturation,” *Proceedings of the National Academy of Sciences*, vol. 106, pp. 15025–15030, Aug 2009.
- [23] X. Huang, Y. M. Elyada, W. H. Bosking, T. Walker, and D. Fitzpatrick, “Optogenetic assessment of horizontal interactions in primary visual cortex,” *Journal of Neuroscience*, vol. 34, pp. 4976–4990, Apr 2014.
- [24] K. L. Montgomery, A. J. Yeh, J. S. Ho, V. Tsao, S. M. Iyer, L. Grosenick, E. A. Ferenczi, Y. Tanabe, K. Deisseroth, S. L. Delp, and A. S. Y. Poon, “Wirelessly powered, fully internal optogenetics for brain, spinal and peripheral circuits in mice,” *Nature Methods*, vol. 12, pp. 969–974, Aug 2015.
- [25] S. Jarvis and S. R. Schultz, “Prospects for optogenetic augmentation of brain function,” *Frontiers in Systems Neuroscience*, vol. 9, Nov 2015.
- [26] X. Liu, S. Ramirez, P. T. Pang, C. B. Puryear, A. Govindarajan, K. Deisseroth, and S. Tonegawa, “Optogenetic stimulation of a hippocampal engram activates fear memory recall,” *Nature*, Mar 2012.



- [27] A. Castonguay, S. Thomas, F. Lesage, and C. Casanova, "Repetitive and retinotopically restricted activation of the dorsal lateral geniculate nucleus with optogenetics," *PLoS ONE*, vol. 9, p. e94633, Apr 2014.
- [28] A. M. Aravanis, L.-P. Wang, F. Zhang, L. A. Meltzer, M. Z. Mogri, M. B. Schneider, and K. Deisseroth, "An optical neural interface: in vivo control of rodent motor cortex with integrated fiberoptic and optogenetic technology," *Journal of Neural Engineering*, vol. 4, pp. S143–S156, May 2007.
- [29] C. Crocini, C. Ferrantini, R. Coppini, M. Scardigli, P. Yan, L. M. Loew, G. Smith, E. Cerbai, C. Poggesi, F. S. Pavone, and L. Sacconi, "Optogenetics design of mechanistically-based stimulation patterns for cardiac defibrillation," *Scientific Reports*, vol. 6, Oct 2016.
- [30] A. M. Packer, B. Roska, and M. Husser, "Targeting neurons and photons for optogenetics," *Nature Neuroscience*, vol. 16, pp. 805–815, Jun 2013.
- [31] I. Reutsky-Gefen, L. Golan, N. Farah, A. Schejter, L. Tsur, I. Brosh, and S. Shoham, "Holographic optogenetic stimulation of patterned neuronal activity for vision restoration," *Nature Communications*, vol. 4, p. 1509, Feb 2013.
- [32] N. Farah, A. Levinsky, I. Brosh, I. Kahn, and S. Shoham, "Holographic fiber bundle system for patterned optogenetic activation of large-scale neuronal networks," *Neurophotonics*, vol. 2, p. 045002, Nov 2015.
- [33] M. M. Sidor, T. J. Davidson, K. M. Tye, M. R. Warden, K. Diesseroth, and C. A. McClung, "In vivo optogenetic stimulation of the rodent central nervous system," *Journal of Visualized Experiments: JoVE*, Jan 2015.
- [34] N. G. Laxpati, B. Mahmoudi, C.-A. Gutekunst, J. P. Newman, R. Zeller-Townson, and R. E. Gross, "Real-time in vivo optogenetic neuromodulation and multielectrode electrophysiologic recording with neurorighter," *Frontiers in Neuroengineering*, vol. 7, p. 40, Oct 2014.
- [35] K. Y. Kwon, A. Khomenko, M. Haq, and W. Li, "Integrated slanted microneedle-LED array for optogenetics," in *2013 35th Annual International Conference of the IEEE Engineering in Medicine and Biology Society (EMBC)*, IEEE, Jul 2013.
- [36] M. Welkenhuysen, L. Hoffman, Z. Luo, A. D. Proft, C. V. den Haute, V. Baekelandt, Z. Debyser, G. Gielen, R. Puers, and D. Braeken, "An integrated multi-electrode-optrode array for in vitro optogenetics," *Scientific Reports*, vol. 6, Feb 2016.
- [37] A. Steude, E. C. Witts, G. B. Miles, and M. C. Gather, "Arrays of microscopic organic LEDs for high-resolution optogenetics," *Science Advances*, vol. 2, pp. e1600061–e1600061, May 2016.
- [38] "Thorlabs implantable fiber optic cannulae." Internet: [https://www.thorlabs.com/navigation.cfm?guide\\_id=2256](https://www.thorlabs.com/navigation.cfm?guide_id=2256). 2018 [Feb. 21, 2018].
- [39] B. A. Duffy, M. Choy, M. R. Chuapoco, M. Madsen, and J. H. Lee, "MRI compatible optrodes for simultaneous LFP and optogenetic fMRI investigation of seizure-like afterdischarges," *Neuroimage*, vol. 123, pp. 173–184, Dec 2015.

- [40] K. R. Dhakal, L. Gu, S. Shivalingaiah, T. S. Dennis, S. A. Morris-Bobzean, T. Li, L. I. Perrotti, and S. K. Mohanty, “Non-scanning fiber-optic near-infrared beam led to two-photon optogenetic stimulation *in-vivo*,” *PLoS ONE*, vol. 9, p. e111488, Nov 2014.
- [41] P. Anikeeva, A. S. Andalman, I. Witten, M. Warden, I. Goshen, L. Grosenick, L. A. Gunaydin, L. M. Frank, and K. Deisseroth, “Optetrode: A multichannel readout for optogenetic control in freely moving mice,” *Nature Neuroscience*, vol. 15, p. 163, Dec 2012.
- [42] K. Xie, G. E. Fox, J. Liu, and J. Z. Tsien, “512-channel and 13-region simultaneous recordings coupled with optogenetic manipulation in freely behaving mice,” *Frontiers in Systems Neuroscience*, vol. 10, p. 48, Jun 2016.
- [43] J. Lee, I. Ozden, Y.-K. Song, and A. V. Nurmikko, “Transparent intracortical microprobe array for simultaneous spatiotemporal optical stimulation and multichannel electrical recording,” *Nature Methods*, vol. 12, pp. 1157–1162, Oct 2015.
- [44] M. N. Polyanskiy, “Refractive index database.” <https://refractiveindex.info>. 2018 [Feb. 21, 2018].
- [45] C. A. Faick and A. N. Finn, “The index of refraction of some soda-lime silica glasses as a function of the composition,” *Bureau of Standards Journal of Research*, vol. 6, pp. 993–1002, 1931.
- [46] T. Collins, “ImageJ for microscopy,” *BioTechniques*, vol. 43, pp. S25–S30, Jul 2007.
- [47] W. Rosenfeld, “Open beam profiler version 1.3.” Internet: [https://sourceforge.net/projects/beamprofiler/files/BeamProfiler/BeamProfiler\\_1.3/](https://sourceforge.net/projects/beamprofiler/files/BeamProfiler/BeamProfiler_1.3/). Updated: 2015 [Feb. 21, 2018].
- [48] A. Kumar and M. Thirumalesh, “Use of dyes in ophthalmology,” *Journal of Clinical Ophthalmology and Research*, vol. 1, no. 1, p. 55, 2013.
- [49] T. J. Bennett, D. A. Quillen, and R. Coronica, “Fundamentals of fluorescein angiography,” *INSIGHT: Journal of ASORN*, pp. 5–11, 2016.
- [50] M. Manutchehr-Danai, ed., *Devitrification. Dictionary of Gems and Gemology*, pp. 245–245. Berlin, Heidelberg: Springer Berlin Heidelberg, 2009.
- [51] S. D. Davis, D. F. Gibbons, R. L. Martin, S. R. Levitt, J. Smith, and R. V. Harrington, “Biocompatibility of ceramic implants in soft tissue,” *Journal of Biomedical Materials Research*, vol. 6, no. 5, pp. 425–49, 1972.

## CHAPTER 6

### CONCLUSIONS AND FUTURE WORK

This dissertation presented two optogenetic devices (a  $9\times 9$  UOA with 1.1 mm long optrodes and an  $8\times 6$  UOA with 400  $\mu\text{m}$  long optrodes) that are capable of transmitting from the surface to specifically targeted neocortical layers of the brain. Three journal publications covered the UOA's microfabrication, the UOA's ability to be customized using a 3D CAD model of a specific area of the brain, and characterized its light output using bench testing and simulation. Previous optrode arrays were made using expensive materials, difficult processes to replicate part-to-part, required photolithography for patterning and alignment, and required certified cleanrooms to control particulate contamination to the devices. The paper "Maskless wafer-level microfabrication of optical penetrating neural arrays out of soda-lime glass: Utah Optrode Array" demonstrated an improved process for fabricating the UOA. This research reduced the complexity of building an array to allow for the device to be built outside an ISO cleanroom, and without photolithography. A maskless fabricated UOA is inherently mass producible even when it is necessary to customize the device to meet the needs of a specific neuroscientist.

In the paper, "Utah optrode array customization using stereotactic brain atlases and 3D CAD modeling for optogenetic neocortical interrogation in small rodents and nonhuman primates," a customized UOA is designed in Solidworks. A single  $8\times 6$  device was created for chronic implantation into a wild-type mouse C57BL/6 (*Mus musculus*) motor cortex and an acute insertion into macaque (*Macaca fascicularis*) dorsal visual cortex region 4 (V4D). The  $8\times 6$  device incorporated many design improvements of a  $13\times 13$  prototype device that caused cortical damage in marmoset (*Callithrix jacchus*) primary visual cortex. This research proved the  $8\times 6$  UOA could be inserted with minimal tissue damage and proved the device could be implanted for extended periods of time.

Optrode shape, tip shape, and glass imperfections have profound effects on the amount

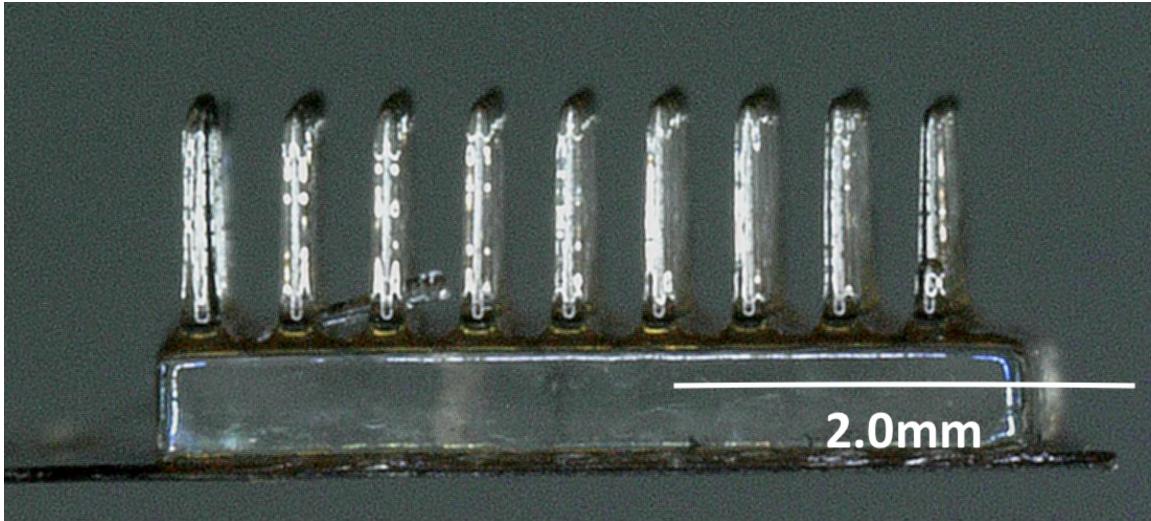
of light that can be transmitted from the back-plane of the UOA thru the tip and into tissue. “Single optrode characterization of the  $9 \times 9$  Utah Optrode Array for neocortical illumination” demonstrated that sufficient light can be transmitted via the optrode and into tissue to elicit depolarization and hyperpolarization as needed. This paper shows the insertion loss of input power vs. output power, the beam’s output shape, and discusses the contribution of surface roughness seen on portions of the optrode.

The UOA is destined to be a stand-alone device capable of simultaneously illuminating tissue, neurophysiological recording, and wireless transmission for signal processing—the hybrid computer brain implant (hCBI). In order to accomplish this goal, several items need to be completed in future work. Many process improvements are expected to reduce the errors to better control the final shape of the optrode by reducing the taper and tip’s radius of curvature. Process improvements are also necessary to improve the dicing yield by further reducing the hydraulic fracture during dicing. Since the hCBI will have the capability of selectively illuminating individual optrodes, a method for combining readily available MEMS switches to a  $2 \times 2$  UOA has been proposed that does not require carefully aligned/low-power LEDs. A coupler will connect 4 optical fibers to the back-plane of the UOA for short behavioral experiments while being under binary patterned illumination patterns from a single laser source. The optical coupler and MEMS switch patterned illumination will be introduced in this chapter as future work.

## 6.1 Maskless wafer-level microfabrication

Figure 6.1 shows a completed UOA suitable for both acute and chronic optogenetic studies. It has  $1100 \mu\text{m} \times 100 \mu\text{m}$  optrodes and a  $500 \mu\text{m}$  planar back-plane. The  $9 \times 9$  array was developed for a general purpose array that is capable of being implanted into several types of tissue. Insertion depth can be controlled by adjusting the insertion pressure of Blackrock’s multielectrode array inserter. At its maximum insertion, Layers IV–VI of the nonhuman primate brain can be optogenetically interrogated. Round vs. square cross-sectional geometry reduces insertion damage by  $\sim 25\%$ . Round corners reduce the damage to the blunt force seen during insertion by eliminating the four sharp corners which may lacerate blood vessels.

Soda-lime silica glass has been notoriously difficult to micromachine, but the process of



**Figure 6.1.** A completed  $9 \times 9$  Utah Optrode Array with  $1100 \mu\text{m} \times 100 \mu\text{m}$  optrodes and a  $500 \mu\text{m}$  planar back-plane. Several key design features can be seen: a  $2^\circ$  optrode taper and round cross section, a convex lens tip which allows for large tissue volume illumination, a flat back-plane which allows for insertion using Blackrock’s multielectrode array inserter, and curved grooves on the front-plane which allow tissue irrigation during testing. Used by permission from Biomedical Microdevices [1].

fabricating a  $9 \times 9$  Utah Optrode Array uses standard microelectronic back-end processes of dicing, wet etching, and fire polishing without need of a cleanroom or masking. UOAs made for this work are set for use in optogenetic studies of nonhuman primate visual cortex to interrogate neurons. Neurons will be polarized, depolarized, or hyperpolarized using specific opsins that have been genetically modified to respond to light within the visual spectrum of  $\sim 390 \text{ nm}$ — $700 \text{ nm}$  by launching light onto the back-plane of the UOA and transmitting it to a depth of  $1.5 \text{ mm}$  deep below the surface of the brain. Research has shown that the UOA can be repeatably fabricated in large batch quantities sufficient to support the growing optogenetics community with arrays capable of large tissue volume illumination, capable of both acute and chronic implantation, and 25% reduced tissue damage from previous fused silica/quartz optrode arrays. back-plane

## 6.2 Utah Optrode Array customization

This study shows that UOAs can be customized using Solidworks 3D CAD model of the visual cortical area V4D of the macaque and of the motor cortex of C57BL/6 wild-type mouse. The  $8 \times 6$  UOA has been inserted in wild-type mouse for over 6 months with no

adverse reactions, showing excellent biocompatibility. Based on histological assessment, the device causes a small amount of sharp force trauma at the base of the optrode tips, but this damage is easily repaired during postimplantation recovery. A customized  $8 \times 6$  array was successfully fabricated reducing blunt force trauma and laceration of tissue, and the device successfully inserted at the boundary between layers III and IV for optogenetic illumination of layer IV. Insertion damage was far less than that caused by using a  $13 \times 13$  high density UOA. Final dimensions of the customized  $8 \times 6$  were optrode length ( $400 \mu\text{m}$ ), optrode width ( $75 \mu\text{m}$ ), optrode pitch ( $400 \mu\text{m}$ ), back-plane thickness ( $500 \mu\text{m}$ ), and overall form factor ( $3.45 \text{ mm} \times 2.65 \text{ mm}$ ). It was reported that a through glass via was fabricated using  $25 \mu\text{m}$  grit ablation to drill through the back-plane of the  $8 \times 6$  UOA. This design allows for simultaneous electrical recording in the middle of the UOA and back-plane illumination.

Solidworks 3D CAD was successfully used to create a 3D model of Paxinos [2] region visual macaque visual cortical area V4D. Calabrese [3] atlas plates were imported into Solidworks from The Scalable Brain [4], the region of interest was B-Splined, and each B-Splined region was lofted together. The UOA was designed, modeled in Solidworks, and virtually inserted into the 3D CAD model of the brain region of interest. This allowed for the array design to be iterated without the need of multiple insertions into a live animal reducing the cost of animals for future study. The major differences between the prototype and the stereotactically designed UOAs are rounded optrodes, tuned optrode length for specific layer targeting, smaller footprint, reduced numbers of optrodes per array, and lower light intensity requirements. In each of the parameters we see a marked improvement over the  $13 \times 13$  array.

This study proves that previous anatomical atlases can be exploited to create virtual 3D anatomical models in order to customize implantable multioptrode and multielectrode arrays without the use of animals in trial and error experiments. Prior to *in vivo* experimentation, researchers can use 3D CAD software to create a 3D anatomical model of the region of interest and use that virtual model to design a device suitable for implantation to minimize invasiveness and injury to the animal. By eliminating the need for live animals to design a device, this method dramatically accelerates device development by optimizing the device for size and placement within the anatomical region of interest. An additional benefit of this research is that it shows that atlas coordinate systems can be used in conjunction

with 3D CAD to assist in the placement of the actual device. This is achieved by using the 3D CAD anatomical model, virtually placing the device, and using the CAD's internal measurement system to determine the placement during the actual surgery. In this work, stereotaxic coordinates were used in both the 3D anatomical model as well as the virtual placement of the device; the virtual placement measurements were then transferred to the stereotactic-mounted pneumatic hammer used for UOA placement. Overall, this work shows great utility to the functional anatomist as well as the neuroscientist.

### 6.3 Single optrode characterization

Despite some observed surface roughness, the UOA is more than capable of interfacing with the brain during optogenetic studies, and due to its excellent biocompatibility it is capable of being used in either acute or chronic studies [5]. The UOA can be backlit with individually addressable light sources to optrodes such as individual LEDs, butt-coupled optical fibers, spatial light modulators, small full color displays, etc. One of the strengths of the UOA is the versatility to be used for large tissue volume illumination or for fine single neuron illumination by spatiotemporal light patterning.

Aside from 3.6 dB per optrode of loss, which can be overcome by additional input power, the UOA is capable of precisely delivering light deep into tissue for optogenetic experiments. Radiometric testing proved the surface roughness was of little consequence in the functioning UOA. Measured results showed a 9% coupling inefficiency, 48% back scattering out of the optrode, and a 43% transmission. These results compared nicely to the Zemax ray trace simulation with only a 15.4% difference between actual and simulated results.

Visual inspection showed the UOA had 1.1 mm long optrodes that are capable of penetrating to Layer V where it can illuminate Layers VIa and VIb. Each round optrode has a 112  $\mu\text{m}$  diameter with a round tip with a 37  $\mu\text{m}$  radius of curvature. A 500  $\mu\text{m}$  back-plane is thick enough to support all the optrodes during the insertion process. Two degrees of optrode taper assists in the insertion process by pushing displaced tissue away from the thicker optrode areas near the front-plane, where there is a trough to relieve pressure at the front-plane. All of these geometric features serve to reduce the trauma to tissue during implantation by reducing the amount of tissue squeezed between the optrodes and sliced by sharp edges. Surface roughness was observed during SEM and

AFM, but SEM/EDS analyses showed the roughness to be devitrification. Devitrification is the unwanted crystallization process in glass; it is characteristically seen on the surface of glass as nucleation sites as those seen on some of the UOA's optrodes during SEM analysis. Average and root mean square roughness were measured as  $R_a = 13.5$  nm and  $R_q = 20.6$  nm, respectively, with maximum amplitude of roughness reaching 120 nm in some scans.

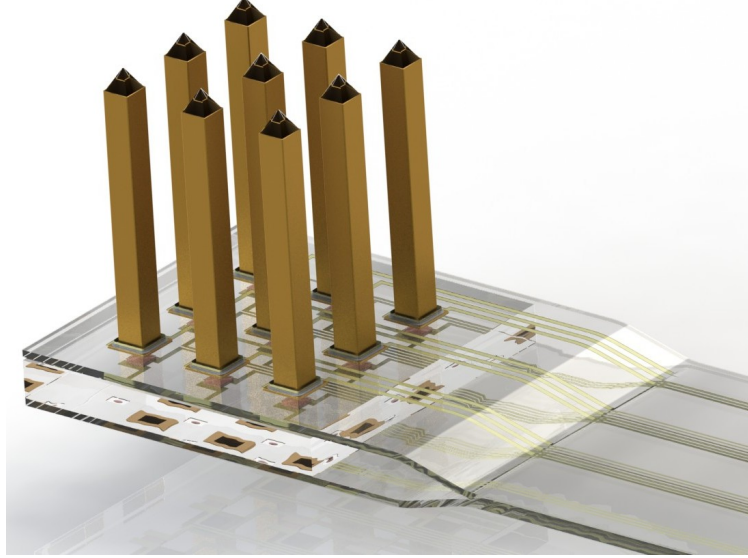
## 6.4 Future work

The future of the UOA is dominated by yield improvement and its incorporation into a hCBI that allows for simultaneous light transmission, electrical recording of neural action potentials, and wireless transmission. LED array coupling is a key milestone with the bonding of a  $\mu$ LED array to the planar back-plane. Eventually a wafer of  $\mu$ LED arrays can be aligned to a wafer of UOAs for true wafer-to-wafer microfabrication. Glass metallization and printed circuitry are needed on the UOA to record action potentials close to the point of illumination. Several additional items of work have been identified for the future of the UOA as well. Several process improvements are needed to improve the wafer-level microfabrication for higher UOA yield. Each optrode of the hCBI will be capable of independent illumination for binary patterned illumination. In order to prove the concept of patterned illumination with a UOA, a  $2 \times 2$  UOA is needed for a specially designed optical carrier that will be implanted at the same time as the UOA. The  $2 \times 2$  UOA will be illuminated with four  $1 \times 1$  MEMS fiber optic switches that are connected to a single laser source via a fast switching  $1 \times 4$  MEMS switch. This will give a psuedo-binary pattern for behavioral studies in small rodents and nonhuman primates. Finally, it is left to future work to understand the error associated with 3D CAD models of the brain and potentially other organs. This chapter will identify several areas of initial improvement of the 3D models, such as layer targeting, surface modeling, and others.

### 6.4.1 Hybrid computer brain interface

Figure 6.2 shows the proposed fully rendered version of the hCBI. This device incorporates platinum metallized optrodes for neurophysiological recording near the tip of the optrode. Optical transparency can be maintained around 95% by sputtering thin films, so masking is unnecessary on the tips of the shanks. This is advantageous because



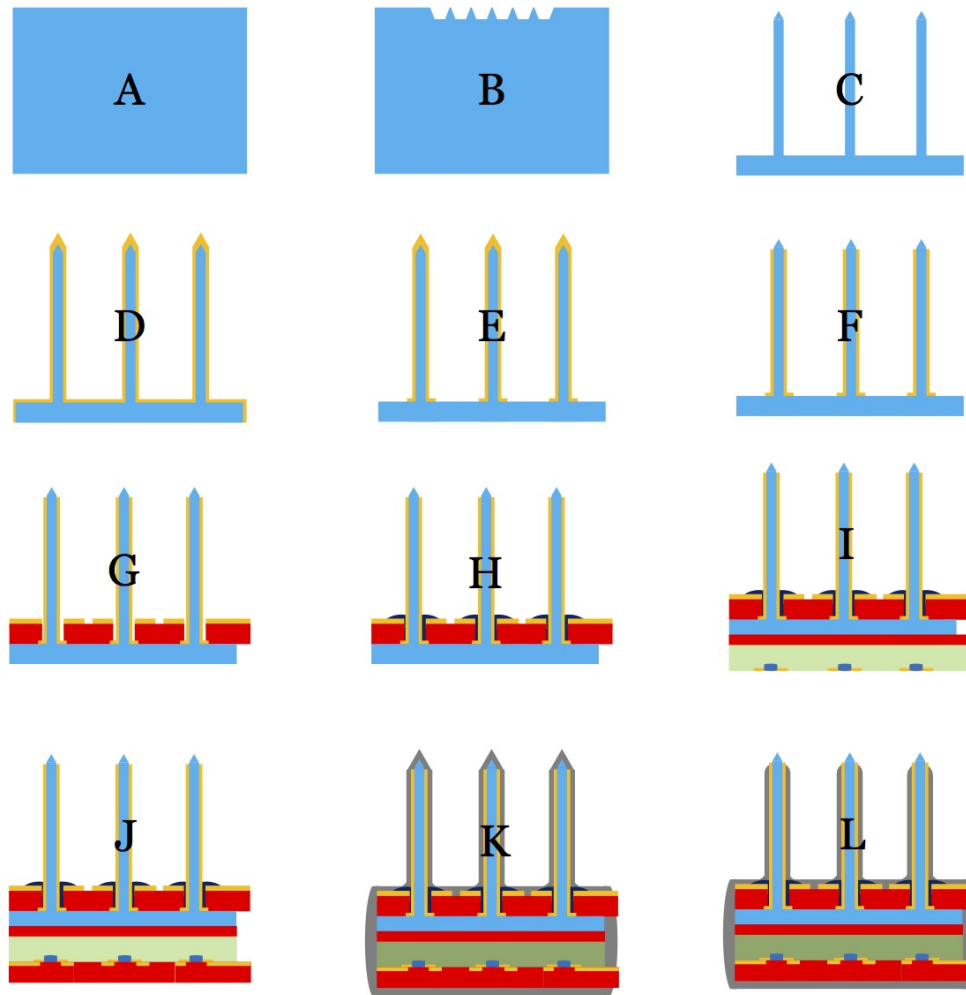


**Figure 6.2.** Fully rendered conceptual 3D model of a  $3 \times 3$  hybrid computer brain interface (hCBI). The hCBI is capable of simultaneous illumination and electrical recording. Each optrode is individually addressed with a  $\mu$ LED for independent illumination.

sputtering the entire device can be done with no front-plane masking. Floss can be used to mechanically remove the platinum from between each shank to prevent the shanks from electrically shorting out to each other. After metalization, a  $\mu$ m LED array with flexible microcircuit board is flip-chip bonded to the back-plane. A second flexible microcircuit board is slid over the optrodes of the UOA and secured to the front plane via biocompatible electrically conductive epoxy to the base of the metallized optrode. The entire device is then passivated to isolate the biological tissue from the electrical traces, and a final etch step is performed to remove the passivation layer very near the tip for electrical contact at the point of illumination. Selective removal of passivation along the optrode allows for electrical recording at different depths of insertion. Figure 6.3 shows a conceptual cross sectional processing of the soda-lime UOA into the hCBI.

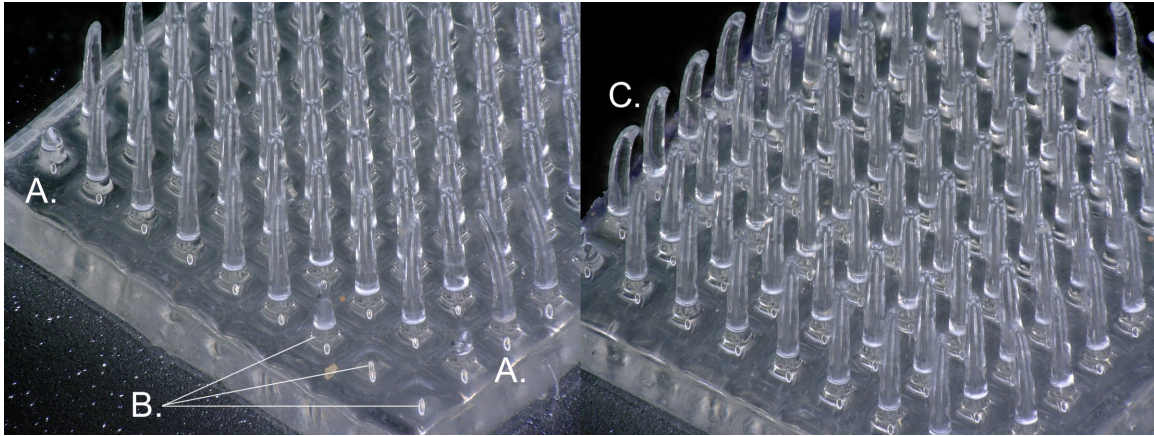
#### 6.4.2 UOA fabrication process improvements

During the course of this research, several areas of improvement to the fabrication have been identified. Figure 6.4 shows several errors seen during UOA processing. Each of the key areas of fabrication—dicing, etching, and firing—have areas to be improved. Improved



**Figure 6.3.** Process steps for the  $3 \times 3$  hCBI: A. Soda-Lime Wafer Blank, B. Diced Tips, C. Shanks diced and wet etched, D. Metalization, E. Singulate metalization, F. Wet etch tips if needed, G. Flexible circuit board added, H. Conductive epoxy connects flex-print's traces to hybrid electrodes, I.  $\mu$ LED Board added, J. Flexible/Wire-bond circuit board added, K. Paralene passivation of entire device, L. Etch passivation layer at tips.

dicing can be achieved with coolant and blade selection optimization. Several variables are at play during the dicing process like specimen feed speed, depth steps during cutting, coolant flow, coolant type, blade base material, blade grit, and many others. For this research a Fractional-Factorial DOE was used to minimize the electrical current flow the dicing saw experienced during fixed feed speeds and cutting depths. Coolant flow rate was allowed to be adjusted, but minimizing blade electrical current flow required higher coolant flow. The higher coolant flow rate caused higher hydraulic fracture, so it is left to future



**Figure 6.4.** Three error types had a negative impact on the overall UOA yield. A. Postfiring optrode fracture, B. Prefiring optrode hydraulic fracturing, and C. Over-temperature optrode sagging.

work to optimize a higher number of variables with a Full-Factorial DOE. Diamond dicing blades have differing base materials and grit sizes, which can also be added to the DOE and optimized. It is recommended that the DOE incorporate synthetic water soluble coolant additives that cool and lubricate the blade and specimen during cutting.

Wafer support during dicing is done by a silicon carrier wafer and WaferGrip adhesive. This setup has a secondary benefit of protect the back-plane's optical properties during etching by providing a barrier to the etchant. Carrier wafers add many millimeters of height to the stack during dicing, and they need to be removed by a special cleaning process that releases the glass from the silicon wafer. It is recommended that ultraviolet releasable wafer tape be used to support the wafer during dicing to eliminate the need for chemical removal of wafer grip because several UOA die were lost in the air drying process.

High surface roughness was observed on soda-lime from the paste etchant process, so an etching DOE is recommended that would vary glass types and etchants to achieve better geometrical control during etching. Etch rates can be adjusted in the DOE to identify an etchant that doesn't require long etch times.

Surface roughness reflow, self healing, and annealing require high temperatures and dwell times. Several UOA die were lost during firing for over-temperature caused optrode droop where the optrodes annealed in a bent fashion. These devices could not be inserted into tissue because of this, so it is recommended that an annealing method be developed that

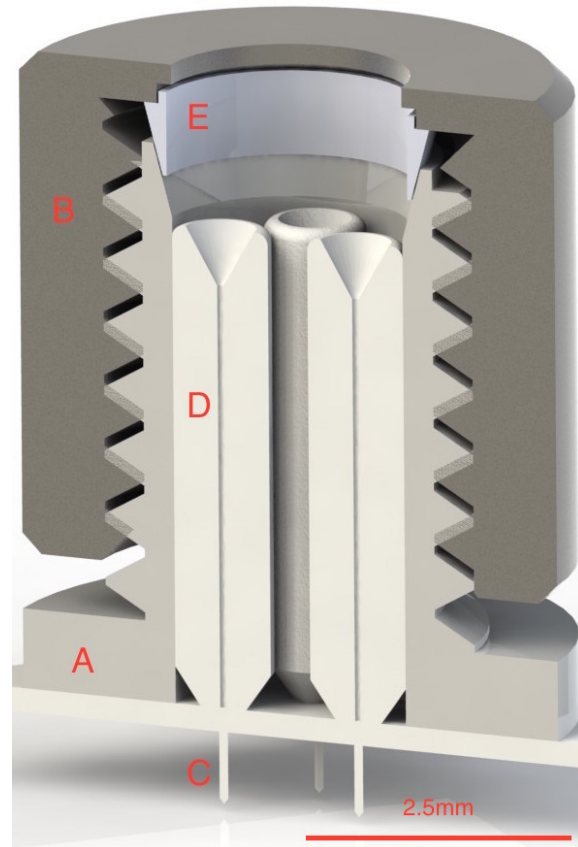
allows for the die to be fired with down-facing optrodes rather than the current process of upward-facing die firing. A Fractional-Factorial DOE was used to identify temperatures and dwell times that would be acceptable to the UOA; however, devitrification was sporadically identified on some of the outer perimeter optrodes. A Full-Factorial DOE is recommended to optimize the ramp rates, dwell temperatures, and dwell times. A dental annealing furnace was used in this research which could only ramp up in temperature. Down-ramping relied upon thermal load of the station and the ambient air, so there was a slow down ramp. This is normally preferred to reduce thermal shock, but better down ramp control is recommended in order to allow for flash firing of the arrays allowing for self-healing but preventing devitrification.

#### **6.4.3 $2 \times 2$ Ferrule Port for chronic *in vivo* quasi-binary patterning**

Optically aligning multiple cannulae poses a particular challenge, so a preliminary design for an optical holder has been created to assist in the tethering of animals to a single light source but with four outputs. The design is based on a standard compression fitting, and it will hold a single patch cable containing two pairs of 125  $\mu\text{m}$  fibers. Figure 6.5 shows the  $2 \times 2$  Ferrule Port. The threaded cap of the port can be swapped out with a solid cap to fully enclose the port for post-op recovery of the small rodent or small nonhuman primate. Special attention has been paid to the compression fitting to ensure a proper grip on the outer jacket of an armor jacketed fiber to ensure animals under behavioral studies cannot easily dislodge the optical fiber from the ferrules. Compression is accomplished with a wedge-shaped ring that is slid onto the outer armor jacket of the patch cable and a threaded compression cap that secures the wedge as the cap is torqued into place. The compression cap can be removed and replaced with a cap that has no port; this is important to untether the animals such as during recovery from the implantation surgery, when not under behavioral studies, etc. and still keep the area sterile.

#### **6.4.4 *In vivo* quasi-binary patterning with four MEMS switches and a single source laser**

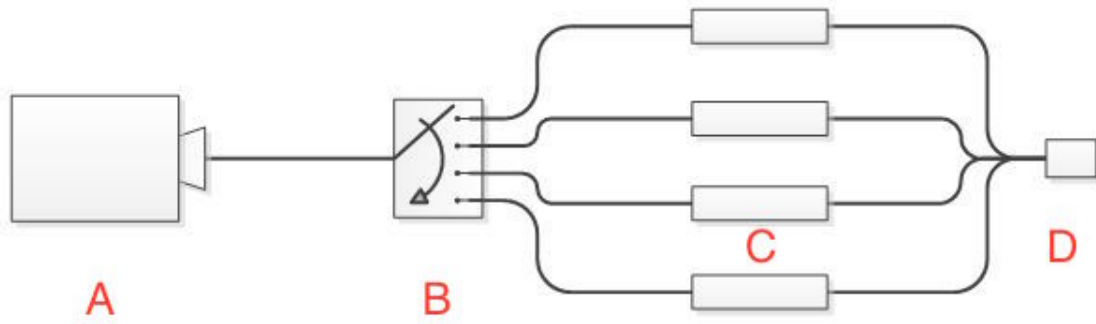
The  $2 \times 2$  Ferrule Port makes it possible to spatially and temporally deliver light to tissue using four a bit pattern like 0000, 0001, 0100, 1111, etc. Binary illumination techniques like this are easily accomplished with multiple light sources; for example, it is easy to purchase



**Figure 6.5.** Cross section of the  $2 \times 2$  Ferrule Port used to secure a single fiber optic patch cable with two pairs of  $125 \mu\text{m}$  diameter fibers. A. Biocompatible threaded plastic port B. Threaded cap secures the compression ring (E.) in place around the outer diameter of the patch cable C. Optical fiber portion of the cannulae D. Shows the ceramic ferrule of the cannulae where bare fiber couples to the cannulae fibers.

and attach four 473 nm Thorlabs fiber coupled lasers to four patch cables and patch the fibers onto four ferrules and temporally illuminate the tissue. This “brute force” method, while easy to do, is quite expensive and not very practical for binary studies where many sources may be needed. One blue Thorlabs multimode laser is  $\sim 7000$  USD, so a method was conceptualized to emulate multiple sources by having one  $1 \times 4$  main MEMS switch switching between all outputs and connecting up four individual  $1 \times 1$  MEMS switches to the  $2 \times 2$  Ferrule Port. Figure 6.6 shows a schematic design and Figure 6.7 shows a repeating binary sequence of 1000, 1100, 1110, 0111, and 0011 when the  $1 \times 4$  switch is run at its fastest switching rate.

Figure 6.7 shows a quasi-binary conceptual clocking design to illuminate tissue. A  $1 \times 4$

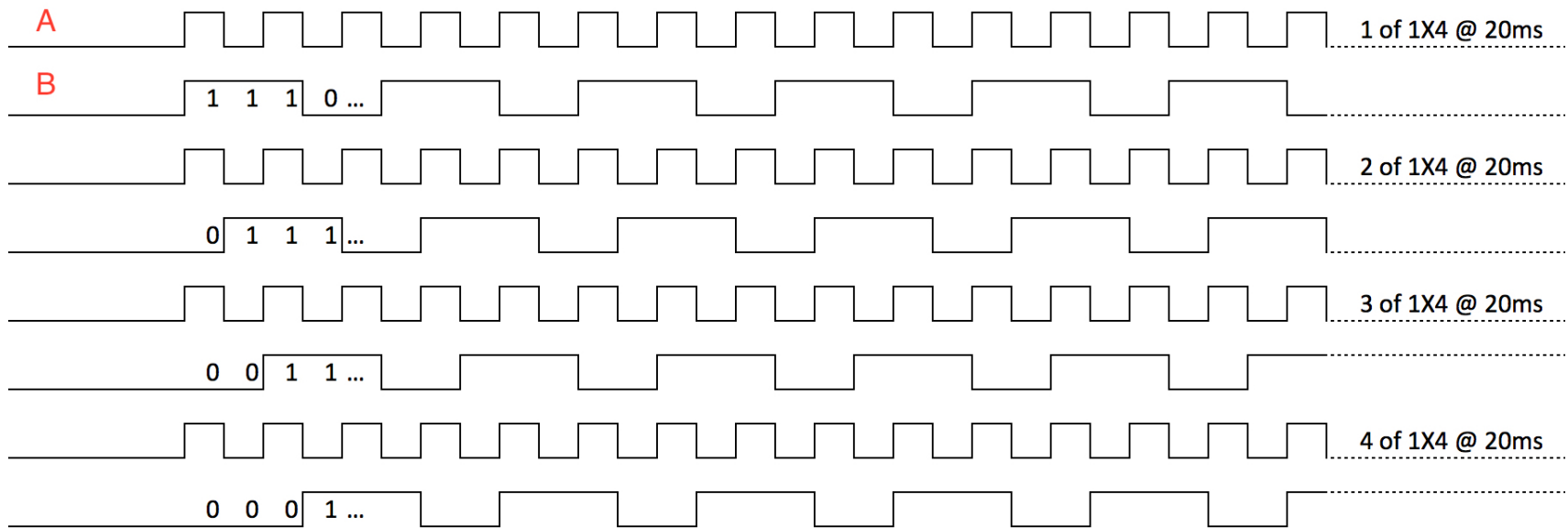


**Figure 6.6.** Binary illumination with a single source and MEMS fiber optic switches: A. Single light source, B.  $1 \times 4$  MEMS switch operated at its fastest rate creating a mock “always-on” signal, C. fiber optic MEMS on/off switches (qty. 4), and D. is a  $2 \times 2$  Ferrule Port with  $2 \times 2$  UOA.

MEMS switch runs at its fastest rate creating a mock “always-on” signal that is passed from the single light source to four on/off MEMS switches. Each of these on/off switches is then patterned into a binary arrangement that is needed for a particular experiment. In addition to understanding if the mock always-on signal can produce acceptable threshold signals for the on/off switches, it is also left to future work to reduce the stiffness associated to the four optical fibers. Corning’s ClearCurve bare optical fibers have been selected due to their ease of bending and bend tolerance. These optical fibers can be cleaved very short and supported so that the tethered animal can freely move about the experiment arena.

## 6.5 Final words

Several contributions to the optogenetics field have been realized for this dissertation: three journal papers on the simulation, characterization, and testing of two monolithic optical arrays and a comprehensive device study found in contemporary optogenetic literature. A maskless microfabrication method was developed for two-inch-square glass wafers. This virtual CAD/CAM process was used to microfabricate a  $9 \times 9$  and a  $8 \times 6$  UOA with minimal process changes between the two different devices. The  $8 \times 6$  UOA was created as part of an effort to customize the  $9 \times 9$  UOA using readily available brain atlases. The atlases were used to create a 3D CAD model of the brain, and then using the 3D brain model to design the UOA to fit within a specific brain region of interest. It was determined the  $8 \times 6$  array produced minimal acute damage during insertion, and it was also tolerated for 8+ months



**Figure 6.7.** Quasi-binary illumination patterning: A. is a mock “always-on” pattern generated by switching the  $1 \times 4$  MEMS switch at its fastest rate, whereas B. is the quasi-binary pattern produced by a single on/off switch. By combining the four on/off switches it is possible to produce quasi-binary patterns such as 1000, 1100, 1110, 0111, etc.

in a chronic insertion. Bench testing was used to fully characterize the geometrical features of the  $9 \times 9$  UOA, the surface defects on the optrodes, and the light transmission profile out of the optrode. It was determined that the UOA has  $3.6dB$  of insertion loss per optrode during this testing.

## 6.6 References

- [1] R. W. Boutte and S. Blair, “Maskless wafer-level microfabrication of optical penetrating neural arrays out of soda-lime glass: Utah optrode array,” *Biomedical Microdevices*, vol. 18, Dec 2016.
- [2] G. Paxinos, X. Huang, and A. Toga, *The Rhesus Monkey Brain in Stereotaxic Coordinates*. San Diego, CA. Academic Press, 2000.
- [3] E. Calabrese, A. Badea, C. L. Coe, G. R. Lubach, Y. Shi, M. A. Styner, and G. A. Johnson, “A diffusion tensor MRI atlas of the postmortem rhesus macaque brain,” *NeuroImage*, vol. 117, pp. 408–416, Aug 2015.
- [4] R. Bakker, P. Tiesinga, and R. Kötter, “The scalable brain atlas: Instant web-based access to public brain atlases and related content,” *Neuroinformatics*, vol. 13, pp. 353–366, Feb 2015.
- [5] S. D. Davis, D. F. Gibbons, R. L. Martin, S. R. Levitt, J. Smith, and R. V. Harrington, “Biocompatibility of ceramic implants in soft tissue,” *Journal of Biomedical Materials Research*, vol. 6, pp. 425–449, Sep 1972.



## APPENDIX A

### VIRTUAL CAM: DISCO DAD-3220 DICING RECIPES

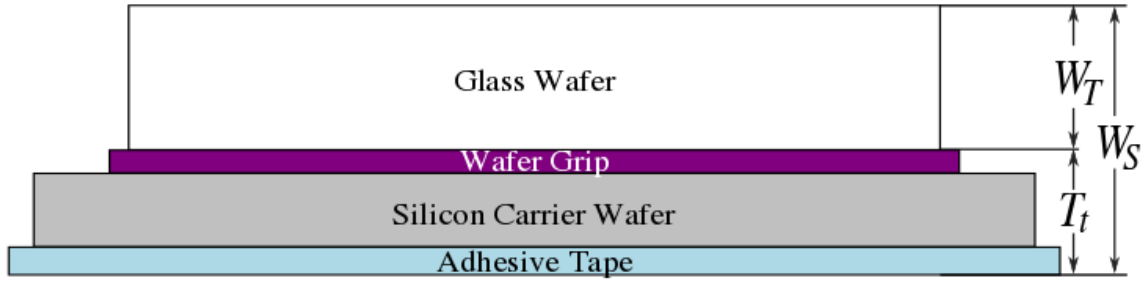
Appendix A illustrates the VCAM method mentioned in Chapter 3. VCAM was created as a method of bridging the gap between 3D CAD and 2D blueprints with the Disco DAD3220 precision dicing saw. The DAD3220 requires cutting parameters to be entered into the “Device Data” entry screen. Each Device Data routine requires a full VCAM recipe consisting of 3 parts: Tips, Shanks, and Die Singulation. Each of these parts is included for an  $8 \times 6$  UOA:

1.  $8 \times 6$  Tip Dicing with the Disco DAD 3220 “Device Data” screen.
2.  $8 \times 6$  Virtual CAM worksheet for  $60^\circ$  tips.
3.  $8 \times 6$  “Device Data” entry items for  $60^\circ$  tips.
4.  $8 \times 6$  Shank Dicing with the Disco DAD 3220 “Device Data” screen.
5.  $8 \times 6$  Virtual CAM worksheet for shanks.
6.  $8 \times 6$  “Device Data” entry items for shanks.
7.  $8 \times 6$  Array singulation with the Disco DAD 3220 “Device Data” screen.
8.  $8 \times 6$  Virtual CAM worksheet for array singulation.
9.  $8 \times 6$  “Device Data” entry items for array singulation.

#### A.1 Determining beveled blade height

Disco’s DAD3220 lowers the blade onto the sample and then cuts down to a user-set “Blade Height”  $[BH]$  by default. This terminology can be difficult to remember when working between standard CAD tools and the DAD3220’s Device Data entry screen. Figures A.1, A.2, and A.3 show the method for calculating the Blade Height that was employed for two blade angles:  $60^\circ$  and  $45^\circ$ . *Note: subscripts  $[T]$ ,  $[L]$ , and  $[S]$  are measured parameters.*

1. Measure thickness of the glass wafer  $[W_T]$  prior to adhering it to the carrier wafer with WaferGrip: This dicing saw parameter will be called the “Work Thickness” and



**Figure A.1.** The wafer stack  $[W_S]$  and the glass wafer's  $[W_T]$  thicknesses are measured and subtracted from each other yielding the “Tape thickness”  $[T_t]$  for input into the Device Data screen of the DAD3220. It is more correct to call  $T_t$  the “Effective Tape Thickness.”

entered into the DAD3220's Device Data entry screen.

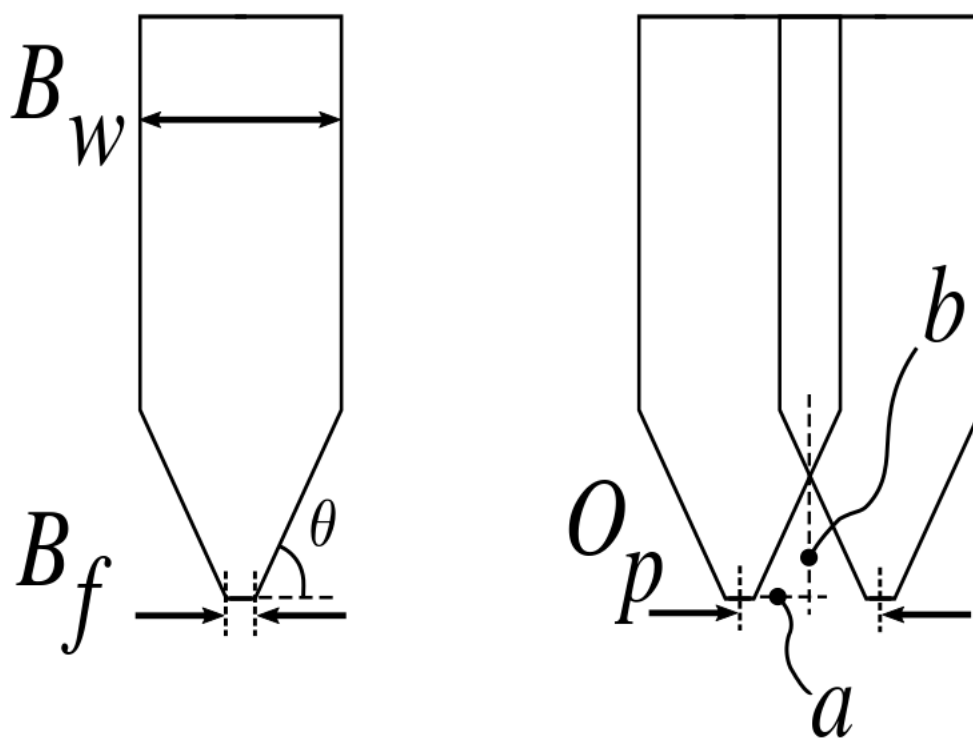
2. Measure thickness of the stack  $[W_S]$  (see Figure A.1) to be diced: glass wafer, Wafer-Grip, silicon carrier wafer, and adhesive tape: This will be called the “Wafer Stack Thickness.”
3. Subtract Work Thickness from Wafer Stack Thickness: This saw parameter will be called “Tape Thickness”  $[T_t]$  and entered into the DAD3220 ( $T_t = W_s - W_T$ ).

Two different Disco diamond beveled blades were used for this Dissertation:

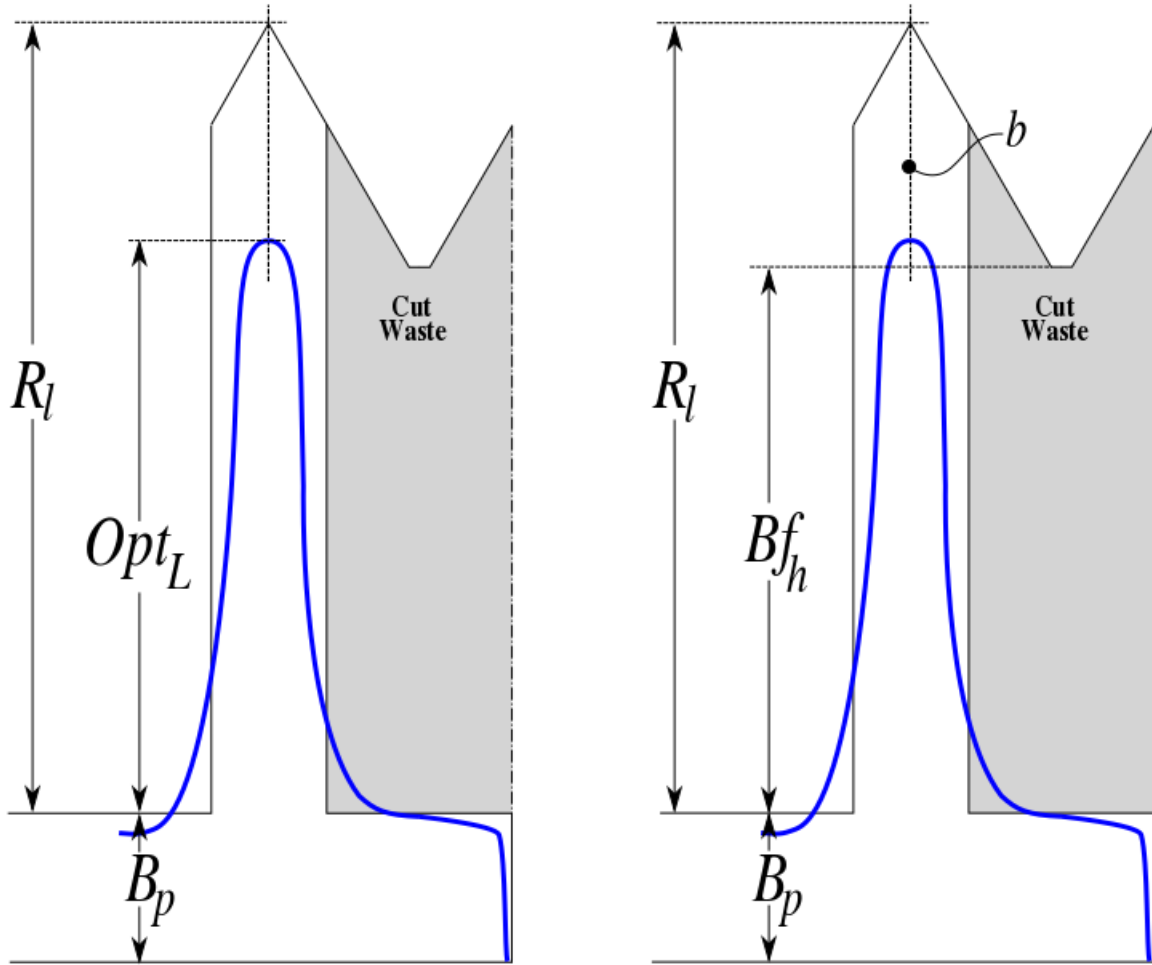
1. 60° Beveled blade model number: B1N862 SD600L75MT38 54x0.55x40x60x0.08
2. 45° Beveled blade model number: B1N862 SD600L75MT38 54x0.55x40x45x0.15

Table A.1 shows the key parameters from Figure A.2 for both blade types. All of the parameters from Table A.1 can be entered into the following equation to calculate  $BH$  for the 60° blade.

For this Blade Height example, the 60° blade parameters from Table A.1 and Figure A.3 will be used, where  $OPT_L = 0.500\text{mm}$ , so  $R_l = OPT_L \cdot 1/0.8 = 0.625\text{ mm}$ . The two parameters from the Figure A.1 are measured at  $W_T = 1.081\text{ mm}$  and  $W_S = 1.673\text{ mm}$ , and the Tape Thickness is calculated as  $T_t = W_S - W_T = 0.592\text{ mm}$ . It is recommended that the bevel blade be lowered far enough down to make a sharp pyramidal tip, so the “Floor” function will be used to round down to the nearest 0.10 mm according to the following calculation in A.1.



**Figure A.2.** Blade cross-section schematic showing key parameters for calculating “Blade Height”  $[BH]$ . (Left)  $B_w$  is the blade’s overall width supplied by the manufacturer;  $B_f$  is the flat portion of the blade, and  $\theta$  is the bevel’s angle also supplied by the blade’s manufacturer. (Right)  $O_p$  is the optrodes’ pitch as supplied by the neuroscientist;  $a$  is the half-width of the freshly cut optrodes; and  $b$  is the pyramidal height of the optrodes’ tips.



**Figure A.3.** Key parameters for calculating “Blade Height” [BH]. (Left) The rough optrode length [ $R_l$ ] will lose 20% of its length, so the optrodes desired final length [ $OPT_L$ ] must be known from layers of interest within the animal under study. Backplane [ $B_p$ ] thickness is determined for structural stability during fabrication and insertion. (Right) The blade’s flat height [ $Bf_h$ ] is the distance from the front plane to the flat portion of the blade. [ $b$ ] is the aforementioned distance the blade must be lowered to get the desired optrode pitch.

**Table A.1.** Disco Diamond Blade Parameters

Angle $\theta$	$B_w$ [ $\mu\text{m}$ ]	$B_f$ [ $\mu\text{m}$ ]	$O_p$ [ $\mu\text{m}$ ]	$a$ [ $\mu\text{m}$ ]	$b$ [ $\mu\text{m}$ ]
$60^\circ$	550	80	400	$\frac{O_p - B_f}{2} = 160$	$a \tan \theta_{60^\circ} = 277.1$
$45^\circ$	550	15	400	$\frac{O_p - B_f}{2} = 192.5$	$a \tan \theta_{45^\circ} = 192.5$

$$BH = \lfloor T_t + B_p + R_l - b \rfloor$$

$$BH_{60^\circ} = \lfloor 0.592 + 0.500 + 0.625 - 0.277 \rfloor \text{ mm} \quad (\text{A.1})$$

$$\therefore BH_{60^\circ} = 1.400 \text{ mm}$$

## A.2 Determining flat blade heights for shanks and die singulation

A single 250  $\mu\text{m}$  flat blade is used to create the shanks of the optrodes (obelisk shaped), and the same blade is used to singulate each die into an array ready for wet etching. Disco's R07-SD600-BB200-50 58x0.25 A2x40 blade was used with a single "hairline" adjustment needed. For the shanks all that is needed for "Blade Height" is to know  $T_t$  and  $B_p$  such that  $BH = B_p + T_t$ , and for array singulation into individual die all that is needed is to cut into  $T_t$ .

## A.3 VCAM recipes for $8 \times 6$ UOA

Each of the three recipes are included in Figures A.4 to A.12 to assist in setting up the DAD3220. The parameters mentioned earlier are input into 3 worksheets for tips, shanks, and die singulation, 3 "Device Data" entry spreadsheets, and finally each of the 3 "Device Data" screens are shown. *Note: only the initial measurements for  $W_T$  and  $W_S$  are used because it is difficult to get these measurements after the tips have been diced.*

Z-EM

2017/06/15 14:19:35

Sensor

Terminal

Alarm/Clr

### Device Data (3.1.2)

Device data No. ronnie / TIP8X6

ID 8X6 60 DEGREE TIPS

☐ Round 80.000 mm

☒ Square

Ch1 20.000 mm

Ch2 20.000 mm

Work Thickness 1.081 mm  
Tape Thickness 0.592 mm

Spindle rev. 5000 /min  
Precut process No. 0  
Cutting ch seq. 12

	Ch 1			Ch 2		
	SEQ1	SEQ2	SEQ3	SEQ1	SEQ2	SEQ3
Blade height	1.400	1.400	0.0	1.400	1.400	0.0
Feed speed	1.000	1.000	0.0	1.000	1.000	0.0
Y-index	0.4000	0.5000	0.00	0.4000	0.5000	0.00
Repeat times	8	1		6	1	
Depth steps	0.000	0.000	0.0	0.000	0.000	0.0

	Ch 1	Ch 2
θ Deg.	0.000 °	90.000 °
Cut mode	A	A
Cut dir.	REAR	REAR
Cut	0 lines	0 lines
Offset Y	0.1250	0.1250
Noncut F	0.000	0.000
Noncut R	0.000	0.000

F2  
Ch 3 & Ch 4

F3  
Align Data

F4  
Function Selection

F6  
Proc Control

F7  
Precut Spec

F8  
Kerf Check

F9  
User Special

F10  
Measure

ENTER

EXIT

123

qwe

Figure A.4. 8 × 6 Tip Dicing with the Disco DAD 3220 “Device Data” screen.

8X6 TIPS WORKSHEET									
<b>Disco DAD3220 Parameters to enter into the Device Data Screen</b>									
Device data No.	ronnie/TIP8X660								
ID	THICK								
Spindle Rev.				5,000 RPM					
Precut process No.	0								
Unit	mm								
Cutting ch seq.	Channel1-->Channel 2								
Work shape	SQUARE								
Work size	CH1			13.000 mm					
	CH2			13.000 mm					
Work Thickness				1.081 mm					
Tape Thickness (Effective)				0.592 mm					
θ Deg.	CH1			0 degrees					
	CH2			90 degrees					
Cut mode	A cutting mode								
Cut dir.	REAR (from front to rear)								
Blade height	CH1	SEQ1=	1.400 mm						
(Amount left uncut)		SEQ2=	1.400 mm						
	CH2	SEQ1=	1.400 mm						
		SEQ2=	1.400 mm						
Feed Speed	CH1			1.000 mm/sec					
	CH2			1.000 mm/sec					
Offset Y	CH1			0.125 mm					
	CH2			0.125 mm					
Y-index	CH1	SEQ1=	0.400 mm						
		Repeat	8						
		SEQ2=	0.500 mm						
		Repeat	1						
	CH2	SEQ1=	0.400 mm						
		Repeat	6						
		SEQ2=	0.500 mm						
		Repeat	1						
Depth steps	CH1	SEQ1=	0.000 mm						
		SEQ2=	0.000 mm						
	CH2	SEQ1=	0.000 mm						
		SEQ2=	0.000 mm						
Air curtain sweep speed				Default mm					
Auto down	Wear Comp dist=			Default mm					
(Blade wear compensation)	Wear Comp=			Default mm					
<b>Enter Measurements</b>									
[W_T]: Glass Wafer Thickness (As measured)				Distance		1.081 mm			
Glass Wafer Thickness/Wafer Grip/Si Carrier Wafer (As measured)				Distance		1.543 mm			
Adhesive Tape Thickness (As measured)				Distance		0.130 mm			
Cortical Layer Depth (From Atlas or Neuroscientist)				Distance		0.500 mm			
Cortical Column Width (From Atlas or Neuroscientist)				Distance		0.400 mm			
Beveled Blade Thickness (From manufacturer)				Distance		0.550 mm			
Beveled Blade Flat Thickness (From manufacturer)				Distance		0.080 mm			
Beveled Blade Angle (From manufacturer)				Distance		60 degrees			
[B_p]: Back Plane Thickness				Distance		0.500 mm			
<b>Key Parameters to enter into the Device Data recipe</b>									
[W_S]: Glass Wafer Thickness/Wafer Grip/Si Carrier Wafer/Tape (Calculated)				Distance		1.673 mm			
Convert Beveled Blade Angle (Calculated)				Distance		1.047 radians			
[a]: Pyramidal base half-length of uncut tip (Calculated)				Distance		0.160 mm			
[b]: Pyramidal height of uncut tip (Calculated)				Distance		0.277 mm			
[R_L]: Rough Shank Length (Calculated)				Distance		0.625 mm			
[BH]: Blade Height (Calculated)				Distance		1.400 mm			

Figure A.5. 8 × 6 Virtual CAM worksheet for 60° tips.





2017/06/15 14:22:47

### Device Data (3.1.2)

Device data No. ronnie / SHANK8X6

ID 8X6 150um SHANKS

Work shape and size  
☐ Round 80.000 mm  
☒ Square Ch1 20.000 mm  
Ch2 20.000 mm

Work Thickness 1.081 mm  
Tape Thickness 0.592 mm

Spindle rev. 5000 /min

Precut process No. 0

Cutting ch seq. 12

Full Auto

Unit  
☒ mm  
☐ inch

ENTER

EXIT

	Ch 1		Ch 2			
	SEQ1	SEQ2	SEQ3	SEQ1	SEQ2	SEQ3
Blade height	1.090	1.090	0.0	1.090	1.090	0.0
Feed speed	1.000	1.000	0.0	1.000	1.000	0.0
Y-index	0.4000	0.1250	0.00	0.4000	0.1250	0.00
Repeat times	8	4		6	4	
Depth steps	0.250	0.250	0.0	0.250	0.250	0.0
	◀		▶		◀ ▶	

θ Deg. 0.000 °

Cut mode A

Cut dir. REAR

Cut 0 lines

Offset Y -0.2000

Noncut F 0.000

Noncut R 0.000

Ch 1 0.000 °

Ch 2 90.000 °

A A

REAR REAR

0 lines 0 lines

-0.2000 -0.2000

0.000 0.000

0.000 0.000

F2 Ch 3 & Ch 4

F6 Proc Control

F3 Align Data

F7 Precut Spec

F8 Kerf Check

F9 User Special

F10 Measure

123

qwe

Direct

Figure A.7. 8 × 6 Shank Dicing with the Disco DAD 3220 “Device Data” screen.

103

8X6 SHANKS WORKSHEET									
Disco DAD3220 Parameters to enter into the Device Data Screen					Enter Measurements			Distance	Units
Device data No.	ronnie/TIP8X660				[W_T]: Glass Wafer Thickness (As measured)			1.081	mm
ID	THICK				Glass Wafer Thickness/Wafer Grip/Si Carrier Wafer (As measured)			1.543	mm
Spindle Rev.					Adhesive Tape Thickness (As measured)			0.130	mm
Precut process No.	0				[B_p]: Back Plane Thickness			0.500	mm
Unit	mm				Cortical Layer Depth (From Atlas or Neuroscientist)			0.500	mm
Cutting ch seq.	Channel1-->Channel 2								
Work shape	SQUARE								
Work size	CH1			13.000	mm				
	CH2			13.000	mm				
Work Thickness				1.081	mm				
Tape Thickness (Effective)				0.592	mm				
θ Deg.	CH1			0	degrees				
	CH2			90	degrees				
Cut mode	A cutting mode								
Cut dir.	REAR (from front to rear)								
Blade height	CH1	SEQ1=	1.090		mm	Key Parameters to enter into the Device Data recipe			
(Amount left uncut)		SEQ2=	1.090		mm	[W_S]: Glass Wafer Thickness/Wafer Grip/Si Carrier Wafer/Tape (Calculated)			
	CH2	SEQ1=	1.090		mm	1.673			
		SEQ2=	1.090		mm				
Feed Speed	CH1			1.000	mm/sec				
	CH2			1.000	mm/sec				
Offset Y	CH1			-0.200	mm				
	CH2			-0.200	mm				
Y-index	CH1	SEQ1=	0.400		mm				
		Repeat	8						
		SEQ2=	0.125		mm				
		Repeat	4						
	CH2	SEQ1=	0.400		mm				
		Repeat	6						
		SEQ2=	0.125		mm				
		Repeat	4						
Depth steps	CH1	SEQ1=	0.250		mm				
		SEQ2=	0.250		mm				
	CH2	SEQ1=	0.250		mm				
		SEQ2=	0.250		mm				
Air curtain sweep speed			Default	mm					
Auto down	Wear Comp dist=			Default	mm				
(Blade wear compensation)	Wear Comp=			Default	mm				

Figure A.8. 8 × 6 Virtual CAM worksheet for shanks.

8X6 SHANKS DEVICE DATA											
Device data No.	ronnie/	8X6 150um SHANKS			Spindle rev.	5,000	RPM		Unit	mm	
ID	THICK				Precut process No.	0					
Work shape and size	SQUARE	CH1	20.000	mm	Cutting ch seq.	12					
		CH2	20.000	mm							
Work Thickness			1.081	mm							
Tape Thickness (Effective)			0.592	mm							
	Ch 1	Ch 2			Blade height	1.090	1.090	0.000	1.090	1.090	0.000
θ Deg.	0.000	90.000			Feed Speed	1.000	1.000	0.000	1.000	1.000	0.000
Cut mode	A	A			Y-index	0.400	0.125	0.000	0.400	0.125	0.000
Cut dir.	REAR	REAR			Repeat times	8	4	0	6	4	0
Offset Y	-0.200	-0.200			Depth Steps	0.250	0.250	0.000	0.250	0.250	0.000
Noncut F	0.000	0.000									
Noncut R	0.000	0.000									

**Figure A.9.**  $8 \times 6$  “Device Data” entry items for shanks.

2017/06/15 14:23:10

Sensor

Terminal

Alarm/Clr

**Device Data (3.1.2)**  
 Device data No. ronnie / SING8X6  
 ID 8X6 SINGULATION

Work shape and size  
☐ Round 80.000 mm  
☒ Square
 

Ch1
20.000 mm

Ch2
20.000 mm

Spindle rev. 5000 /min  
 Precut process No. 0  
 Cutting ch seq. 12

Work Thickness 1.081 mm  
 Tape Thickness 0.592 mm

	Ch 1			Ch 2		
	SEQ1	SEQ2	SEQ3	SEQ1	SEQ2	SEQ3
Blade height	0.500	0.000	0.0	0.500	0.000	0.0
Feed speed	1.000	0.000	0.0	1.000	0.000	0.0
Y-index	3.450	0.0000	0.00	2.650	0.0000	0.00
Repeat times	1	0		1	0	
Depth steps	0.250	0.000	0.0	0.250	0.000	0.0

Full Auto  
  
 Unit  
☒ mm  
☐ inch

	Ch 1	Ch 2
θ Deg.	0.000 °	90.000 °
Cut mode	A	A
Cut dir.	REAR	REAR
Cut	0 lines	0 lines
Offset Y	3.2500	2.4500
Noncut F	0.000	0.000
Noncut R	0.000	0.000

Blade height	0.500	0.000	0.0
Feed speed	1.000	0.000	0.0
Y-index	3.450	0.0000	0.00
Repeat times	1	0	
Depth steps	0.250	0.000	0.0

ENTER

EXIT

◀

▶

ENTER  
  
 EXIT

F2  
Ch 3 & Ch 4

F3  
Align Data

F4  
Function Selection

F5  
Measure

F6  
Proc Control

F7  
Precut Spec

F8  
Kerf Check

F9  
User Special

F10  
Measure

F11  
Direct

123 | qwe |  
 Direct

Figure A.10. 8 × 6 Array singulation with the Disco DAD 3220 “Device Data” screen.

106

8X6 DIE SINGULATION WORKSHEET									
<b>Disco DAD3220 Parameters to enter into the Device Data Screen</b>					<b>Enter Measurements</b>				
Device data No.	ronnie/TIP8X660				[W_T]: Glass Wafer Thickness (As measured)	1.081 mm		Distance	Units
ID	THICK				Glass Wafer Thickness/Wafer Grip/Si Carrier Wafer (As measured)	1.543 mm			
Spindle Rev.					Adhesive Tape Thickness (As measured)	0.130 mm			
Precut process No.	0				[B_p]: Back Plane Thickness	0.500 mm			
Unit	mm				Cortical Layer Depth (From Atlas or Neuroscientist)	0.500 mm			
Cutting ch seq.	Channel1-->Channel 2								
Work shape	SQUARE								
Work size	CH1			13.000 mm					
	CH2			13.000 mm					
Work Thickness									
Tape Thickness (Effective)									
θ Deg.	CH1			0 degrees					
	CH2			90 degrees					
Cut mode	A cutting mode								
Cut dir.	REAR (from front to rear)								
Blade height	CH1	SEQ1=	0.500 mm		<b>Key Parameters to enter into the Device Data recipe</b>				
(Amount left uncut)		SEQ2=	0.000 mm		[W_S]: Glass Wafer Thickness/Wafer Grip/Si Carrier Wafer/Tape (Calculated)	1.673 mm		Distance	Units
	CH2	SEQ1=	0.500 mm						
		SEQ2=	0.000 mm						
Feed Speed	CH1			1.000 mm/sec					
	CH2			1.000 mm/sec					
Offset Y	CH1			3.250 mm					
	CH2			2.450 mm					
Y-index	CH1	SEQ1=	3.450 mm						
		Repeat	1						
		SEQ2=	0.000 mm						
		Repeat	0						
	CH2	SEQ1=	2.650 mm						
		Repeat	1						
		SEQ2=	0.000 mm						
		Repeat	0						
Depth steps	CH1	SEQ1=	0.250 mm						
		SEQ2=	0.000 mm						
	CH2	SEQ1=	0.250 mm						
		SEQ2=	0.000 mm						
Air curtain sweep speed					Default	mm			
Auto down	Wear Comp dist=			Default	mm				
(Blade wear compensation)	Wear Comp=			Default	mm				

Figure A.11. 8 × 6 Virtual CAM worksheet for array singulation.



8X6 DIE SINGULATION DEVICE DATA											
Device data No.	ronnie/	8X6 SINGULATION			Spindle rev.	5,000 RPM			Unit	mm	
ID	THICK				Precut process No.	0					
Work shape and size	SQUARE	CH1	20.000	mm	Cutting ch seq.	12					
		CH2	20.000	mm							
Work Thickness			1.081	mm		Ch 1			Ch 2		
Tape Thickness (Effective)			0.592	mm		SEQ1	SEQ2	SEQ3	SEQ1	SEQ2	SEQ3
	Ch 1	Ch 2			Blade height	0.500	0.000	0.000	0.500	0.000	0.000
θ Deg.	0.000	90.000			Feed Speed	1.000	0.000	0.000	1.000	0.000	0.000
Cut mode	A	A			Y-index	3.450	0.000	0.000	2.650	0.000	0.000
Cut dir.	REAR	REAR			Repeat times	1	0	0	1	0	0
Offset Y	3.250	2.450			Depth Steps	0.250	0.000	0.000	0.250	0.000	0.000
Noncut F	0.000	0.000									
Noncut R	0.000	0.000									

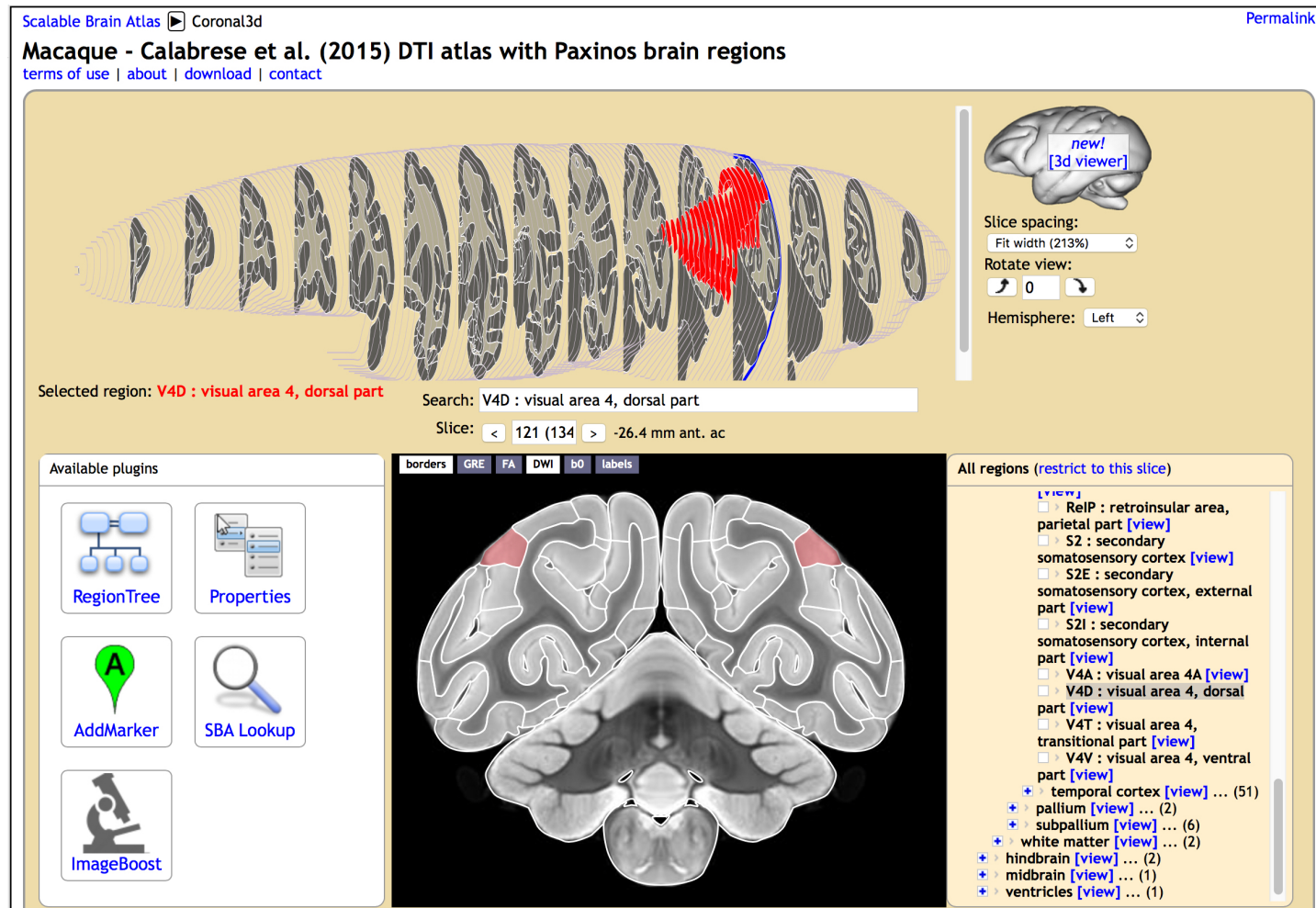
**Figure A.12.**  $8 \times 6$  “Device Data” entry items for array singulation.

## APPENDIX B

### VIRTUAL BRAIN MODELING IN SOLIDWORKS

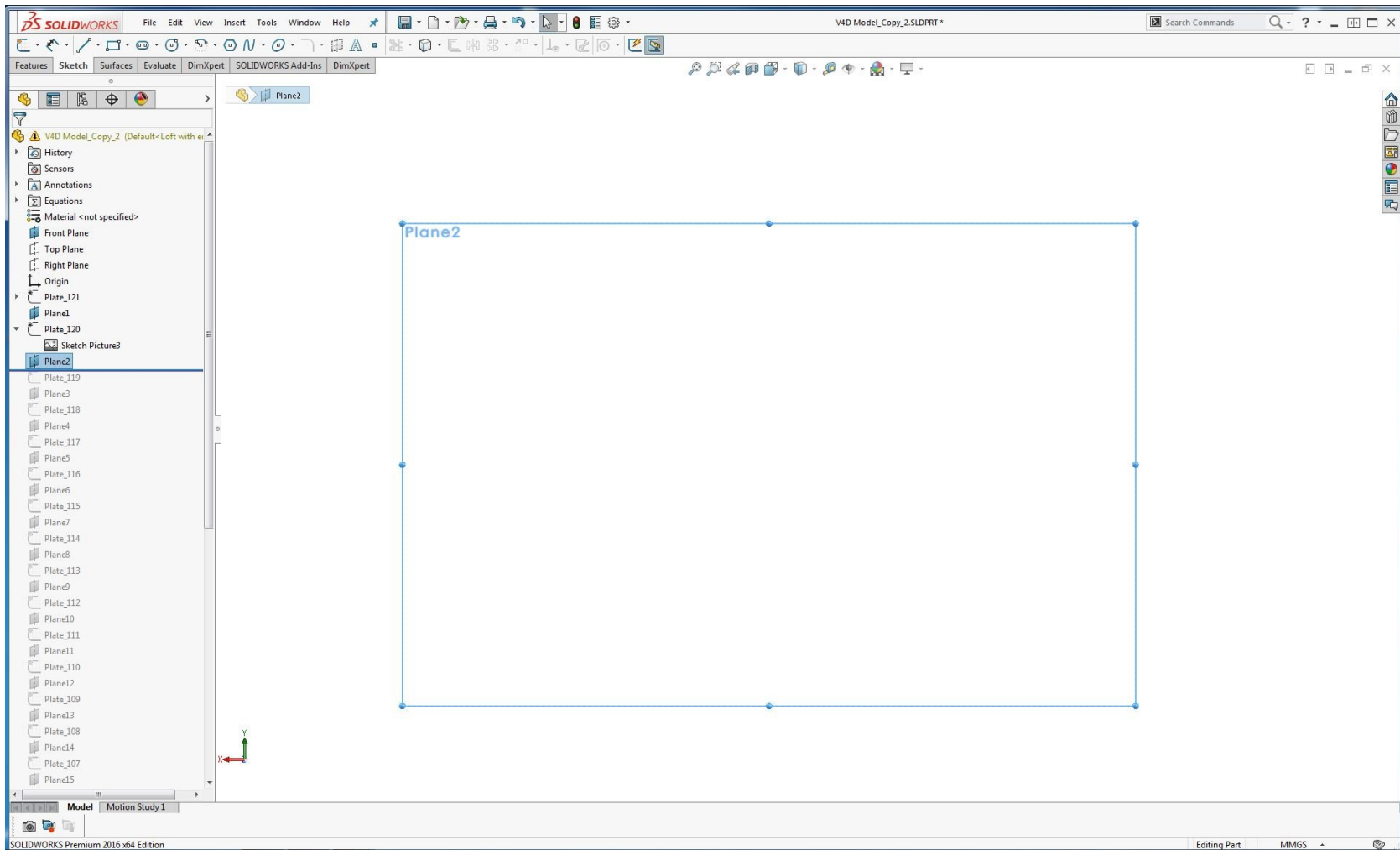
Appendix B is the process for creating a 3D CAD model in Solidworks and explains how to fit an optrode array within the brain's region of interest. This demonstration uses the Calabrese [1] macaque brain atlas as screen captured from the Scalable Brain Atlas [2] website with the Paxinos [3] dorsal region visual 4 (V4D) highlighted (See Figure B.1). For this example, the DWI (Diffusion Weighted Image) atlas was selected because the neocortex is sufficiently highlighted for depth control of the array once the 3D CAD model is completed. This image also has the Paxinos [3] region overlaid and regions of interest listed in the Scalable Brain Atlas's [2] hierarchical list view. Distances of the Calabrese [1] atlas's coordinate system are referenced against the anterior commissure (a.c), but the Paxinos [3] atlas references Bregma on the macaque skull. Lengths in Solidworks were adjusted to the Paxinos reference to Bregma because Bregma is readily available during the insertion surgeries. Calabrese [1] MRI slices are spaced at 450  $\mu\text{m}$  between 75  $\mu\text{m}$  slices, but the .jpg images screen captured have zero thickness when imported into Solidworks. Distance and thickness are simulated in Solidworks by creating sketch planes for each .jpg spacing them 60  $\mu\text{m}$  for all the slices of V4D. Figures B.2, B.3, and B.4 illustrate the process.

Once the images have been imported onto the appropriate sketch planes, the Paxinos region needs to be encircled using the "Spline" sketch tool of Solidworks as shown in Figure B.5. Each subsequent plate's V4D region is splined using this method and is shown in Figures B.6 and B.7. Each spline is then connected via the "Loft" function; Figures B.8 and B.9 show these results of the lofting. The resultant 3D CAD Brain model can then be viewed and rotated as shown in Figures B.10 through B.14. The UOA can then be refined using this model shown in the remaining Figures B.15 through B.18.

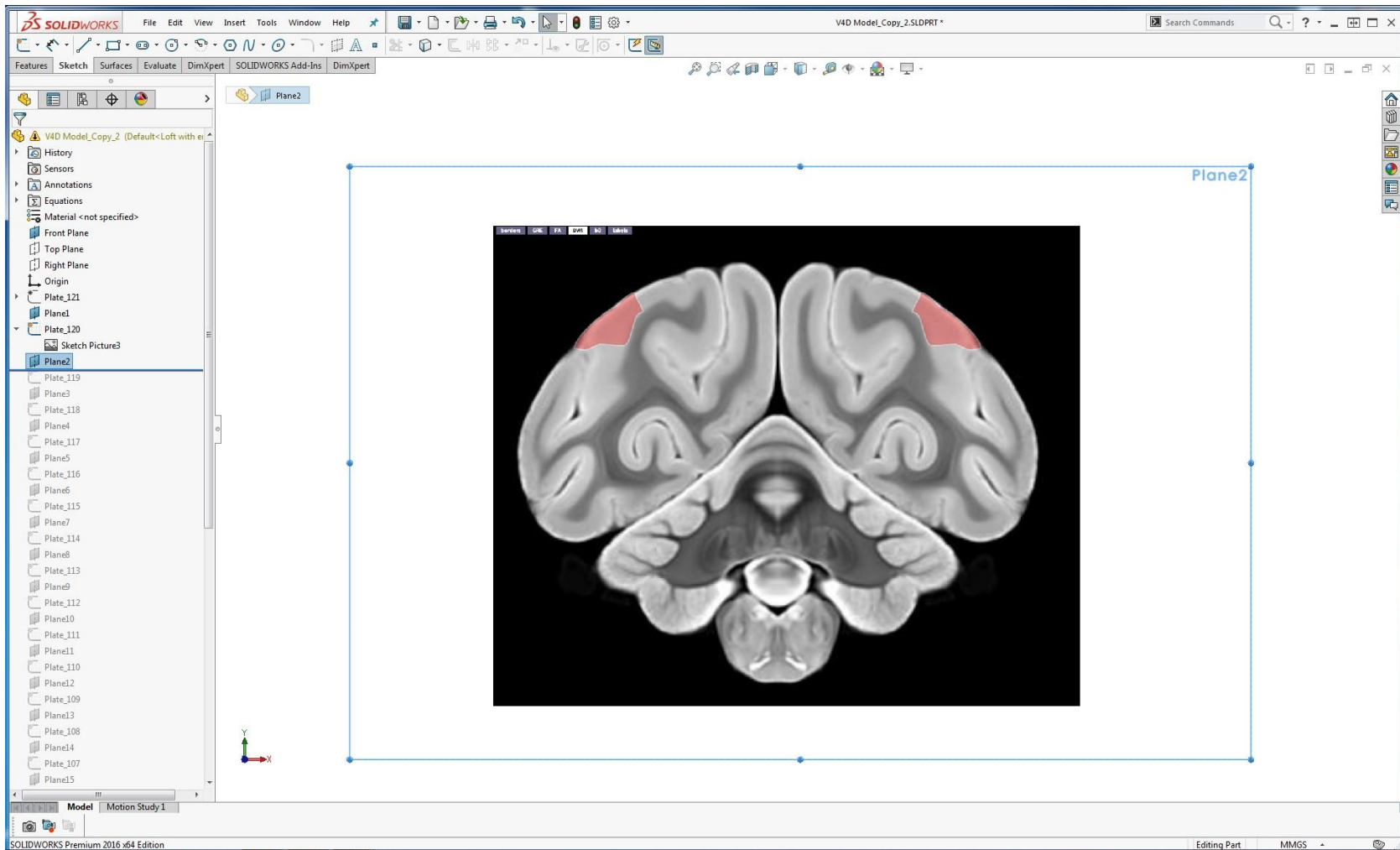


**Figure B.1.** The Scalable Brain Atlas [2] showing the Calabrese et al. [1] atlas plate with Paxinos V4D: Visual Area 4, Dorsal overlaid. This plate is 26.4 mm posterior of the anterior commissure. The Calabrese atlas has 75  $\mu$ m MRI slices spaced at 450  $\mu$ m; these measurements will be transferred to Solidworks.

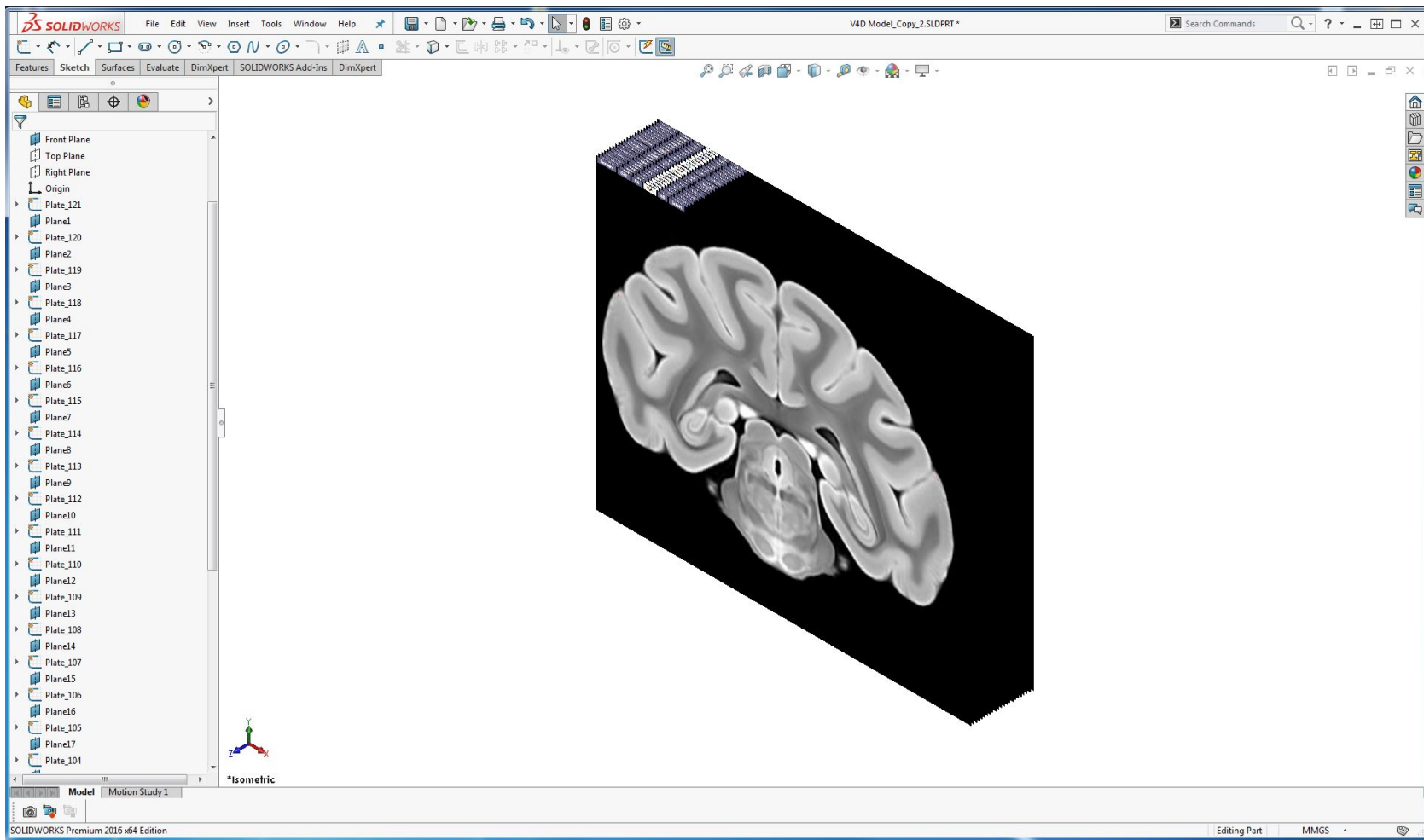




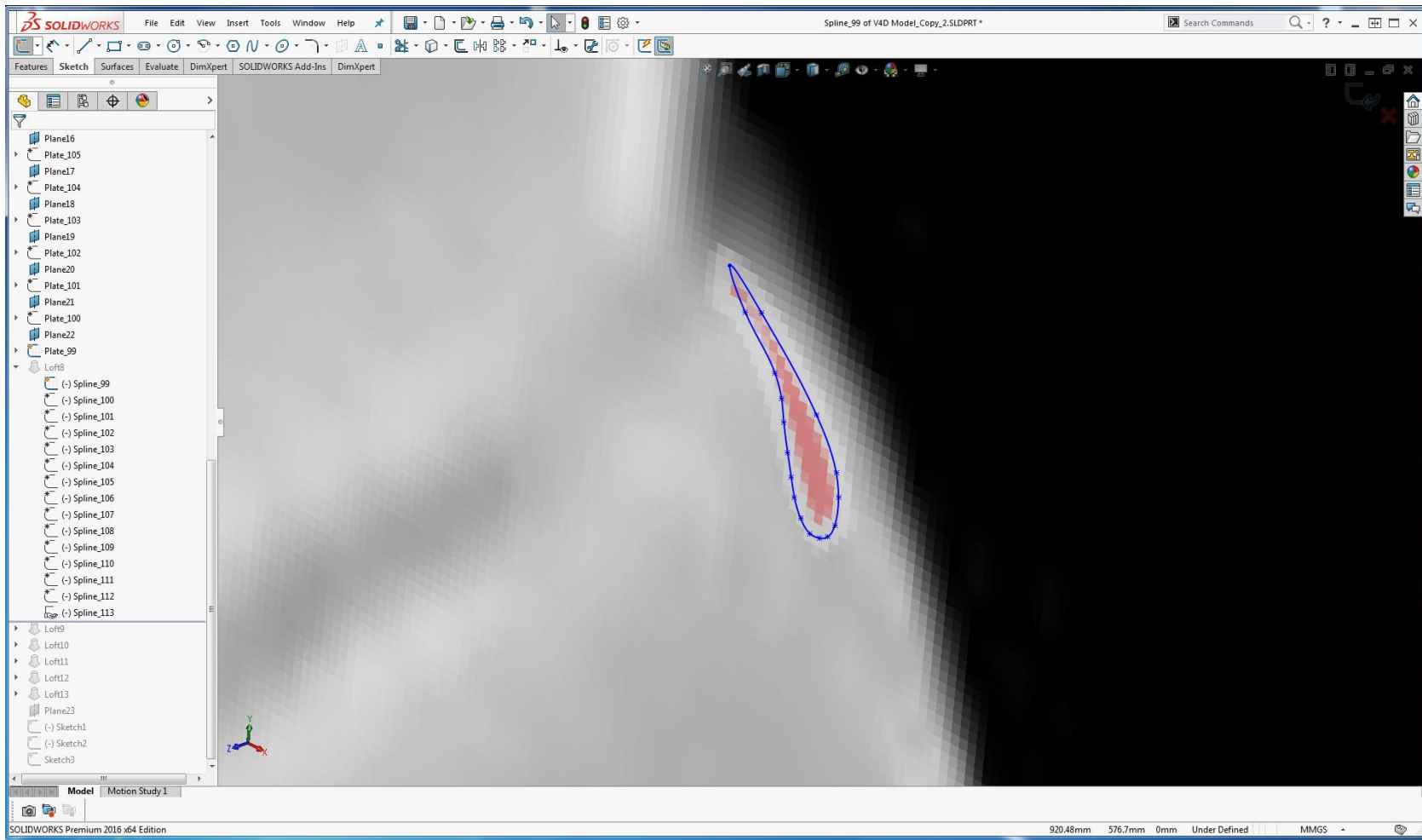
**Figure B.2.** Planes are created, in Solidworks, for the screen captured atlas plates. Each plane is placed at  $525\text{ }\mu\text{m}$  which is the MRI slices' thicknesses of  $75\text{ }\mu\text{m}$  and slice spacing at  $450\text{ }\mu\text{m}$ . It is helpful to only create the visible portion of the plane roughly the same size as the atlas plate; this will reduce confusion later as more plates are added.



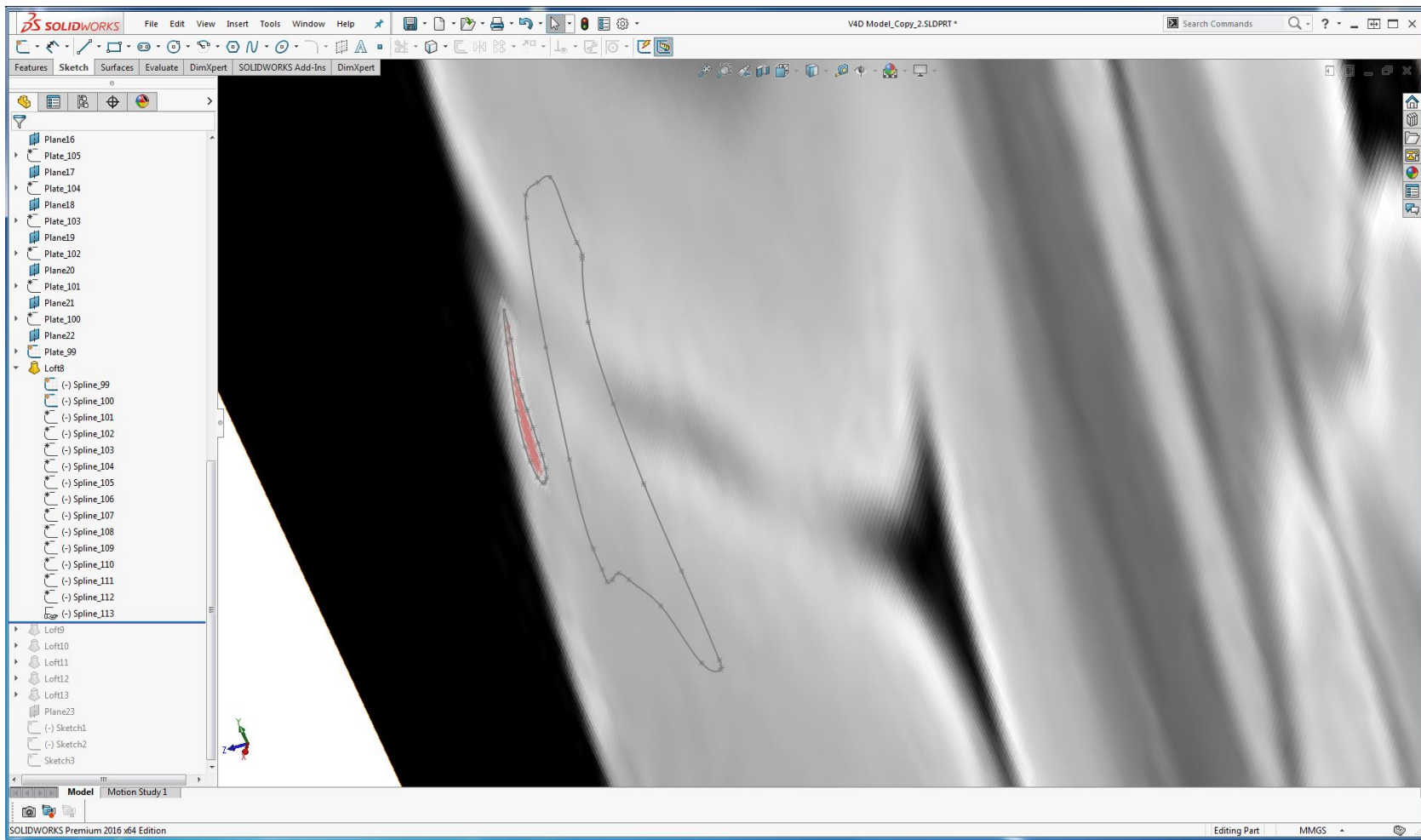
**Figure B.3.** An atlas plate is placed on Plane2 where the Paxinos [3] region for V4D is highlighted. The perimeter of this region is to be traced using the “Spline” sketch tool in Solidworks for each atlas plate in the region. Plane2’s perimeter is shown for alignment purposes of the plate. This will be turned off after the plate is positioned.



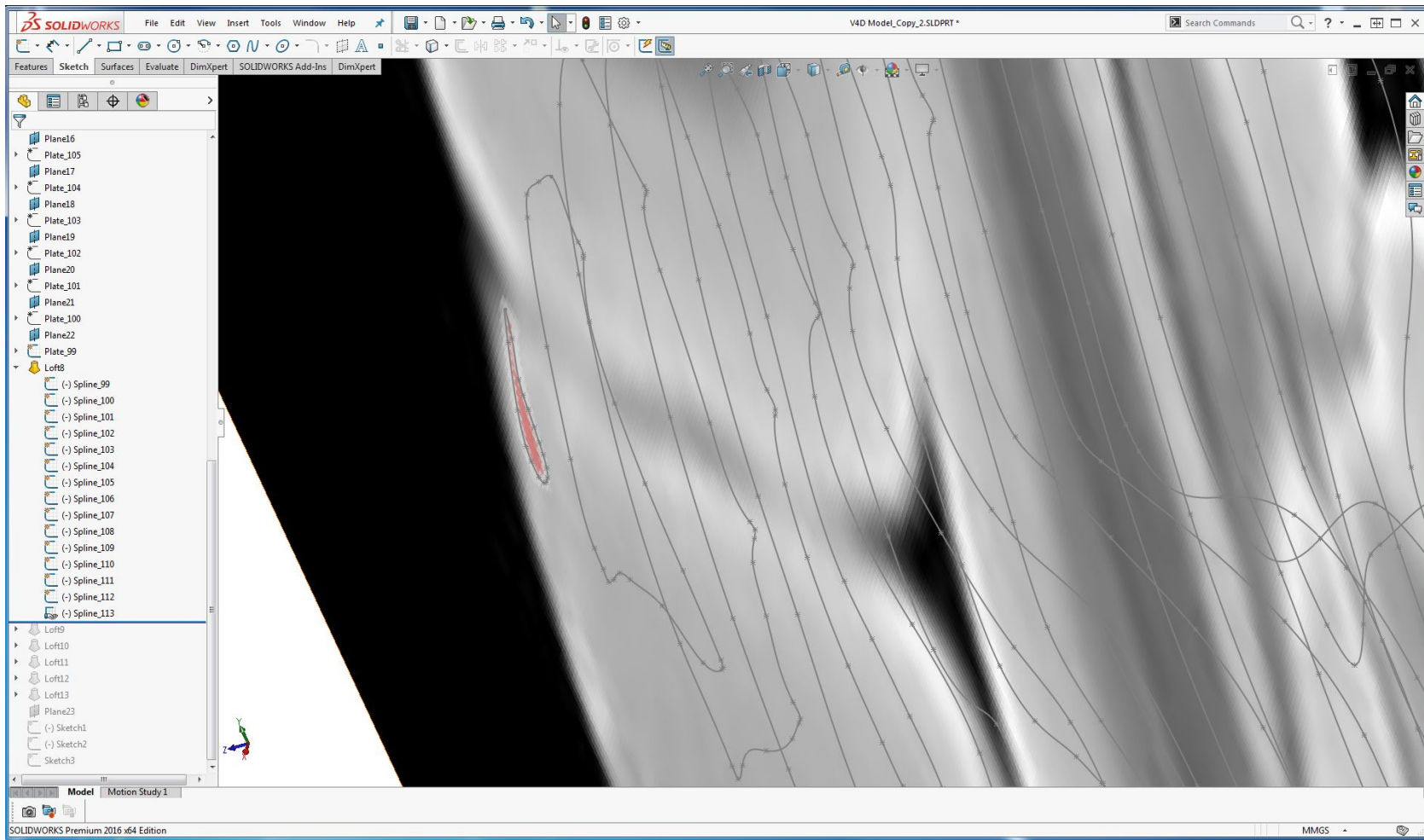
**Figure B.4.** All atlas plates for V4D have been placed on planes. Each plane perimeter has been hidden from view, which makes the plates easier to see. In this manner, the plates can now individually be hidden from view as well, and this will make it easier to see the V4D's perimeter on each plate to be splined.



**Figure B.5.** A small portion of the V4D slice is shown with the regions' perimeter splined together. No two brains have the exact same shapes or sizes, so it is not necessary to be exact with the splining operation. Splines can be adjusted for better fit by moving the handles shown on the blue line.

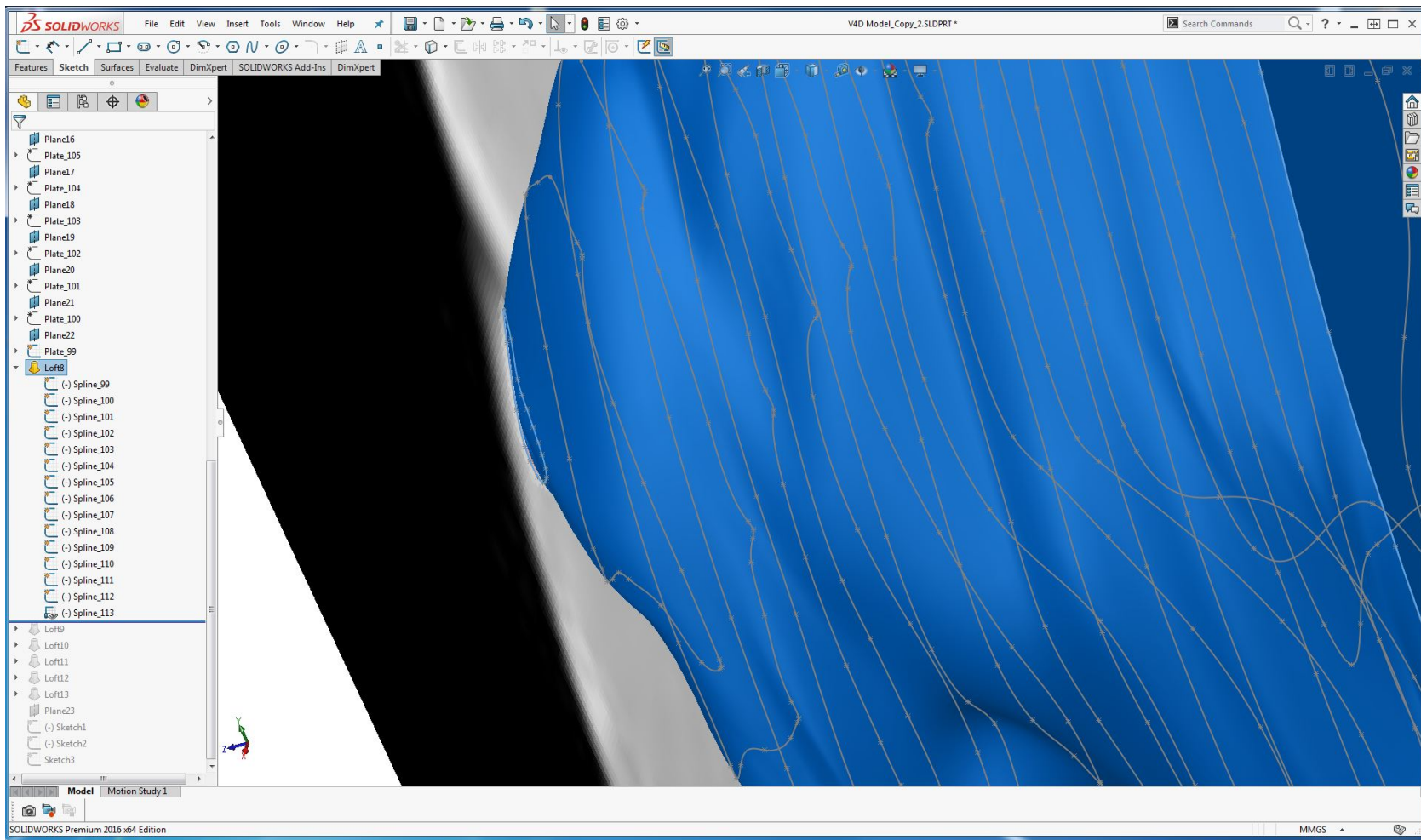


**Figure B.6.** Two plate splines are shown where one of the plates has been hidden for clarity. The larger spline is the next plate in the series as they were captured from The Scalable Atlas [2] viewer for the Calabrese et al. [1] macaque brain atlas.

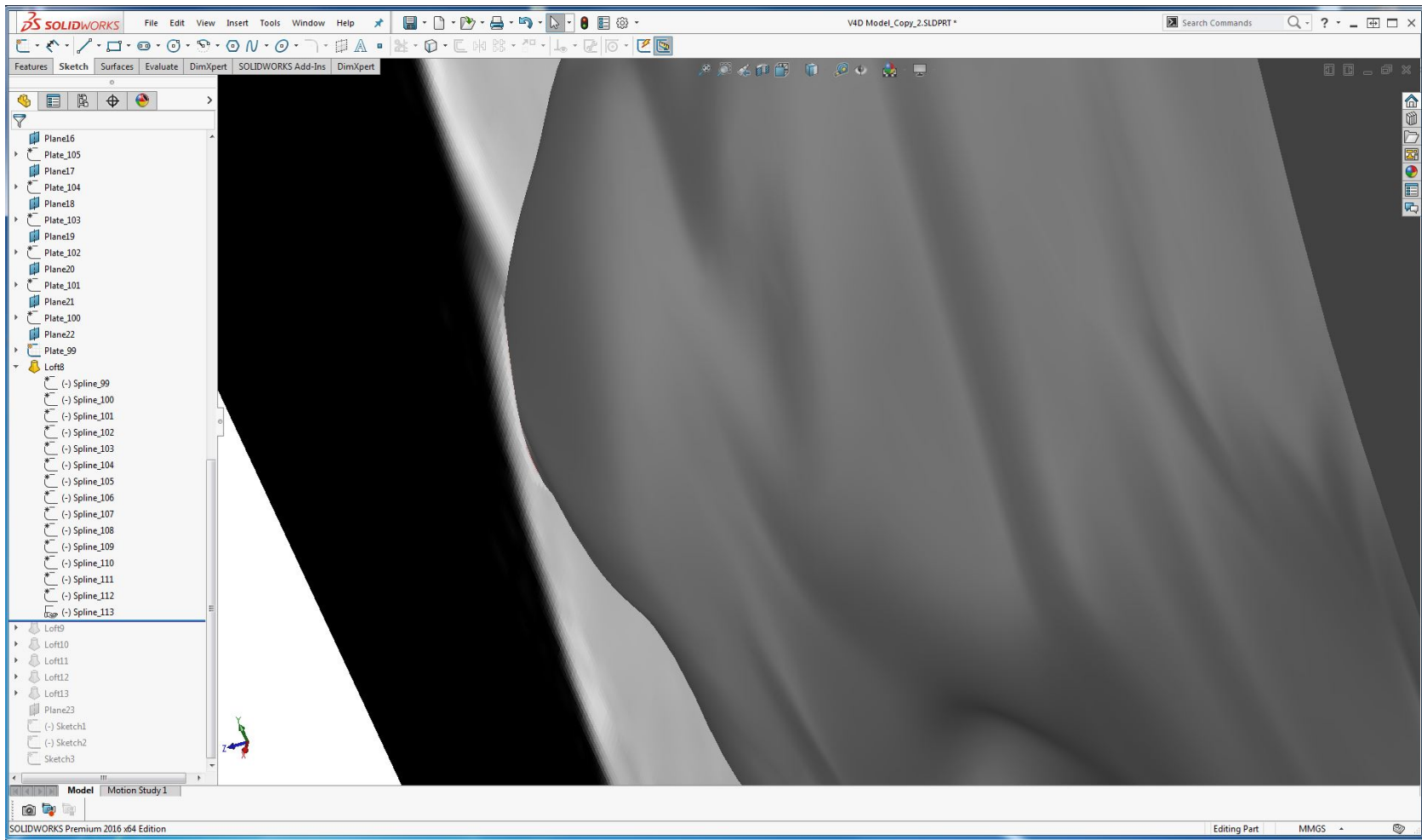


**Figure B.7.** Simultaneously viewing all splines can be confusing, but Solidworks allows for the area to be rotated for easier viewing. Each of these splined perimeters will be linked via the “Loft” command, which is the 3D version of the Spline command.



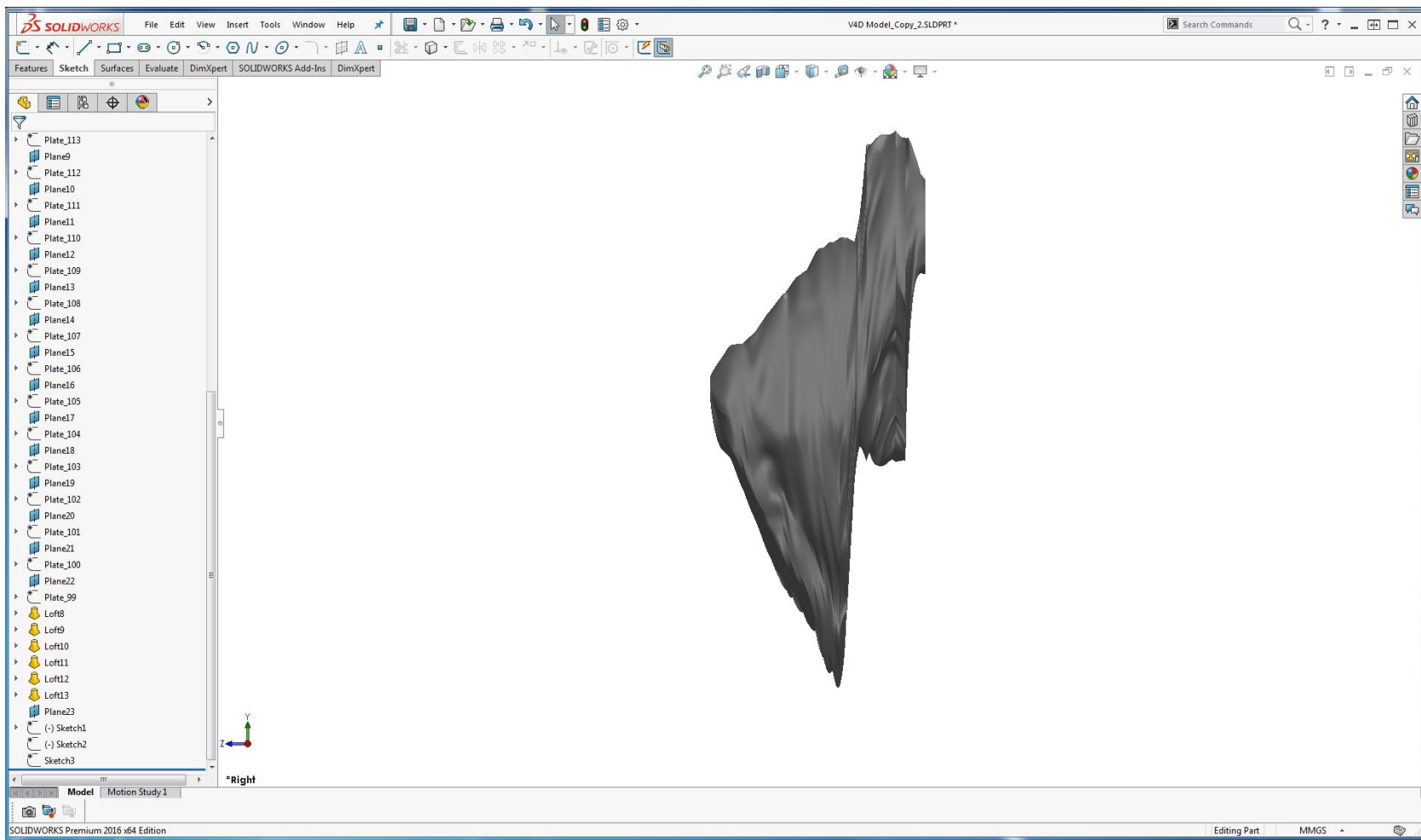


**Figure B.8.** Lofting must not create overlapping shapes or else Solidworks will display an error. Overlapping loft errors can occur in brain modeling because the slice regions may change size rapidly. It is shown here that each spline has been connected properly with no errors.

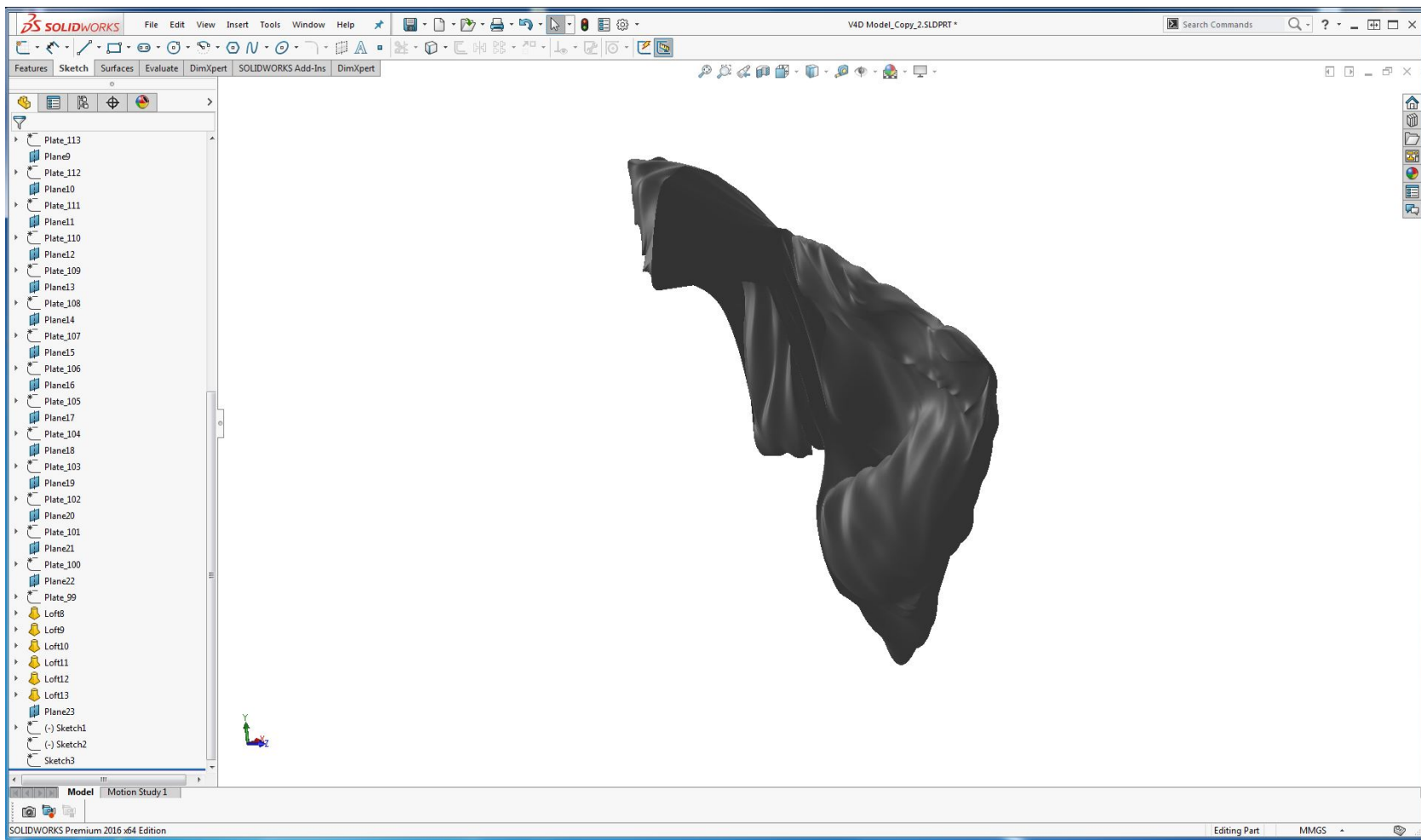


**Figure B.9.** Loft contour is seen in this image by dark shading on the virtual surface that has been created. Once each spline is lofted together, and the surface contours are shown, a solid model is automatically created at the same time.





**Figure B.10.** Front view of the modeled V4D as spline/lofted together in Solidworks. Some error is seen in the image, but overall this model is sufficient for designing a computer brain interface.



**Figure B.11.** Right view of V4D, where the concave nature of the region is clearly shown. There is a thin walled region in the center where it is critical to make sure the optrodes of the UOA do not penetrate.

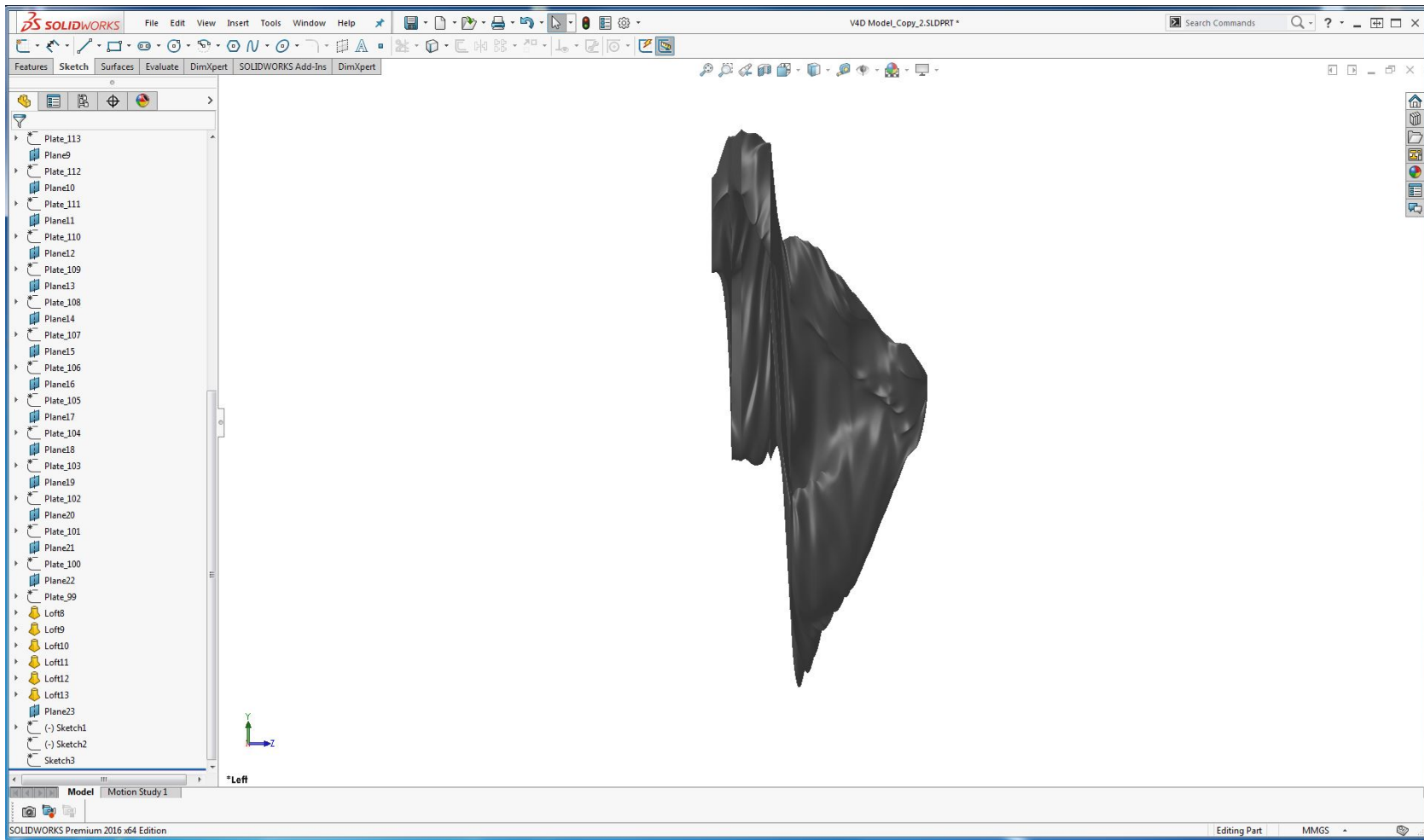


Figure B.12. Rear view of modeled V4D.

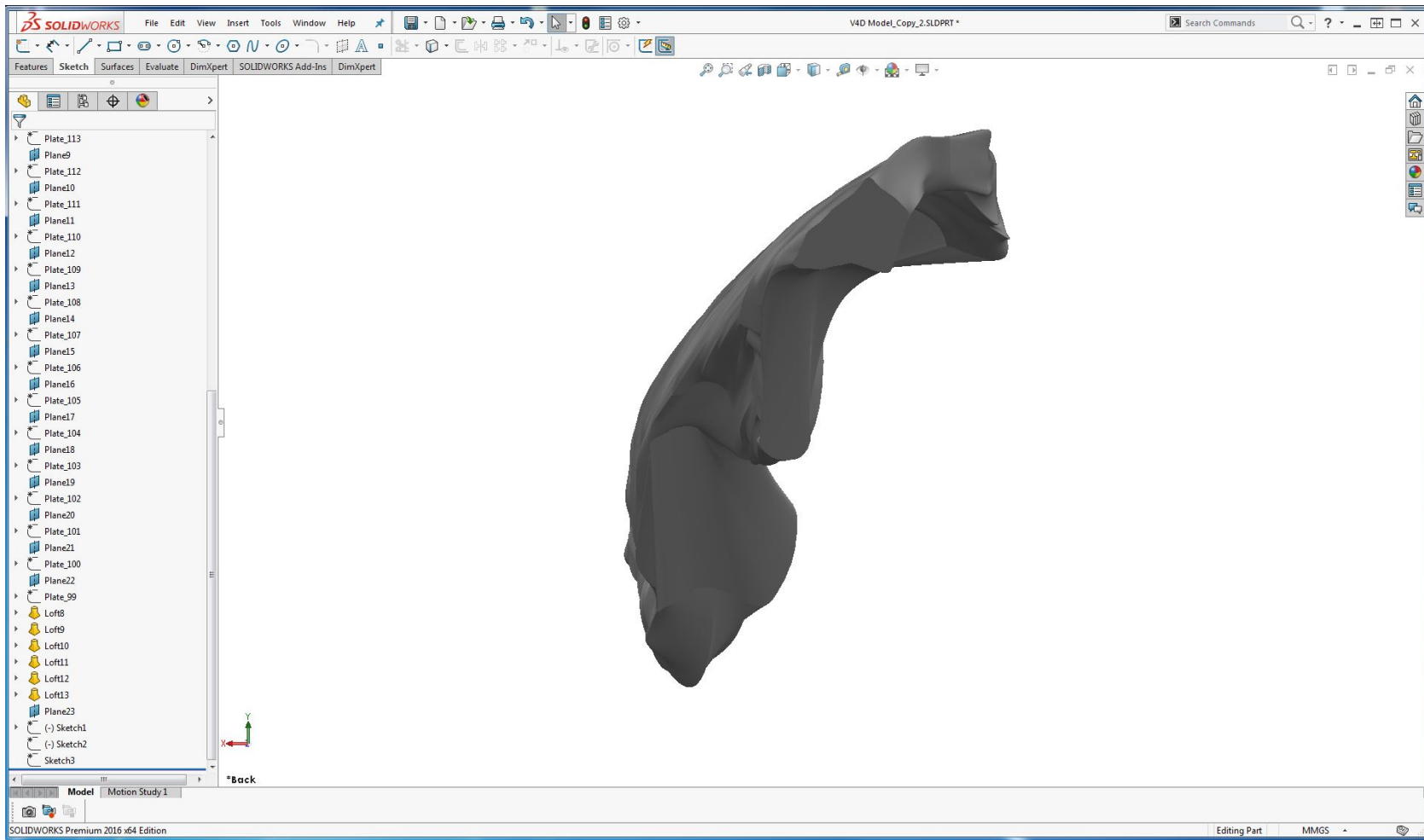
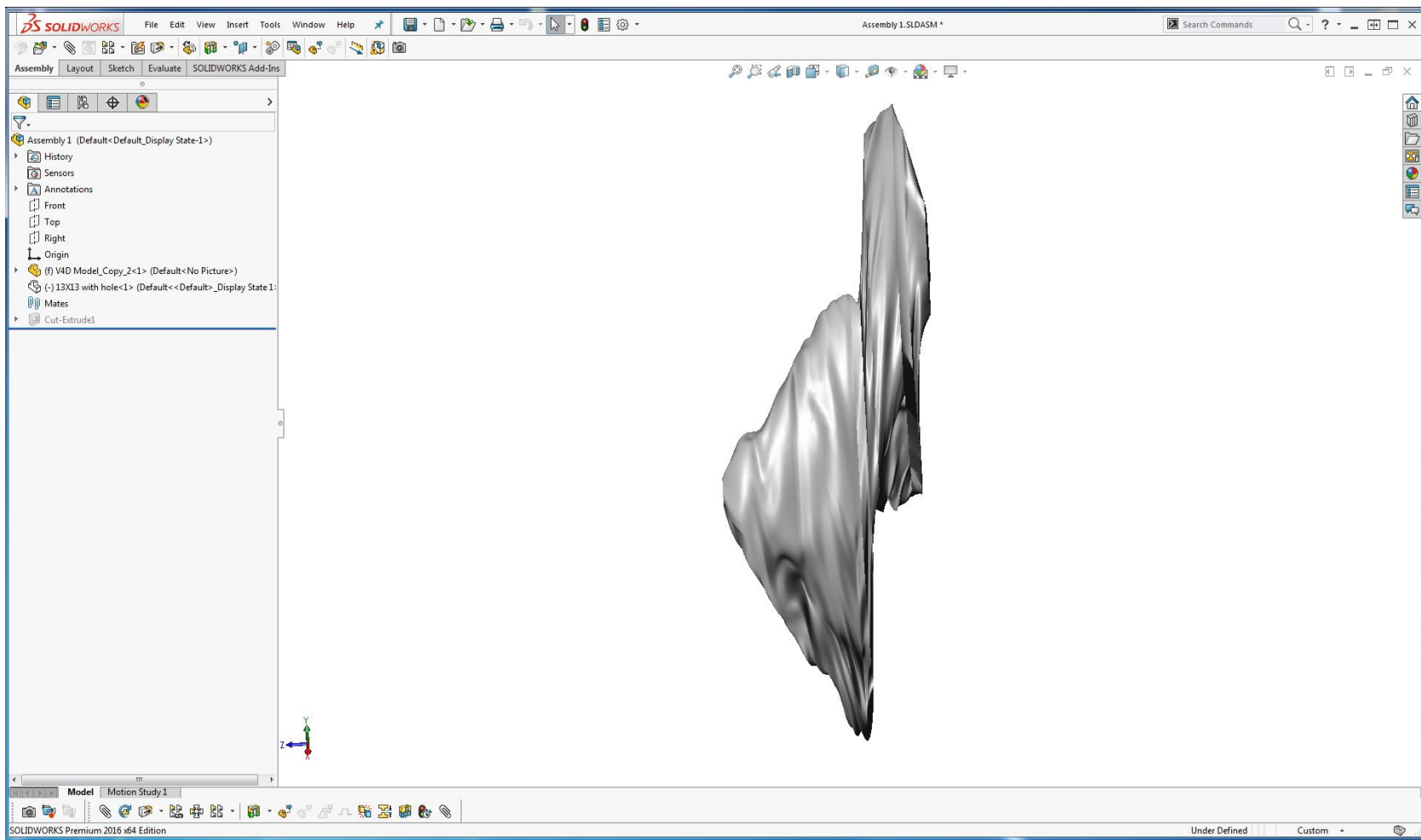
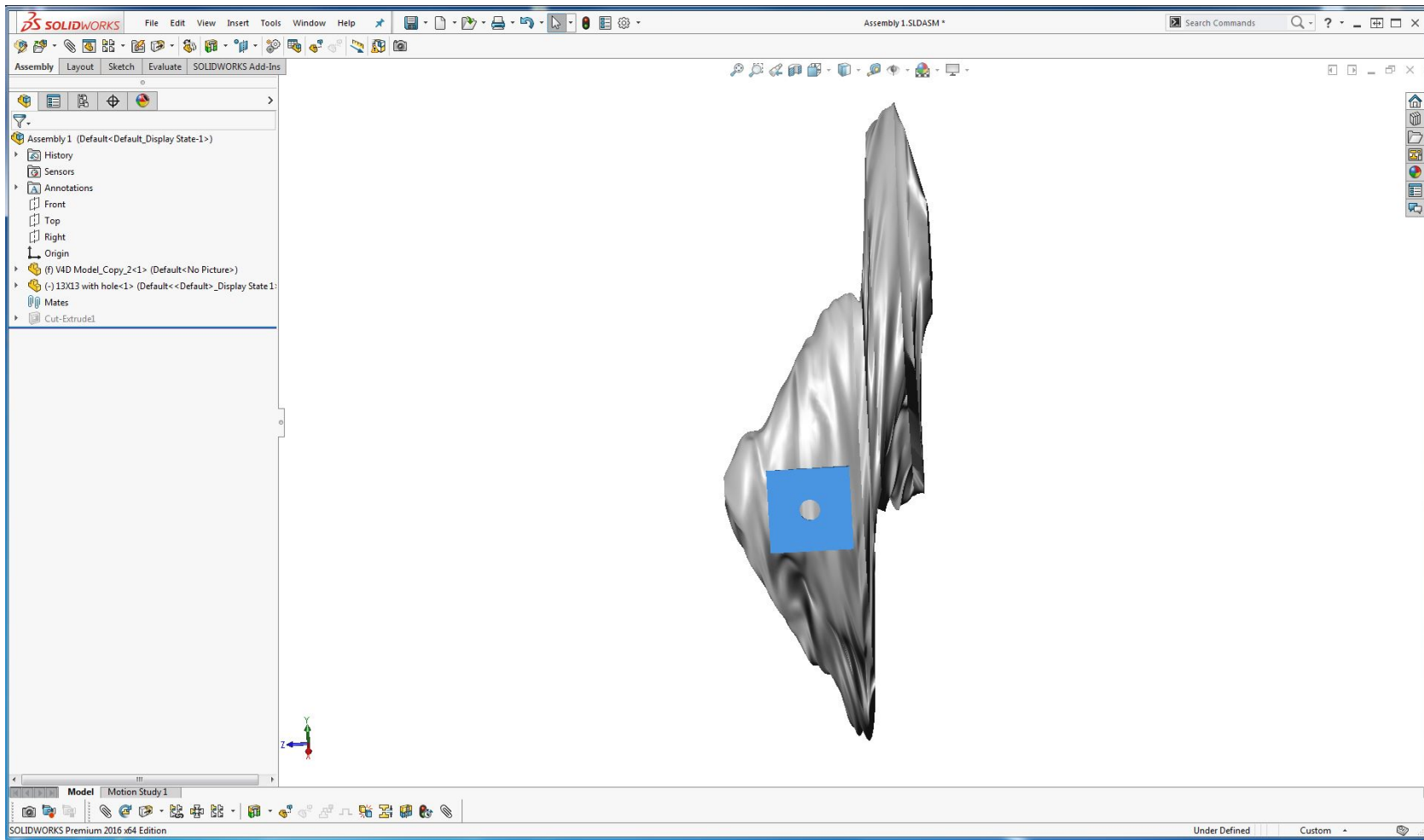


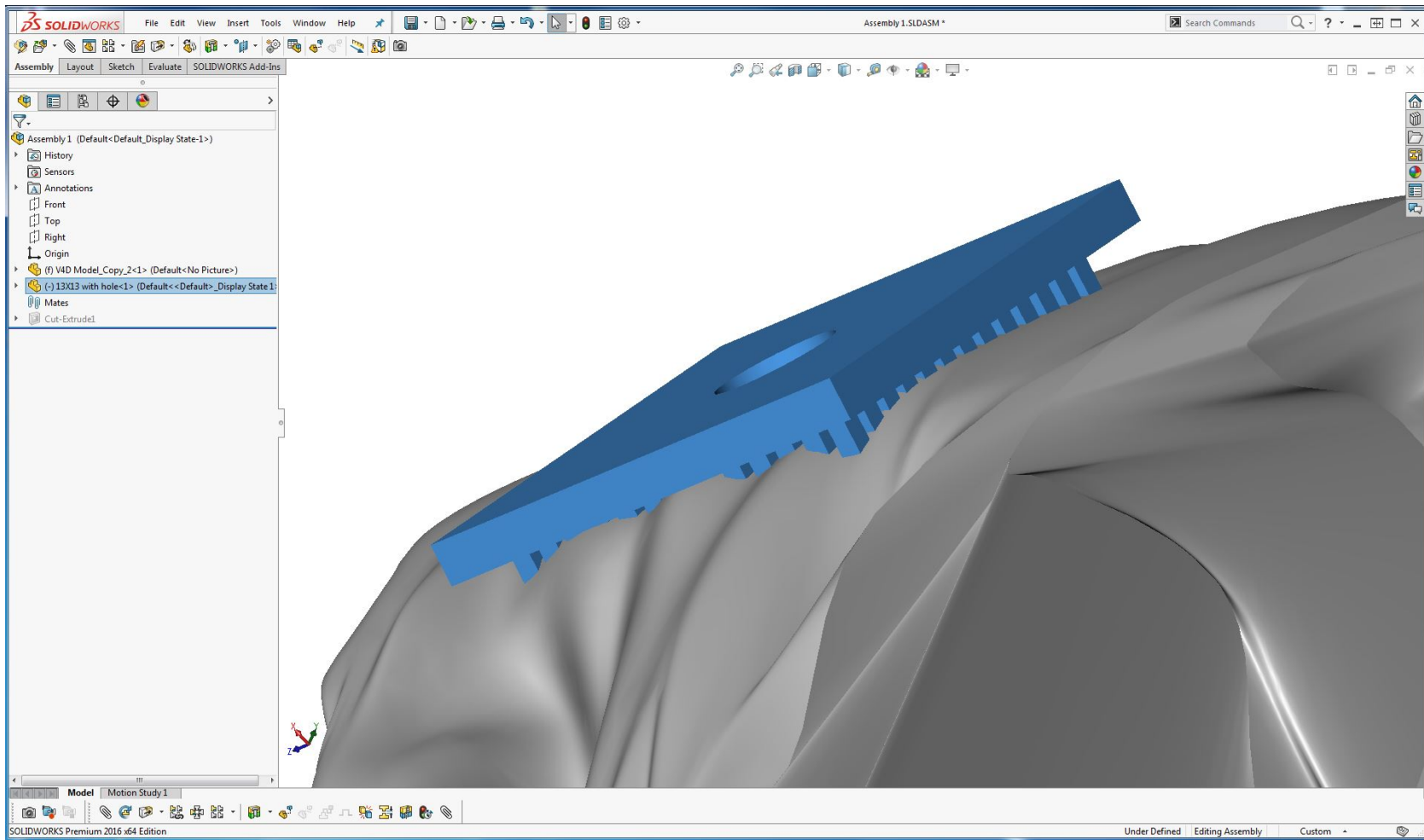
Figure B.13. Left view of modeled V4D.



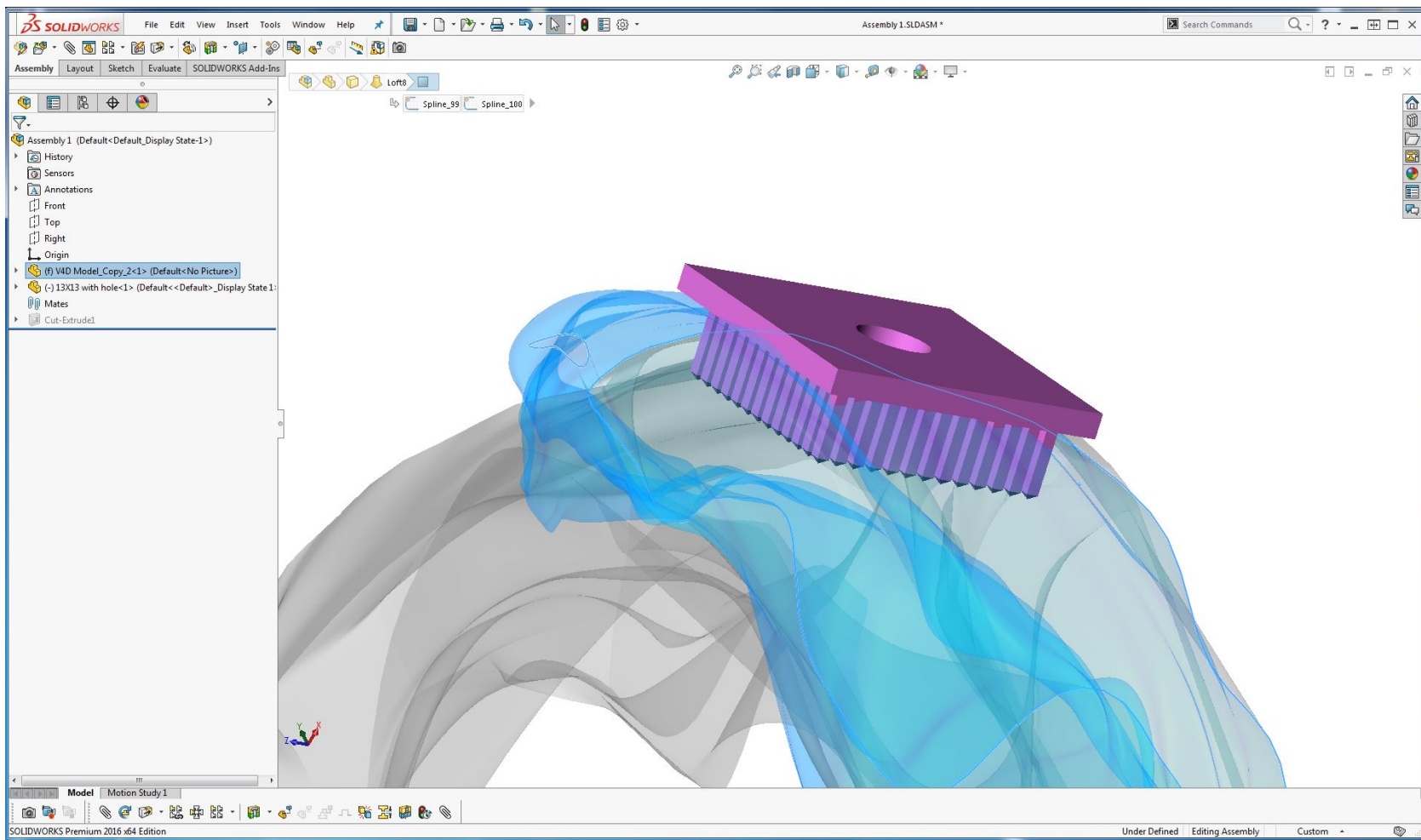
**Figure B.14.** Front view of modeled V4D rendered in contrasting color. The contrast will highlight the implanted array's optrodes when it is virtually inserted.



**Figure B.15.** Front view of modeled V4D rendered in contrasting color with  $13 \times 13$  UOA with through glass via. The TGV allows for a microelectrode to be passed, so electrical neurophysiological signals can be recorded.

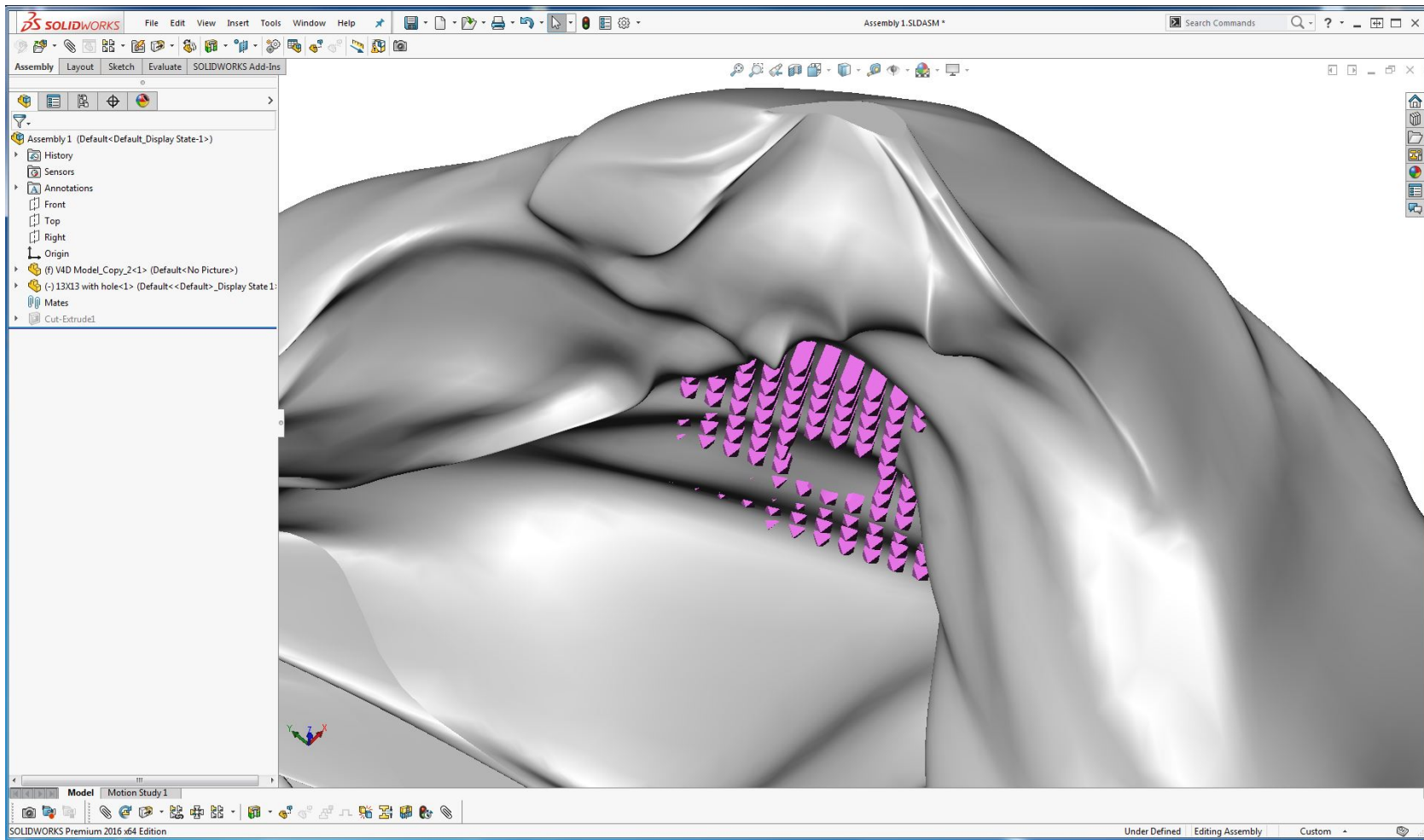


**Figure B.16.** Close up view of the 13×13 inserted on the surface. It is clear from the image that the 3D model cannot compress, so the implant rests tangentially against the tight radius of curvature of the tissue and the front-plane of the array. Microscopic scale peaks and valleys can be seen where the loft model was created. Contours are not actual sulci of the brain due to the scale of this model.



**Figure B.17.** An important feature of the 3D model is that its transparency can be changed to allow the device engineer to “see inside” the virtual tissue to make sure the implant is fully contained in the region of interest. It can be seen here the UOA is fully enclosed in tissue, proving this device capable of inserting fully into the region. Tissue compression is not represented with this technique.





**Figure B.18.** The narrow cavity on the back side of V4D is shown with a UOA that does not fall completely within the boundary of the atlas plates; therefore, a redesign of the array is necessary to reduce the length of the optrodes to better target the neocortical layers of interest.

## B.1 References

- [1] E. Calabrese, A. Badea, C. L. Coe, G. R. Lubach, Y. Shi, M. A. Styner, and G. A. Johnson, “A diffusion tensor MRI atlas of the postmortem rhesus macaque brain,” *NeuroImage*, vol. 117, pp. 408–416, Aug 2015.
- [2] R. Bakker, P. Tiesinga, and R. Kötter, “The scalable brain atlas: Instant web-based access to public brain atlases and related content,” *Neuroinformatics*, vol. 13, pp. 353–366, Feb 2015.
- [3] G. Paxinos, X. Huang, and A. Toga, *The Rhesus Monkey Brain in Stereotaxic Coordinates*. San Diego, CA. Academic Press, 2000.